Numerical Study of High Lift Configurations

by

Nirajan Adhikari

A thesis submitted to the Graduate Faculty of
Auburn University
in partial fulfillment of the
requirements for the Degree of
Master of Science

Auburn, Alabama
Aug 05, 2017

Keywords: CFD, High Lift Configuration, Turbulence Model

Approved by

D. Stephen Nichols, Assistant Professor of Aerospace Engineering
Brian S. Thurow, Department Chair, Professor of Aerospace Engineering
David Scarborough, Assistant Professor of Aerospace Engineering

Abstract

This study investigates the numerical prediction capability of Computational Fluid Dynamics (CFD) in resolving the high-lift aerodynamics. Various numerical aspects in CFD is explored in this research which includes different forms of flow governing equations with variety of turbulence models using *TENASI* as a CFD solver. The High-Lift Common Research Model (HL-CRM) is used for a grid convergence study in which the effects of grid refinements in resolving the high-lift flow features are studied. Grid refinement shows improvement in the lift prediction. JAXA Semi-Span High Lift Configuration Model (JSM) is also used in this research to investigate the effects of nacelle and pylon installation on a high lift configuration. The wind tunnel test data of JSM is compared with CFD to validate the numerical parameters used for this research. The arbitrary Mach formulation of the governing equations in *TENASI* failed to predict the stall characteristics. The incompressible solution showed some promising results with accurately predicting the angle of attack for $C_{L,max}$ but the maximum lift coefficient remains underpredicted. In the linear region of the lift curve, the numerical solution matches experiment data impressively. At a higher angle of attack, unnecessary separation on the upper surface of the wing makes the CFD solution inaccurate. The addition of nacelle and pylon to JSM shows improvements in the lift characteristics in this study and the results are consistent with the experiments.

Acknowledgments

I would like to acknowledge Dr. D. Stephen Nichols for his time and effort dedicated to this research. I would also like to extend my gratitude towards the fellow researchers in the CFD lab for maintaining a productive and motivating work environment. Also, I cannot pass on this thesis without acknowledging the wonderful HPC team at Auburn University for maintaining the availability of computational capabilities on hand throughout the progress of this research.

Table of Contents

List of Figures

List of Tables

Chapter 1

Introduction

An aircraft has additional elements attached to its wing like slats and flaps which help to maximize its lift characteristics during landing and take-off conditions. These additional elements are known as high-lift elements and a wing with inboard and outboard slats and flaps assembly is termed as a high-lift configuration. This type of multi-elements wing attachments involve complex flow-fields due to an interaction between wakes coming out of different wing elements with boundary layers. At a high angle of attack (landing and take-off conditions), high-lift elements help to maintain the flow attached to all the elements of a wing thus maximizing the lift while preventing the flow separation which might lead to aerodynamic stall. Although this type of configuration has been in practice for years, there is a lack of research models in the public domain. NASA is trying to fill out this void by developing models that are readily available to the public for the study of high-lift flow features. NASA's version of high-lift configuration is called the High Lift Common Research Model (HL-CRM) and represents a commercial transport aircraft. The main objective behind the development of the common research model is to develop high quality data sets for future validation of Computational Fluid Dynamics (CFD) studies and to serve as a platform for high-lift configuration research.

In recent years, CFD has emerged to be a powerful tool for the study of a variety of flow fields and it is in active development to solve more challenging problems like turbulence and combustion. The flow features of high-lift configurations is manly characterized by turbulence. Thus, the overall efficiency of a numerical solution is heavily dependent on turbulence models. Although current advancement of CFD tools has produced some impressive results in the field of turbulence modeling, there is a lack of effective numerical schemes that can

accurately predict the high-lift flow fields. With the main objective to assess the numerical prediction capability of current generation CFD tools and to create a common ground for the comparison of advancements and shortcomings of the state of the art in CFD methods for simulation of high-lift flow fields, American Institute of Aeronautics and Astronautics (AIAA) and NASA organized series of High Lift Prediction Workshops (HiLiftPW). The first high lift prediction workshop (HiLiftPW-1) was held in June 2010 and after successful completion of a second workshop in 2013, the third workshop was held on June 2017. As a part of the workshop, Computer Aided Design (CAD) models of high-lift configurations are provided by the organizing committee and the participants will use their preferred CFD solver to simulate the flow fields. The solutions and findings are submitted to the organization committee. This thesis presents one such study of high-lift configurations that fulfills the objectives of the 3rd high lift prediction workshop (HiLiftPW-3).

1.1 Objectives

The main objective of this thesis is to fulfill the objectives of the HiLiftPW-3, which involves:

1. Assess the numerical prediction capability of current generation CFD technology for high-lift configurations.

2. Develop practical modeling guidelines for CFD prediction of high-lift flow fields.

3. Determine the elements of high-lift flow physics that are critical for modeling to enable the development of more accurate methods and tools.

4. Enhance CFD prediction capability for practical high-lift aerodynamic design and optimization.

The specific objectives are discussed in detail below.

1.1.1 Objective 1: Generate Unstructured Mesh

This objective includes generation of high quality unstructured meshes using the CAD models provided by the HiLiftPW-3 committee. The meshes generated are used to perform the numerical computations.

1.1.2 Objective 2: Perform Numerical Simulations

The second objective provides CFD solutions by performing numerical computation on the generated meshes using appropriate boundary conditions and flow numerics parameters. This objective also includes the proper selection of a CFD solver and turbulence models to produce accurate solutions.

1.1.3 Objective 3: Analyze and Validate Numerical Solutions

Comparison of numerical solutions with experimental results is important to validate the different numerical schemes that are used to simulate the flow fields. CFD results are compared with the experimental results provided by the HiLiftPW-3 committee. Comparisons are done on the basis of grid convergence studies where lift, drag, and moments at different angle of attack are compared.

1.2 Literature Review

The HiLiftPWs were followed by abundant publications and proceedings in which the organizing committee and the participants published their findings and experiences on high-lift configurations. The major part of the literature reviewed for this research include those publications that helped draw a general guideline and identify possible challenges involved with this type of research. The summary of the first workshop was presented in the paper by Rumsey, et. al. [1] and Slotnick, et. al. [2]. The first workshop (HiLiftPW-1) involved the study of three-element swept wing tested at NASA which is referred as the NASA Trapezoidal (Trap) Wing model and the experimental data were taken from the experiments in the NASA

Langley wind tunnel. There were 21 participants in this workshop and the participants mainly solved the Reynolds Averaged Navier-Stokes Equations (RANS) for flow solutions with some participants using the Lattice-Boltzmann method. The most common turbulence model among the participants was the one equation Spalart-Allmaras (SA) or some variation of the SA model while few participants used the Menter Shear Stress Transport k-ω (SST), k-ϵ, Reynolds Stress transport Model (RSM), Wilcox k-ω, and Very Large Eddy Simulation (VLES). The results from the first workshop indicated that unstructured grids show greater sensitivities to grid refinements than its counterpart structured grids. Among unstructured grids, hybrid unstructured grid (grid with boundary layer tetrahedra merged into prisms) produced better results than unstructured tetrahedral. In overall, CFD underpredicted the coefficient of lift (C_L) and drag (C_D) in the linear region of the lift and drag curve and performed poorly at high angle of attack (near stall), and the trend was similar for pitching moment coefficient (C_M) where CFD underpredicted the magnitude of the moment. Also, CFD showed greater sensitivities towards the initial conditions at high angle of attack where CFD predicted early stall. However, initializing the simulation from the solution of lower angle of attack resolved this issue to some extent. Regarding the turbulence models, the one equation SA model performed relatively superior to other turbulence models and was in close agreement with experiments. The flow field near the wing tip turned out to be very difficult to resolve for CFD and the results submitted were not consistent, some results were fairly in agreement with experiments while others acted poorly. Since the wing tip vortex influences the flow field near the tip of the wing, accurately capturing this vortex will produce some significant improvements in the CFD solutions.

The second workshop (HiLiftPW-2) was patterned like the first workshop (HiLiftPW-1) and received 26 participants. HiLiftPW-2 involved the study of DLR-F11 model (DLR-F11 was used in the European High Lift Programme (EUROLIFT)) which represents a commercial wide-body twin-jet high-lift configuration and consists of a leading edge slat and a trailing edge Fowler flap. Like first workshop, HiLiftPW-2 was also followed by various

publications. The overview of the workshop was presented by Rumsey and Slotnick [3]. The study by Mavriplis, et. al. [4] as well as Murayama, et. al. [5] are also included in this research to understand more about the experience of working with an unstructured solver for this type of research. This workshop produced diverse sets of flow solution methods (methods that are not Reynolds-averaged Navier-Stokes) like the Galerkin adaptive finite element method, Lattice-Boltzmann (LB), and wall-modeled local-eddy simulation (WMLES) model. For turbulence models, most participants used the SA model and its variants (SA was also common in HiLiftPW-1) while several participants used the SST, the shear-stress transport with vorticity production (SST-V), the k-ϵ, the explicit algebraic Reynolds-stress model (EARSM), and the Wilcox k-ω. Contrast to HiLiftPW-1, CFD results predicted lift with good agreement in the linear region of the lift polar (up to about 16 deg) while over-predicting lift at higher angle of attack. Despite the over prediction of lift, the angle of attack for $C_{L,max}$ was predicted with reasonable accuracy. With the grid refinement, it is generally expected for various CFD results to come closer to one another but this trend was not evident in the results. Due to a lack of clear trend among turbulence models, it was difficult to draw any conclusion regarding the performance of a particular type of turbulence model, however in the study by Mavriplis [4], the k-ω model was reported to be in close agreement with experiments despite the fact it under-predicted the maximum lift value. The SA model was found to have less sensitivity towards the grid refinement in the study by Murayama [5], and the study suggests to use SA models where computation has to be carried out in a coarser grid. Regarding the flow physics, from the comparison of results between configurations, with and without the brackets, it has been summarized that the stall mechanism of a high-lift configuration is driven by the slat brackets.

The CFD results from both workshops lacked consistency and was very difficult to draw conclusions, but the overall outcome seems promising for future workshops. The high-lift flow fields are difficult to model for CFD, and further investigation is needed in this field. Continuous advancement of CFD techniques including meshing capabilities and turbulence

modeling will improve the CFD predictabilities of high-lift flow fields and therefore continuous research is needed in this area.

1.3 Computational Fluid Dynamics

Computational Fluid Dynamics (CFD) is the numerical solution of fluid governing equations. Any fluid flow can be represented by the Navier-Stokes equations, whereas an inviscid flow can be simply modeled by the Euler equations. Since these equations are non-linear Partial Differential Equations (PDE), there is not an analytical solution, they can only be solved numerically. The numerical approach to solve a non-linear PDE involves discretization of the PDE into an algebraic form and solving iteratively until the solution is converged. The discretization of the governing equations is achieved through various techniques like Finite Difference Method (FDM), Finite Volume Method (FVM), and Finite Element method (FEM). For most aerodynamic flows, FVM is popular as it directly calculates fluxes through fluid domains. However, FDM and FEM are also equally applicable based on specific cases.

The most generic form of governing equations particularly represented in CFD is given as in Eq. 1.1 with appropriate boundary conditions.

$$\partial_t U + \nabla \cdot \vec{F^c} - \nabla \cdot \vec{F^\nu} = S \quad \text{in } \Omega, \text{ t} > 0 \tag{1.1}$$

In this general form U represents state variables, $\vec{F^c}$ and $\vec{F^\nu}$ are convective and viscous fluxes respectively, and $S(U)$ is a generic source term.

$$U = \begin{bmatrix} \rho \\ \rho u_1 \\ \rho u_2 \\ \rho u_3 \\ \rho E \end{bmatrix}, \vec{F_i^c} = \begin{bmatrix} \rho u_i \\ \rho u_i u_1 + P\delta_{i1} \\ \rho u_i u_2 + P\delta_{i2} \\ \rho u_i u_3 + P\delta_{i3} \\ \rho u_i h \end{bmatrix}, \vec{F_i^\nu} = \begin{bmatrix} 0 \\ \tau_{i1} \\ \tau_{i2} \\ \tau_{i3} \\ u_j \tau_{ij} + \mu^*_{tot} C_p \partial_i T \end{bmatrix} \quad i, j = (1, 2, 3) \tag{1.2}$$

In Eq. 1.2, ρ is the density, ρu_1, ρu_2, ρu_3 are the flux component of x-momentum, y-momentum and z-momentum respectively, ρE is the flux of total energy, P is the static pressure, h is the fluid specific enthalpy, δ_{ij} is the Kronecker delta function, C_p is the specific heat capacity at constant pressure, T is temperature which is determined from ideal gas law: $T = P/(\rho R)$, R is the specific gas constant, and τ_{ij} is the viscous stress which can be given as:

$$\tau_{ij} = \mu_{tot}(\partial_j u_i + \partial_i u_j - \frac{2}{3}\delta_{ij}\nabla \cdot \vec{u}) \tag{1.3}$$

where μ_{tot} is the sum of dynamic and eddy viscosity (or total viscosity) where dynamic viscosity is calculated using Sutherland's law and eddy viscosity is calculated using the turbulence models. The total viscosity is given as in Eq. 1.4

$$\mu_{tot} = \mu_{dyn} + \mu_t \quad \text{and} \quad \mu^*_{tot} = \frac{\mu_{dyn}}{Pr_d} + \frac{\mu_t}{Pr_t} \tag{1.4}$$

where Pr_d and Pr_t are dynamic and turbulent Prandtl numbers respectively.

1.3.1 Turbulence Modeling

An attempt to model turbulence dates back to Boussinesq when he proposed a shear stress/strain relationship of a time-averaged one dimensional flow in the form:

$$\overline{\tau_{xy}} + \tau^R_{x,y} = (\mu_{dyn} + \mu_t)\frac{\partial \overline{u_x}}{\partial y} \tag{1.5}$$

in which $\overline{\tau_{xy}}$ is the average viscous stress and τ^R_{xy} (or τ^R_{ij} in tensor notation) is called *Reynolds Stress* which is equal to $-\overline{\rho u'_i u'_j}$ (u' and v' are the fluctuating components of the velocity and Boussinesq's approximation relates $-\overline{\rho u'_i u'_j}$ to $\mu_t(\partial_j u'_i + \partial_i u'_j)$), the term is obtained from averaging the Navier-Stokes equation (Reynolds Averaged Navier-Stokes Equation (RANS)). The term $\overline{\rho u'_i u'_j}$ couples the mean flow with the turbulence as if the turbulent fluctuation has given additional stress to the mean flow, hence the name Reynolds stress. Prandtl was

first to propose a theory to estimate ν_t (where $\nu = \mu/\rho$) known as *mixing length theory* which is analogous to predicting molecular viscosity using Kinetic theory of gases. Prandtl proposed the momentum exchange between eddies moving between different layers gives rise to turbulent viscosity in the same manner as the exchange of momentum by movement of molecules between different layers results in molecular viscosity. The equation for turbulent viscosity is thus given as in Eq. 1.6.

$$\nu_t = l_m V_T \tag{1.6}$$

where l_m is the mixing length and V_T is the suitable measurement of $|u'|$ (this applies that with energetic turbulence there will be a greater exchange in momentum). For one-dimensional shear flow, mixing length theory leads to Eq. 1.7 which determines the turbulent viscosity as:

$$\nu_t = l_m^2 |\frac{\partial \bar{u_x}}{\partial y}| \tag{1.7}$$

The mixing length can be determined from an experiment, and this model works reasonably well for simple one-dimensional shear flows which only has one characteristics length scale. However, this eddy viscosity model is a highly simplified model which assumes turbulent eddies to be discrete as molecules which is not true as the eddies constantly interact with each other. Another shortcoming of this model is that it assumes a scalar relation between strain rate and viscosity rather than through a tensor.

Another approach to produce better modeling of turbulence takes V_T as $k^{1/2}$ (where k is the turbulence kinetic energy, $k = \frac{1}{2}\bar{u'^2}$) with the idea that the more energetic the turbulence, the greater the momentum exchange; hence, the larger value of ν_t. Further, the mixing length (l_m) is of the same order of magnitude as the integral length scale (l) as large eddies contribute most to the momentum exchange. Thus, Eq. 1.6 becomes

$$\nu_t \sim k^{1/2} l \tag{1.8}$$

The majority of turbulence models available today use Eq. 1.8 or similar form. Most popular among them are the one equation Spalart-Allmaras model and two equation $k-\epsilon$ model and $k-\omega$ model. For example, in the $k-\omega$ model, the above equation is expressed in the form:

$$\nu_t = k/\omega \tag{1.9}$$

where ω is the specific dissipation rate ($\omega \sim u/l$). In this model, k and ω are solved by using the transport equations of k and ω respectively. Among various turbulence models, the basic idea remains the same i.e. to solve for turbulent viscosity.

The transport equations in Wilcox $k-\omega$ model [6] in the conservative form are as follows:

$$\frac{\partial(\rho k)}{\partial t} + \frac{\partial(\rho u_j k)}{\partial x_j} = \tau_{ij}\frac{\partial u_i}{\partial x_j} - \beta^*\rho\omega k + \frac{\partial}{\partial x_j}\left[(\mu + \sigma_k\frac{\rho k}{\omega})\frac{\partial k}{\partial x_j}\right] \tag{1.10}$$

$$\frac{\partial(\rho\omega)}{\partial t} + \frac{\partial(\rho u_j \omega)}{\partial x_j} = \frac{\gamma\omega}{k}\tau_{ij}\frac{\partial u_i}{\partial x_j} - \beta\rho\omega^2 + \frac{\partial}{\partial x_j}\left[(\mu + \sigma_\omega\frac{\rho k}{\omega})\frac{\partial \omega}{\partial x_j}\right] \tag{1.11}$$

The constants associated with transport equations are:

$$\sigma_k = 0.5 \quad \sigma_\omega = 0.5 \quad \beta^* = 0.09 \quad \beta = 0.075 \quad \gamma = \frac{\beta}{\beta^*} - \frac{\sigma_\omega k^2}{\sqrt{\beta^*}} \tag{1.12}$$

1.3.2 Flow Solver

The CFD solver used for this research is *Tenasi* which is an unstructured solver developed at University of Tennessee SimCenter at Chattanooga and jointly maintained with researchers at Auburn University. *Tenasi* is node-centered, finite volume solver which is able to solve variety of flow regime: Incompressible, Incompressible Surface Capturing, Compressible, Arbitrary Mach Number and Compressible Multi-Species, which makes this solver a powerful tool for solving any fluid dynamics problem. The inviscid fluxes are evaluated

using either ROE or HLLC flux-differencing scheme while the viscous fluxes are evaluated using a directional derivative approach. Additional advantage of *Tenasi* is that it offers the hybrid large eddy and RANS solution along with many popular turbulence models when compared to other flow solvers. It has the one equation Spalart-Allmaras model, the one equation Menter SAS model, the two equation $q-\omega$ model, the two equation $k\epsilon k\omega$ hybrid model, the two equation $k-\epsilon$ model, the modified Wilcox Stress$-\omega$ model, and various modified version of the Launder-Shima Reynolds stress model. The solution algorithm has a loose coupling between mean flow and turbulence where the mean flow is calculated using the eddy viscosity and then the turbulent quantities are computed with the new mean flow values. The turbulence models are solved in a similar manner as mean flow except the advection term in turbulent models are upwinded because of the dependency on the direction of information propagation. The hybrid large eddy and RANS model is an attractive feature for this research as it is expected to produce better resolution of turbulence structures which significantly improve the efficiency of the solution of high-lift flow fields.

The preconditioned unsteady three-dimensional Reynolds-averaged Navier-Stokes equations used for this research that is incorporated in *Tenasi* in Cartesian coordinate are [7]:

$$M\Gamma^{-1}\frac{\partial}{\partial t}\int_{\Lambda} Q d\mathcal{V} + \int_{\partial\Lambda} \vec{F}_c \cdot \hat{\vec{n}} dA = \int_{\partial\Lambda} \frac{\vec{F}_\nu \cdot \hat{\vec{n}}}{Re_L} dA \tag{1.13}$$

where $\hat{\vec{n}}$ is the outward pointing normal vector to the control volume $\mathcal{V}$. The Eq. 1.13 is in non-conservative form and the vector of the dependent variables and the components of flux vectors are given as:

$$Q = \begin{bmatrix} \rho \\ u \\ v \\ w \\ P \end{bmatrix} \tag{1.14}$$

$$\vec{F}_c \cdot \hat{\vec{n}} = \begin{bmatrix} \rho\Theta \\ \rho u\Theta + \hat{n}_x P \\ \rho v\Theta + \hat{n}_y P \\ \rho w\Theta + \hat{n}_z P \\ (e_t + abP)\Theta - a_t abP \end{bmatrix} \tag{1.15}$$

$$\vec{F}_\nu \cdot \hat{\vec{n}} = \begin{bmatrix} 0 \\ \Psi_x \\ \Psi_y \\ \Psi_z \\ Q_h \end{bmatrix} \tag{1.16}$$

$$\begin{aligned} \Psi_x &= \hat{n}_x\tau_{xx} + \hat{n}_y\tau_{xy} + \hat{n}_z\tau_{xz} \\ \Psi_y &= \hat{n}_x\tau_{yx} + \hat{n}_y\tau_{yy} + \hat{n}_z\tau_{yz} \\ \Psi_z &= \hat{n}_x\tau_{zx} + \hat{n}_y\tau_{zy} + \hat{n}_z\tau_{zz} \\ Q_h &= u\Psi_x + v\Psi_y + w\Psi_z + \hat{n}_x q_x + \hat{n}_y q_y + \hat{n}_z q_z \end{aligned} \tag{1.17}$$

where $a = \gamma - 1$, $b = M_r^2$, u, v, and w are the Cartesian velocity components in the x, y, and z directions, and $\hat{n}_x$, $\hat{n}_y$, and $\hat{n}_z$ are the components of the normalized control volume face vector. Θ is the velocity normal to a control volume face:

$$\Theta = \hat{n}_x u + \hat{n}_y v + \hat{n}_z w + a_t \tag{1.18}$$

where the grid speed $a_t = -(V_x\hat{n}_x + V_y\hat{n}_y + V_z\hat{n}_z)$ and the control volume face velocity is given by $\vec{V_s} = V_x\hat{i} + V_y\hat{j} + V_z\hat{k}$. The variables in the preceding equations are normalized with respect to characteristics length scale (L_r) and reference values of velocity (U_r), density (ρ_r), and viscosity (μ_r). Thus, the Reynolds number is defined as $Re = U_r L/\nu_r$. Pressure is normalized by $\rho_r U_r^2$ and the equation of state becomes $P = \rho T/\gamma M_r^2$ where T is Temperature, $M_r = U_r/c_r$ is the reference Mach number, and $c_r^2 = \gamma R T_r$ is the reference speed of sound.

For a perfect gas, the reference enthalpy is expressed as $h_r = C_p T_r$, the specific heat ratio is defined as $\gamma = C_p/C_v$.

The Jacobian for the change to primitive variables is defined as

$$M = \begin{bmatrix} 1 & 0 & 0 & 0 & 0 \\ u & \rho & 0 & 0 & 0 \\ v & 0 & \rho & 0 & 0 \\ w & 0 & 0 & \rho & 0 \\ ab\phi & ab\rho u & ab\rho v & ab\rho w & b \end{bmatrix} \tag{1.19}$$

where $\phi = (u^2 + v^2 + w^2)/2$. The preconditioning matrix is defined as $\Gamma = diag(1, 1, 1, 1, \beta)$ where $\beta = min(M_r^2, 1)$. But for this research, the preconditioning is turned off which means the term β is set to 1.

Also, the incompressible form of the governing equations are also investigated in this study for the solution of high-lift flow fields. The incompressible unsteady three-dimensional Reynolds-averaged Navier-Stokes equations are briefly presented in Cartesian coordinates and in conservative form as [8]:

$$\frac{\partial}{\partial t}\int_\Omega Q d\mathcal{V} + \int_{\partial\Omega} \vec{F}\cdot\hat{\vec{n}} dA = \int_{\partial\Omega} \vec{F}_v \cdot \hat{\vec{n}} dA \tag{1.20}$$

where $\hat{\vec{n}}$ is the outward pointing unit normal to the control volume $\mathcal{V}$. The vector of dependent variables and the components of the inviscid and viscous flux vectors are given as

$$Q = \begin{bmatrix} P \\ u \\ v \\ w \end{bmatrix} \tag{1.21}$$

$$\vec{F} \cdot \hat{\vec{n}} = \begin{bmatrix} \beta\left(\Theta - a_t\right) \\ u\Theta + \hat{n}_x P \\ v\Theta + \hat{n}_y P \\ w\Theta + \hat{n}_z P \end{bmatrix} \tag{1.22}$$

$$\vec{F}_v \cdot \hat{\vec{n}} = \begin{bmatrix} 0 \\ \hat{n}_x\tau_{xx} + \hat{n}_y\tau_{xy} + \hat{n}_z\tau_{xz} \\ \hat{n}_x\tau_{yx} + \hat{n}_y\tau_{yy} + \hat{n}_z\tau_{yz} \\ \hat{n}_x\tau_{zx} + \hat{n}_y\tau_{zy} + \hat{n}_z\tau_{zz} \end{bmatrix} \tag{1.23}$$

where β is the artificial compressibility parameter, u, v, and w are the Cartesian velocity components in the x, y, and z directions, and $\hat{n}_x$, $\hat{n}_y$, and $\hat{n}_z$ are the components of the normalized control volume face vector. Θ is the velocity normal to a control volume face:

$$\Theta = \hat{n}_x u + \hat{n}_y v + \hat{n}_z w + a_t \tag{1.24}$$

where the grid speed $a_t = -\left(V_x\hat{n}_x + V_y\hat{n}_y + V_z\hat{n}_z\right)$ and the control volume face velocity is $\vec{V}_s = V_x\hat{i} + V_y\hat{j} + V_z\hat{k}$. The variables in the preceding equations are normalized with respect to a characteristic length scale (L_r) and reference values of velocity (U_r), density (ρ_r), and viscosity (μ_r). Thus, the Reynolds number is defined as $Re = \rho_r U_r L_r/\mu_r$. Pressure is normalized with $P = \left(P^* - P_\infty\right)/p_r {U_r}^2$ where P^* is the local dimensional static pressure.

The turbulence models incorporated in *Tenasi* include various improvements to the baseline turbulence models [9][10]. In a study by Nichols, et. al. [9], Detached Eddy Simulation (DES) modifications to the hybrid $k-\epsilon, k-\omega(k\epsilon k\omega)$ and the Scale Adaptive Simulation (SAS) modifications to the one-equation $k-\epsilon$ have shown improvements in resolving the wake produced by a surface-mounted cube. The modifications were done as an attempt to alleviate the grid sensitivity for selection of turbulent length scale and calculate

the length scale based on the local flow features for better representation of the turbulence field.

One Equation $k-\epsilon$ Turbulence Model with SAS modifications

The modifications to the baseline $1k\epsilon$ [11][12] turbulence model is presented as [9]:

$$\frac{\partial}{\partial t}\int_{\Omega}\tilde{\nu}_t d\mathcal{V}+\int_{\partial\Omega}\tilde{\nu}_t\Theta dA=\frac{1}{Re}\int_{\partial\Omega}\left(\nu+\frac{\tilde{\nu}_t}{\sigma_m}\right)\overrightarrow{\nabla\tilde{\nu}_t}\cdot\hat{\vec{n}}dA+\mathcal{V}\left[P-D+C\right] \tag{1.25}$$

where

$$P=c_1 d_1 S\tilde{\nu}_t \quad D=\frac{c_2\tilde{\nu}_t^2}{{l_t}^2 Re_L} \quad C=\left(\nabla\cdot\overrightarrow{u}\right)\tilde{\nu}_t \tag{1.26}$$

$$S=\left(2S_{ij}S_{ij}-\frac{2}{3}\left(\nabla\cdot\overrightarrow{u}\right)^2\right)^{1/2} \quad S_{ij}=\frac{1}{2}\left(\frac{\partial u_i}{\partial x_j}+\frac{\partial u_j}{\partial x_i}\right) \quad d_1=1.0+0.4\frac{\nu_t}{\tilde{\nu}_t} \tag{1.27}$$

$$l_t=\min\left(l_1,d_v\right) \quad l_1=\max\left(l_2,C_{SAS}\Delta_{min}\right) \quad {l_2}^2=\frac{S^2}{\nabla S\cdot\nabla S} \tag{1.28}$$

and where $c_1=0.144$, $c_2=1.86$, $\sigma_m=1.0$, d_v is the distance to the nearest viscous surface, $C_{SAS}=0.6$, and Δ_{min} is the local minimum node-to-node distance. The boundary conditions used for this study enforce $\tilde{\nu}_t=0.0$ on a viscous surface and $\tilde{\nu}_t=1.3$ for the farfield boundary. The eddy viscosity is determined by

$$\mu_t=\rho\nu_t=d_2\rho\tilde{\nu}_t \tag{1.29}$$

$$d_2=1.0-\exp\left[-0.2\left(b_1\chi+b_2\chi^3+b_3\chi^5\right)\right] \tag{1.30}$$

$$\chi=\frac{\tilde{\nu}_t}{\nu} \quad b_1=0.001 \quad b_2=0.005 \quad b_3=0.0055 \tag{1.31}$$

Notice that the damping functions d_1 and d_2 are modified from their original form [11] and are not included in recent efforts [12]. The original form of the damping terms generates a turbulent profile, but the model transitions to the freestream further away from the body

than the other models used in the *Tenasi* algorithm, and consequently, produces low values for drag. The modified damping functions noticeably improve these calculations.

The determination of the turbulent length scale l_t also differs from the baseline formulation. From the beginning, the $1k\epsilon$ model [11] was derived with the express intent to design production and destruction terms that were independent of d_v, the distance from the viscous surface. However, testing with the *Tenasi* flow solver showed a weakness in this approach for some wake flows. Modifying l_t to take d_v into account quickly corrected this problem.

Recent efforts with SAS [12] prescribe a different manner of computing l_2 than the one given in Eq. 1.28. However, testing over a variety of test cases has shown no clear advantage of one approach to the other. As such, l_2 given in Eq. 1.28 is used in the *Tenasi* flow solver due to its computational efficiency.

In addition, one of the most important factors in solver selection for this research is the ability of a solver to run in parallel high performance Linux cluster. The meshes used in this research are computationally demanding and are usually of more than 50 million nodes ($\sim$50M for medium grid resolution while $\sim$120M for finer grid resolution). *Tenasi* comes with MPI support for parallel operation and is designed to run computationally demanding grids by proper division of grid and numerical computation to maximize the performance while minimizing the associated memory overhead. Availability of various turbulence models and the ability to run in Linux clusters make *Tenasi* an ideal CFD solver for this research.

Chapter 2

3rd AIAA CFD High Lift Prediction Workshop

The 3rd AIAA CFD High Lift Prediction Workshop (HiLiftPW-3) is a continuation of the series of workshops organized by AIAA for the study of high-lift configurations. HiLiftPW-3 is patterned like HiLiftPW-1 and HiLiftPW-2 and was organized in June, 2017. This workshop is being held in conjunction with a sister-workshop on *Geometry and Mesh Generation*, and similar to previous workshops, geometric CAD models of high-lift configurations are provided with general mesh generation guidelines for participants to generate meshes and run simulations using their preferred CFD solvers.

2.1 Research Models

HiLiftPW-3 involves the study of two different configurations: (1) NASA's High Lift Common Research Model (HL-CRM) and (2) JAXA Semi-Span High Lift Configuration Model (JSM)[1]. The two research models are explained in detail below.

2.1.1 High Lift Common Research Model

The HL-CRM is based on NASA's high speed common research model with modification to enhance suitability for low speed operations. It better represents an actual aircraft than the trapezoidal wing which was used in HiLiftPW-1. Figure 2.1 presents the HL-CRM model with nacelle and pylon assembly. However for HiLiftPW-3, the configuration is provided without the nacelle and pylon assembly, and there is a single slat element along the wing span. The development of the high-lift CRM from the high speed CRM is summarized in the paper by Lacy, et. al. [13]. Incorporating additional elements like slats and flaps to the high

[1]JAXA stands for Japanese Aerospace Exploration Agency

Figure 2.1: High Lift Common Research Model (HL-CRM)

speed model resulted in various modifications to the leading and trailing edge curvature of the wing element. To facilitate future wind tunnel testing, the trailing edge of all individual elements has been set to 0.20 inch full scale so that the model is easy to manufacture and retains robustness even with 5-6% scale model [13]. The uniform trailing edge thickness also facilitates the mesh generation, which otherwise would include sharp corners resulting in highly skewed mesh elements. A high lift element has many surfaces and trim information associated with it. So during modifications, an attempt was made to obtain a minimum number of surfaces by defining multiple individual elements as a single surface.

2.1.2 JAXA Semi-Span High Lift Configuration Model

The JSM is a realistic aircraft model with slats, flaps, nacelle, and pylon assembly and models a typical 100 passenger class regional jet airliner. JAXA team performed a series of wind tunnel tests to study the effect of nacelle-pylon installation to JSM at various angles of attack. The wind tunnel test model has a 2.3 m semi half-wing span and is 4.9 m in fuselage length, and is fitted with 456 static pressure tabs at 7 wing cross sections (Fig. 2.2). In a

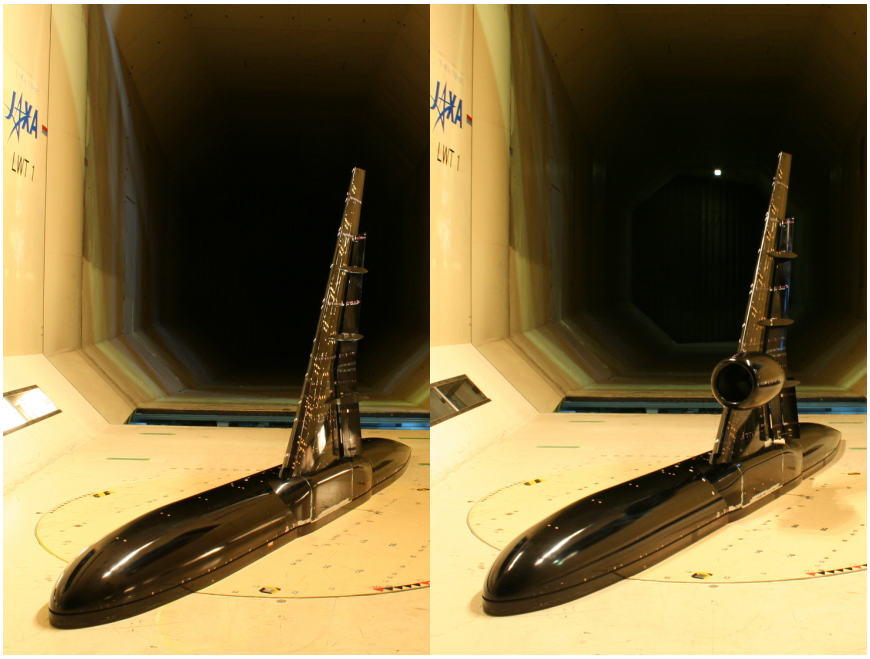

Figure 2.2: JAXA Semi-Span High Lift Configuration Model (JSM)

similar CFD workshop for a high lift configuration in Japan, it was noticed that the CFD results were consistent among participants, but the results did not agree with the experiments [14]. The use of a semi-span model instead of a full aircraft model was identified as one of the reason for such inconsistency as the spacer height (the spacer is located between fuselage and wind tunnel wall) changes the effective angle of attack. The boundary layer building off the wind tunnel wall adds a crossflow component to the free-stream which results in a change in effective angle of attack of the wing. One possible solution to this problem is to increase the spacer height, but a large spacer height changes the effective aspect ratio. In an attempt to reduce the differences between experiment and CFD computation, wind tunnel tests were performed to assess the effect of spacer height on aerodynamic characteristics of the aircraft model. The results were compared with CFD results obtained using a full-span model in a free-flight condition and a half-span model mounted on a no-slip wall. The details of the study are presented in a paper by Yokokawa, et. al. [14], and the study revealed the change in spacer height from 0 mm to 150 mm corresponds to changes in lift, drag, and moment

coefficients by $\Delta C_L = 0.08$, $\Delta C_D = 0.013$, $\Delta C_M = 0.03$, respectively. As a result, spacer height corresponding to $2 \sim 3$ times of the displacement thickness of the floor boundary layer was obtained to be an optimum height for a half-span model experiment which corresponds to 50 mm $\sim$ 110 mm in spacer height. The wind tunnel test data are provided for the comparison with CFD results where the CFD study is performed using a half-span model simulated in a free-stream condition without the wind tunnel walls.

2.2 Test Cases

As mentioned earlier, the HiLiftPW-3 features the study of two different high-lift configurations. NASA's HL-CRM is yet to be tested in a wind tunnel and does not have any experimental results available at present. Thus, the analysis for this configuration is a blind test case where grid convergence is studied without any comparison with the experimental results. On the other hand, JAXA JSM model involves the nacelle installation study in which models, with and without nacelle and pylon assembly, are studied at different angle of attack. The different test cases in HiLiftPW-3 are explained in detail below:

2.2.1 Grid Convergence Study

This effort involves the investigation of series of consistently refined grids (coarse, medium, and fine) of the HL-CRM for the study of grid convergence. The HL-CRM is studied in a nominal landing configuration without nacelle, pylon, tail or support brackets. The thermodynamic conditions and the model specifications associated with the model are shown in the Table 2.1. The simulation condition is fully turbulent flow as free air without the effects of wind tunnel walls or model support system. In this study, the viscosity of the fluid is adjusted to get the desired Reynolds number of $3.26 * 10^6$. The viscosity of the flow in this case is $1.7859E-04$ kg/(ms) instead of $1.7859E-05$ kg/(ms) at 288 K temperature.

Mach Number	0.2
Angle of Attack (α)	8 and 16^0
Mean Aerodynamic Chord (MAC)	275.8 in full scale
Wing Semi-Span	1156.75 in
Reference Area of the Semi-Span Model ($S_{ref}/2$)	297360.0 in^2
Reynolds Number based on MAC	$3.26 * 10^6$
Reference Static Temperature	$518.67^0 R$ (= 288K)
Reference Static Pressure	760.21 mmHg
Moment Reference Center (MRC)*	X= 1325.90 in, Y= 468.75 in, Z= 177.95 in
*The model alignment is such that for any α, the flow direction is (Cosα, 0, Sinα).	

Table 2.1: Model specifications and operating conditions for HL-CRM

2.2.2 Nacelle Installation Study

The study of the JSM is a nacelle installation study which provides insight on the effects of the nacelle and pylon assembly on a high lift system. The study is performed on a nominal landing configuration with support brackets and the nacelle/pylon on/off configurations. The experiment used a semi-span model with a 60 mm spacer height but for this case, the simulation is performed as fully turbulent free air. The model specifications are tabulated in Table 2.2.

Mach Number	0.172
Angle of Attack (α)	4.36, 10.47, 14.54, 18.58, 20.59, and 21.57^0
Mean Aerodynamic Chord (MAC)	529.2 mm model scale
Wing Semi-Span	2300.0 mm
Reference Area of the Semi-Span Model ($S_{ref}/2$)	1123300.0 mm^2
Reynolds Number based on MAC	$1.93 * 10^6$
Reference Static Temperature	$33.40^0 C$
Reference Static Pressure	747.70 mmHg
Moment Reference Center (MRC)*	X= 2375.7 mm, Y= 0.0 mm, Z= 0.0 mm
*The model alignment is such that for any α, the flow direction is (Cosα, 0, Sinα).	

Table 2.2: Model specifications and operating conditions for JSM

Chapter 3

Grid Generation

The preliminary steps leading to numerical computation such as CAD model creation, mesh generation, and numerical parameter setups are categorized as CFD pre-processing. Grid generation is a challenging and time consuming part of a CFD study which dictates the overall success of the study. A CAD model helps to model a real life geometry, and proper modeling enables and accurate numerical simulation. Further, meshes are the approximation of a CAD model, and a good quality mesh leads to high quality CFD results, assuming the availability of robust and efficient CFD algorithms. Honoring the importance of these preliminary steps, each aspect of CFD pre-processing is explained in detail below.

3.1 CAD model

The CAD models for HL-CRM and JSM are provided by the HiLiftPW-3 committee in the IGES[1] format. For this research, *Pointwise*[2] is used to create the mesh, and the provided models were successfully imported to Pointwise. The provided models consist of a HL-CRM with partial gaps between flap elements (Fig. 3.1), JSM without nacelle/pylon assembly (Fig. 3.2) and JSM with nacelle/pylon assembly (Fig. 3.3). The HL-CRM model does not have any support brackets while JSM models have support brackets in both configurations.

The CAD models include numerous trim information and a number of quilt surfaces which make this high-lift configuration a complex geometry on which to create a mesh. The model has to be a water-tight model in order to generate a volume grid and this is generally

[1]IGES stands for Initial Graphics Exchange Specification
[2]Pointwise is a mesh generation software for CFD

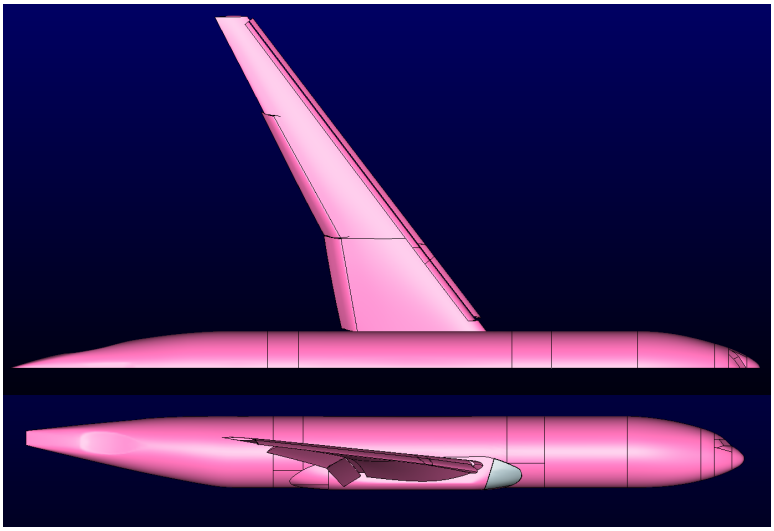

Figure 3.1: HL-CRM CAD Model

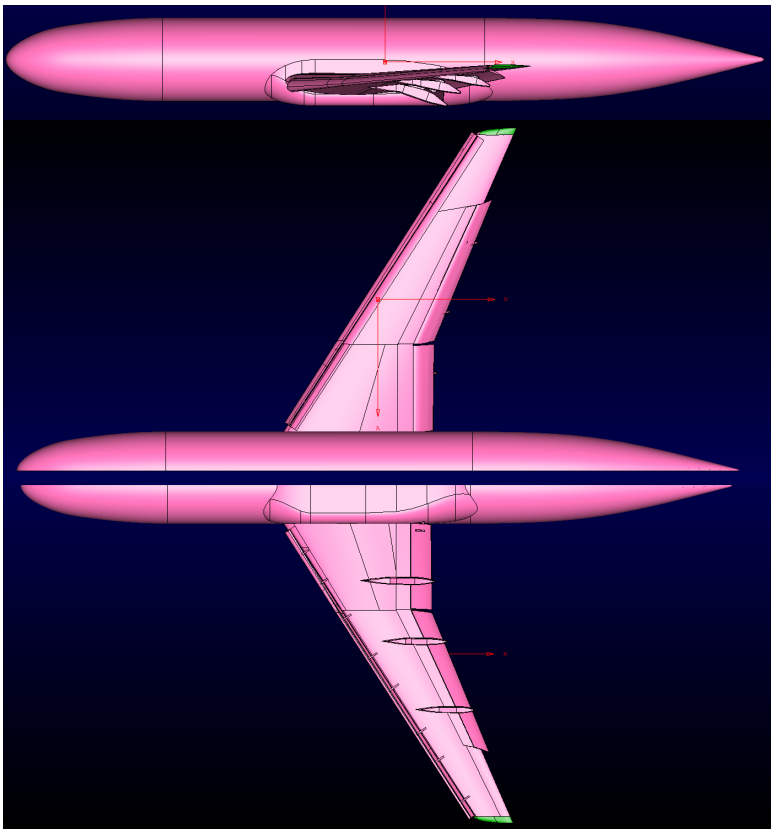

Figure 3.2: JSM CAD Model (Nacelle/Pylon OFF Configuration)

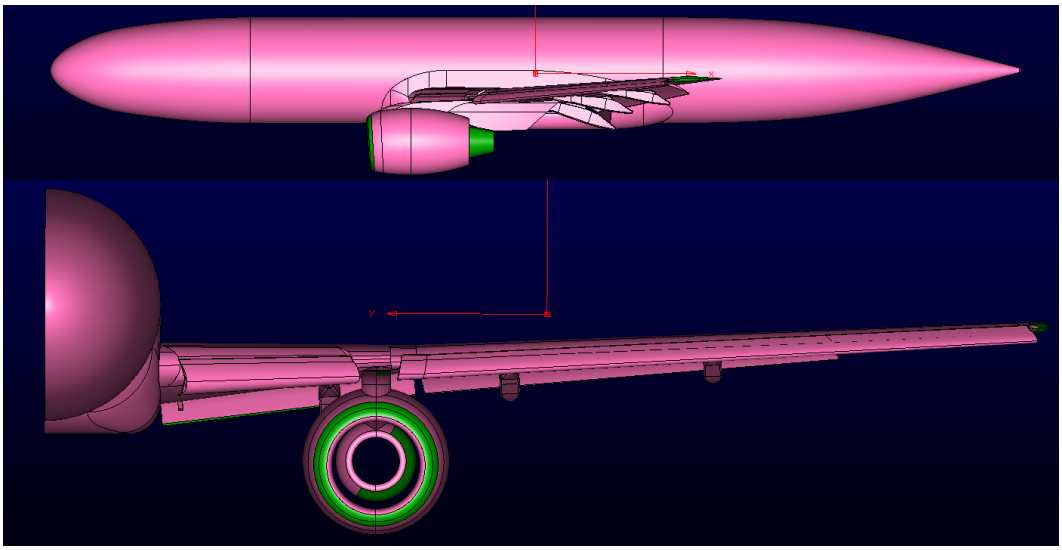

Figure 3.3: JSM CAD Model (Nacelle/Pylon ON Configuration)

achieved by assembling multiple models into a single model. The tolerance for model and quilt assembly is set to a value smaller than the minimum edge length associated with the surface grid so that the mesh surface is properly defined in the region where surface intersection occurs. After the model assembly, different quilt surfaces are combined to minimize the total number of quilts associated with the geometry in order to facilitate surface mesh generation. The quilts are combined in such a way that a single mesh surface can be generated between surfaces with similar surface topography as shown in Fig. 3.4 where different quilts representing the fuselage are assembled to create a single quilt surface.

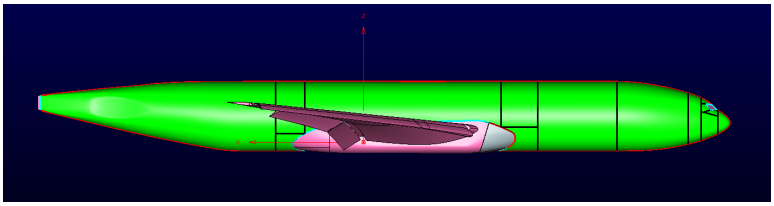

Figure 3.4: Quilts assembly to minimize total number of surfaces

3.2 Mesh Generation Guidelines

As mentioned earlier, CFD is the numerical solution of fluid governing equations where the governing equations are discretized into algebraic equations. The fluid domain is also discretized into smaller fluid elements (control volumes), and the discretized equations are simultaneously solved in each control volumes to resolve the entire flow field. The discretization of the fluid domain (mesh generation) is achieved by a bottom-up technique where the surface mesh is first created (using the CAD surfaces), and the volume elements are generated by the proper extrusion of the surface mesh. The grid density varies throughout the fluid domain based on the features of a flow; the volumes are densely populated in the regions which contain the highest gradients in the fluid flow field such as in boundary layers (in order to compute lift and drag efficiently) and in vortex dominated areas.

For this research, HiLiftPW-3 committee has provided a basic set of mesh generation guidelines as an attempt to maintain consistency among the participants. The grid resolution is categorized into coarse, medium, and fine grid density levels, and the gridding guidelines are provided for the medium level grid. Proper scaling to coarse and fine grids are requested such that the grid size grow approximately three times in size between the different grid levels for the grid convergence study. The gridding guidelines are as follows:

1. The farfield boundary should be located at at least 100 C_{REF} for all grid levels.

2. Cell size near body nose and tail should be at least $\sim 1.0\%$ C_{REF}.

3. Chordwise spacing at the leading edge (LE) and the trailing edge (TE) should be $\sim 0.1\%$ local device chord (slat-element chord for slat grid, wing-element chord for wing grid, and flap-element chord for flap grid).

4. Spanwise spacing at root and tip to be $\sim 0.1\%$ semispan.

5. Grid spacing normal to symmetry plane to be considerably larger than viscous wall spacing.

Model	Grid Resolution Level	Y^+ Value	Δy	Number of Cells on TEs
HL-CRM	Coarse	1.0	0.00175 in	5
	Medium	2/3	0.00117 in	9
	Fine	4/9	0.00078 in	13
JAXA JSM	Coarse	1.0	0.00545 mm	5
	Medium	2/3	0.00363 mm	9
	Fine	4/9	0.00242 mm	13

Table 3.1: Y^+ values and corresponding wall spacings for different cases

In addition, the viscous wall spacing and the number of cells for trailing edges are also specified. The viscous spacing and viscous spacing growth rate play an important role in the proper resolution of a boundary layer which is paramount to the calculation of aerodynamic forces on any surface. The viscous spacing is defined based on a non-dimensional normal distance to a wall, Y^+ value, which is defined as:

$$Y^+ = \frac{u^* y}{\nu} \tag{3.1}$$

where u^* is the friction velocity at the nearest wall, y is the distance to the nearest wall, and ν is the local kinematic viscosity of the fluid. The height of the first mesh cell (initial wall spacing) perpendicular to the no-slip wall boundary is calculated using Eq. 3.1. The Y^+ value will ensure that there are at least a few cells present in the viscous sub-layer region of a turbulent boundary layer. For the grid convergence study, Y^+ dictates the grid resolution level. Since Y^+ is dependent on the friction velocity which is unknown before solving the flow, it involves an iterative approach to get the required Y^+. For simplicity, Y^+ and the corresponding wall spacing are provided by the organizing committee along with the gridding guidelines. The Y^+, the corresponding initial wall spacing (Δy), and the required number of cells in the trailing edges are tabulated in Table 3.1. For this research, medium level grids are used for the JAXA JSM test cases (as the coarse and fine grid levels are optional for the HiLiftPW-3 and are not included in this study). Since the wakes from one element interact with the boundary layer of another, it is requested to create a tighter spacing in

the wake regions in order to resolve this phenomenon properly. More detail regarding the gridding guidelines is present on HiLiftPW-3 website [15]. The grids created for this research conforms with most of the provided guidelines however, some deviation is present which were unavoidable in order to create a high quality mesh grid. These deviation from the gridding guidelines are explained in details in later chapters.

3.3 Surface Mesh Generation

In order to minimize the number of mesh surfaces (domains in Pointwise), different quilts are assembled and the mesh surfaces are created on the assembled quilts (a single database after assembly). However, during the quilt assembly, one of the quilts (one of the surfaces in fuselage-wing fairing) in the fuselage of the NASA HL-CRM model could not be assembled to its neighboring quilts (evident in Fig. 3.5) because this surface had overlapping boundaries with its neighboring surfaces. Similar concern regarding the invalid surface is mentioned in the study by Dey, et. al. [16], where the mesh generation problem is avoided by coarsening the mesh size in the invalid surfaces. Most of the time, surface trimming helps to remove such overlapping boundaries, but the trimming process did not help in this case. So, a separate domain is created on the faulty quilt and the domain is combined with its neighboring domain by merging the associated connectors with the connectors of the neighboring domains. As the domains are associated with a model (quilts) and the cell size on the domain is greater than the overlapping length, the joined domain produced uniform elements without any discontinuity. Figure 3.5 shows the subsequent steps leading to combined domain from two overlapping domains. Since the domains are created on different database entities, there are overlapping connectors on domain boundaries, and these overlapping boundaries are merged into single connectors to achieve a water-tight surface.

A fixed number of points are requested on the trailing edges, so structured grids are created along all trailing edges and are diagonalized in order to convert them into unstructured grids. Also, structured grids are created and diagonalized in various locations like the wing

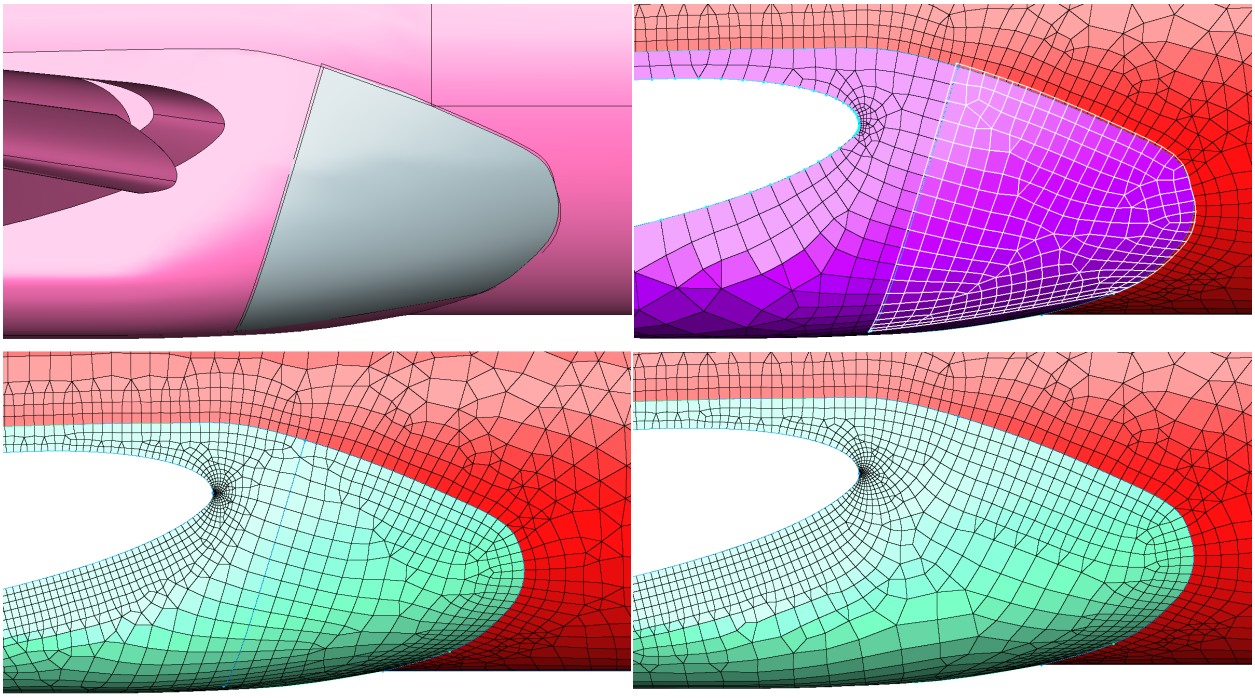

Figure 3.5: Merging of connectors to avoid faulty geometry

tip in the HL-CRM and the nacelle and filleted surfaces of support brackets in the JSM to get uniform cells which otherwise are difficult to achieve using unstructured grid alone.

To resolve the high curvature geometry near the leading edges and trailing edges, high aspect ratio anisotropic cells (known as T-Rex cells in Pointwise) are used with the chord wise spacing specified by the gridding guidelines (0.1 % local device chord). Since the chord length for each element varies with the wing span, minimum chord is used to determine the spacing on the leading and trailing edges. A different approach is taken by Chan [17], where the average chord is used for leading and trailing edge spacings. The reason for using minimum chord among the elements for this research is to avoid the lack of mesh resolution with the average spacing on the minimum chord location due to the high aspect ratio of the wing geometry. The minimum chord among the outboard and the inboard flap is used on both flaps in order to maintain consistency among the grid spacing. The single spacing among different chord location is used to create a uniform grid across the span and to avoid

the abrupt transition at intersection of two different elements. Also, the same spacing among two different flaps facilitate the uniform matching of grid cell (for better mesh quality) in the gap (fully gapped configuration) between the flaps while creating the volume grid.

The chord wise cell spacing from the leading edge grows with a fixed growth rate up to a specified number of layers until the cell size matches with an unstructured cell size. For the wing element, maximum allowed cell size for an unstructured cell is specified to be $\sim 1\%$ MAC. The resolution of the high curvature near the leading edge and trailing edge of the wing of the JSM using T-Rex layers is shown in Fig. 3.6. Throughout the mesh generation process, high aspect ratio anisotropic cells are used whenever the unstructured cells alone cannot resolve the geometry to a desirable effect.

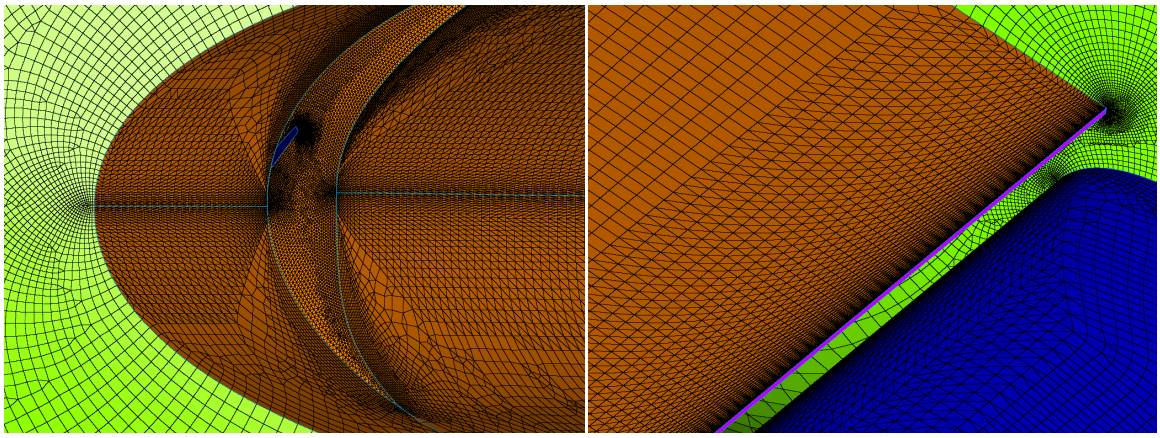

Figure 3.6: High aspect ratio anisotropic cell layers to resolve high curvature elements. (Left) Leading edge of a wing, (Right) Trailing edge of a wing

The surface mesh generated for this research is quad dominant where tetrahedral cells (tets) in unstructured domains are combined to create quad cells. The quad dominant surface enables the creation of high quality hexahedral elements (hex elements) in the viscous region while creating a volume grid.

Farfield and Symmetry plane

After the generation of surface grids on the aircraft model, the farfield domain is created with the specified guidelines which request the farfield to be ∼100 C_{REF} away from the aircraft geometry. The farfield domain is a hemisphere which has a uniform distance from the aircraft body. Since all the research models are half span models, a symmetry plane is needed to ensure a water tight boundary for the fluid domain.

3.3.1 Grid Quality

Volume grid generation is a computationally demanding process and can take multiple iterations to get a high quality grid. So, it is necessary to check the quality of the surface grid in order to create a high quality volume grid in a minimum number of iterations. There is not any absolute definition of a high quality grid. However, a high quality grid can be defined as a grid which produces a desirable solution with maximum accuracy while utilizing minimum computational cost and time. Most of the time, a grid which has less skewness fulfills the grid quality criteria, but the acceptable skewness value is solver dependent and varies from one solver to another. A few of the most important parameters that dictates the quality of a grid are: *area ratio, minimum included angle, maximum included angle, and aspect ratio.*

The area ratio is the ratio of areas between the neighboring cells. The volume grid is generated by inserting a point normal to the surface at a specified distance that increases with a fixed growth rate, so a larger area will grow faster than a smaller area and can create a skewed element in between them. Normally, for a domain with tetrahedral elements, the area ratio up to 3-5 is reasonable while in a quad dominant domain, the area ratio up to 6-10 is desired to prevent high skewness. However, it is not always possible to restrict the area ratio to a recommended range. The area ratio is usually high, around 30, in the corners of the trim surface of the Wing Under Slat Surface (WUSS) as demonstrated in Fig. 3.8 for the JSM. In such circumstances, during volume grid generation, if an anisotropic cell normal

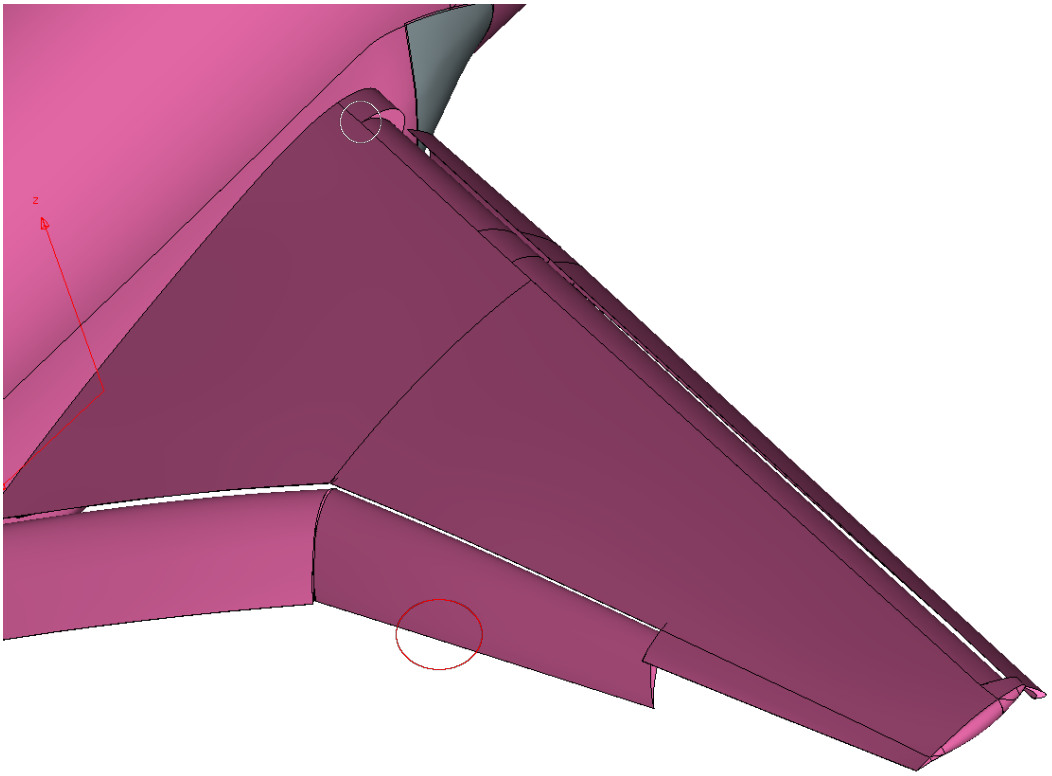

Figure 3.7: Possible locations for highly skewed surface elements with spacing provided by gridding guidelines (Trim surface of the WUSS and the trailing edges)

to the surface creates highly skewed elements, the anisotropic cell layer growth stops locally and tetrahedral element is placed to improve skewness.

Minimum and Maximum included angle are the minimum angle and maximum angle in a grid element (2D or 3D element) respectively. For domains (surface grid), the maximum included angle is usually kept below 150^0 in order to prevent high skewness. The acceptable minimum included angle on the other hand is solver dependent but a value greater than 2^0 is usually desired. However, it can be extremely difficult to achieve a better minimum angle in the sharp corners. The trim location of WUSS are the regions where this quality criteria is usually violated (Fig. 3.7). If the angles are extremely small (below or close to 1^0), the connectors can be split at some location and then recombined to a single connector at the corner to improve the minimum included angle. One such improvements in minimum

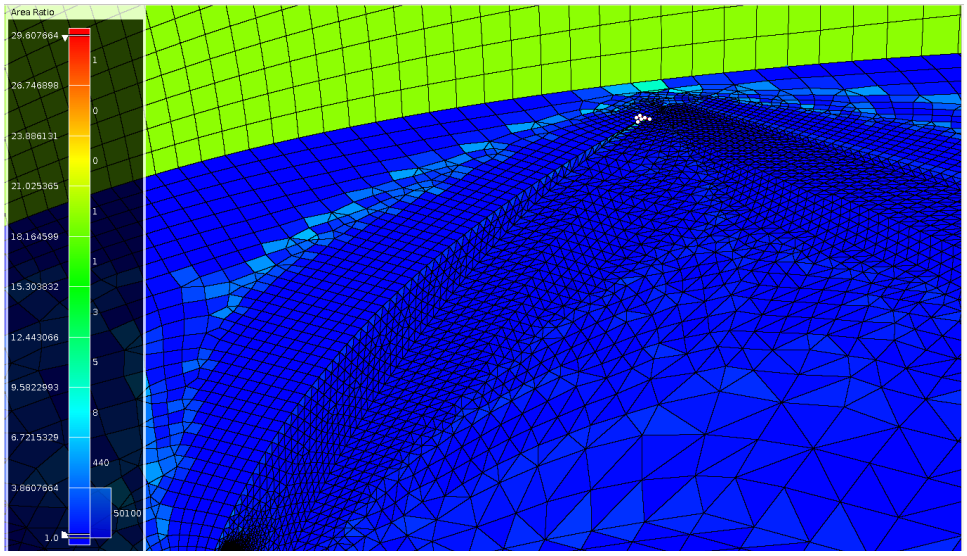

Figure 3.8: High area ratio in the trim surface location of WUSS

included angle by this technique is evident in Fig. 3.9 where the corner has a single connector which is obtained by merging two split connectors.

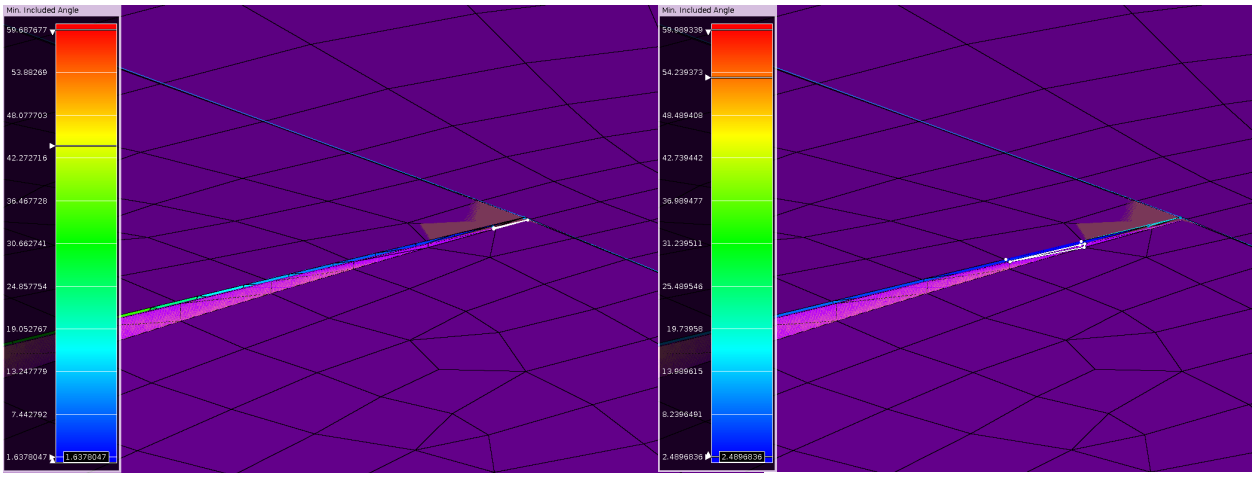

Figure 3.9: Improvement in minimum included angle (from 1.6^0 to 2.5^0) by joining connectors at corners of WUSS

Another quality criteria, aspect ratio is the ratio between the average length to the average width in a quadrilateral and is the ratio of long edge to short edge in a triangle. The aspect ratio directly effects the skewness of grid elements that are built on top of a cell. Usually, for a cell with an aspect ratio of 50 creates a grid element with an interior angle

of $\sim 178^0$. However, this is not an overly restrictive quality criteria because the creation of highly skewed elements can be avoided by inserting tetrahedral elements while creating volume grid. For example, in the slat element of HL-CRM, the trailing edge has 9 points such that the average cell spacing for a cell, $\Delta S \sim 0.012$ in and the span of slat is around 1000 in. In order to limit the aspect ratio under 50, the number of points along the span of the slat has to be around 1700 ($\sim$ 1000 /(50 * 0.012)) which can be a little restrictive from a computational point of view. So, in such cases a high aspect ratio is acceptable and the skewness is checked during volume grid generation.

3.3.2 Deviation from HiLiftPW-3 Gridding Guidelines

In order to create high quality grids, some deviation from the provided gridding guidelines were unavoidable. The gridding guidelines request a fixed number of cells in the trailing edges (9 cells for a medium grid level) and also provide a spacing for the chordwise elements in the trialling edges. For a medium grid level in the HL-CRM, average ΔS is $\sim$0.012 in the trailing edge of the wing. However, the chordwise spacing for wing tip is 0.1 inch (0.1 % of local chord of 100 in). This large variation in the size of two adjacent cells next to each other is not ideal in a critical geometric feature like trailing edges. Fig 3.10 shows the area ratio with the spacing provided by the gridding guidelines. In order to avoid this issue, the spacing on the chord wise trailing edge is set to 0.018, so that the area variation across the trailing edge elements are minimized. The same approach is applied throughout the mesh generation process for all other elements and configurations.

The gridding guidelines also provide the spanwise spacing at the root and tip of each elements based on the span of the elements. The area ratio at the root and tip of the elements (wing, slat, and flaps) with the spacing specified by the gridding guidelines (spanwise spacing of 1.0 for wing and 0.9 for slat) violates the acceptable quality criteria. The problem was even more pronounced in the slat elements, evident in Fig. 3.11. Various adjustment in the spacing is done in order to bring the area ratio to an acceptable range in all three

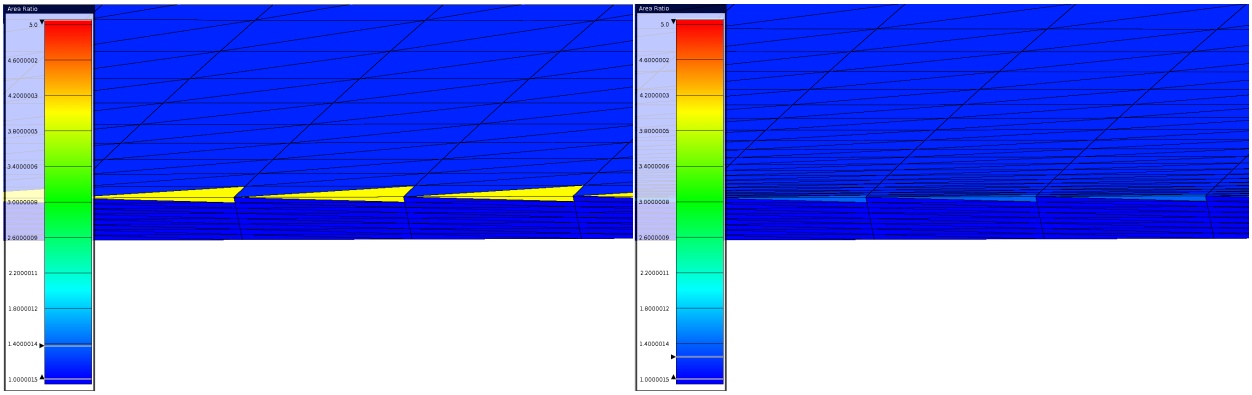

Figure 3.10: Improvement in the area ratio in the trailing edge of the wing tip in HL-CRM by adjusting the spacing different from the gridding guidelines

configurations (HL-CRM, JSM Nacelle OFF, and JSM Nacelle ON). The change in the spacing is not consistent throughout the grid. Specifically, different spacings are used in leading edge and trailing edge in a single element, and the spacing also varies from root to tip. For example, adjusted spacings in the HL-CRM are tabulated in the Table 3.2.

Model	Element	Location	Gridding Guideline Spacing	Adjusted Spacing
HL-CRM (Medium)	Wing root	LE	1.04	0.50
		TEs	1.04	0.20
	Wing tip	LE	1.04	0.05
		TEs	1.04	0.10
	Slat	LEs	0.97	0.08
		TEs	0.97	0.03
	Flap	LEs	0.70	0.08
		TEs	0.70	0.08

Table 3.2: Adjusted spanwise spacing at various location in the HL-CRM

Improvements in the area ratio by adjusting the span wise spacings at various location in HL-CRM is shown in Fig. 3.12. Similar changes for the chord wise spacing and span wise spacing in the HL-CRM grid are discussed by Woeber, et. al. [18], during the grid generation process and the grids are made available to the participants.

Another deviation from the gridding guidelines is on the trailing edge of the wing tip for the HL-CRM where the requested number of cells is 8, but in order to preserve the curvature

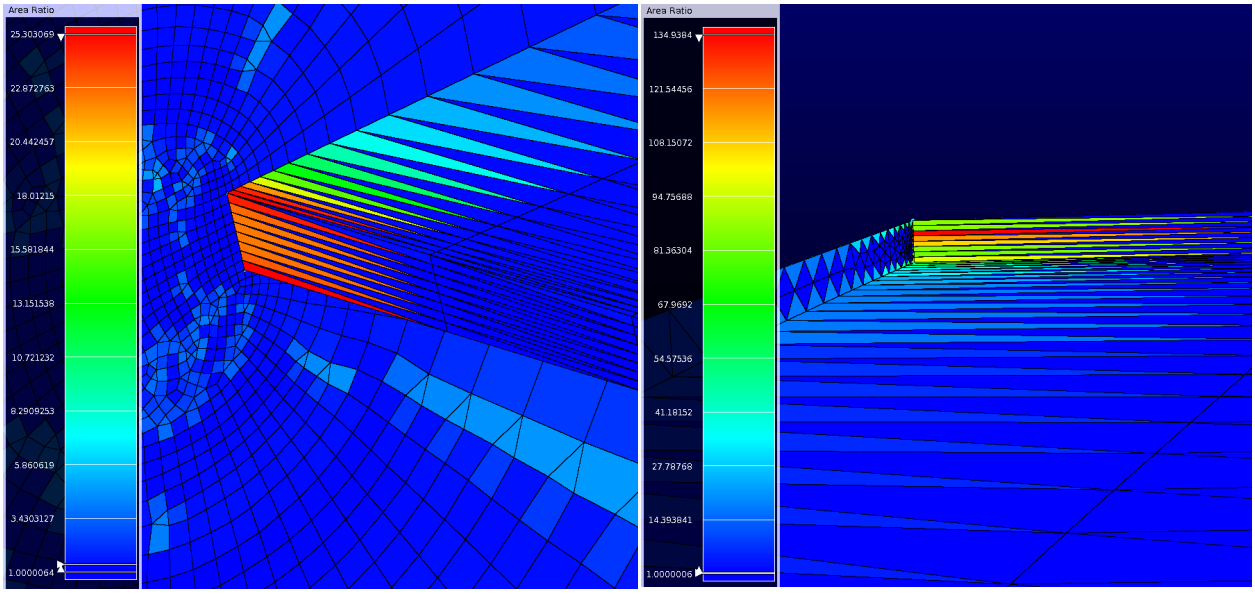

Figure 3.11: Large area ratio in the elements with the span wise spacing provided by gridding guidelines. (Left) Wing root, (Right) Slat root of HL-CRM

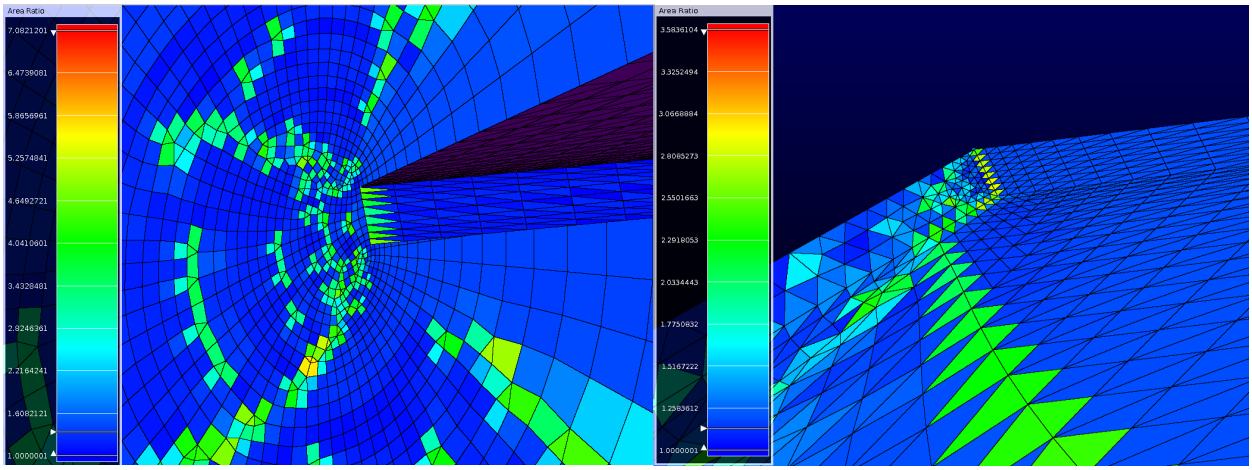

Figure 3.12: Span wise spacing adjusted to get better area ratio at the root and tip of different elements. (Left) Wing root, (Right) Slat tip of HL-CRM

of the wing tip and to minimize the total number of nodes on the wing tip domain, the total cell count is changed to 16. A structured grid is created and diagonalized as a wing tip domain which produced uniform growth of cell size (across the radial direction on wing tip) along the chord of the wing hence reducing the total number of points on the domain. The reduction of the number of nodes on the wing tip domain can be seen in Fig. 3.13 where

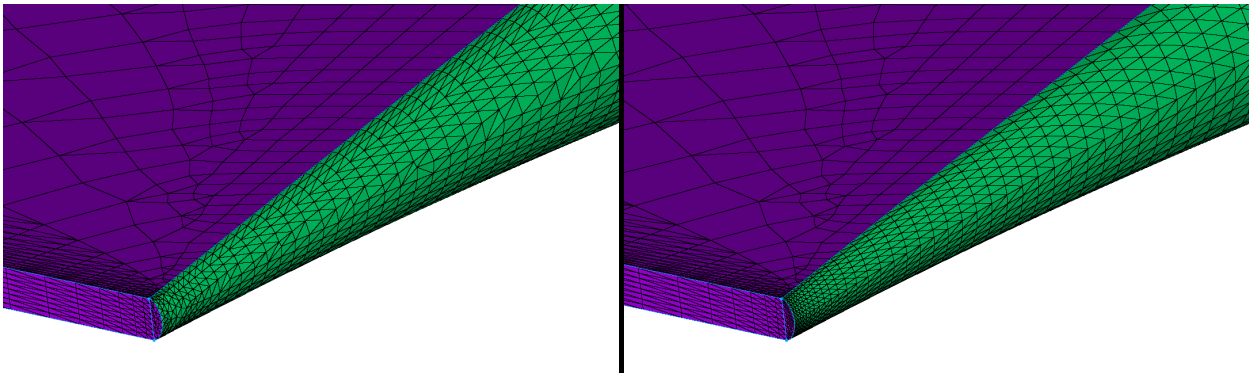

Figure 3.13: Trailing edge of the wing tip in HL-CRM. (Left) Wing tip TE with 9 points (gridding guidelines), (Right) Wing tip TE with 15 points

T-Rex cells (high aspect ratio anisotropic cells) have a greater number of nodes and the area ratio is also increasing drastically along the wing chord (Left figure) from the trailing edge to the leading edge. Another approach that might limit the area ratio is to create T-Rex layers on the intersection of the wing and wing tip (span wise T-Rex layers) with a comparable spacing, but this will increase the total nodes on the wing by a considerable amount.

3.4 Volume Grid Generation

After all the surface of the fluid domain is properly defined, the volume is populated using isotropic and anisotropic elements. Volume grid generation is carried out by generating anisotropic elements with a specified initial distance and a fixed growth rate followed by population of the remaining portion of the fluid domain with isotropic tetrahedral elements.

The volume elements in the anisotropic layers (T-Rex layers) are created by placing a point normal to the surface at a specified distance (distance dictated by Y^+ value as in Table 3.1) from the wall (domain of aircraft body) and the spacing continues to grow with a specified growth rate until the maximum layers are reached. The growth rate for the viscous layers are specific for each grid resolution level. The coarse grid has a growth rate of 1.25, the medium grid has a growth rate of 1.16, and the fine grid has a growth rate of 1.10. The gridding guidelines request the growth rate be less than 1.25 for a coarse grid (GR_1) and

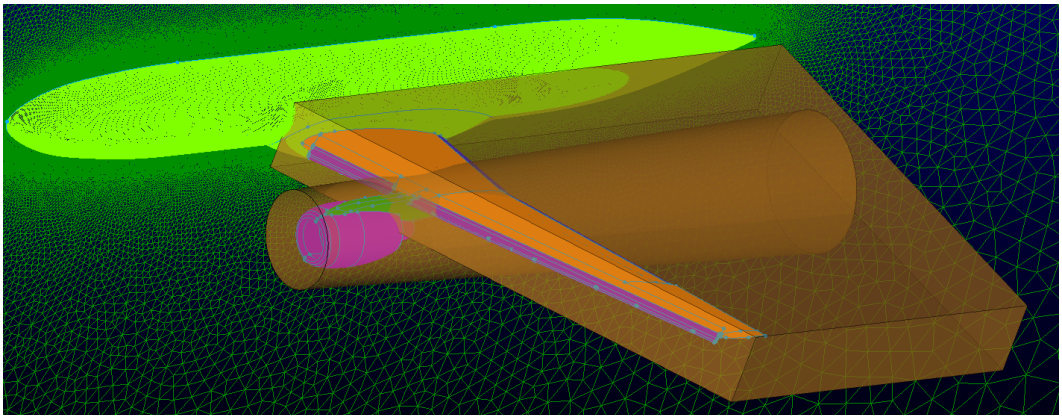

Figure 3.14: Bladder like structure for better control on size of isotropic elements

scale appropriately to refine grid levels based on the following expression:

$$\text{Growth Rate} = GR_1^{\frac{1}{F^n}} \tag{3.2}$$

where F is approximately equal to 1.5 and $n = 1$ and 2 for the medium and fine grid levels respectively. The growing of T-Rex layers is locally stopped in locations where the created elements violate the specified skewness criteria, and the tetrahedral elements are placed instead. Skewness is based on the maximum included angle of an element and for T-Rex layers, maximum included angle is set to 175^0 so that any T-Rex element having maximum included angle greater than 175^0 will stop the growth of T-Rex layers.

The remaining portion of the fluid domain is populated using isotropic tetrahedral elements. The size of the isotropic elements around the areas of interest is controlled by defining a region where the size of tetrahedrals are fixed to a specified value. The Fig. 3.14 shows one such predefined region around the wing and nacelle of the JSM (For such predefined region in the JSM, the specified size for tetrahedral is 8 mm while in HL-CRM, it is 5 in). Such bladder like structure (Sources in Pointwise) allows better control of the size in the isotropic region of the fluid domain and provides better resolution of the flow features near an object.

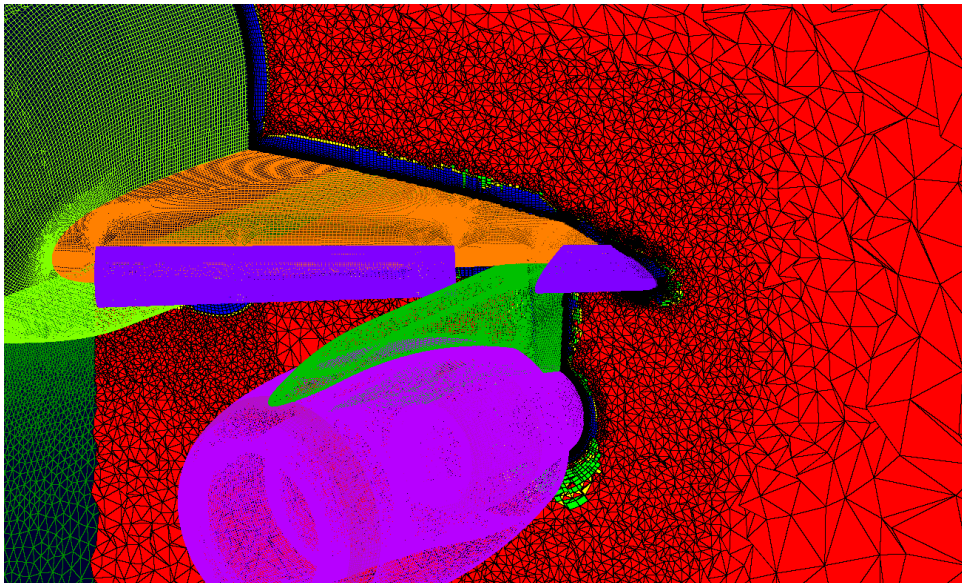

Figure 3.15: Multi-element grid with hexahedral, prism, pyramid, and tetrahedral elements

Grids with a combination of different elements; hexahedrals, prisms, pyramids, and tetrahedrals are known as a multi-element grid (In Fig. 3.15, blue elements are Hexes, green elements are prisms, yellow elements are pyramids and red elements are tets).

The total node count and cell count for different grid configurations are tabulated in Table 3.3.

Model	Grid Level	Nodes	Hexahedrals	Prisms	Pyramids	Tetrahedrals
HL-CRM	Coarse	13,758,812	9,579,038	1,706,194	2,657,235	1,335,4087
	Medium	42,422,679	32,293,629	5,304,366	5,698,791	30,733,420
	Fine	117,586,322	96,656,886	9,201,914	10,380,628	72,395,548
JSM (OFF)	Medium	43,989,123	33,600,484	3,959,730	5,959,730	35,667,103
JSM (ON)	Medium	54,097,064	42,367,255	4,735,191	7,581,223	37,495,618

Table 3.3: Total number of nodes and cells for different configurations

The overall quality of the grid created for this research are of fairly good quality. The grids are subjected to multiple iterations in order to keep the maximum included angle to be less than 178^0. However, there are few highly skewed elements (elements with maximum included angle around 179^0) present in some configurations. HL-CRM grid has maximum

included angle below 177^0 for all grid levels (medium, coarse, and fine). The resolution of the grid at various span location of the medium grid level in the HL-CRM is presented in Fig. 3.16. However, in JSM for both configurations (Nacelle ON and Nacelle OFF), the number of skewed cells are in fairly small quantities. There are 17 elements in JSM Nacelle OFF configuration and 23 elements in JSM Nacelle ON configuration which have maximum included angle greater than 178^0. Since the solver did not show any issue and the number of skewed cells are relatively low compared to the total number of cells in these configuration, the grids are hence accepted as a valid grid.

3.4.1 Grid Export

The next step after a successful generation of volume grid is to export the grid in a format that is acceptable by the solver. It is also necessary to identify different boundaries in the fluid domain (inflow, outflow, no-slip wall, farfield) so that appropriate boundary conditions can be applied to the grid during the solution process. In order to investigate the aerodynamic characteristics of individual elements in the model, different identification numbers are provided to each element present in the grid (all of the domains representing the wing are exported as a single wing surface and assigned a single identification number).

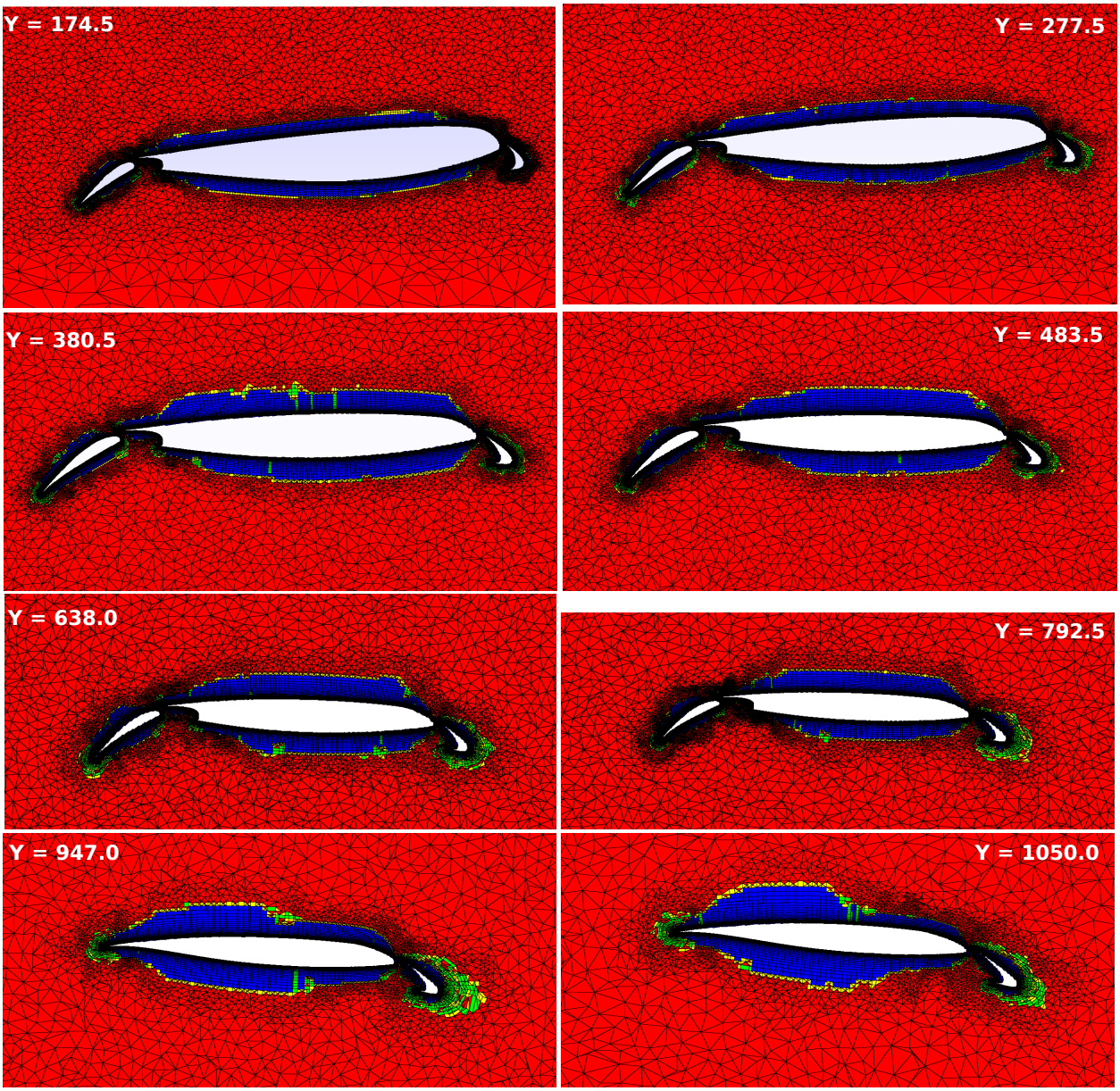

Figure 3.16: Multi-element grid at various location in the wingspan of the HL-CRM

Chapter 4

Numerical Simulation

The next step after the pre-processing in a CFD study is numerical simulation. As mentioned earlier, the CFD solution is an iterative process and the iterations are carried out until some specified convergence is achieved. However, it is not always possible to achieve absolute convergence i.e. to a machine level precision. So, a simulation is accepted to have achieved a solution when the residuals or Lift and Drag coefficients are either not changing with additional iterations or the residuals are under acceptable tolerance (acceptable tolerance is case dependent).

4.1 Flow Solver Parameters

Thanks to the active development in CFD, there are various methods and techniques available to solve any CFD problem. The solver parameters, however, are case dependent, and the selection of the best combination of methods is important for a successful CFD study.

Some of the important parameters used with arbitrary Mach formulation of the governing equations (Eq. 1.13) are listed as follows:

- Temporal accuracy (for time accurate simulation): *Second order*
- Solution algorithm: *Implicit*
- Inviscid flux computation method: *ROE scheme*
- High order inviscid flux controls: *Barth limiter*
- Viscous gradients computation: *Weighted least square*

- Inviscid flux Jacobian computation method: *Complex numerical Jacobians*

Parameters for the incompressible solver (Eq. 1.20) are:

- Solution method: *Steady state*
- Inviscid flux Jacobian computation method: *Approximate Jacobians*

with rest of the parameters same as arbitrary Mach formulation.

The boundary conditions for the aircraft surface is set as *no-slip adiabatic* wall. Since all the research models are half-span model, the symmetry plane has been assigned a "symmetry" boundary condition which sets all fluxes and normal velocities across the boundary to be zero. The free-stream conditions are set at farfield boundaries.

4.2 Simulation Details

HiLiftPW-3 requests at least one solution on provided grids (committee grids) for each case. So, this research presents solution of two different sets of grids; provided committee grid and grid created for this research (called as Auburn grids). Evident in Table 3.3, the grids involved in this research are computationally demanding with total number of nodes over 50 Millions for most cases. These type of grids require massive computation power and can only be run in super computers. For this research, simulations are performed using High Performance Computation Linux Clusters (HPC) present in `Auburn University` known as *Hopper*[1]. Hopper offers state of the art computation power with 190 computation Nodes each with 20 processor cores (2 CPUs) and 128 GB of memory among them. Grids are divided among different cores such that each core receives approximately 300,000 grid nodes for computation for optimum performance.

For this research, the numerical simulations using arbitrary Mach solver are divided among two runs; steady state solutions followed by time accurate solutions. First 500 iterations in the steady state runs are of first order accuracy (inviscid flux computations) followed

[1]https://hpcportal.auburn.edu/hpc/2016_cluster.php

by second order in accuracy for the remaining 500 iterations. Running low order accurate runs help accelerate the solution process as the first order scheme is highly dissipative and can set an approximate mean flow quickly comparing to higher order schemes. On the other hand, the time steps for time accurate solutions are adjusted until the value results in a stable solution. Since a stable time step is grid dependent, different time steps are possible for different grids in a single case. Time averaged solutions of time accurate runs are used to facilitate post processing (evaluate coefficient of pressure (C_P) at different location) in which time averaging is done between last 1000 iterations. The type of grids, CFL number (steady state solution), time step (time accurate solutions), and turbulence models used for different cases are tabulated in the Table 4.1, 4.2 and 4.3 below. Although the study is carried out using different turbulence models, Menter SST is set as a baseline turbulence model for comparison among different cases.

HL-CRM					
Grid level	Grid	No of Cores	CFL	Time Step (s)	Turbulence Model
Coarse	Auburn	60	5.0	1E-05	SAS, Wilcox k-ω, Menter SST
	Committee*	40	5.0	1E-05	SAS, Wilcox k-ω, Menter SST
Medium	Auburn	140	5.0	1E-05	SAS, Wilcox k-ω, Menter SST
	Committee	100	5.0	1E-05	SAS, Wilcox k-ω, Menter SST
Fine	Auburn	400	0.5	1E-06	SAS, Wilcox k-ω, Menter SST
	Committee	300	0.5	1E-06	SAS, Wilcox k-ω, Menter SST
*For HL-CRM, committee grids generated using Pointwise are used.					

Table 4.1: Simulation details for HL-CRM with Variable Mach Solver

JSM (Nacelle OFF)					
Grid level	Grid	No of Cores	CFL	Time Step (s)	Turbulence Model
Medium	Auburn	140	5.0	1E-06	Menter SST
	Committee*	200	5.0	1E-06	Menter SST
JSM (Nacelle ON)					
Medium	Auburn	180	5.0	1E-07	Menter SST
	Committee	200	5.0	1E-07	Wilcox k-ω
*For JSM, committee grids generated using ANSA are used.					

Table 4.2: Simulation details for JSM with Variable Mach Solver

JSM (Nacelle OFF)			
Grid Size ($\sim 10^6$)	No of Cores	CFL	Turbulence Model
56	180	10.0	SAS
JSM (Nacelle ON)			
68	220	10.0	SAS

Table 4.3: Simulation details for Auburn JSM with Incompressible Solver

For JSM flow simulation, the solutions of lower angle of attack are used to initialize the solutions for higher angle of attack. Initialization of simulation from a lower angle of attack solutions facilitates convergence and makes the solution much more accurate by providing better initial guess for Newton iterations.

The overall simulation process for each cases using the variable Mach (arbitrary Mach) solver can be divided into following four steps:

1. Steady state simulation with first order accuracy: 500 iterations
2. Steady state simulation with second order accuracy: 500 iterations
3. Time accurate simulation with second order temporal accuracy: 5000 iterations

The simulation time (CPU time) for each simulation was around 20-22 seconds as the number of grid points partitioned among the computation nodes are consistent among different cases. The total CPU time for a simulation was around 37 hours for 6000 iterations. But, there were some fluctuations in the CPU usage time when the cluster was busy with heavy I/O operations among the users that affects the network speed and communication among the computation nodes.

The flow simulation using the JSM with an incompressible solver only involves steady state runs. Also, using an approximate Jacobians for inviscid flux evaluation with a steady state solver decreases the overall simulation time. The incompressible solution starts with steady state converged solution at 0.0^0 angle of attack and gradually pitching the aircraft to a required angle of attack. The CPU time for each steady state run was about 5-7 seconds for a fixed grid and 29-31 seconds for grid rotation i.e. pitching the aircraft.

Chapter 5

Results and Discussions

The CFD results from this study are analyzed based on the force and moment comparison, C_P at various location on the wing elements, wake velocity and surface streamlines on the aircraft. For validation, CFD results are compared with experiments for the cases whose test data are available and the findings are extended to make conclusions on the blind test case.

5.1 HL-CRM: Grid Convergence Study

The grid convergence study of the HL-CRM is a blind test case in which the effects of grid convergence on the lift and drag characteristics of a high-lift wing is studied. The results for grid convergence study are presented for the medium and coarse grid level using the variable Mach solver in *TENASI*. The numerical scheme used for this study showed high sensitivity towards the size of the mesh elements which resulted in an unstable solution for the fine grid level. The fine grid level has extremely small mesh elements in the viscous spacing corresponding to $Y^+ = 4/9$, which often leads to convergence issue. These extremely small mesh elements introduce more dissipation and stiffness to the numerical schemes especially in the boundary layer. For most study, any spacing corresponding to a value of $Y^+ < 1$ is sufficient to resolve the turbulent boundary layer. Because of the convergence issue with the fine grid level, only medium and coarse grid results are included in this study.

5.1.1 Force and Moment Convergence

For an unstructured grid, grid size is often represented by the expression: $N^{-2/3}$, where N is the total number of nodes, which is equivalent to the step size (h) in a structured grid.

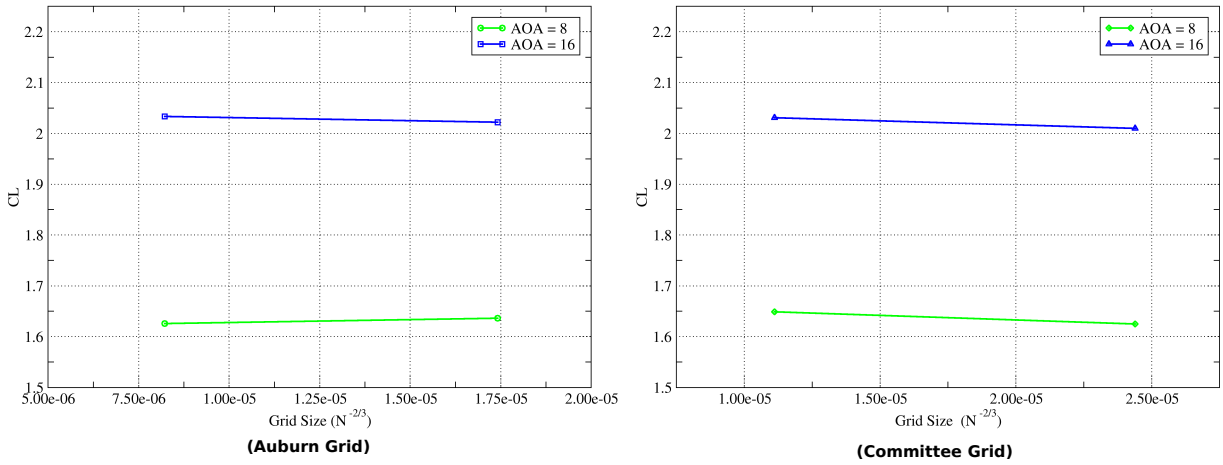

Figure 5.1: HL-CRM: Lift Convergence. (Left) Auburn Grid VS (Right) Committee Grid

The variation in coefficient of lift (C_L) with respect to grid size is represented in Fig. 5.1 for both Auburn and Committee grids with the Menter SST turbulence model. Figure 5.2 shows the variation of C_L predicted by different turbulence models for Auburn grid.

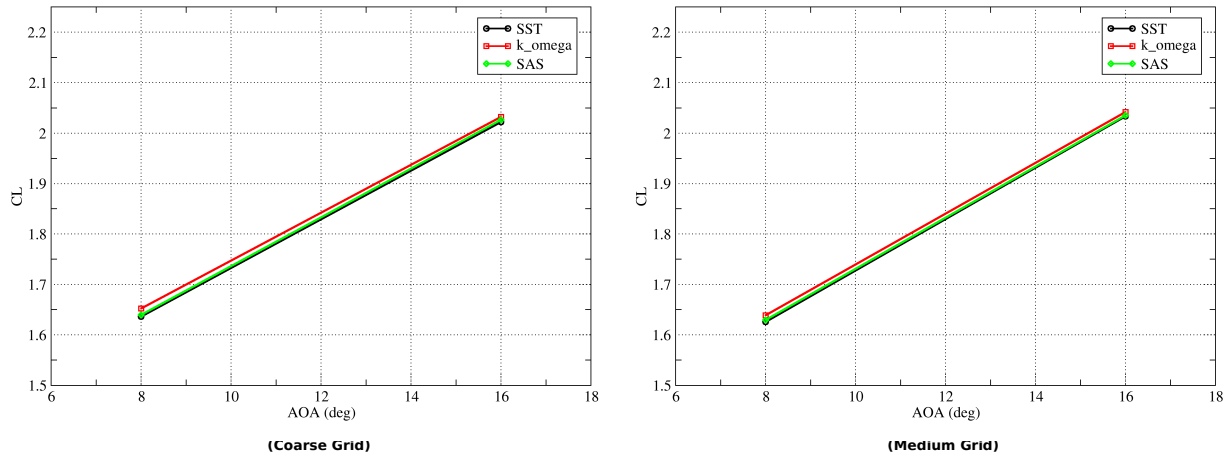

Figure 5.2: HL-CRM: Turbulence Models Lift Comparison for Auburn Grid. (Left) Coarse Grid VS (Right) Medium Grid

The lift convergence on the HL-CRM indicates that the lift characteristics predicted by CFD varies with the grid refinement. For Auburn Grid, at lower angle of attack, the coarse grid has higher C_L value than the medium grid while at higher angle of attack, the coarse grid has lower C_L which increases with the grid refinement. However, results from

Committee grid indicates that the value of C_L increases with the grid refinement for all angle of attack. Despite the differences in the trend, the values of C_L predicted by both grids are almost identical. The prediction of C_L among turbulence models are consistent and the C_L varies slightly among the turbulence models. The Wilcox $k-\omega$ model seems to predict higher C_L than other two models while results from the Menter SST and the SAS models are similar as evident in Fig. 5.2. The different values of C_L obtained on Auburn grid and Committee grid using different turbulence models are shown in Fig. 5.3. The trends in C_L prediction with the grid refinement is consistent among the different turbulence models for both Auburn and Committee grids.

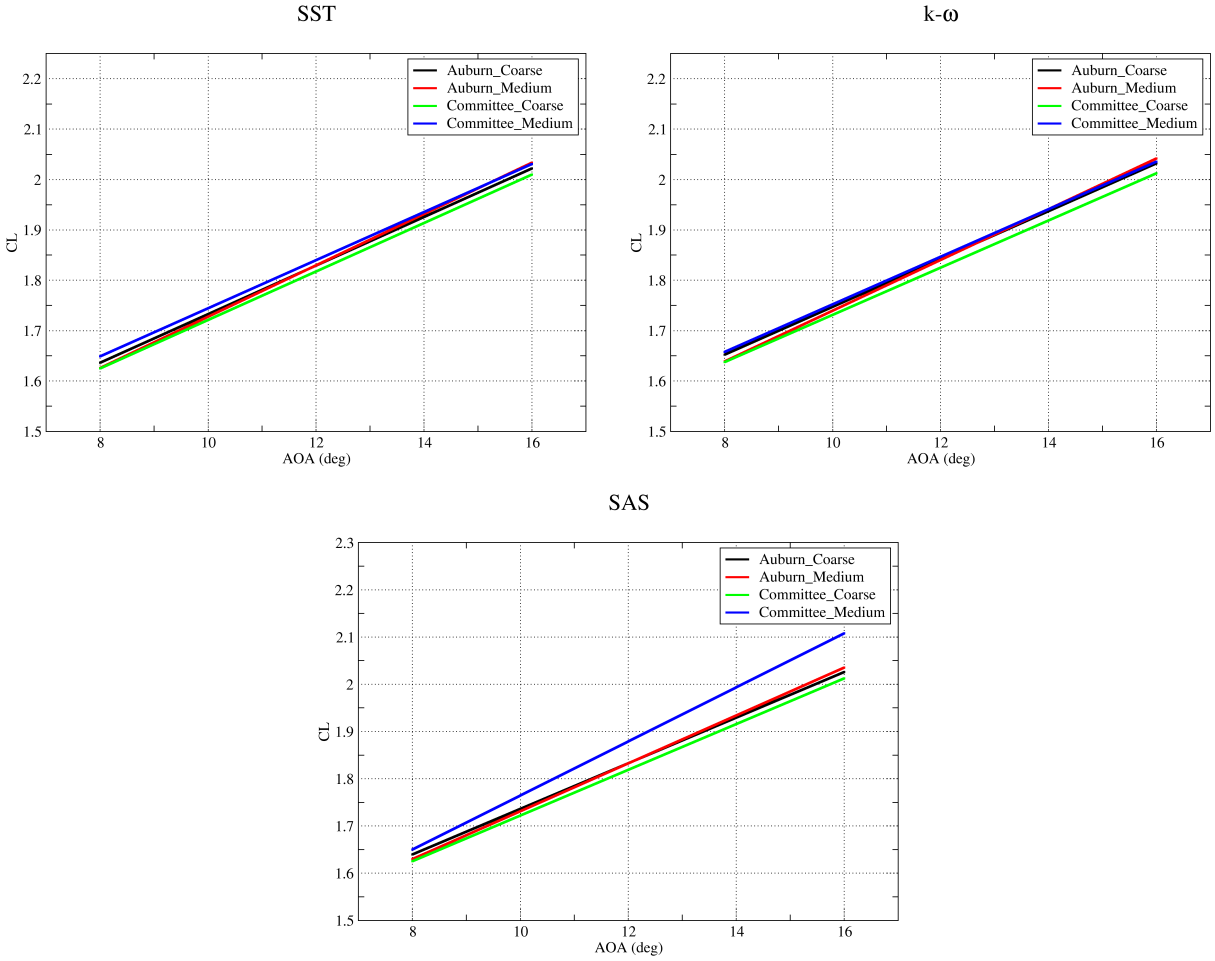

Figure 5.3: HL-CRM: Lift Convergence of Different Turbulence Models

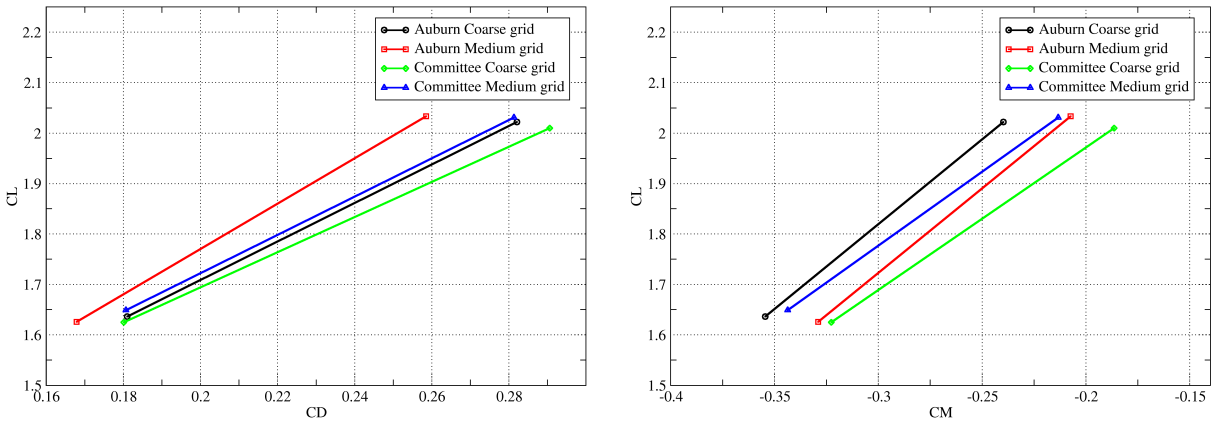

Figure 5.4: HL-CRM: Drag and Moment Curves (Auburn Grid and Committee Grid)

The drag and moment curves in the Fig. 5.4 indicate that for a given C_L, coarse grid overpredicts the C_D and C_M values than a refined grid level (medium grid) for the Auburn grid. Similar to lift convergence, this trend is opposite for the Committee grid. The results of other participants from the workshop might be useful to draw a more definite conclusion on this trend.

5.1.2 C_P Convergence

The figure 5.5 shows the requested location on the HL-CRM for C_P extraction to study the effects of grid refinement on the C_P resolution of the HL-CRM. Figure 5.6 - 5.15 present the effects of grid refinement on the C_P plot for different angle of attack as well as the variation of C_P prediction among turbulence models and different grids (Auburn and Committee).

The grid refinement shows significant change in the C_P prediction of the HL-CRM. The suction peak throughout the wing elements and the midspan of the wing are the most significant location that show high sensitivity towards the grid refinement which is evident in the Fig. 5.6 and 5.11. From the Fig. 5.11, it can be concluded that the C_P for a higher angle of attack is more grid sensitive than in a low angle of attack.

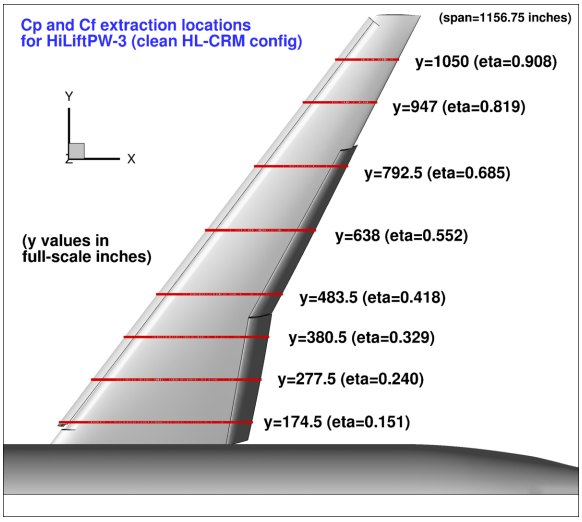

Figure 5.5: HL-CRM: C_P Extraction Locations on Wing Elements [15]

Comparing the Auburn and Committee grid, the differences in the C_P plot is almost negligible for a coarse grid at 8^0 angle of attack (Fig. 5.7) but shows significant differences with the medium grid (Fig. 5.8) especially at the midspan location on the wing and slat element. The differences in the C_P at these locations between the Auburn and Committee grid might be due to the differences in the element size specified during the grid generation. The trend is similar at 16^0 angle of attack.

The C_P plots among the different turbulence models are similar between the grid levels and angle of attacks (Fig. 5.9, 5.10, 5.14, 5.15). However, the Wilcox $k-\epsilon$ model predicts slightly higher suction peak than the Menter SST and the SAS model.

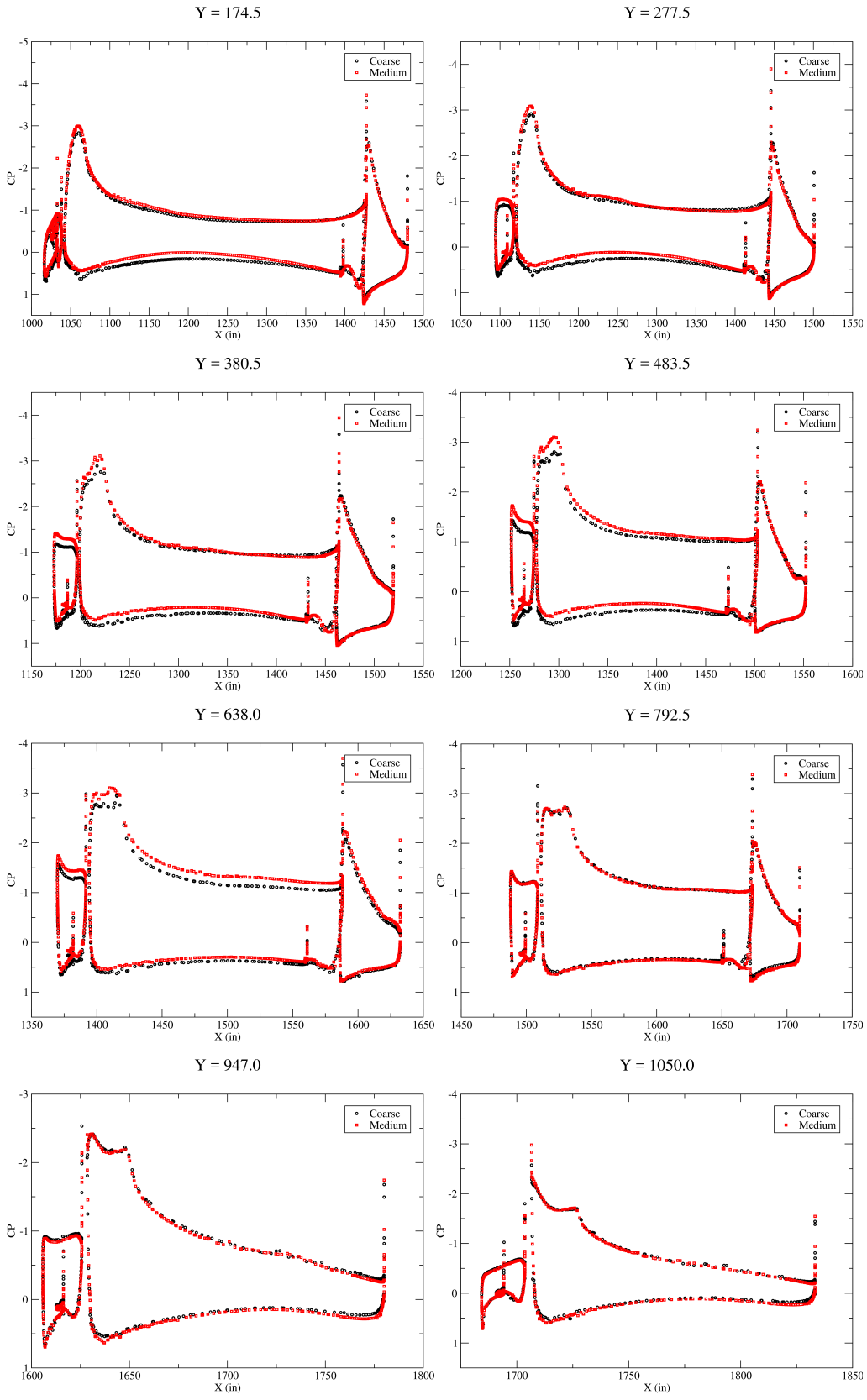

Figure 5.6: HL-CRM: C_P Convergence for Auburn Grid at AOA 8^0 with Menter SST Turbulence Model

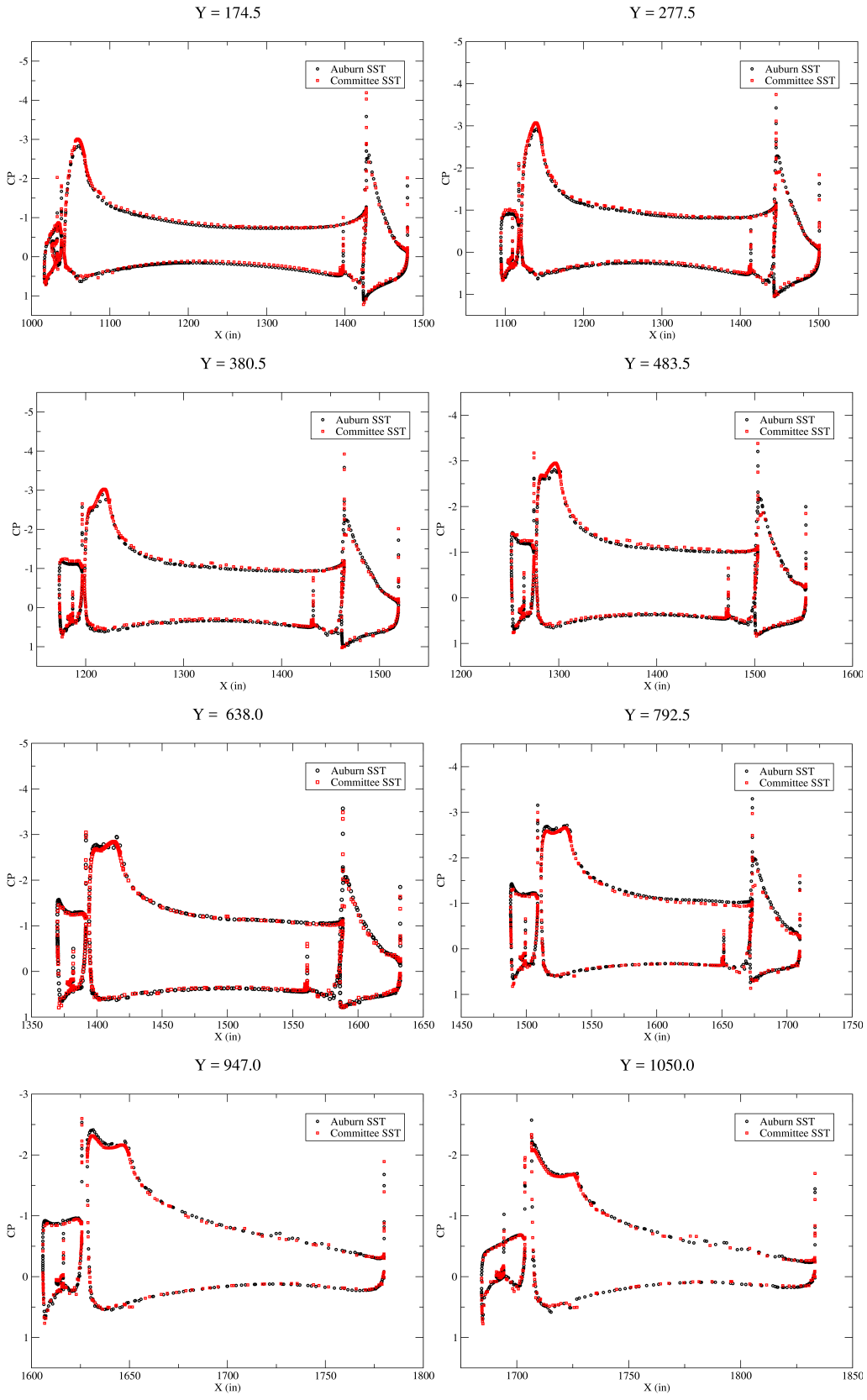

Figure 5.7: HL-CRM: C_P Comparison for Coarse Grid Between Auburn and Committee Grid at AOA 8^0

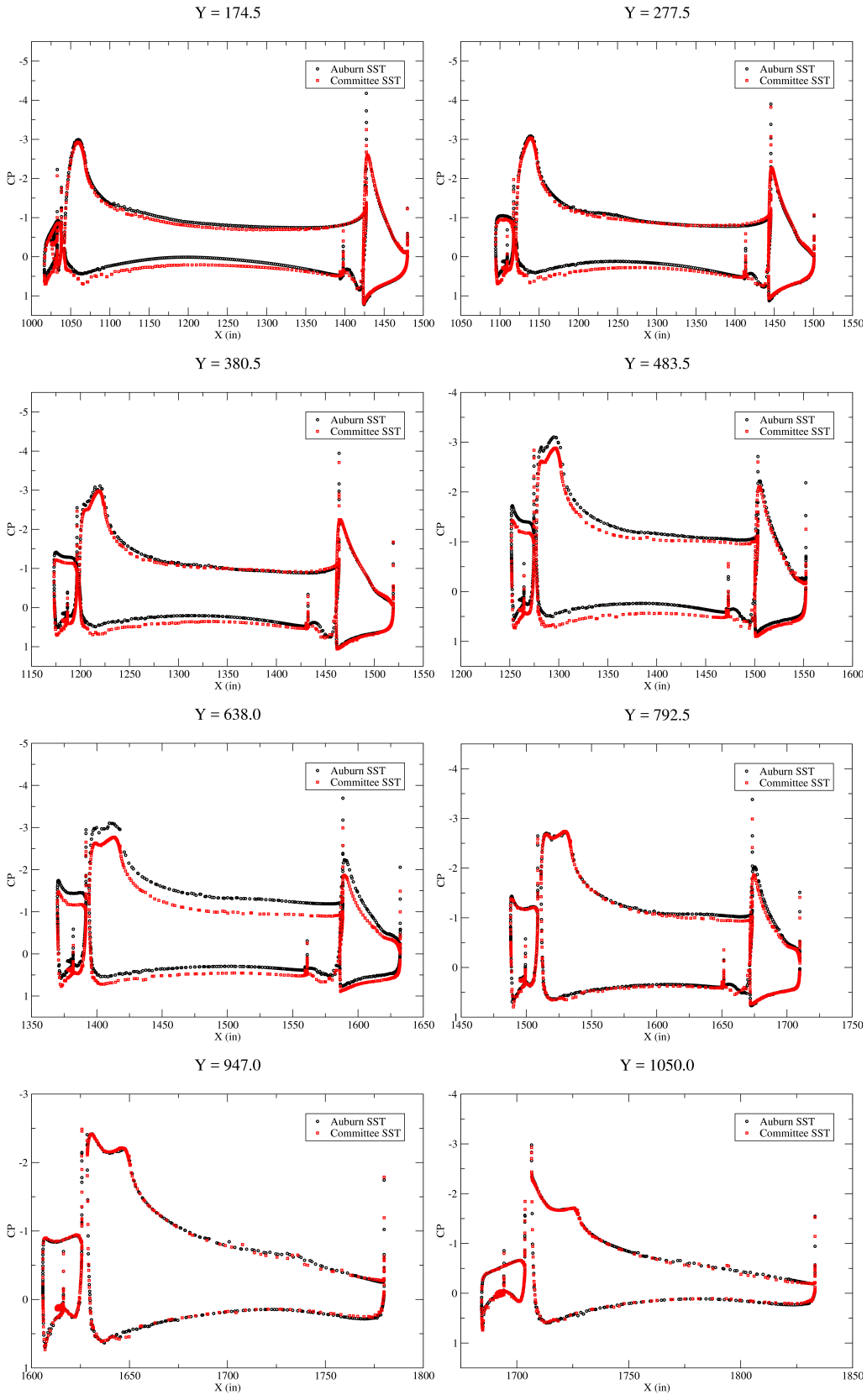

Figure 5.8: HL-CRM: C_P Comparison for Medium Grid Between Auburn and Committee Grid at AOA 8^0

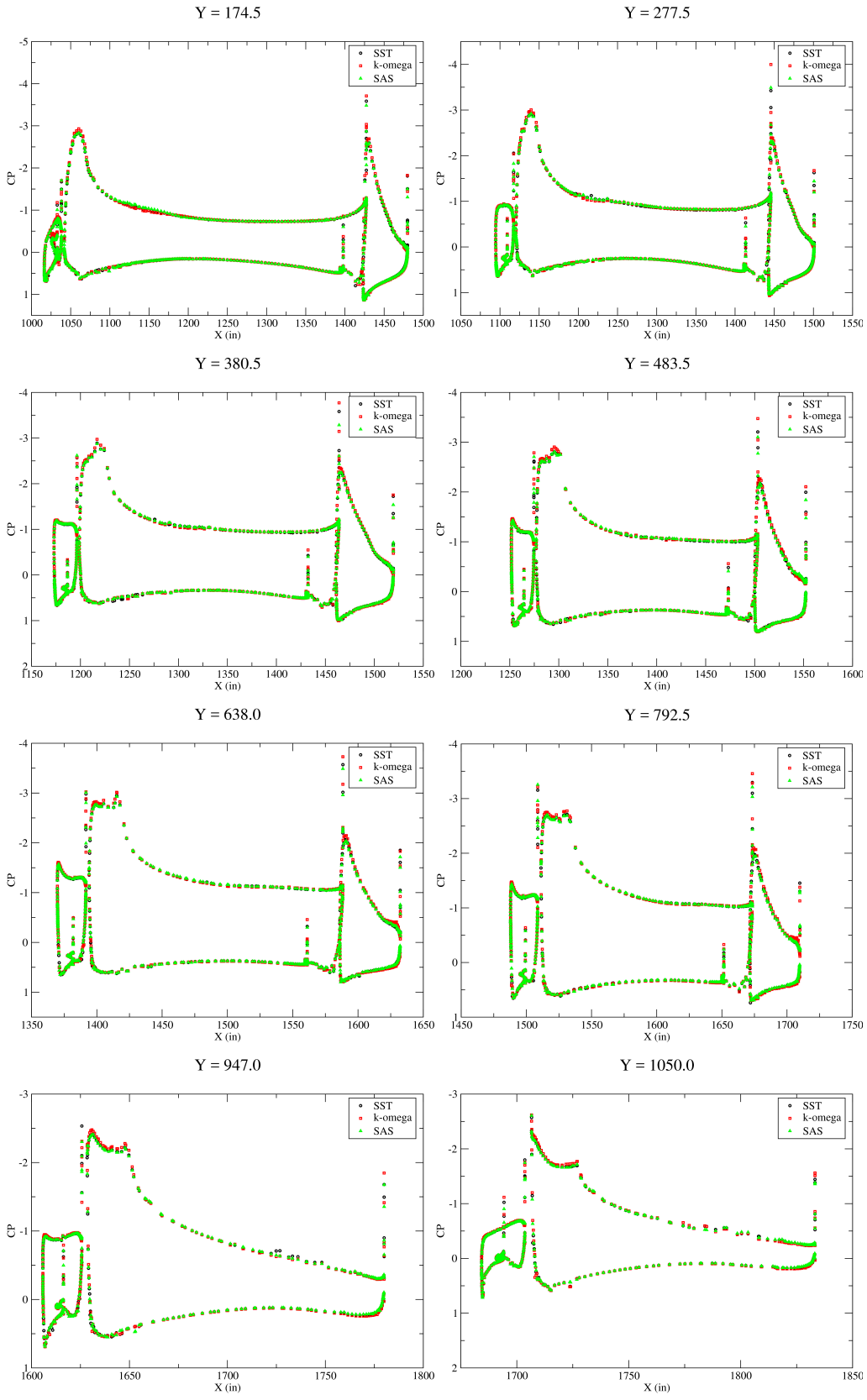

Figure 5.9: HL-CRM: C_P Comparison for Auburn Coarse Grid Between Different Turbulence Models at AOA 8^0

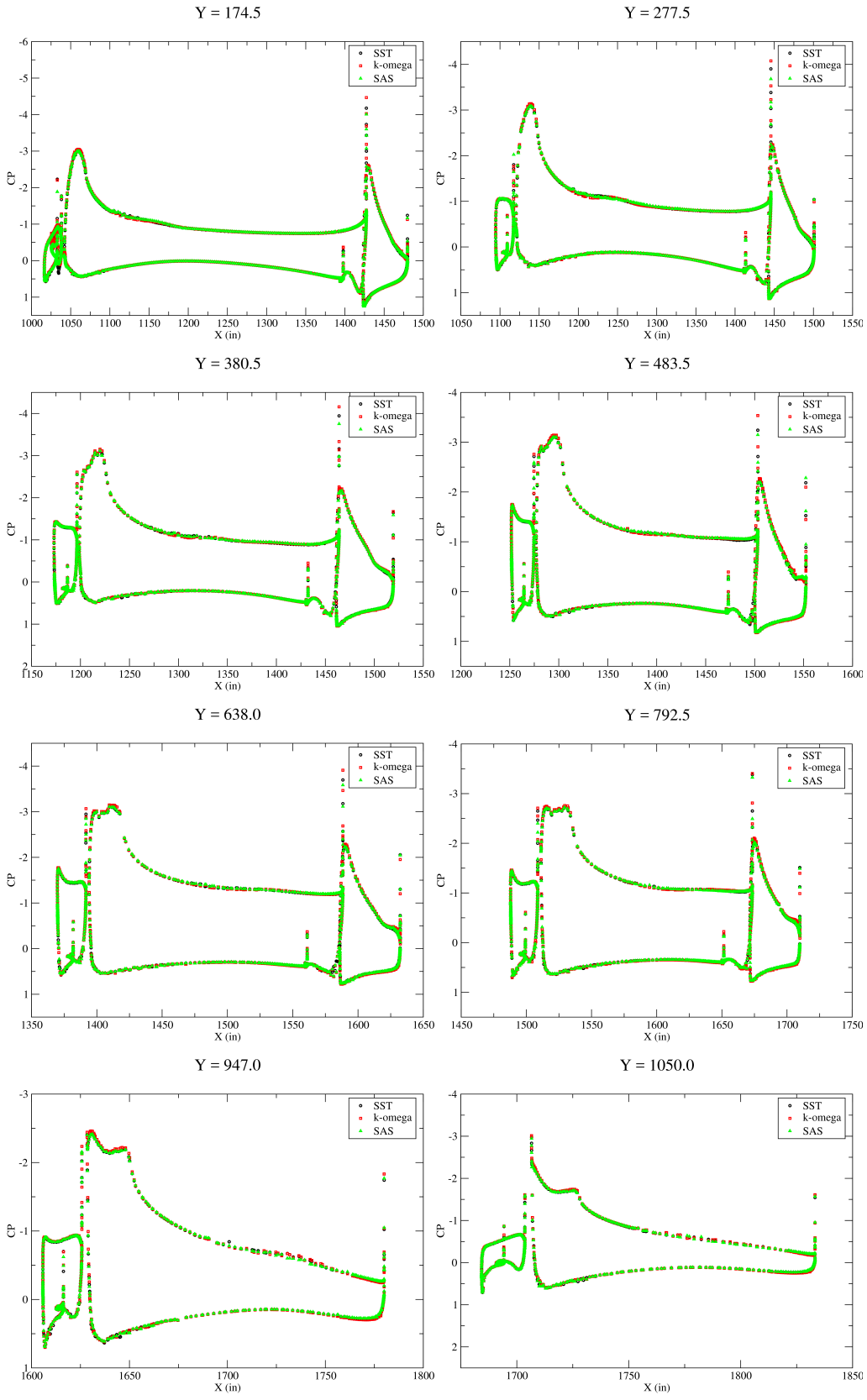

Figure 5.10: HL-CRM: C_P Comparison for Auburn Medium Grid Between Different Turbulence Models at AOA 8^0

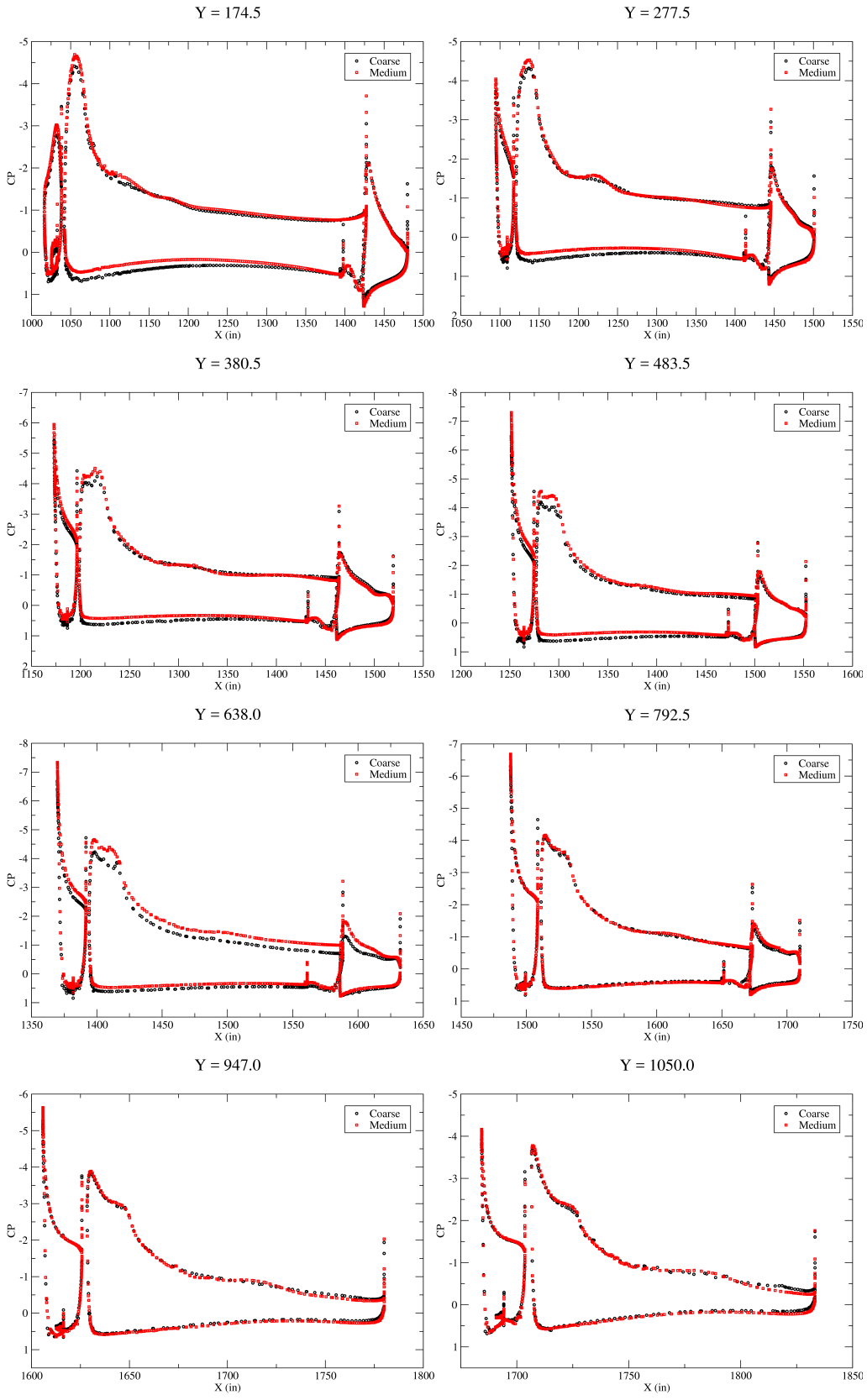

Figure 5.11: HL-CRM: C_P Convergence for Auburn Grid at AOA 16^0 with Menter SST Turbulence Model

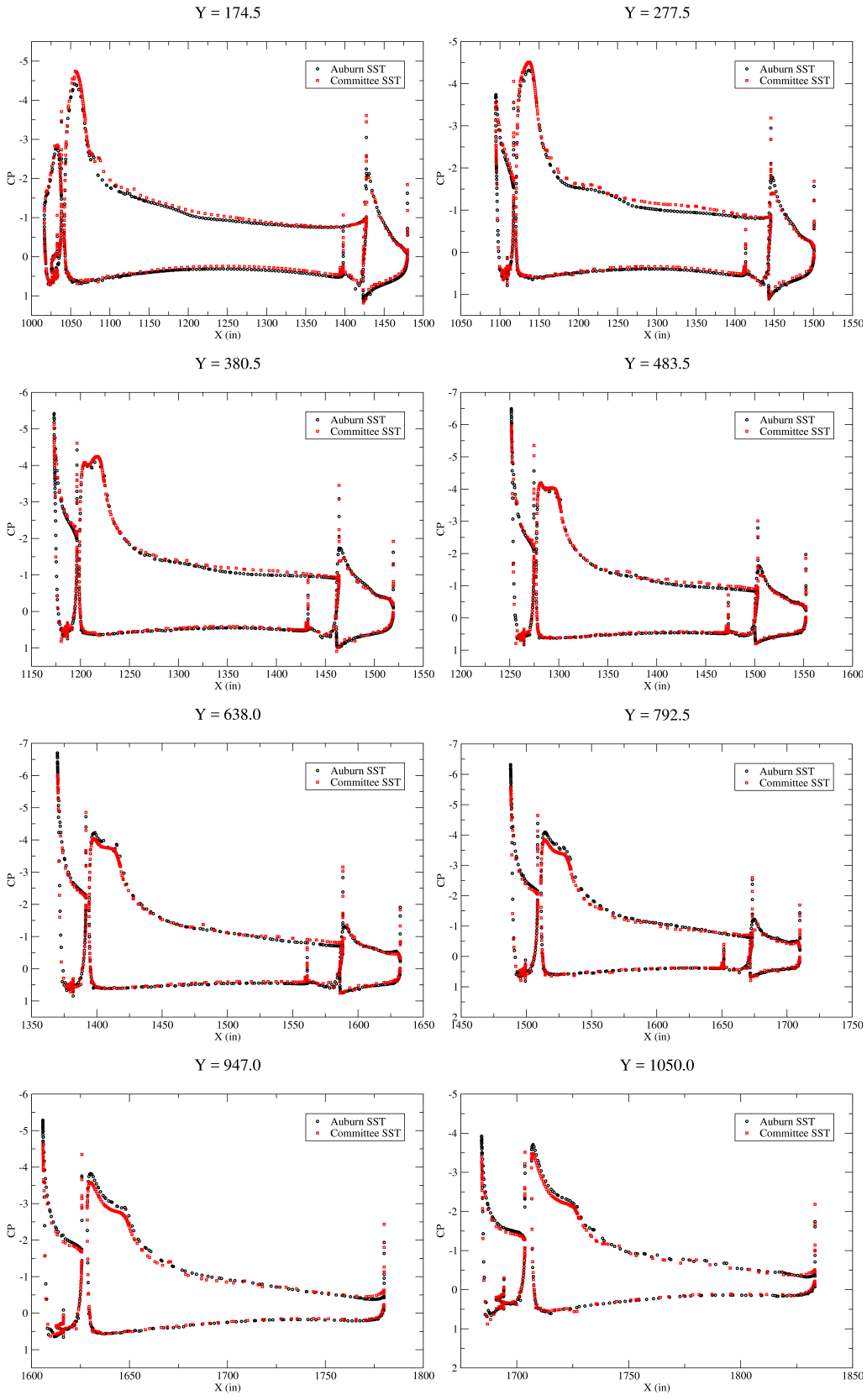

Figure 5.12: HL-CRM: C_P Comparison for Coarse Grid Between Auburn and Committee Grid at AOA 16^0

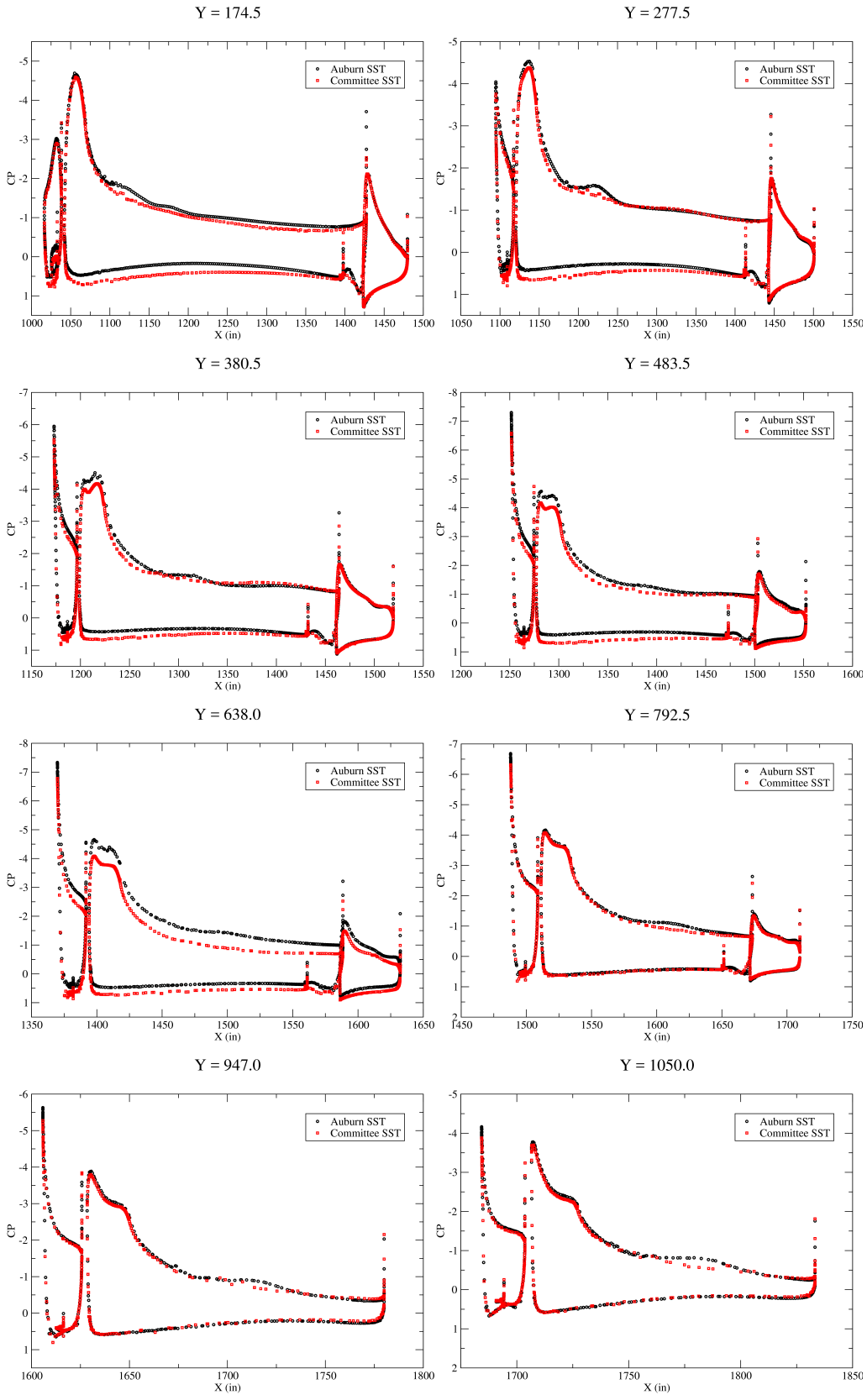

Figure 5.13: HL-CRM: C_P Comparison for Medium Grid Between Auburn and Committee Grid at AOA 16^0

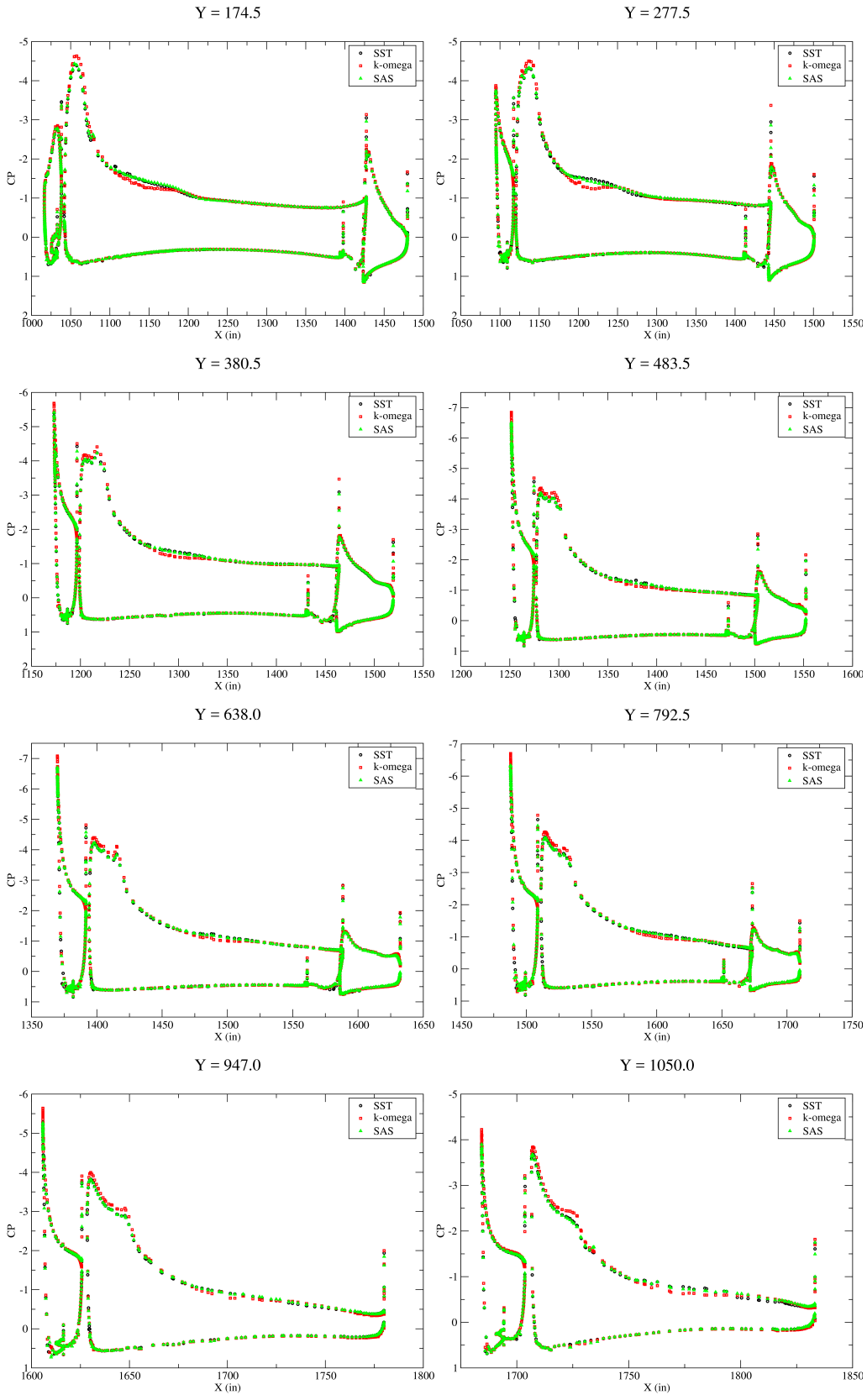

Figure 5.14: HL-CRM: C_P Comparison for Auburn Coarse Grid Between Different Turbulence Models at AOA 16^0

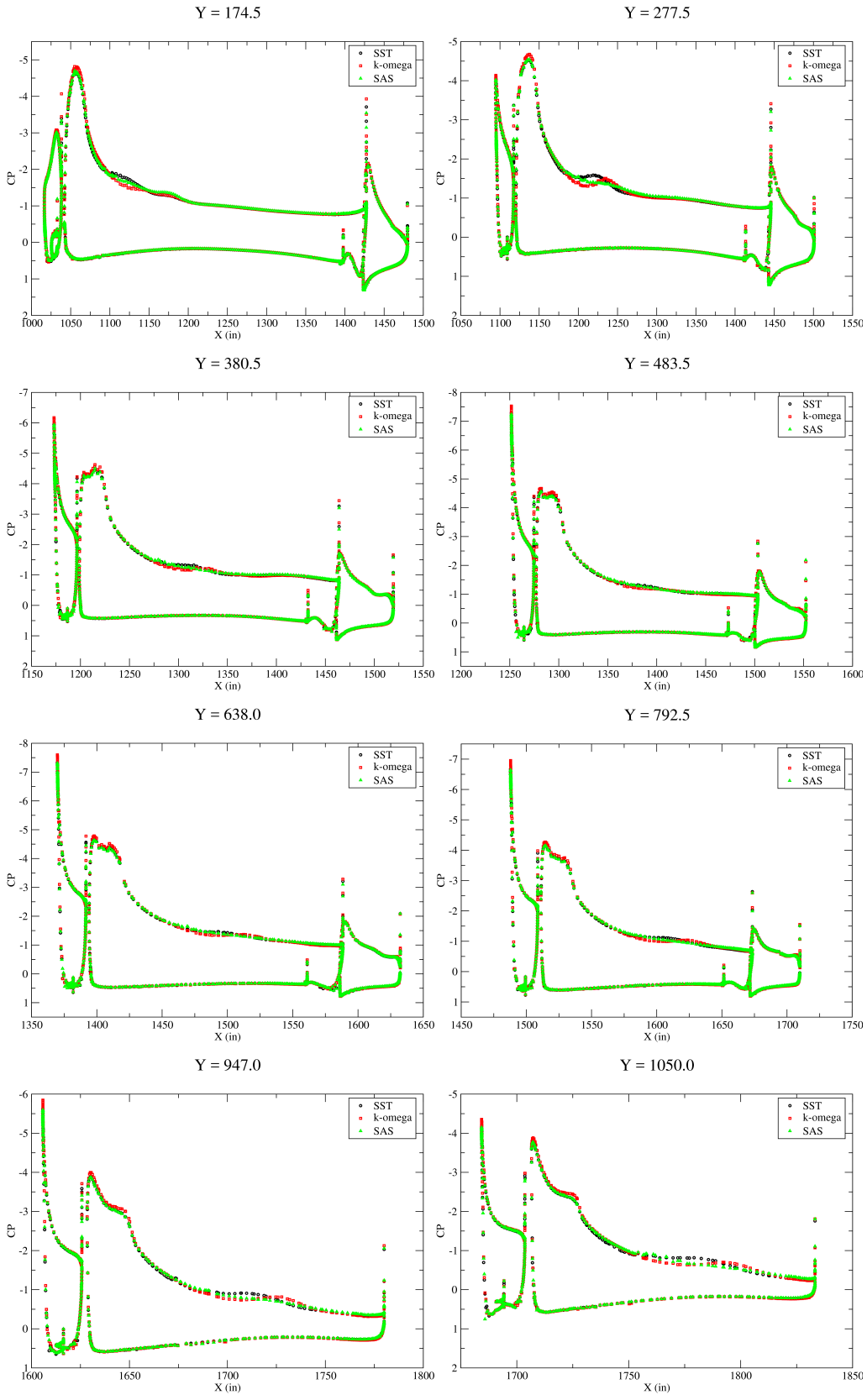

Figure 5.15: HL-CRM: C_P Comparison for Auburn Medium Grid Between Different Turbulence Models at AOA 16^0

5.1.3 Wake Velocity Convergence

The velocity component on the upper surface of the wing elements are compared to check the effects of grid convergence on the resolution of wake velocities. Figure 5.16 shows the velocity extraction location on the HL-CRM for grid convergence study.

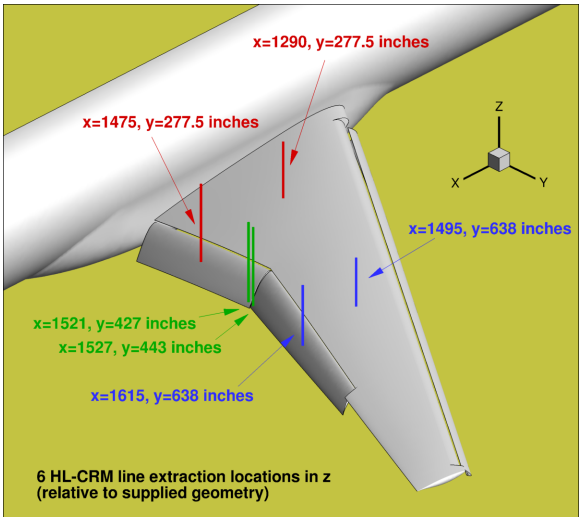

Figure 5.16: HL-CRM: Velocity Extraction Locations on Wing Elements [15]

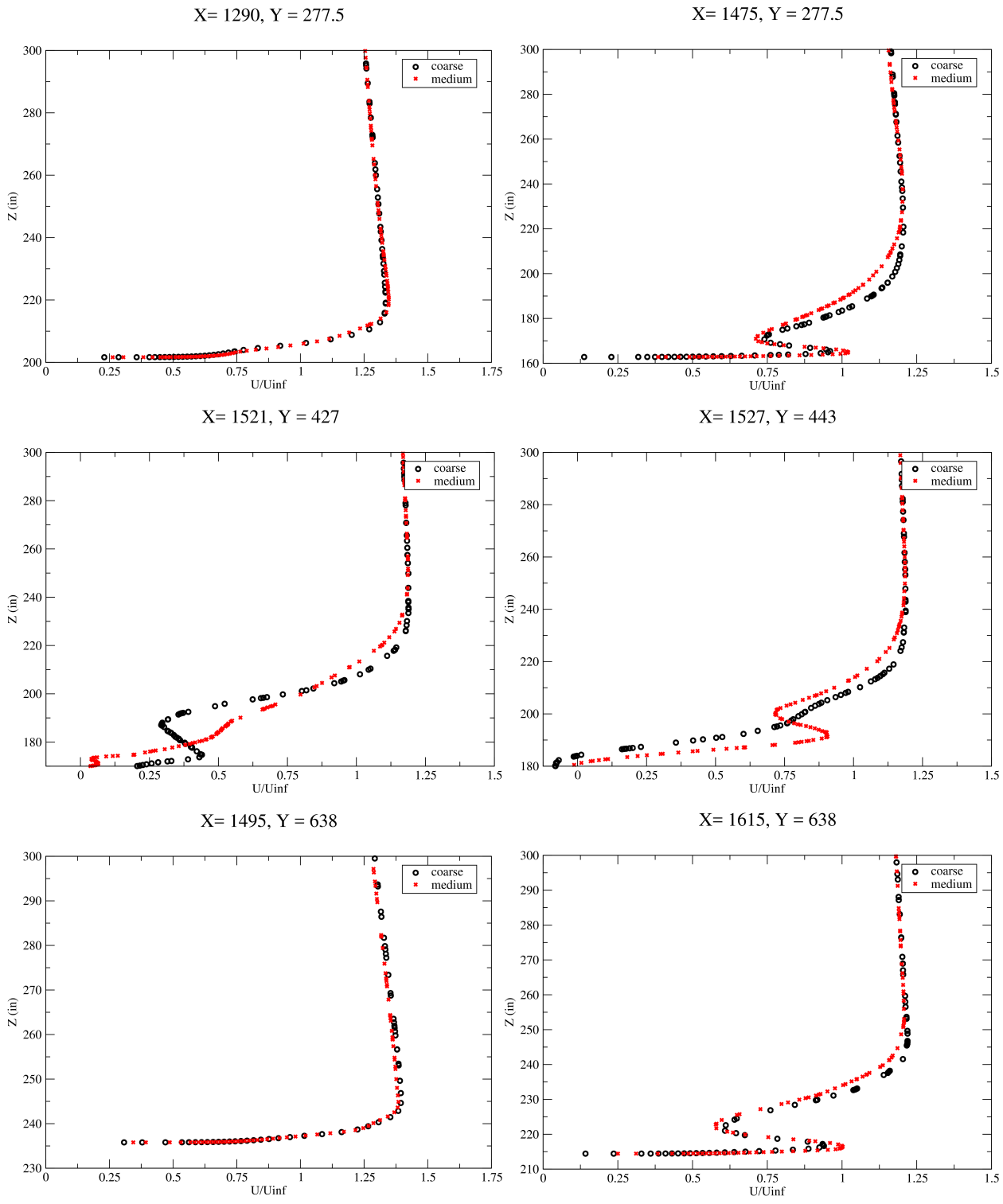

Figure 5.17: HL-CRM: Convergence of U/Uinf for Auburn Grid at AOA 8^0 with Menter SST Turbulence Model

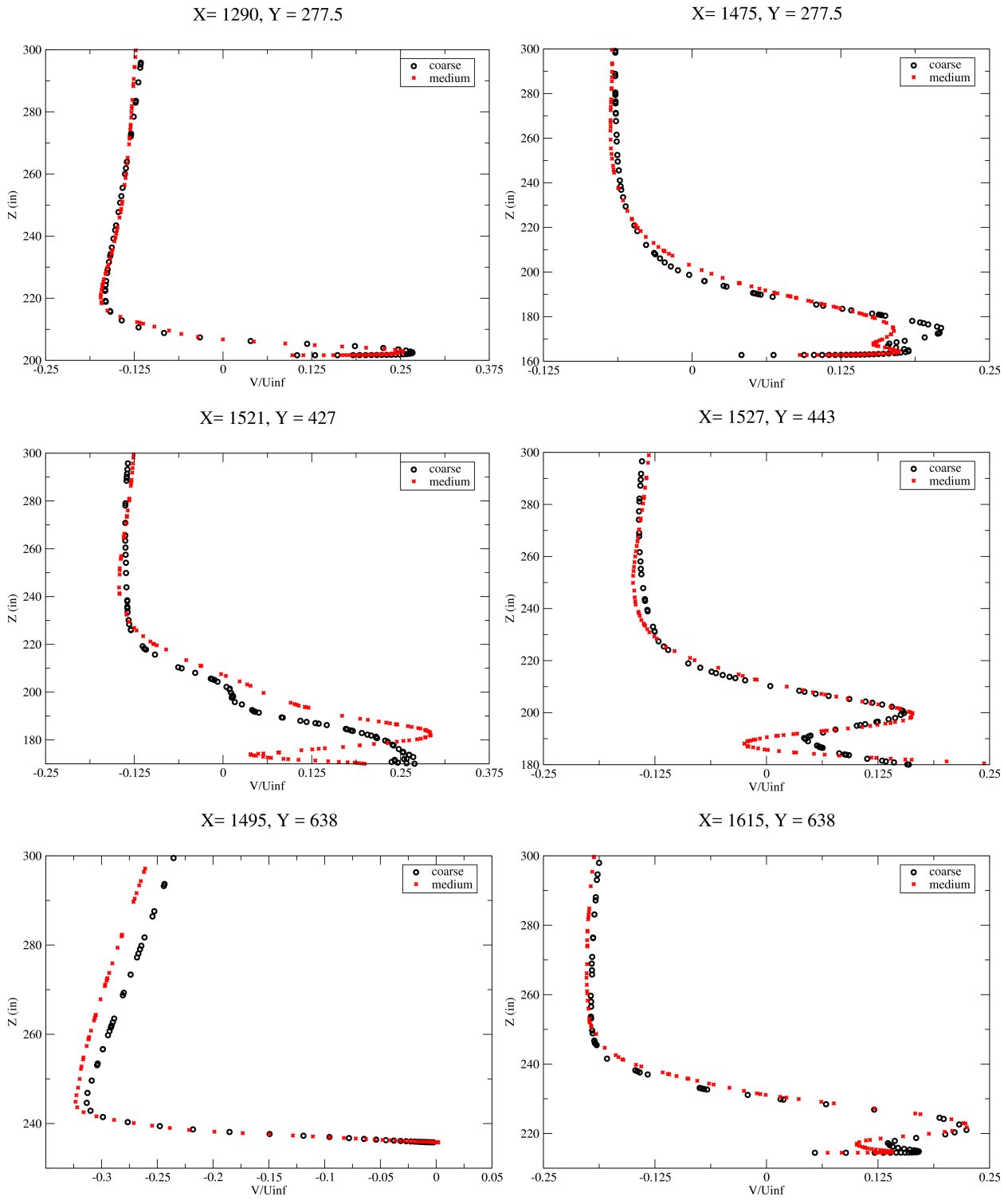

Figure 5.18: HL-CRM: Convergence of V/Uinf for Auburn Grid at AOA 8^0 with Menter SST Turbulence Model

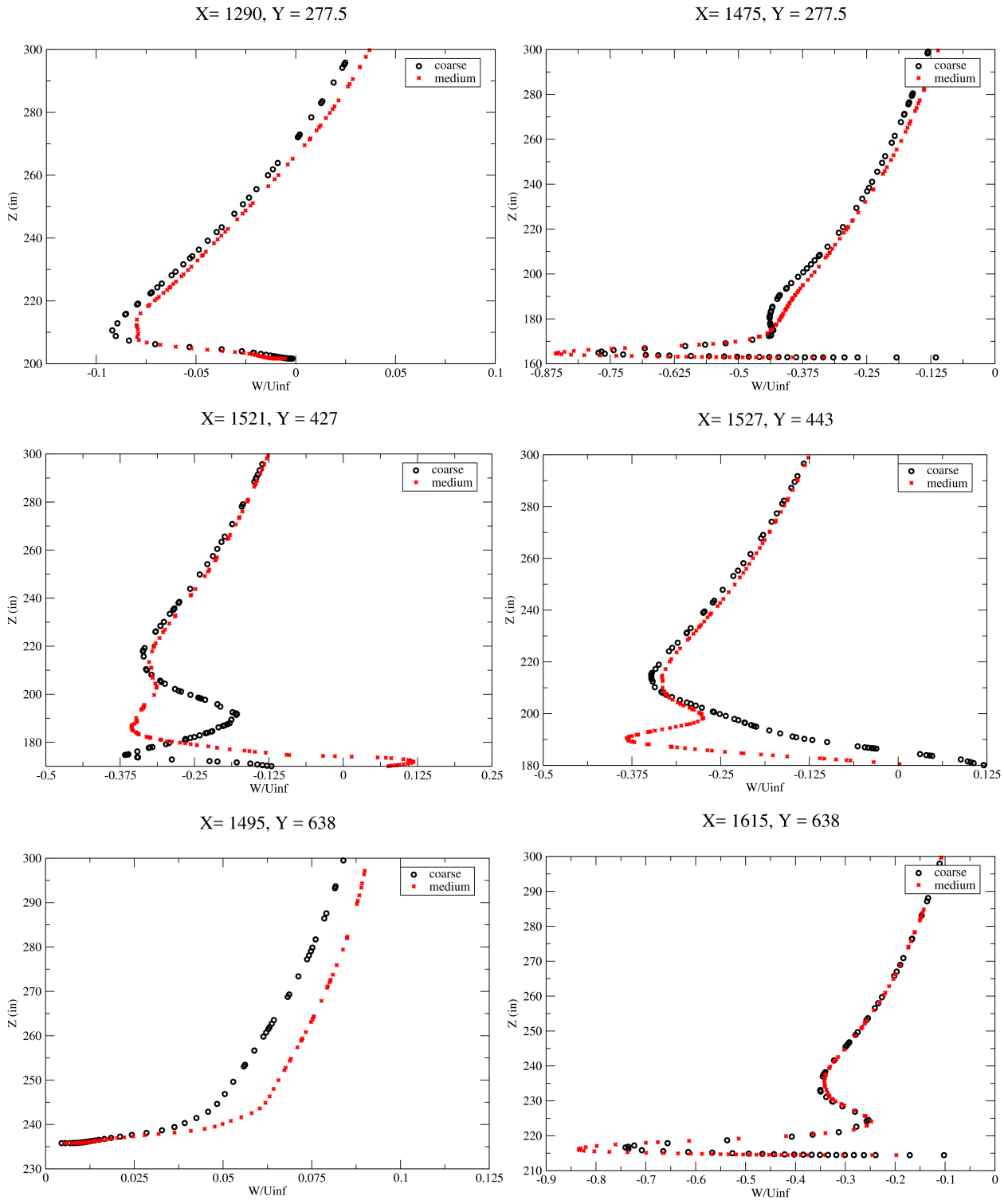

Figure 5.19: HL-CRM: Convergence of W/Uinf for Auburn Grid at AOA 8^0 with Menter SST Turbulence Model

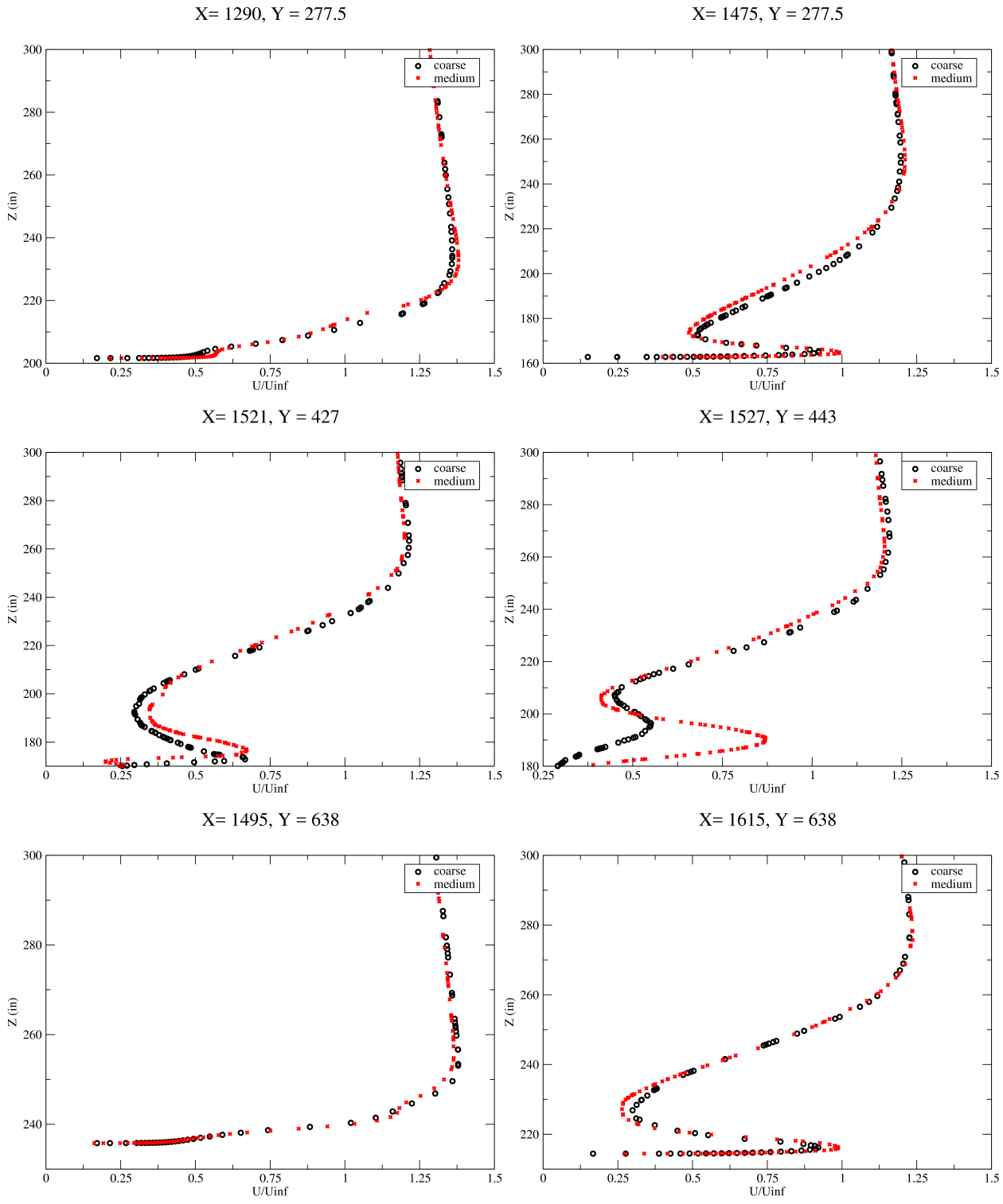

Figure 5.20: HL-CRM: Convergence of U/Uinf for Auburn Grid at AOA 16^0 with Menter SST Turbulence Model

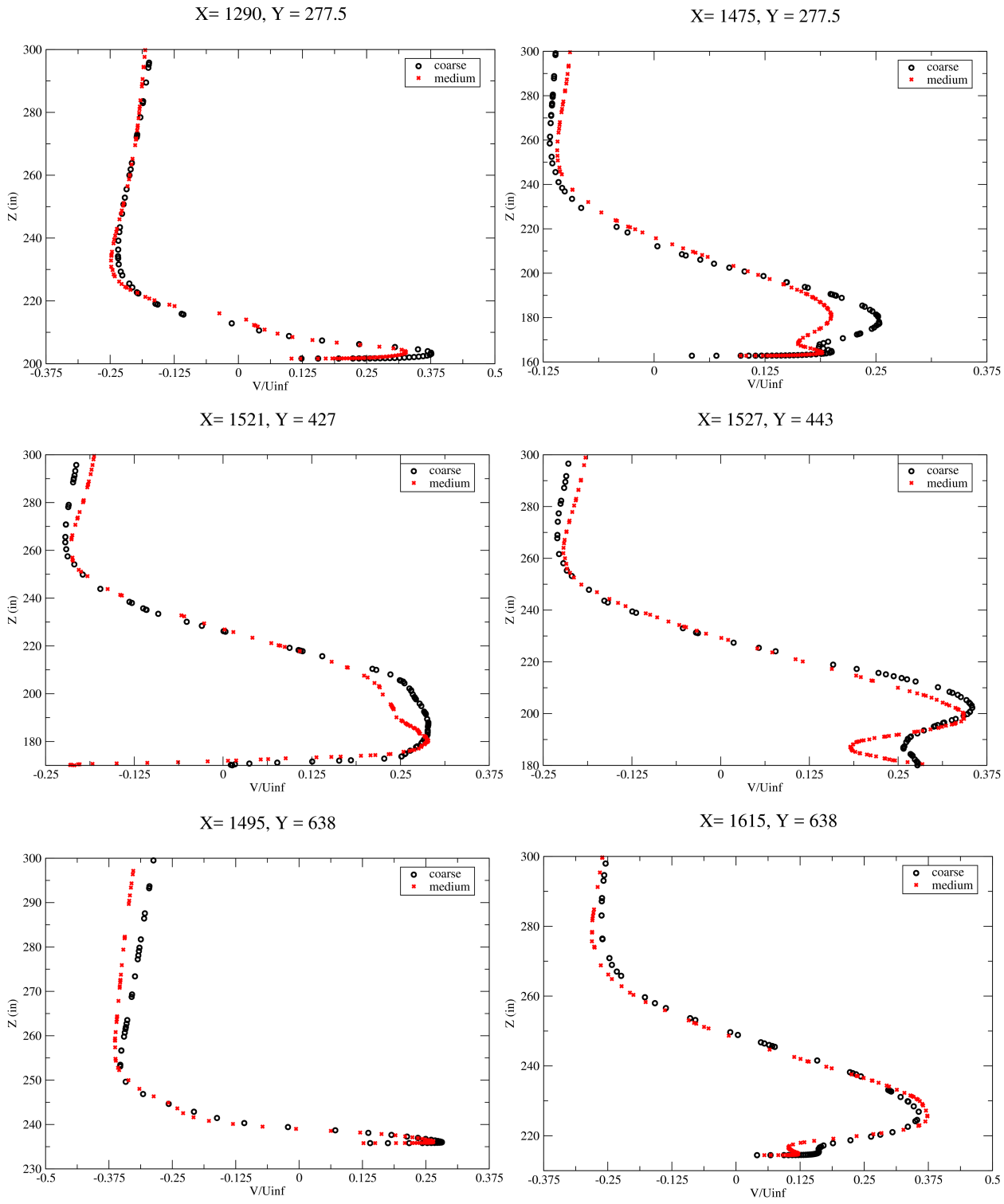

Figure 5.21: HL-CRM: Convergence of V/Uinf for Auburn Grid at AOA 16^0 with Menter SST Turbulence Model

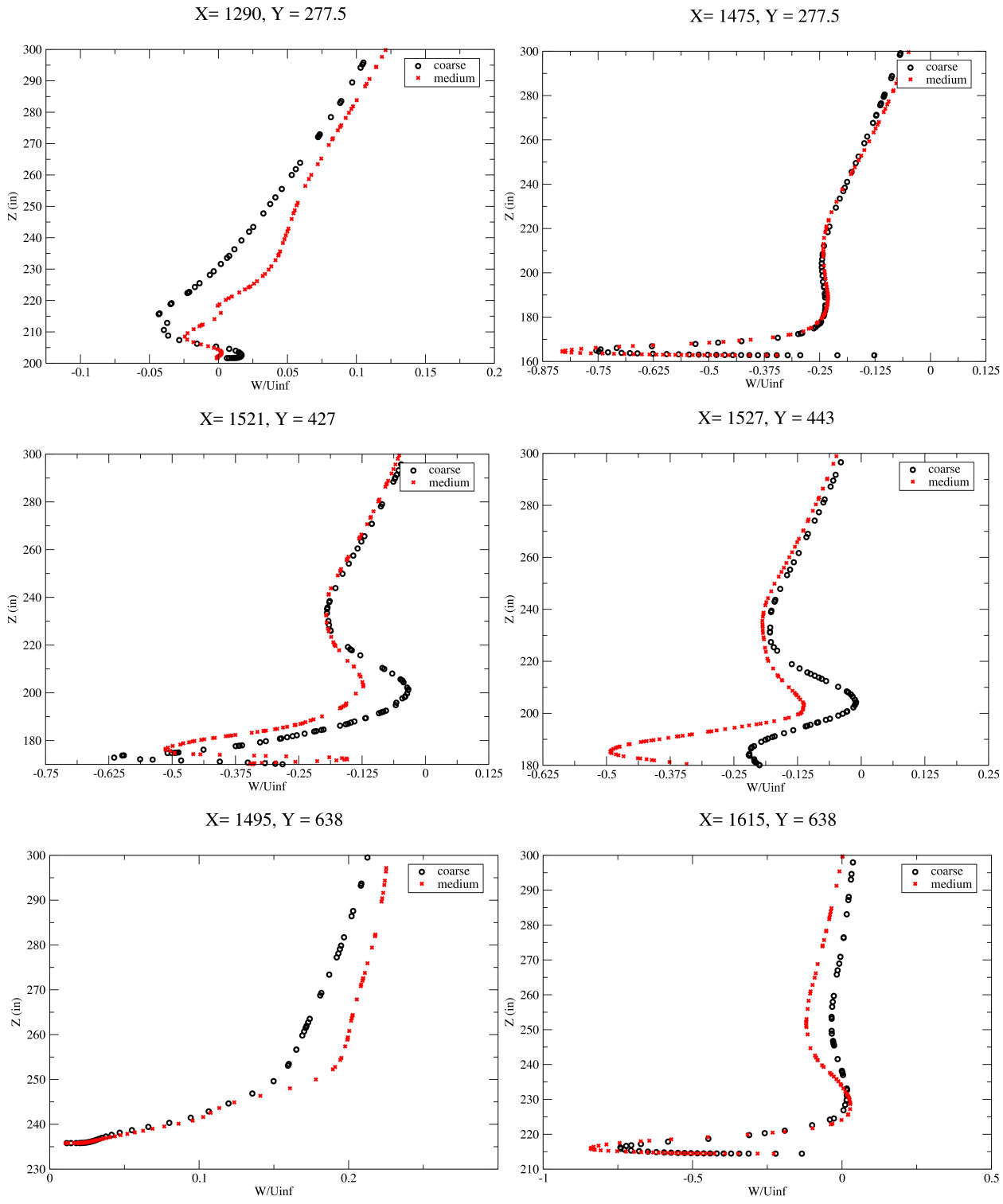

Figure 5.22: HL-CRM: Convergence of W/Uinf for Auburn Grid at AOA 16^0 with Menter SST Turbulence Model

Figure 5.17 - 5.22 indicates that the grid refinement has significant effect on the resolution of the wake velocities. The difference between the coarse and medium grid results for the U/Uinf component is smaller at the midspan of the wing. However towards the flap location, there is a significant differences in the U-velocity among the grid resolution level, evident in the Fig. 5.17 and 5.20. At this locations, the wake of the wing interacts with the flap boundary layer and the results show that there is an improvement in the resolution of this interaction with the grid refinement. This trend is similar in the other components of the velocity as well, V/Uinf and W/Uinf, however the velocity curves at the wing midspan locations for V and W components show that the coarse grid level underpredicts these cross-flow velocity components. The effects of grid refinement in the wake resolution is consistent among the various angle of attack.

5.2 JSM: Nacelle Installation Study

The experimental test data are available for the JSM and the CFD results are compared against the provided test data. This case also provide a ground for validation of the numerical schemes used for the overall study of the high-lift configuration.

5.2.1 Force and Moment Comparison

Variable Mach Solution

The Fig. 5.23 shows the C_L variation with respect to angle of attack (lift curve), C_L vs C_D graph (drag polar), and C_L vs C_M plot (moment plot) for Auburn and Committee grid compared against the experiments for the JSM Nacelle/Pylon OFF configuration. The solutions for the JSM Nacelle/Pylon OFF configuration presented in the Fig. 5.23 are obtained using the variable Mach solver with the Menter SST turbulence model for both Auburn and Committee grids.

The CFD results from this study using the variable Mach solver in *TENASI* follow the lift curve in the same manner as experiments for most part of the curve. The numerical solution

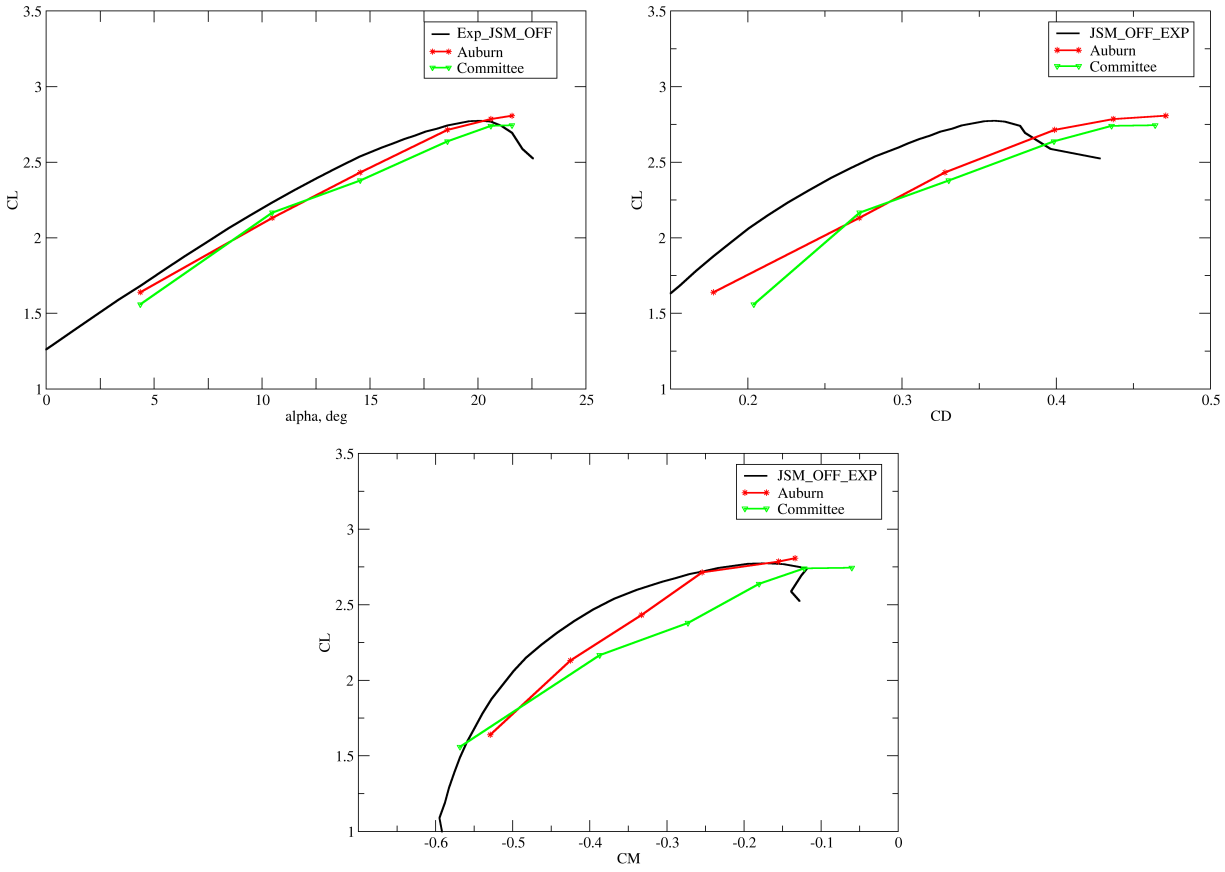

Figure 5.23: JSM: JSM Nacelle/Pylon OFF Configuration with Variable Mach Solver- Force and Moment Plots

underpredicts the lift in the linear region of the lift curve. The $C_{L,max}$ from the solution is slightly higher than the experiments and the $C_{L,max}$ occurs at higher angle of attack than in experiments. The results from the drag polar indicates that for any given C_L, the numerical solution overpredicts the drag value and the pitching moment is underpredicted based on the moment diagram. Comparing the Auburn grid and the Committee grid, Auburn grid results are closer to the experiments than the Committee grid but only with small differences in the values.

Evident in the Fig. 5.23, the solution failed to predict the stall characteristics completely. The inaccuracy in the numerical solution might be due to the unnecessary flow separation on the upper surface of the wing elements introduced due to simulating the aircraft by abruptly

increasing the angle of attack on the wing. Once the separation is introduced in the solution, it is difficult for CFD to recover a smooth solution. One possible approach to avoid this kind of separation from the flow solution is to gradually increase the angle of attack with the number of iterations until the desired angle of attack is achieved i.e. in order to resolve the solution for AOA of 4.36^0, starting the solution at AOA of 0^0 and gradually increasing the AOA with iterations until 4.36^0 is reached. Gradual increase in angle of attack helps to avoid the unnecessary flow separation and the flow remains attached until the actual separation occurs.

The solution with the incompressible solver is obtained using the technique of pitching the aircraft gradually rather than simulating at different angle of attacks with abrupt change in angles.

Incompressible Solution

The force and moment plots from the incompressible flow solution using the SAS turbulence model are represented in Fig. 5.24 for the JSM Nacelle/Pylon OFF Configuration and in Fig. 5.25 for the JSM Nacelle/Pylon ON Configuration.

The results with the incompressible solver with the SAS turbulence model in *TENASI* shows better prediction of the stall properties. However, the lift remains largely underpredicted. The solution matches experiments for most part of the linear region of the lift curve. The location of $C_{L,max}$ is accurately predicted in the solution for both configurations (Nacelle/Pylon ON and OFF) but the predicted $C_{L,max}$ is slightly lower than the experiments. Typical to one-equation turbulence model, SAS tends to underpredict lift and moment while overpredicting drag. This behavior is clearly seen in the above force and moment plots (Fig. 5.24, 5.25 where the drag and moment curves are slightly towards right than the experiments). Since the SAS model was stable with the JSM for both Nacelle/Pylon ON and OFF configurations, SAS was used instead of the Menter SST and the Wilcox $k-\omega$

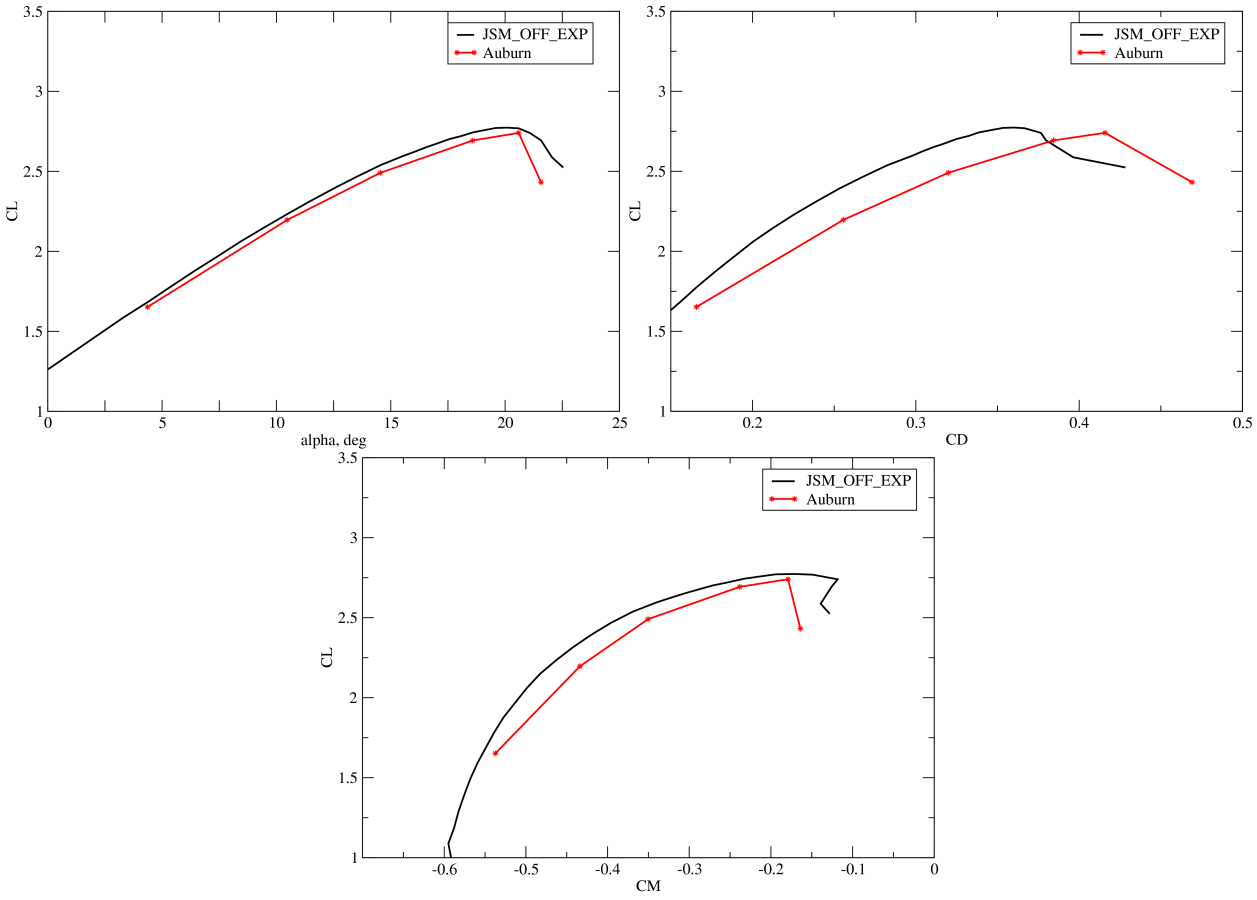

Figure 5.24: JSM: JSM Nacelle/Pylon OFF Configuration with Incompressible Solver- Force and Moment Plots

with the incompressible solver. Also, the Wilcox $k-\omega$ model with JSM Nacelle/Pylon ON configuration showed convergence issue with the variable Mach solver.

The C_L, C_D, and C_M with the incompressible solver show better agreement with the experiments than with variable Mach solution, comparing Fig. 5.23 with 5.24. The deviation of the CFD results from the experiments at high angle of attack indicates that the massive separation is still present and is unavoidable from the CFD solution. The results are consistent among both configurations, with Nacelle/Pylon (N/P) and without N/P.

The differences in the force and moments obtained in this study compared with experiments are tabulated in the Table 5.1 - 5.3. The result in percentage denotes: $(|CFD_{value} - EXP_{value}|)/|EXP_{value}|$.

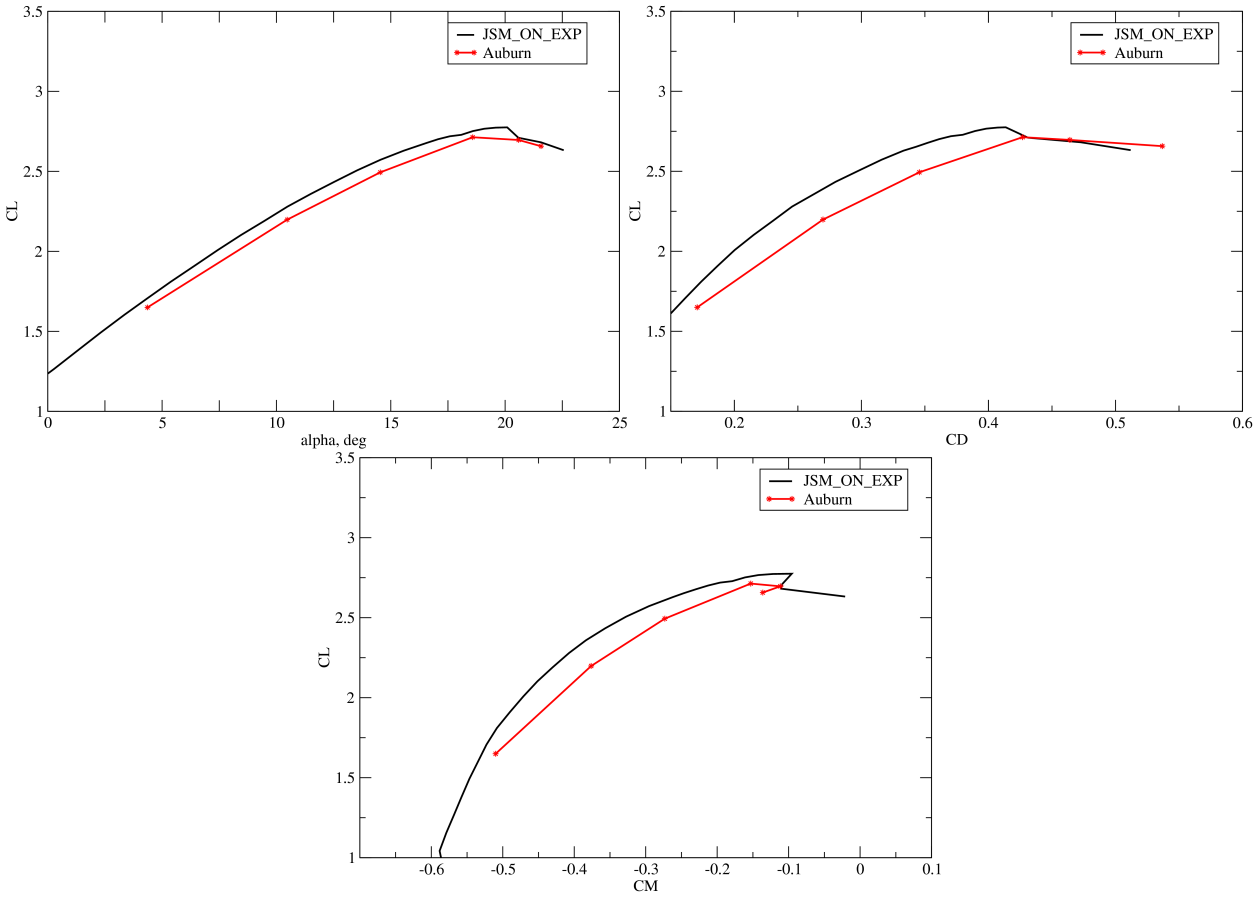

Figure 5.25: JSM: JSM Nacelle/Pylon ON Configuration with Incompressible Solver- Force and Moment Plots

	JSM Nacelle/Pylon OFF			JSM Nacelle/Pylon ON		
AOA (deg)	$C_{L,CFD}$	$C_{L,EXP}$	% diff	$C_{L,CFD}$	$C_{L,EXP}$	% diff
4.36	1.65205	1.68197	1.78	1.64948	1.70702	3.37
10.47	2.19648	2.23268	1.62	2.19814	2.27978	3.58
14.54	2.49076	2.53811	1.86	2.49387	2.57252	3.06
18.58	2.69273	2.74305	1.83	2.71337	2.75168	1.39
20.59	2.74047	2.76878	1.02	2.69592	2.70995	0.52
21.57	2.43176	2.69367	9.72	2.65730	2.68143	0.90

Table 5.1: Differences in C_L between CFD and Experiments at different angle of attack

The study with the JSM is a nacelle installation study. The effects of Nacelle/Pylon installation on the force and moment characteristics of the JSM is represented in the Fig. 5.26. The Nacelle/Pylon installation on the JSM shows that the lift characteristics of the JSM

	JSM Nacelle/Pylon OFF			JSM Nacelle/Pylon ON		
AOA (deg)	$C_{D,CFD}$	$C_{D,EXP}$	% diff	$C_{D,CFD}$	$C_{D,EXP}$	% diff
4.36	0.16569	0.15563	6.46	0.17077	0.16135	5.84
10.47	0.25563	0.22592	13.15	0.26978	0.24548	9.90
14.54	0.31991	0.28260	13.20	0.34566	0.31596	9.40
18.58	0.38419	0.33871	13.43	0.42690	0.38952	9.59
20.59	0.41580	0.36664	13.41	0.46412	0.43112	7.65
21.57	0.46909	0.37966	23.55	0.53688	0.47255	13.61

Table 5.2: Differences in C_D between CFD and Experiments at different angle of attack

	JSM Nacelle/Pylon OFF			JSM Nacelle/Pylon ON		
AOA (deg)	$C_{M,CFD}$	$C_{M,EXP}$	% diff	$C_{M,CFD}$	$C_{M,EXP}$	% diff
4.36	-0.53741	-0.54962	2.22	-0.50999	-0.52279	2.45
10.47	-0.43387	-0.46323	6.34	-0.37631	-0.40718	7.58
14.54	-0.35041	-0.36891	5.01	-0.27325	-0.29527	7.56
18.58	-0.23815	-0.23318	2.13	-0.15306	-0.16103	4.95
20.59	-0.17903	-0.14896	20.18	-0.11156	-0.10892	2.42
21.57	-0.16394	-0.12566	30.46	-0.13620	-0.11073	23.00

Table 5.3: Differences in C_M between CFD and Experiments at different angle of attack

improves with the N/P installation and the CFD results from this study remain consistent with the experiments however, the improvements in C_L (ΔC_L) is fairly underpredicted. Also, the CFD is consistent with the experiments on the stall characteristics of these two configurations and the CFD results show that JSM with N/P configuration stalls earlier than the without N/P configuration. The effects of the nacelle installation on the basis of ΔC_D and ΔC_M predicted by CFD shows greater agreement with the experiments than ΔC_L.

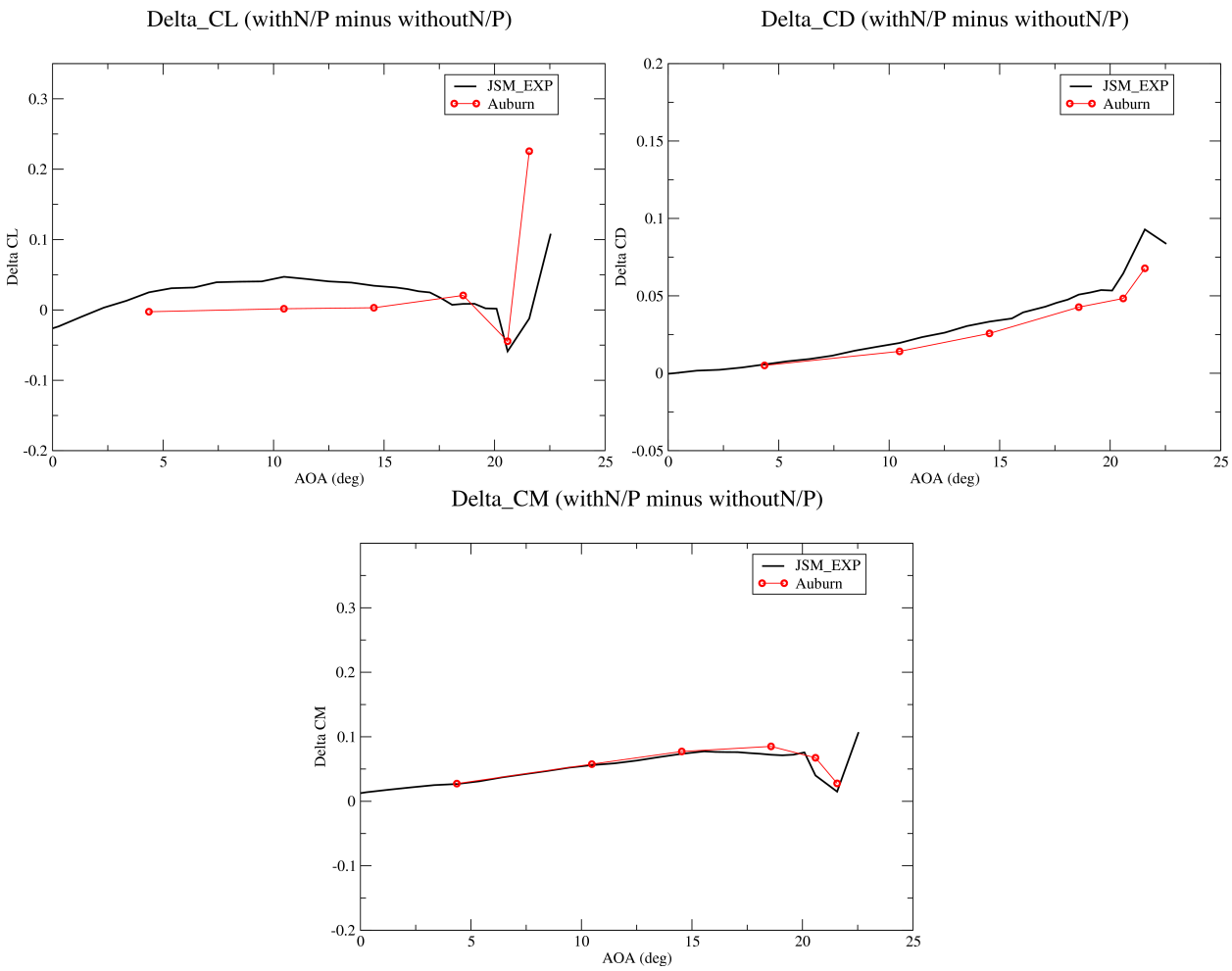

Figure 5.26: JSM: JSM Deltas (with N/P minus without N/P)

5.2.2 C_P Comparison

The HiLiftPW-3 requests extraction of C_P at different locations on the aircraft where the test data were measured from the pressure taps on the experimental setup. Figure 5.27 shows the different cutting planes for C_P extraction and the approximate distance in percentage from root to tip with respect to the wingspan. For this research, the C_P data from the solutions are extracted using the *TecPlot*[1] macro provided by the HiLiftPW-3 committee to facilitate the data extraction process. Minor modifications to the macro were done in order to make the macro compatible with the *Tenasi* output i.e. changing the units on the independent variables (m to mm) and calculating the C_P from pressure variable.

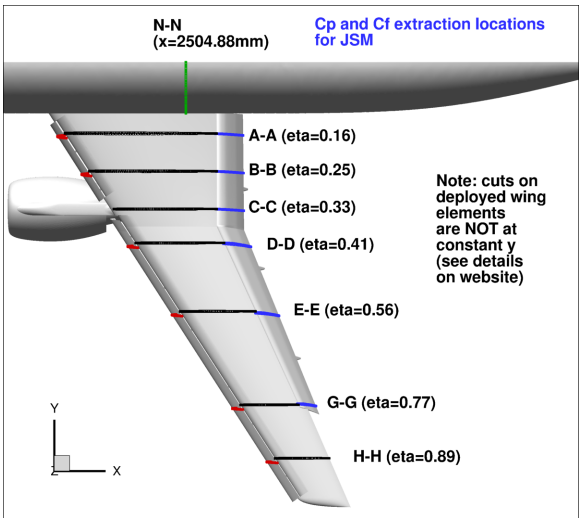

Figure 5.27: JSM: C_P Extraction Locations on Wing Elements [15]

Variable Mach Solution

Figure 5.28 - 5.33 show the comparison of C_P with experiments at different locations on the aircraft determined by the cutting planes at an angle of attack of 4.36^0 to 21.57^0 for the JSM Nacelle/Pylon OFF configuration with Variable Mach solver using the Menter SST turbulence model.

[1]TecPlot is a visual data analysis package

Slat A-A

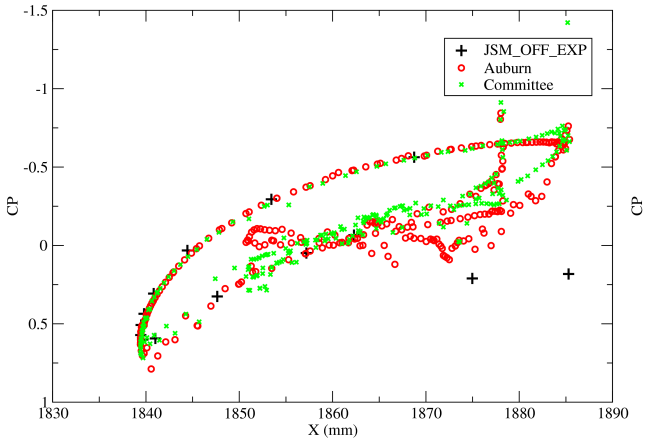

Slat B-B

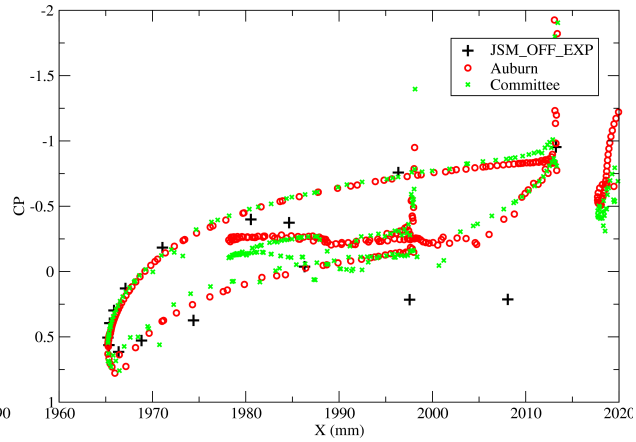

Wing A-A

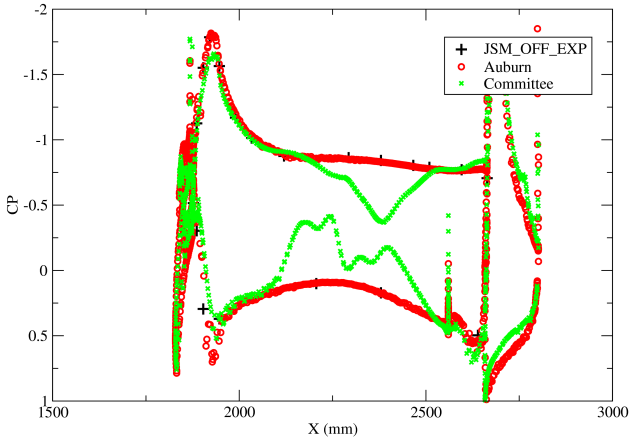

Wing B-B

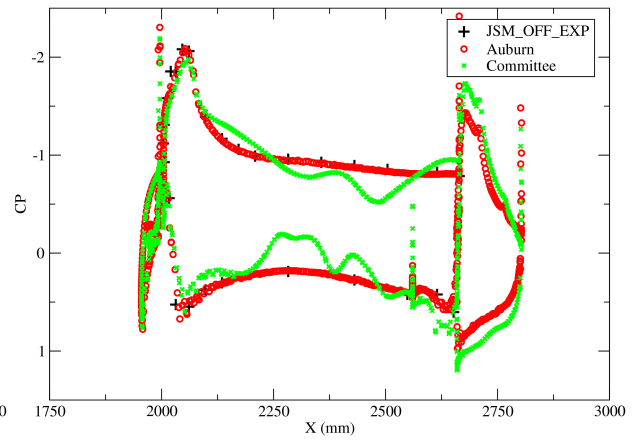

Flap A-A

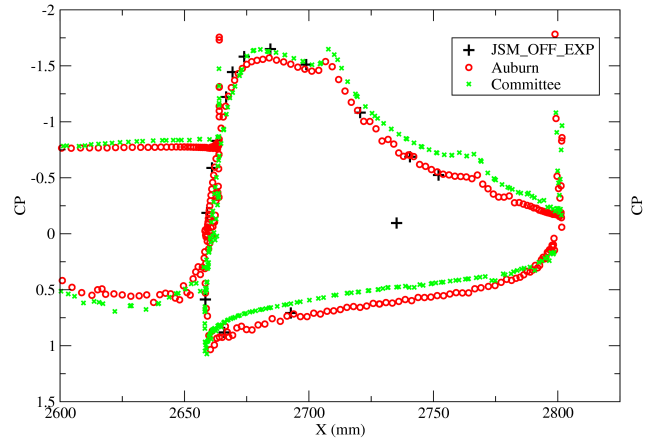

Flap B-B

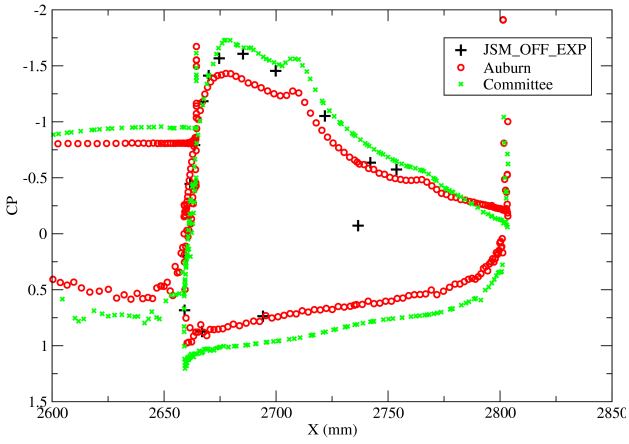

Slat D-D

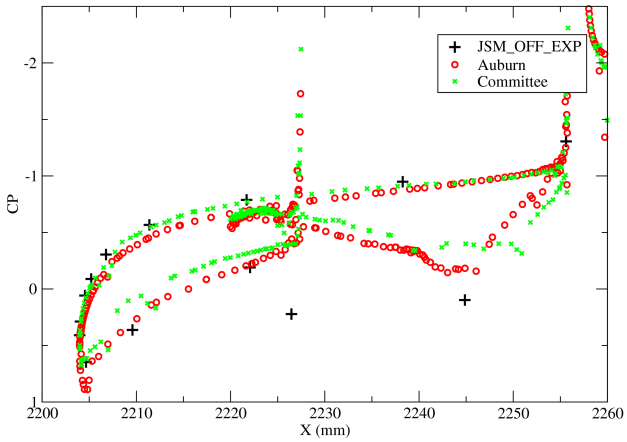

Wing C-C

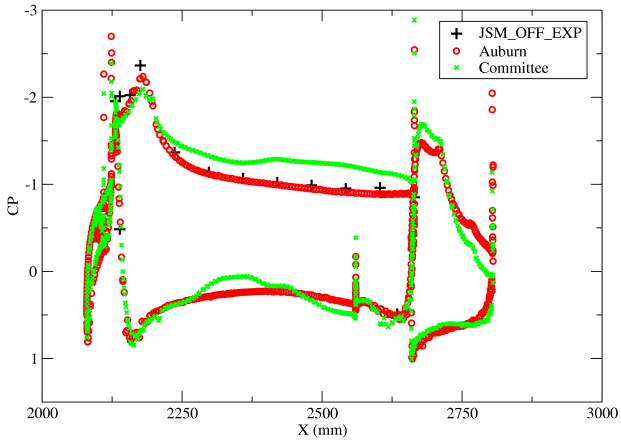

Wing D-D

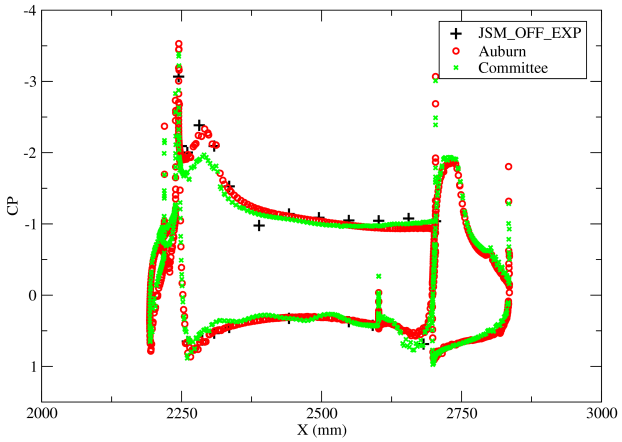

Flap C-C

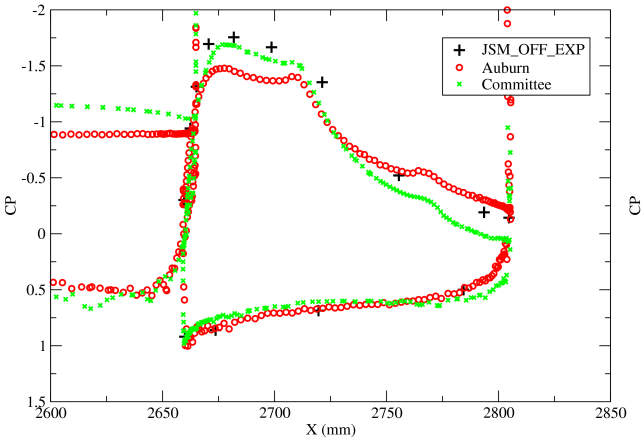

Flap D-D

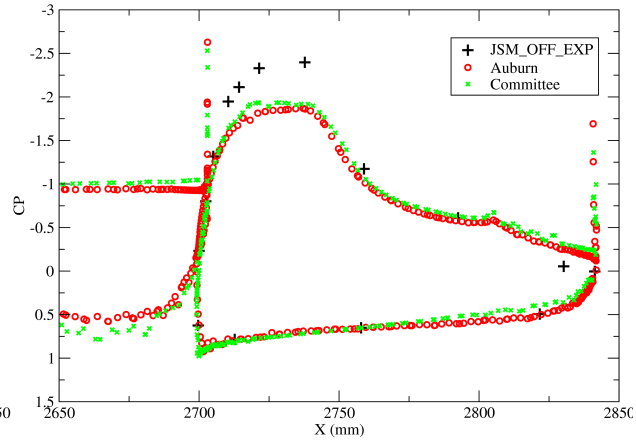

Slat E-E

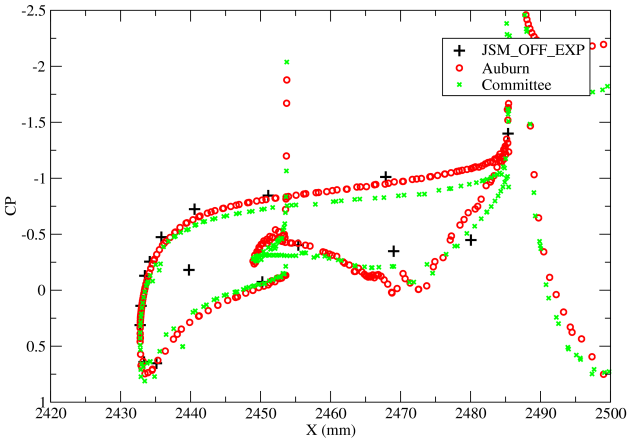

Slat G-G

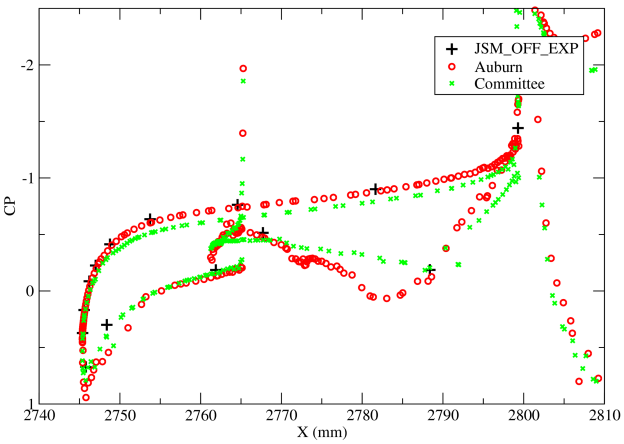

Wing E-E

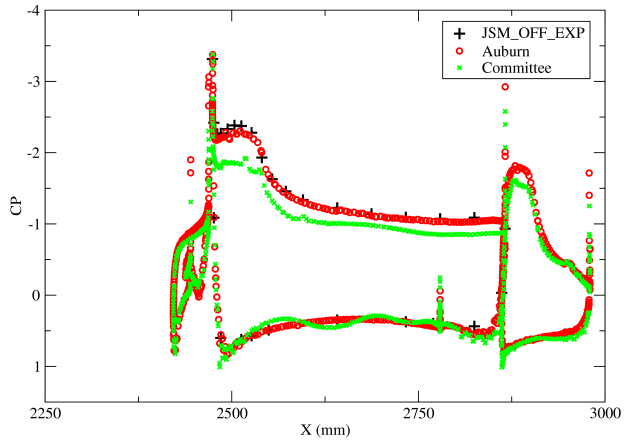

Wing G-G

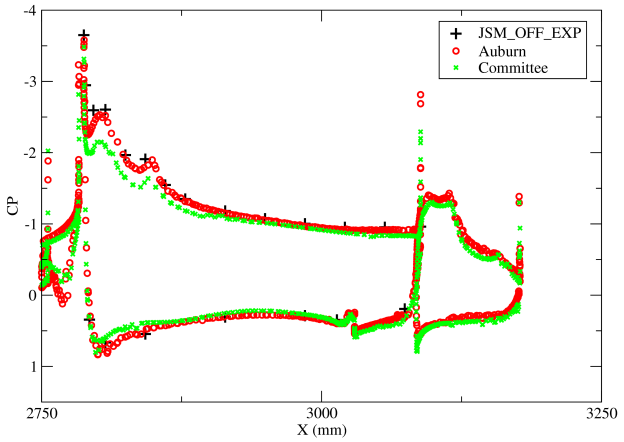

Flap E-E

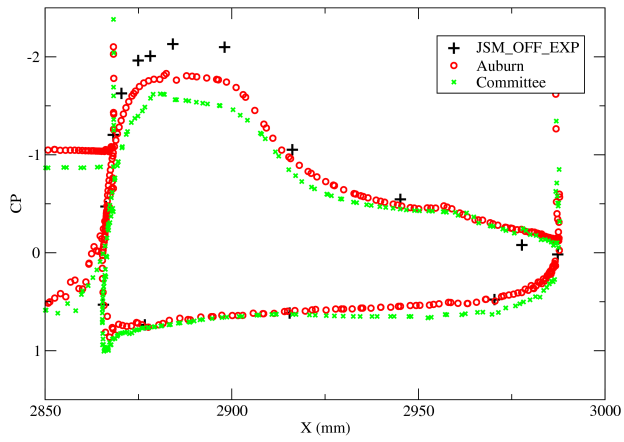

Flap G-G

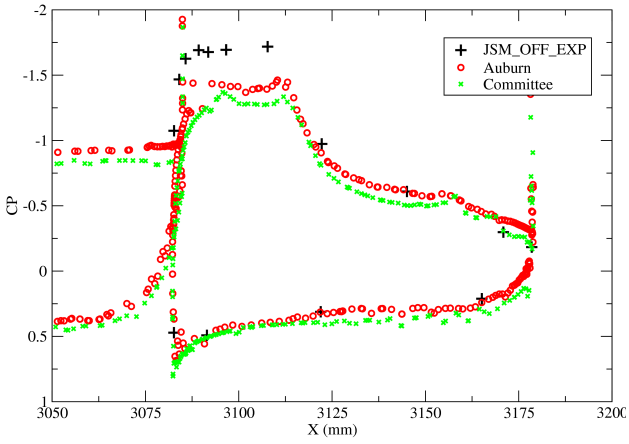

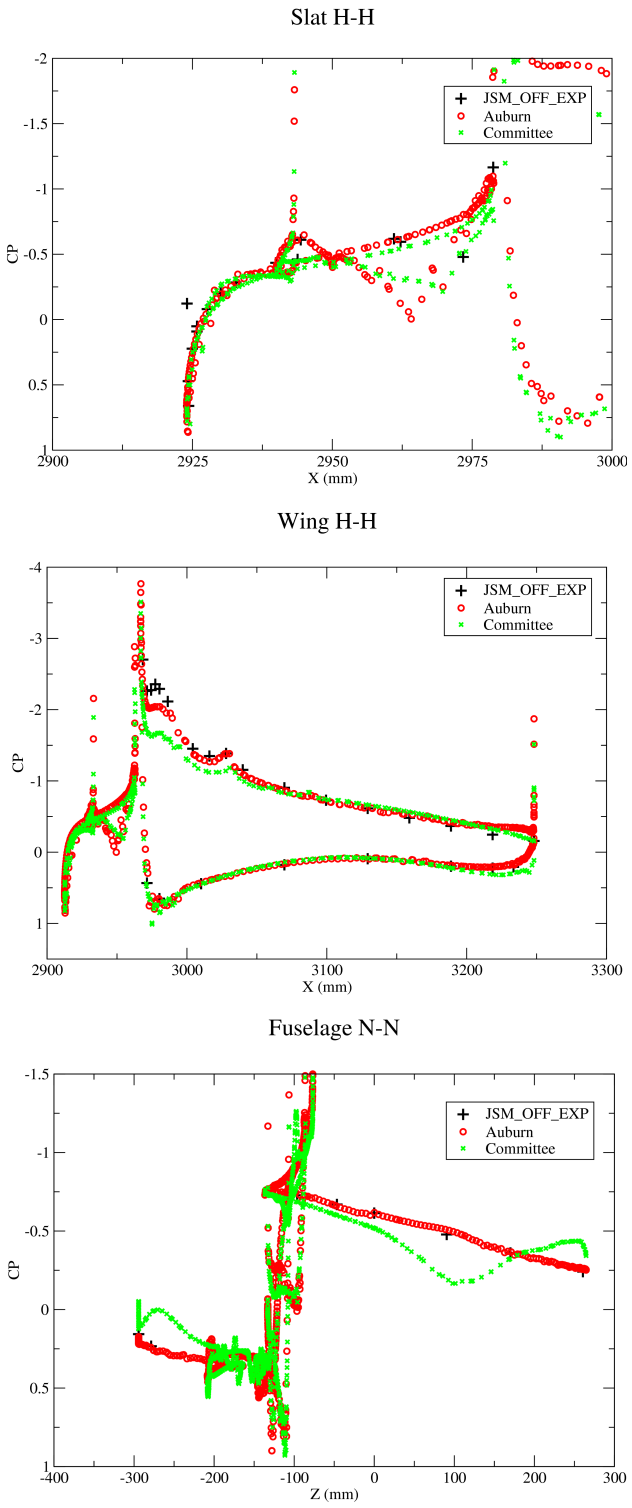

Figure 5.28: JSM: JSM Nacelle/Pylon OFF Configuration with Variable Mach Solver - C_P Comparison at AOA 4.36^0

Slat A-A

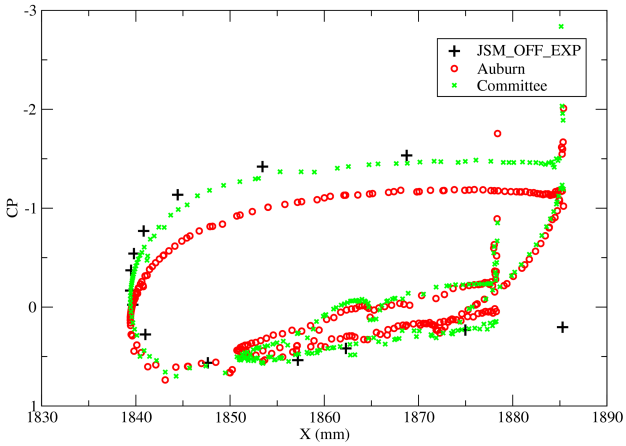

Slat B-B

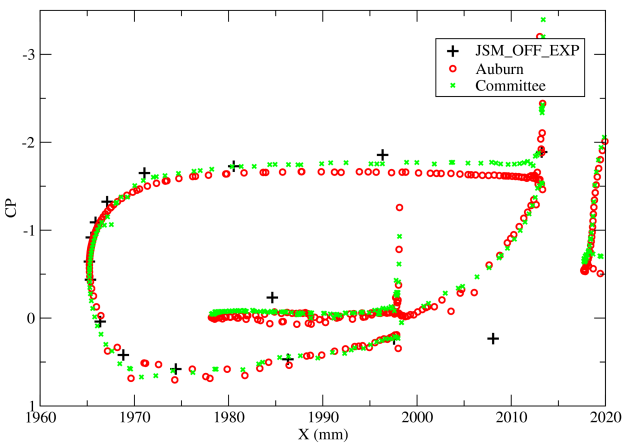

Wing A-A

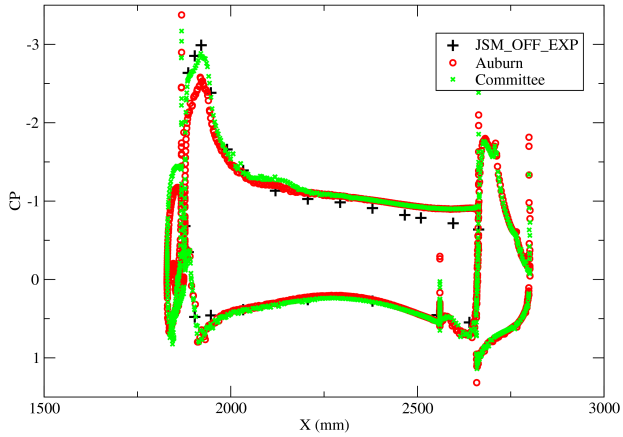

Wing B-B

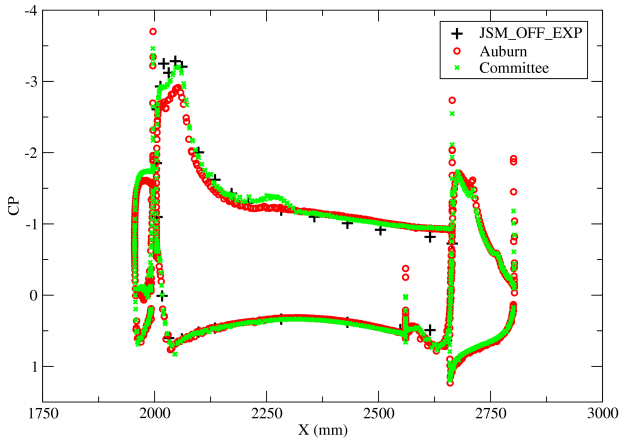

Flap A-A

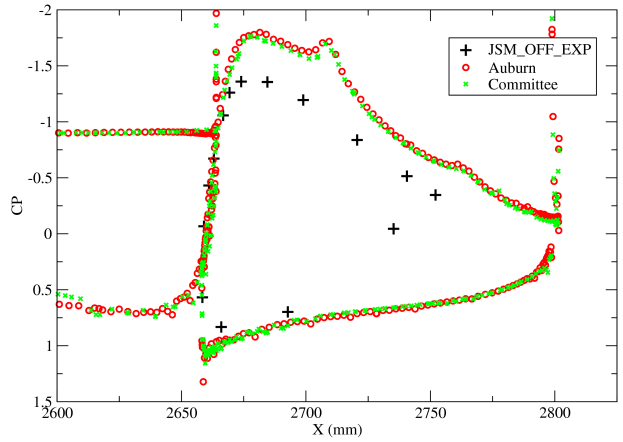

Flap B-B

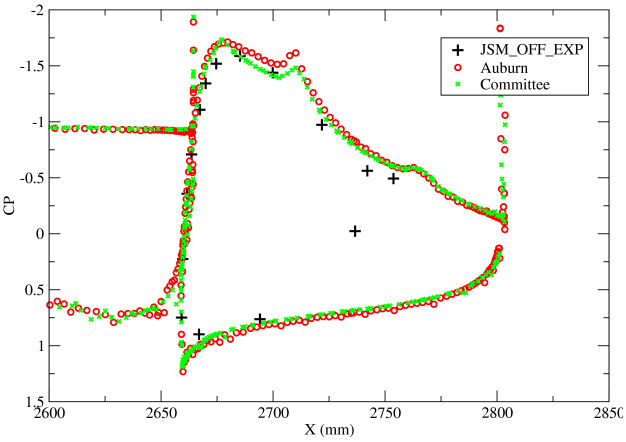

Slat D-D

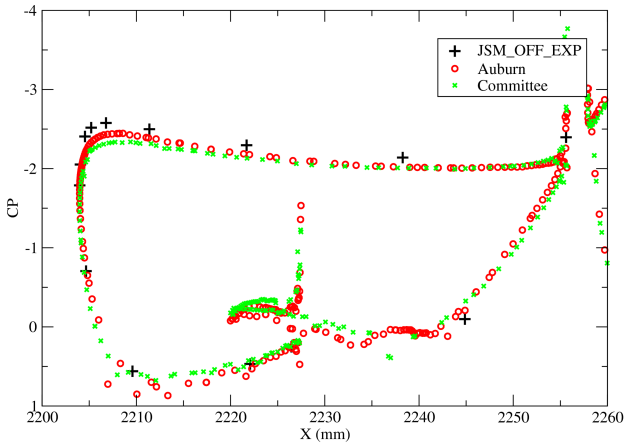

Wing C-C

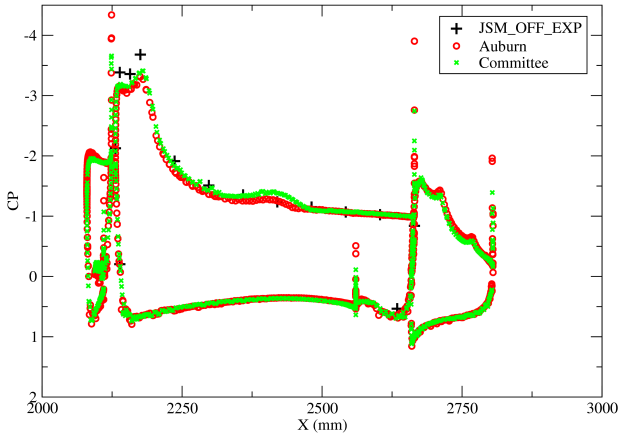

Wing D-D

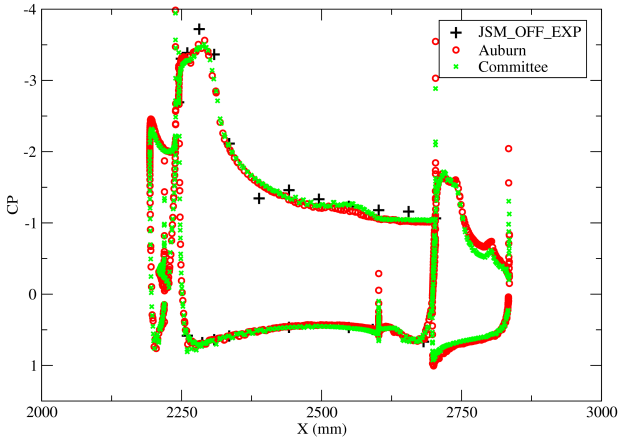

Flap C-C

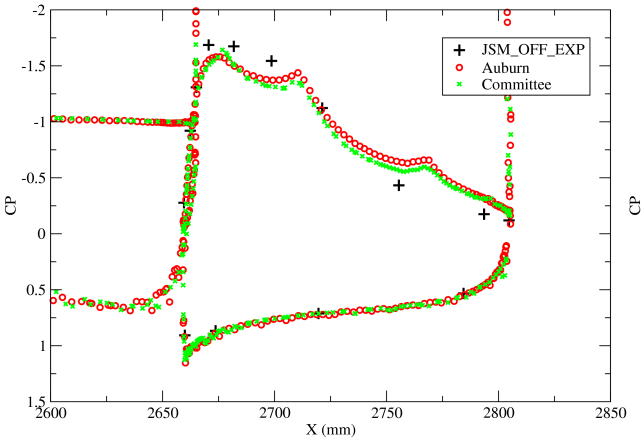

Flap D-D

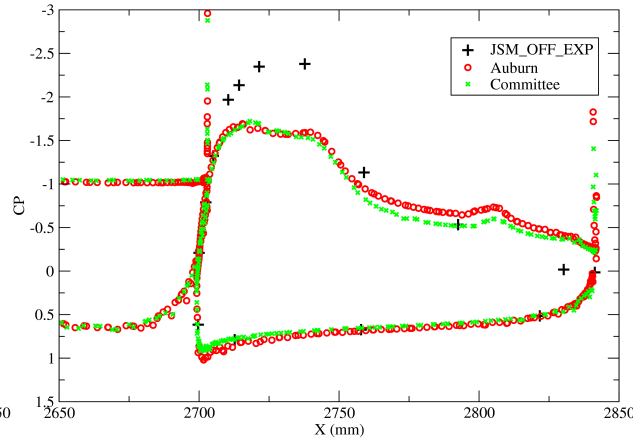

Slat E-E

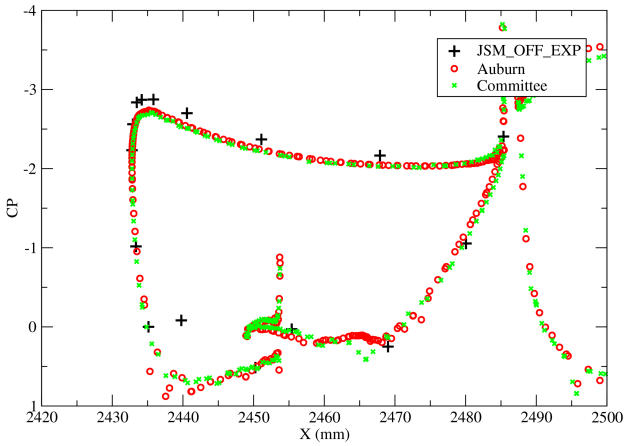

Slat G-G

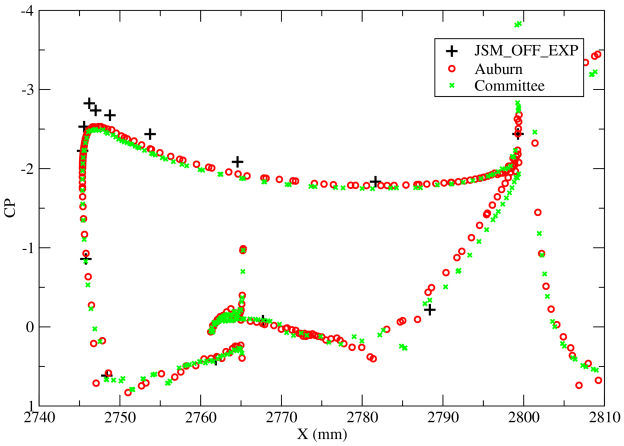

Wing E-E

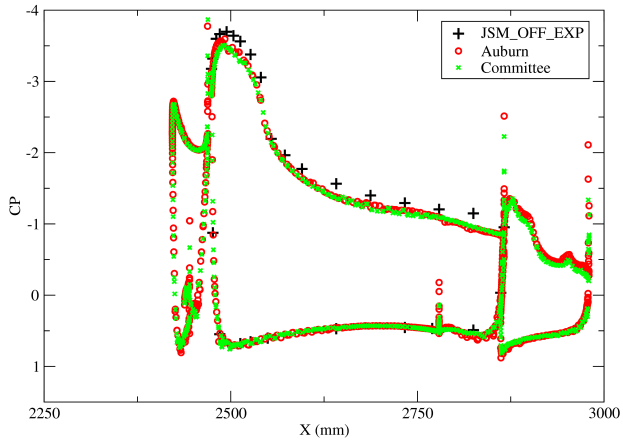

Wing G-G

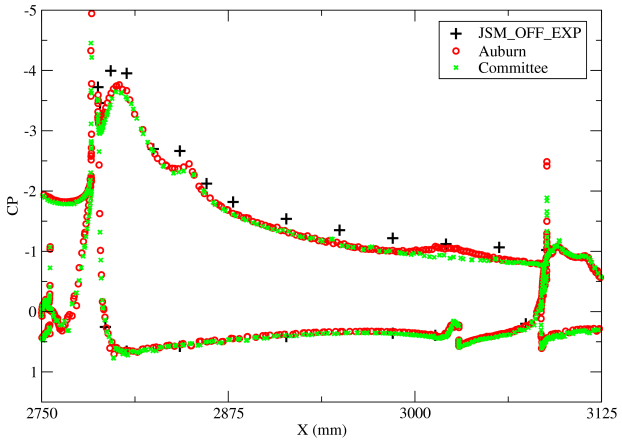

Flap E-E

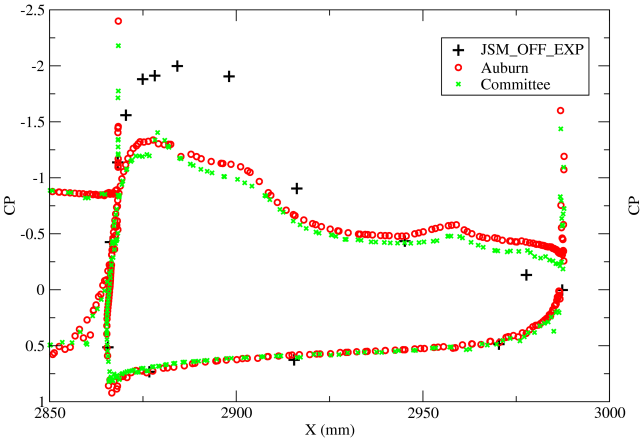

Flap G-G

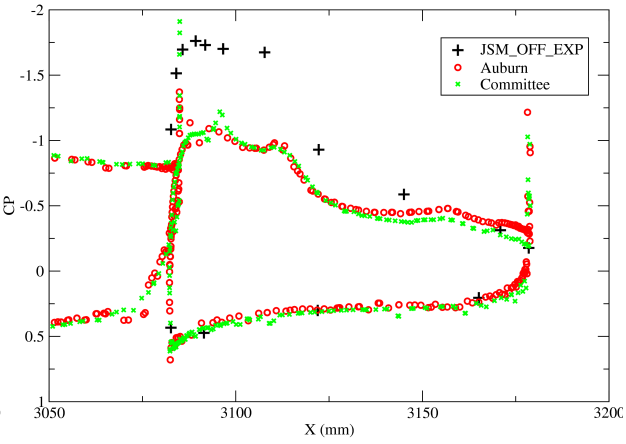

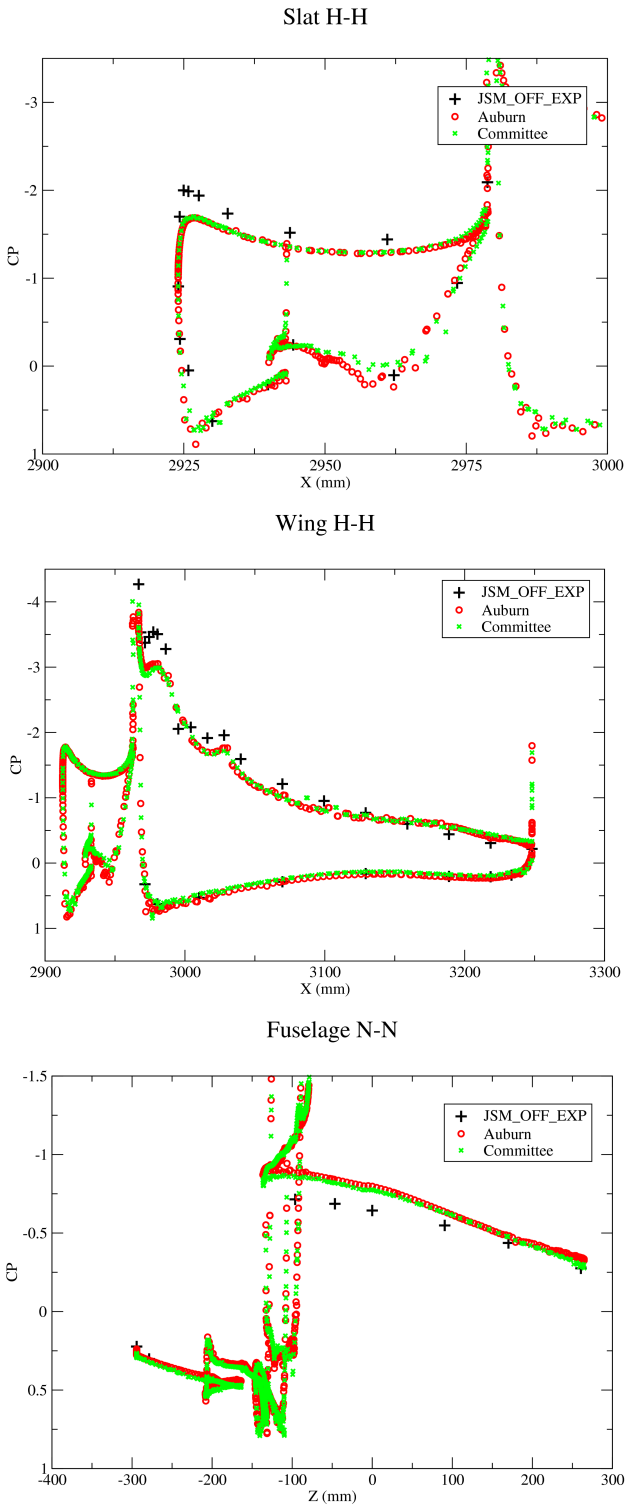

Figure 5.29: JSM: JSM Nacelle/Pylon OFF Configuration with Variable Mach Solver - C_P Comparison at AOA 10.47^0

Slat A-A

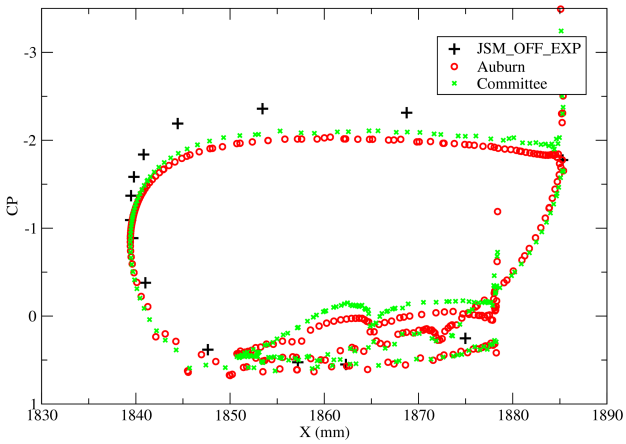

Slat B-B

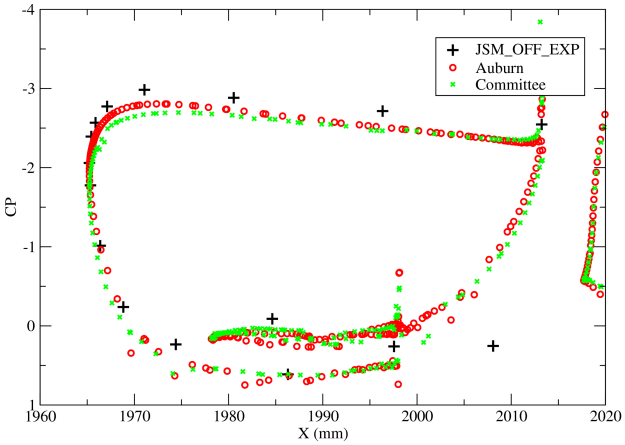

Wing A-A

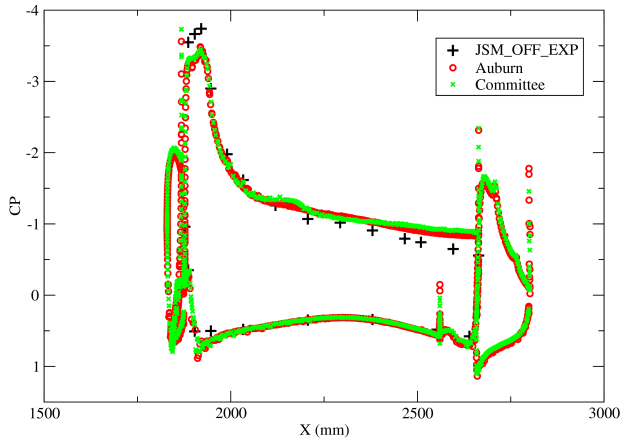

Wing B-B

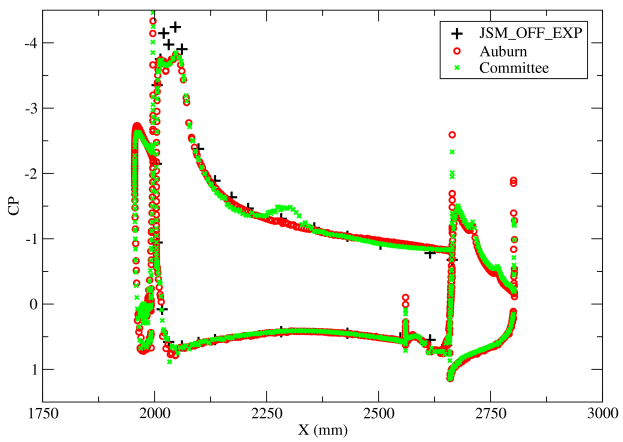

Flap A-A

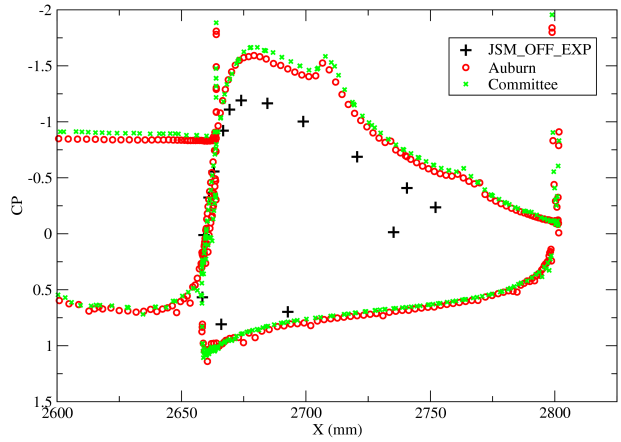

Flap B-B

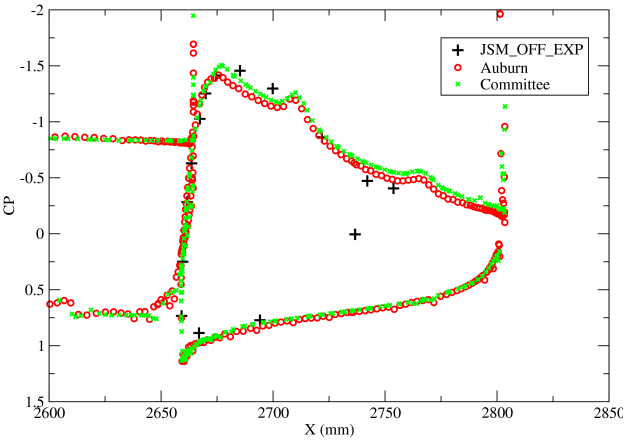

Slat D-D

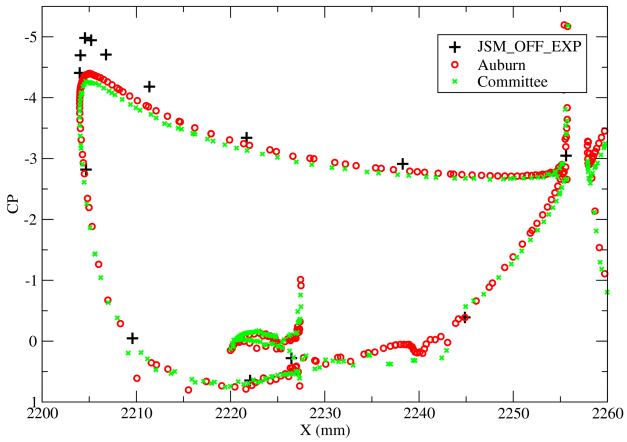

Wing C-C

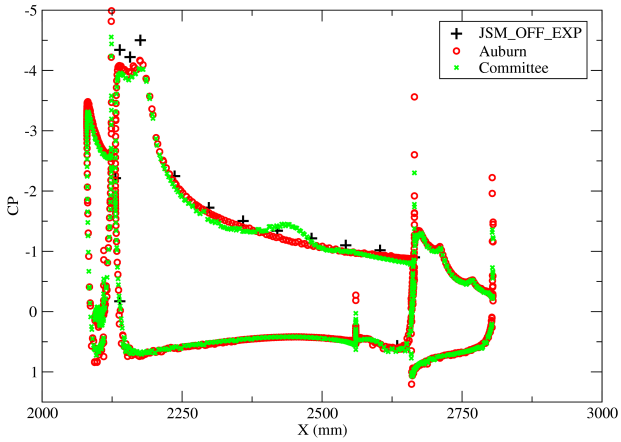

Wing D-D

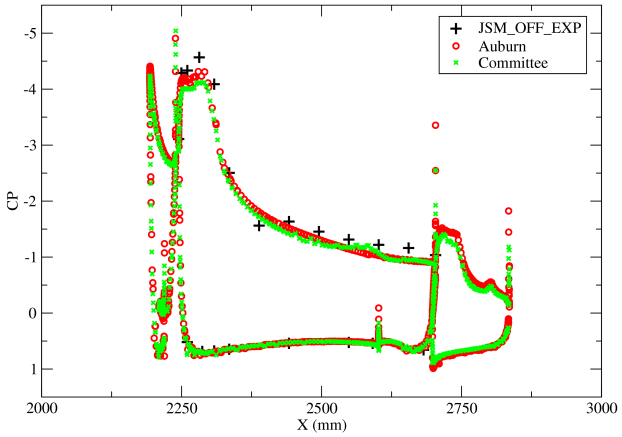

Flap C-C

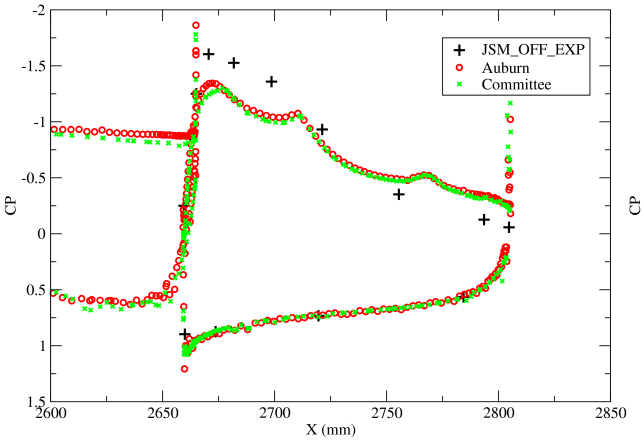

Flap D-D

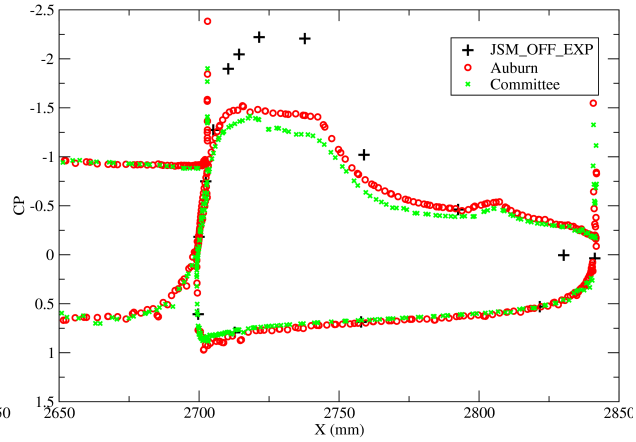

Slat E-E

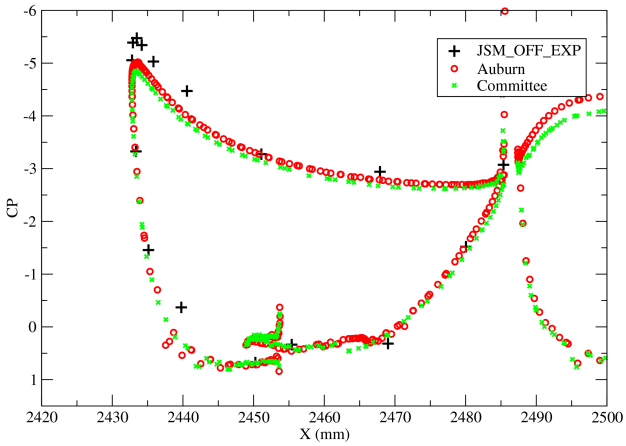

Slat G-G

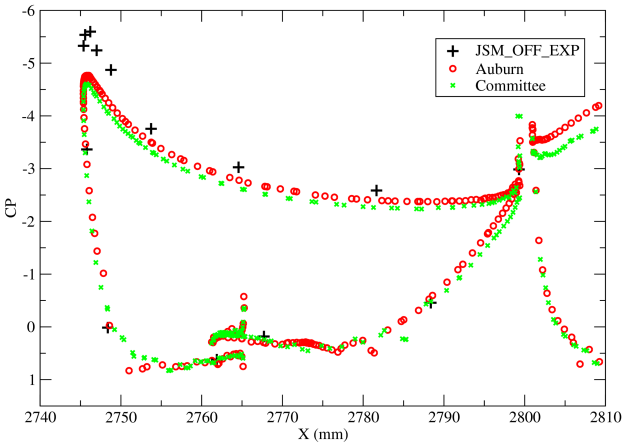

Wing E-E

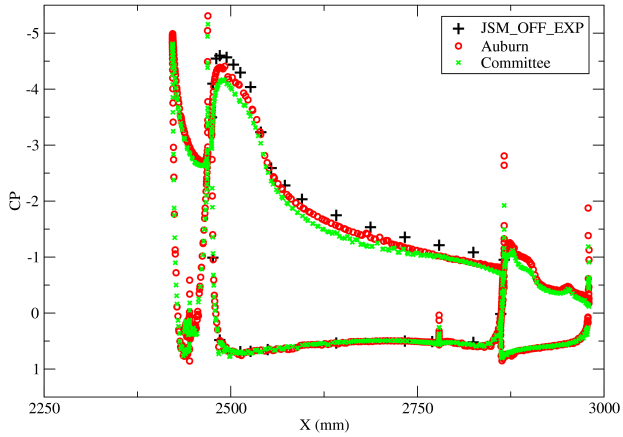

Wing G-G

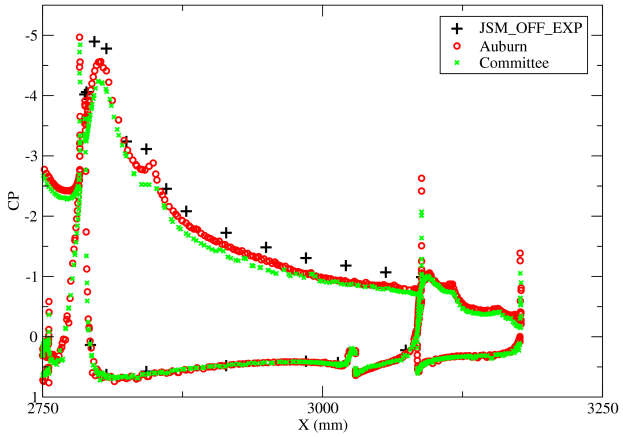

Flap E-E

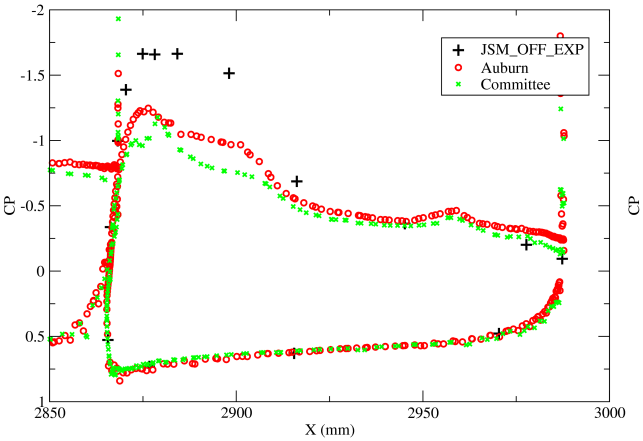

Flap G-G

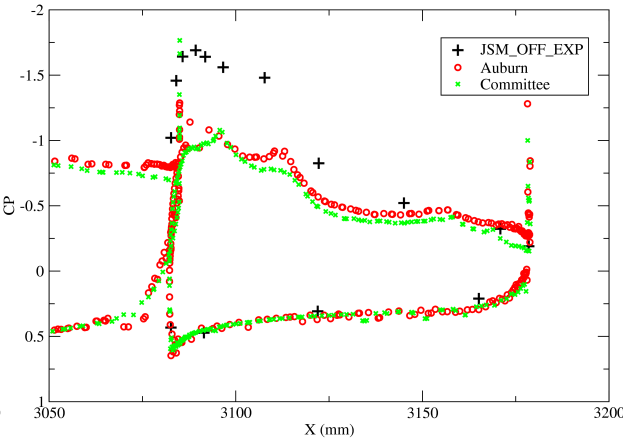

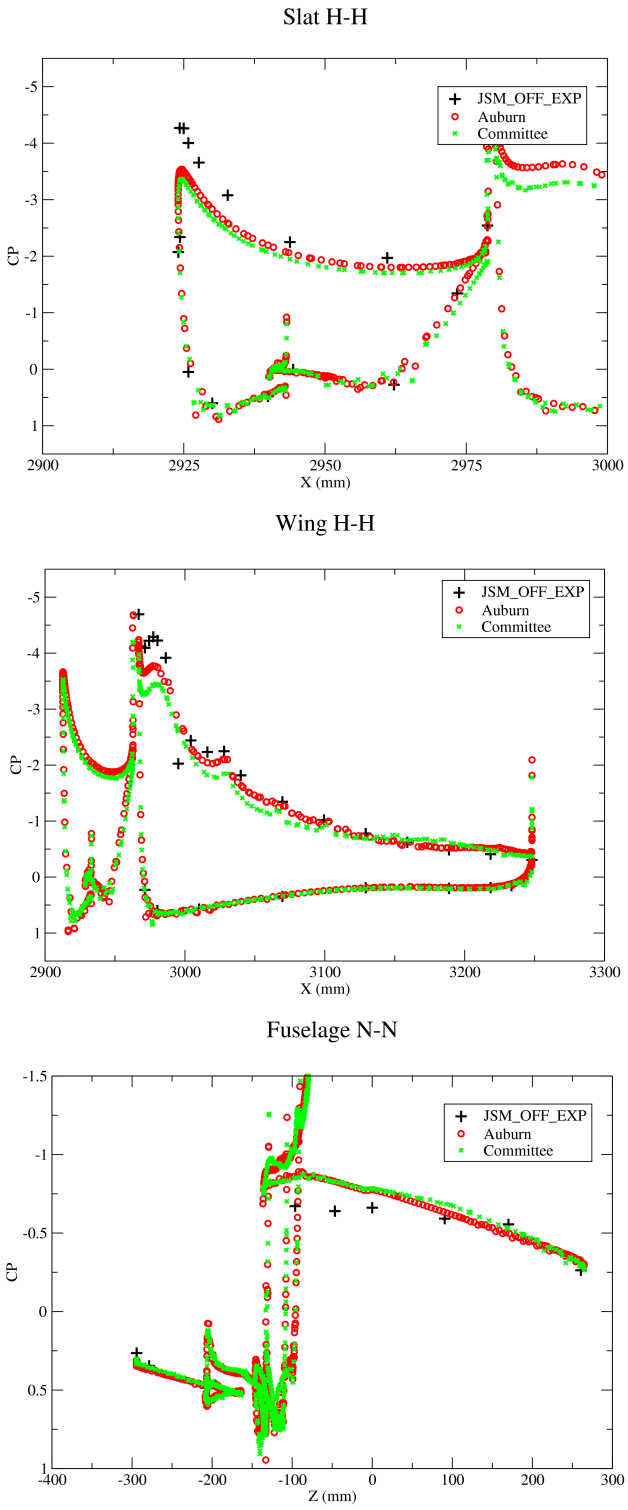

Figure 5.30: JSM: JSM Nacelle/Pylon OFF Configuration with Variable Mach Solver - C_P Comparison at AOA 14.54^0

Slat A-A

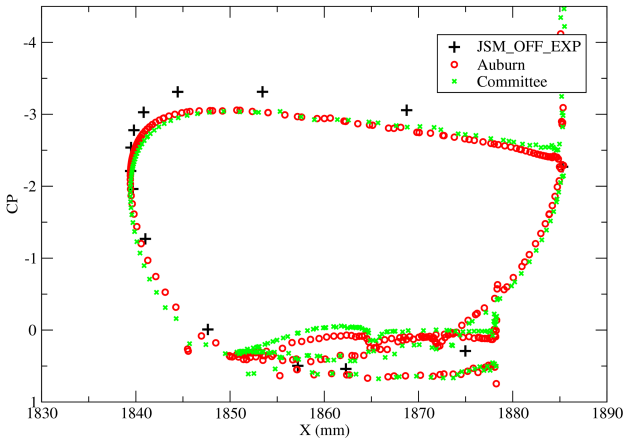

Slat B-B

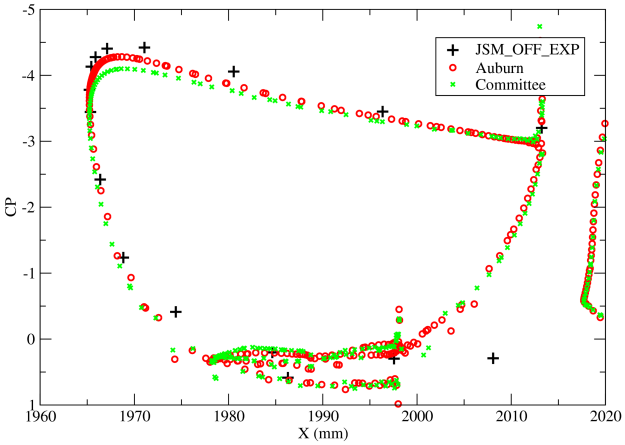

Wing A-A

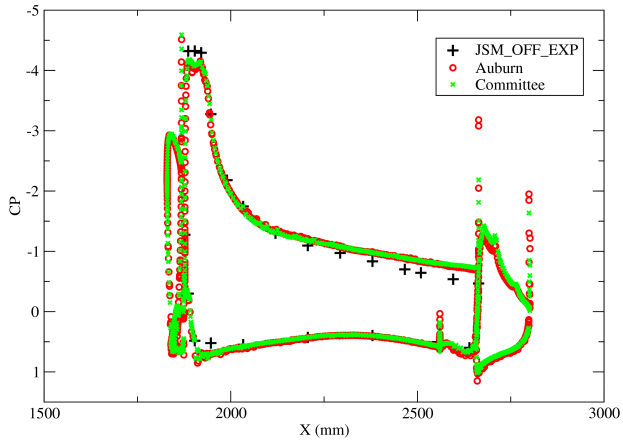

Wing B-B

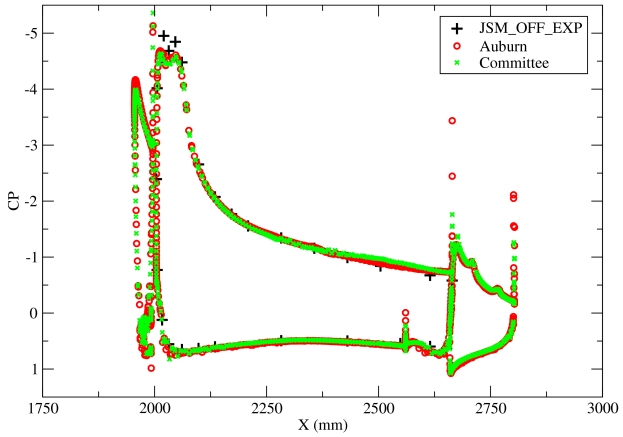

Flap A-A

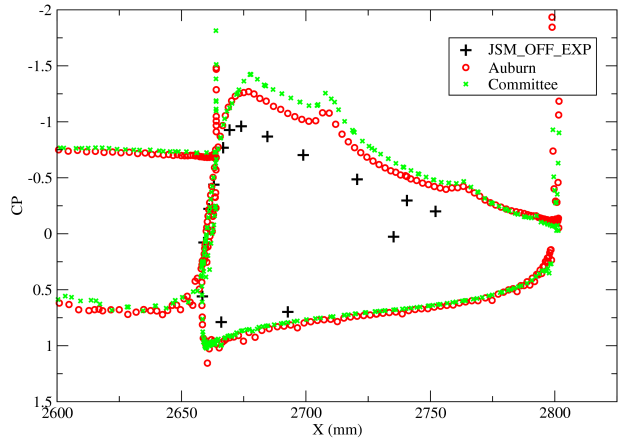

Flap B-B

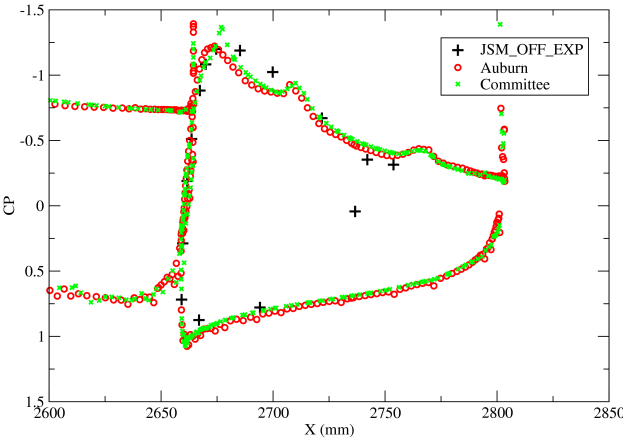

Slat D-D

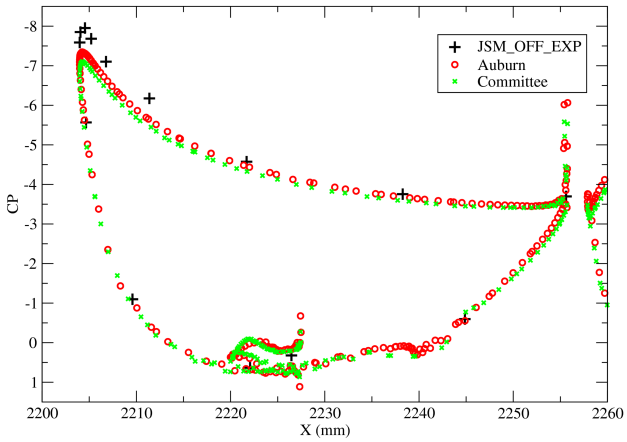

Wing C-C

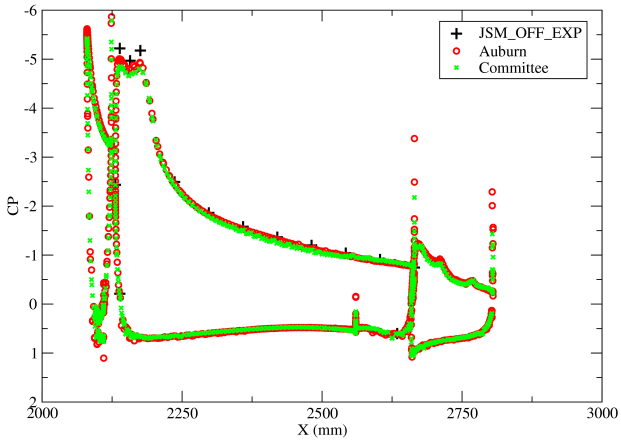

Wing D-D

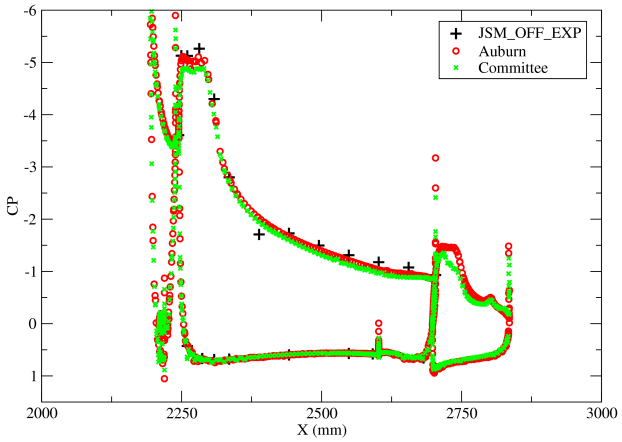

Flap C-C

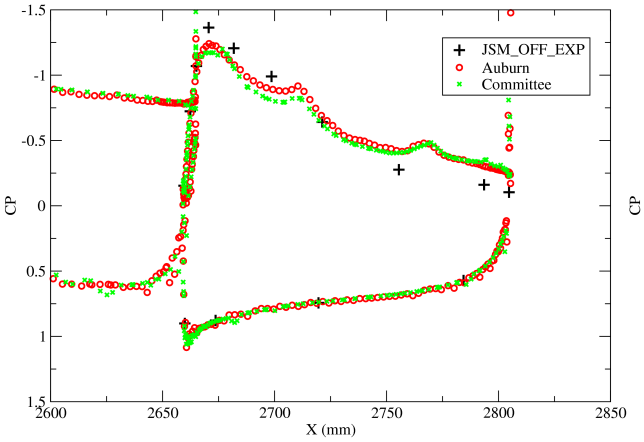

Flap D-D

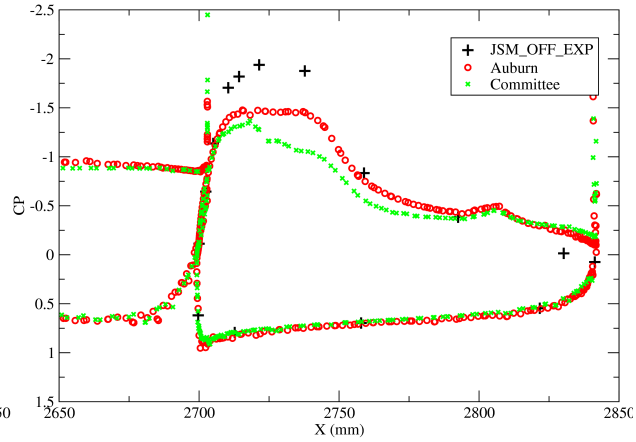

Slat E-E

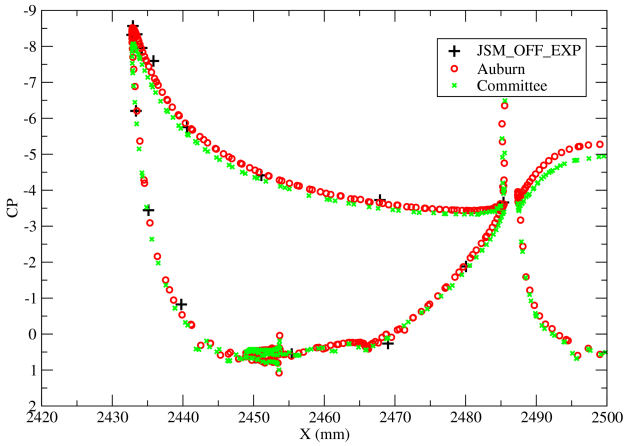

Slat G-G

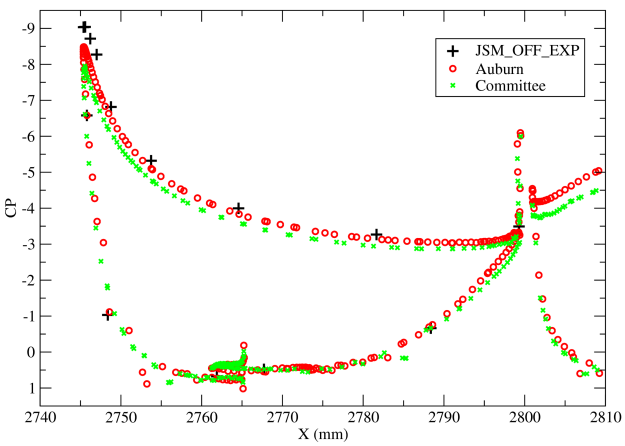

Wing E-E

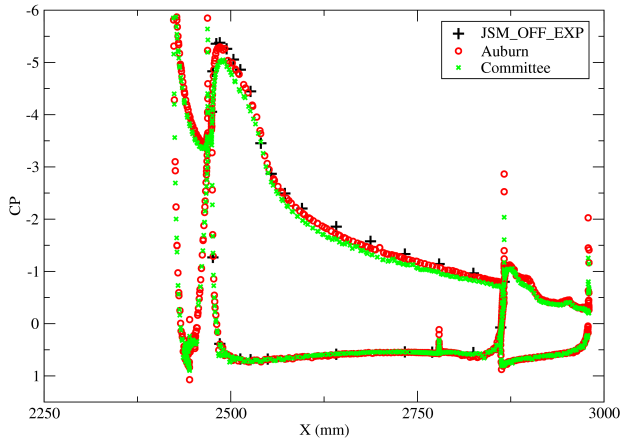

Wing G-G

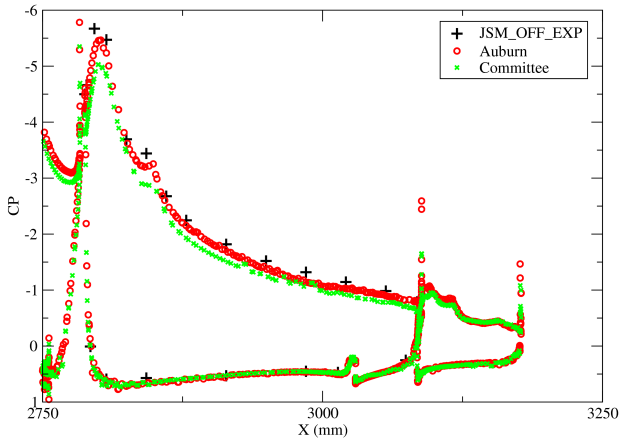

Flap E-E

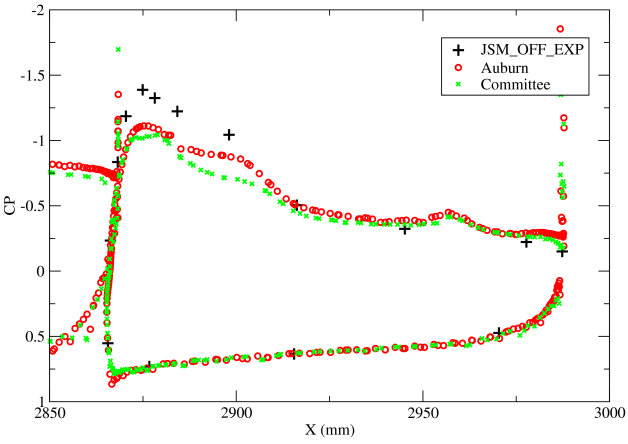

Flap G-G

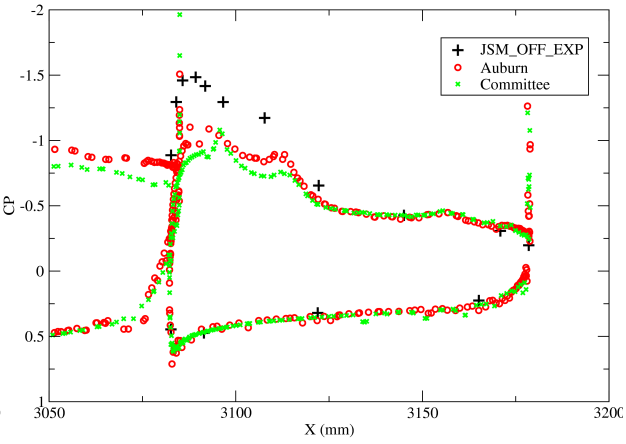

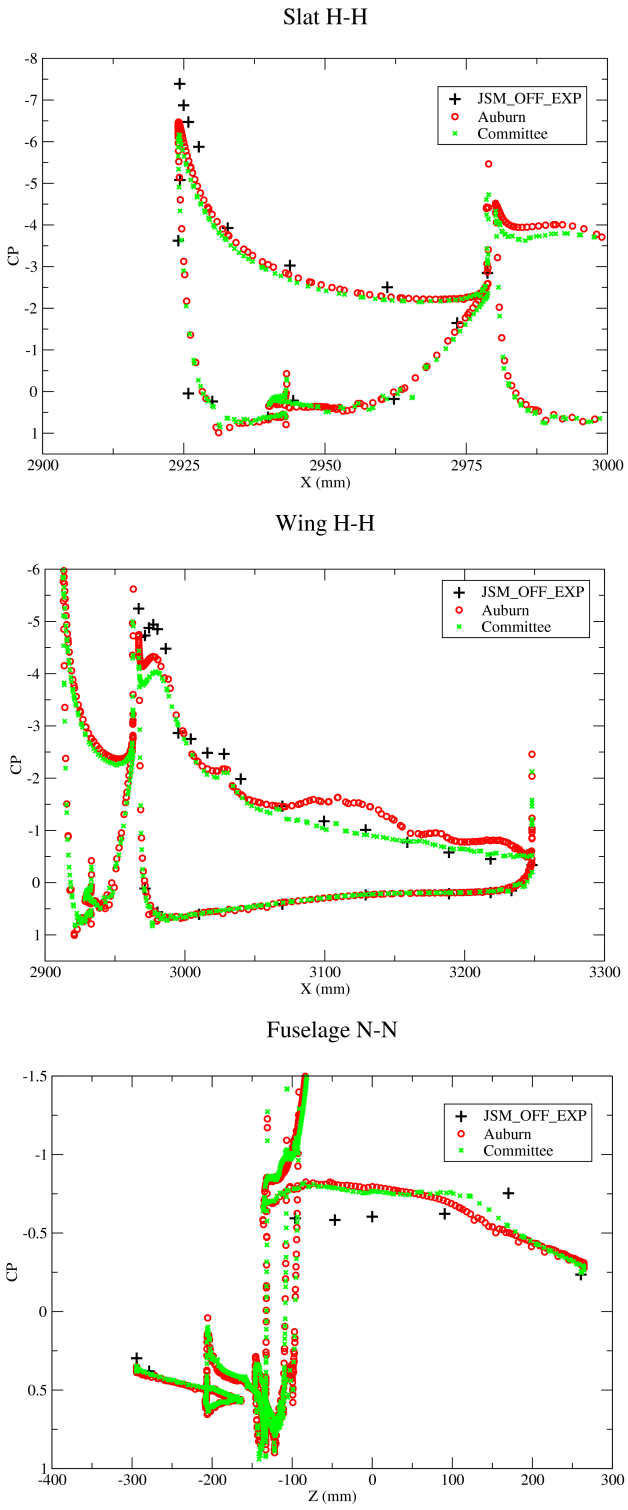

Figure 5.31: JSM: JSM Nacelle/Pylon OFF Configuration with Variable Mach Solver - C_P Comparison at AOA 18.58^0

Slat A-A

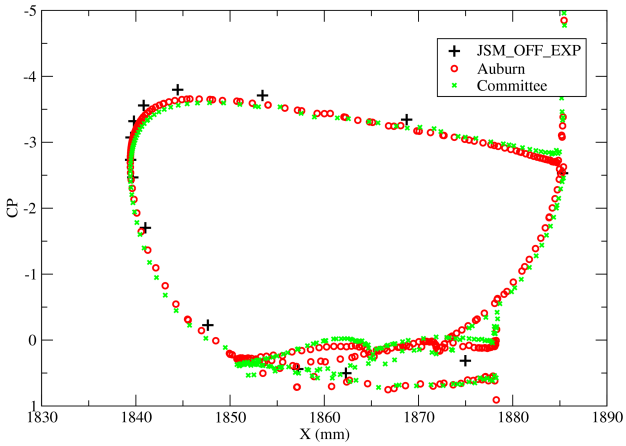

Slat B-B

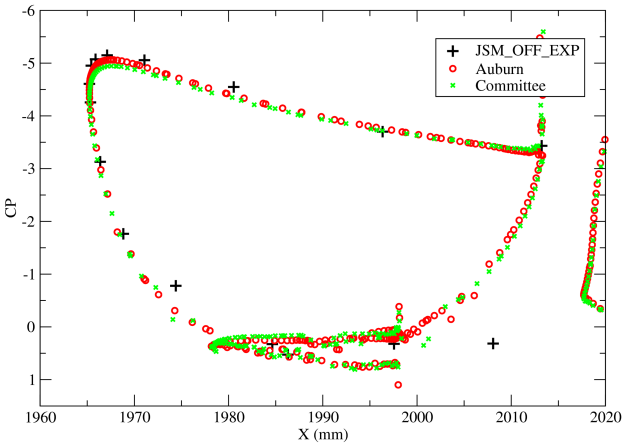

Wing A-A

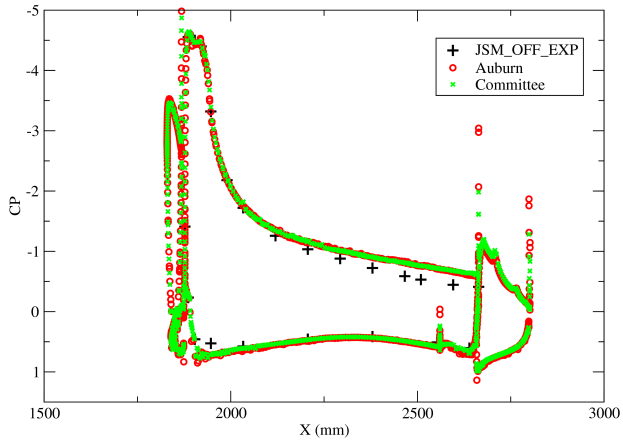

Wing B-B

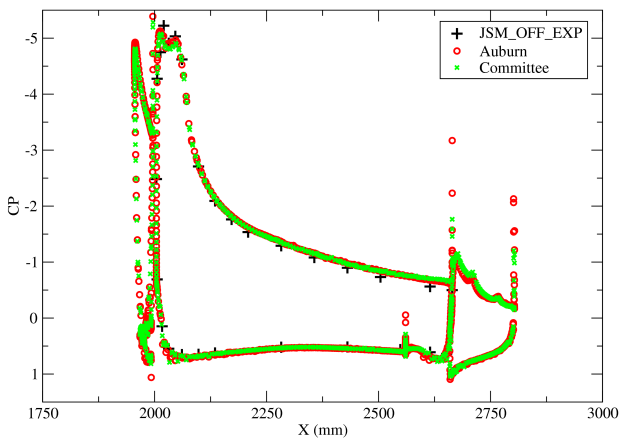

Flap A-A

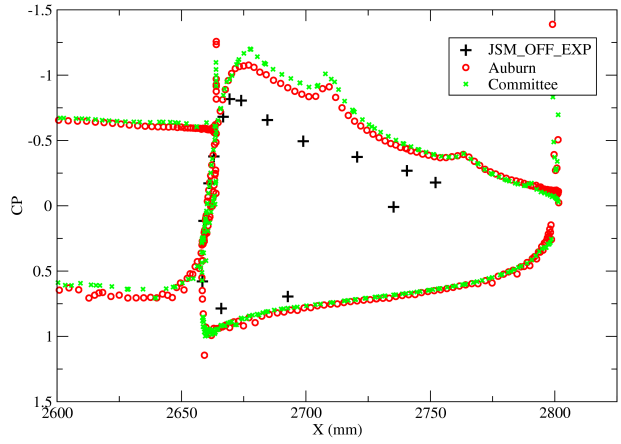

Flap B-B

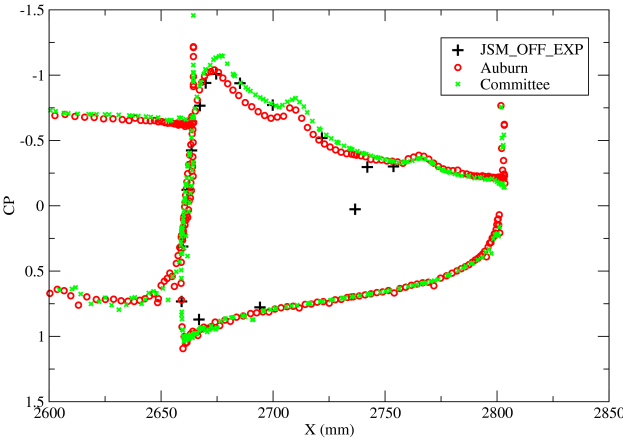

Slat D-D

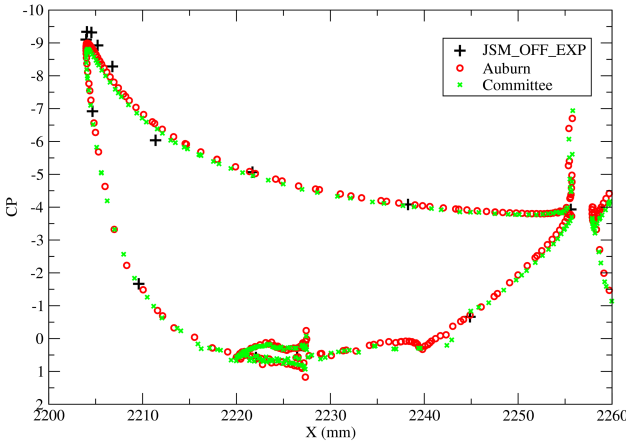

Wing C-C

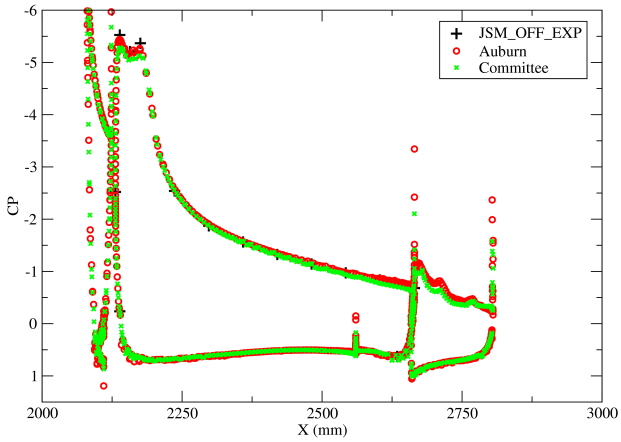

Wing D-D

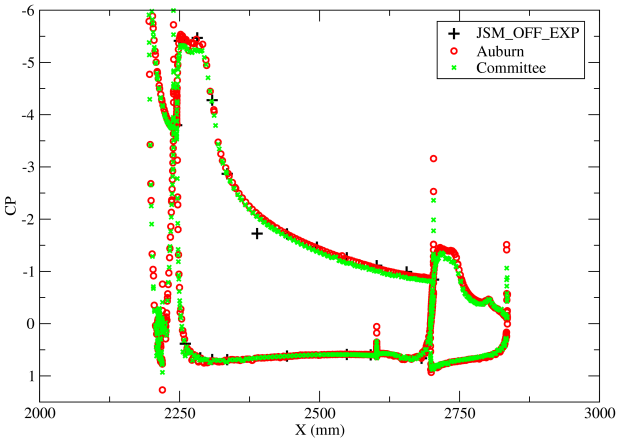

Flap C-C

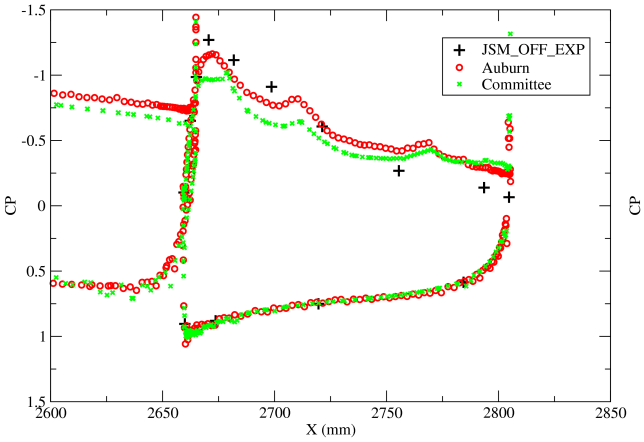

Flap D-D

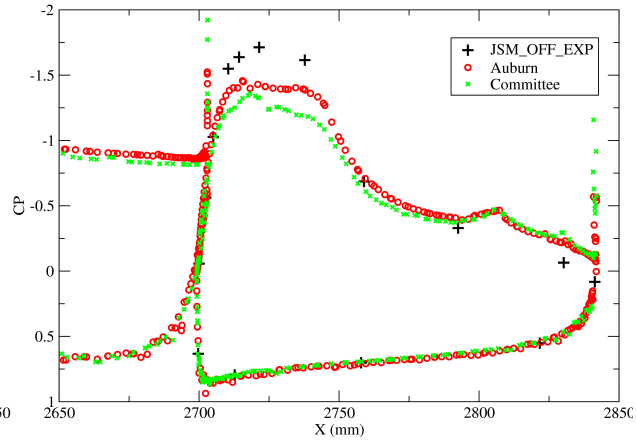

Slat E-E

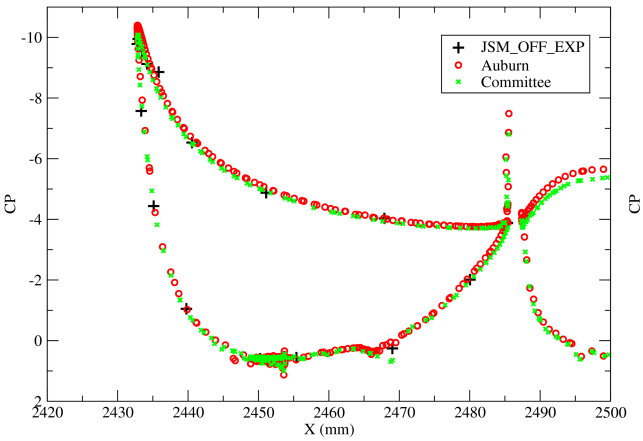

Slat G-G

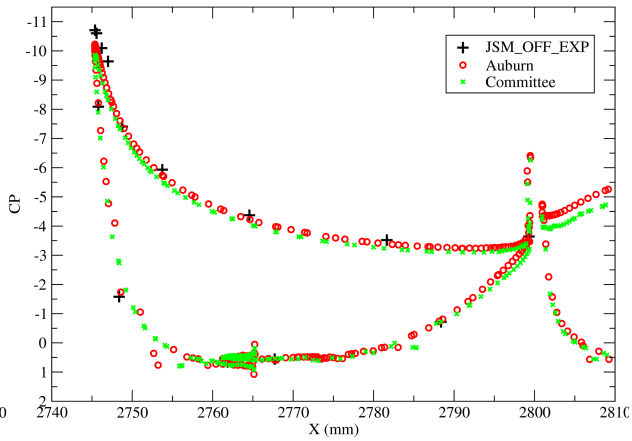

Wing E-E

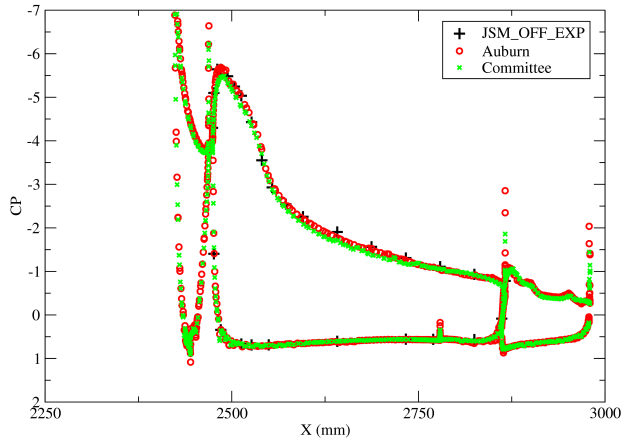

Wing G-G

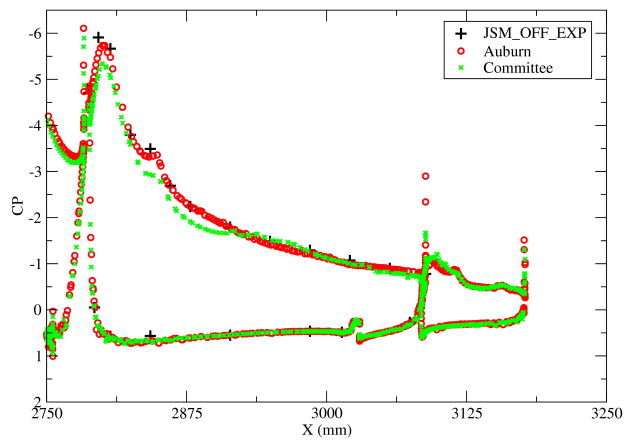

Flap E-E

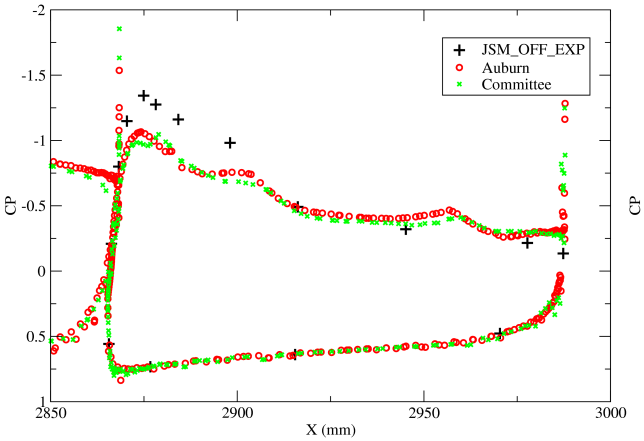

Flap G-G

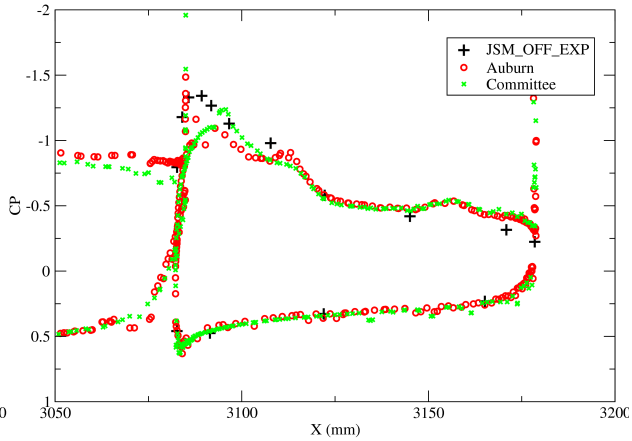

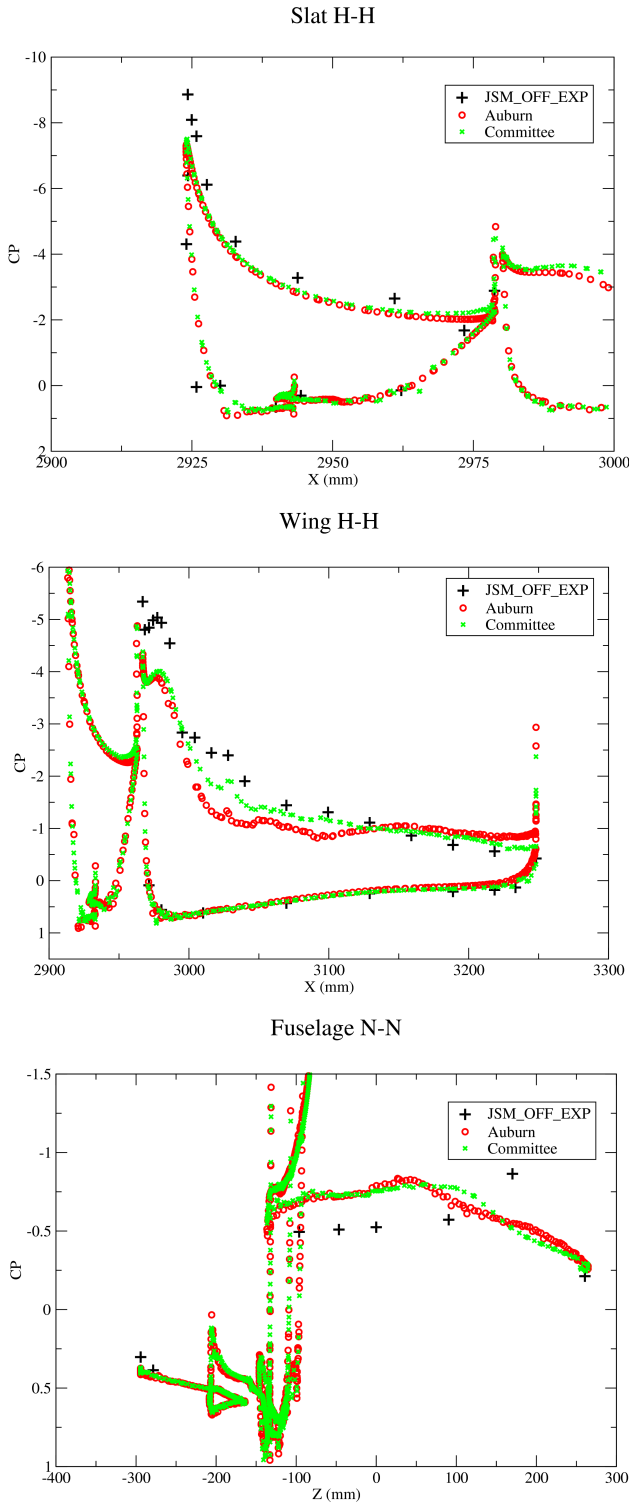

Figure 5.32: JSM: JSM Nacelle/Pylon OFF Configuration with Variable Mach Solver - C_P Comparison at AOA 20.59^0

Slat A-A

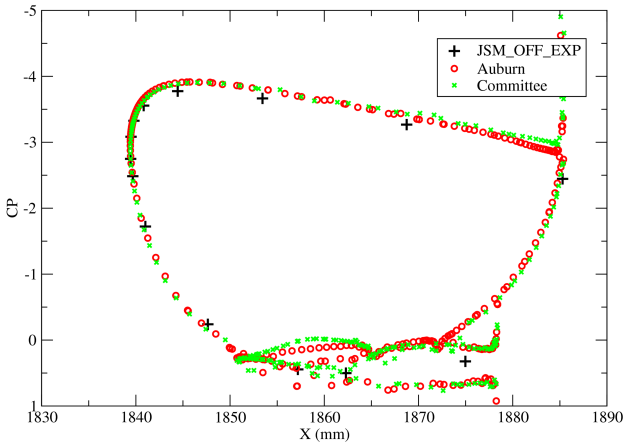

Slat B-B

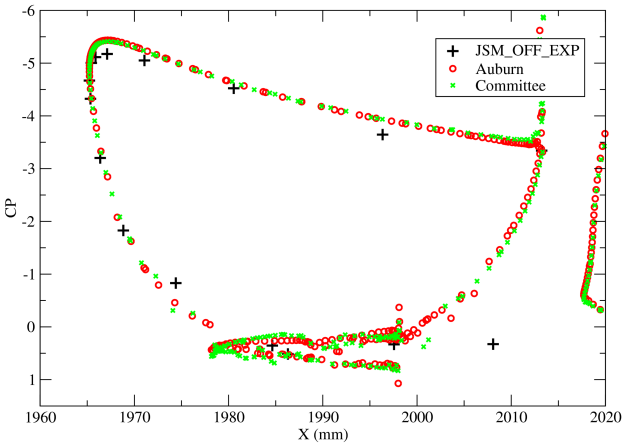

Wing A-A

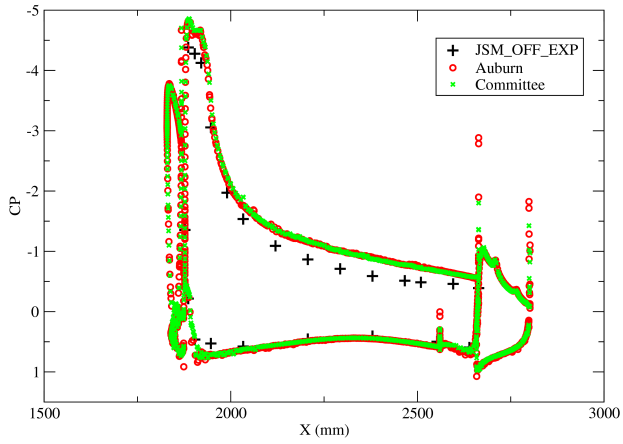

Wing B-B

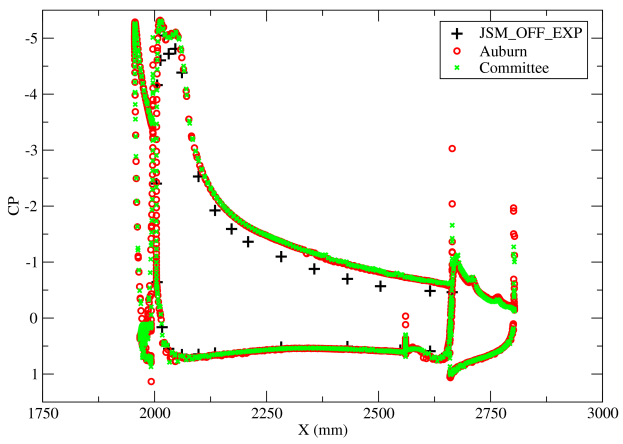

Flap A-A

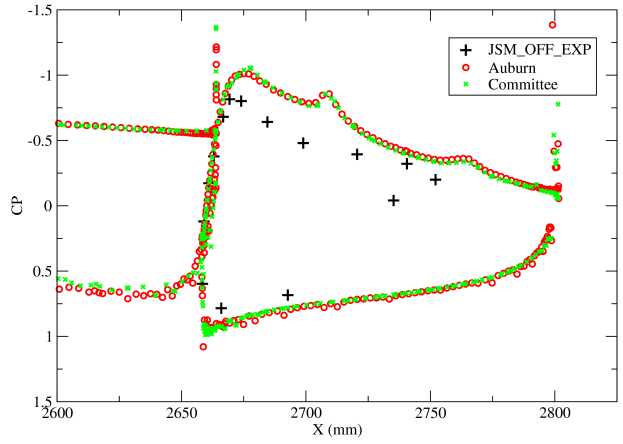

Flap B-B

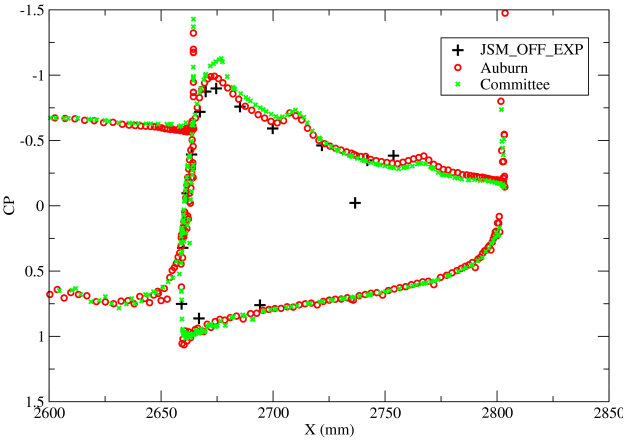

Slat D-D

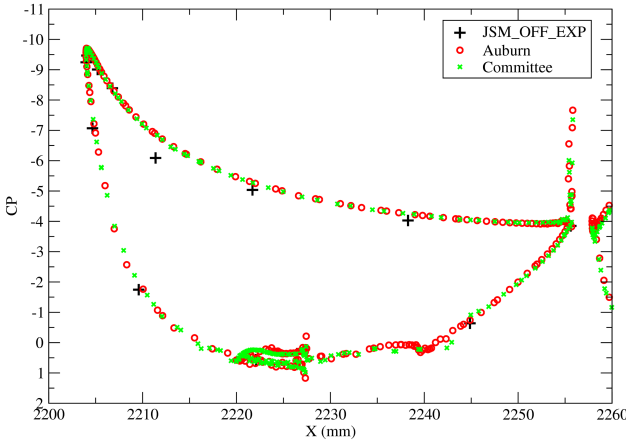

Wing C-C

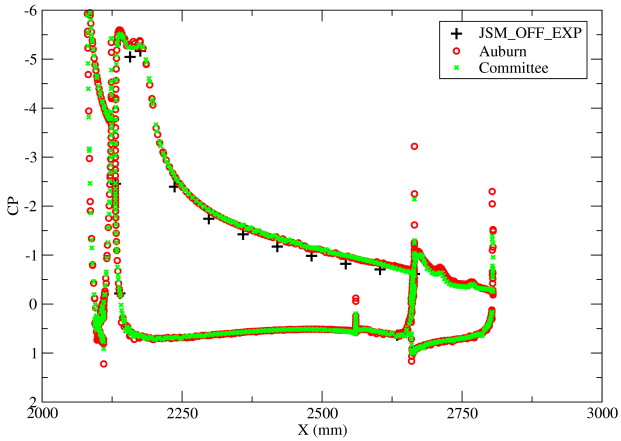

Wing D-D

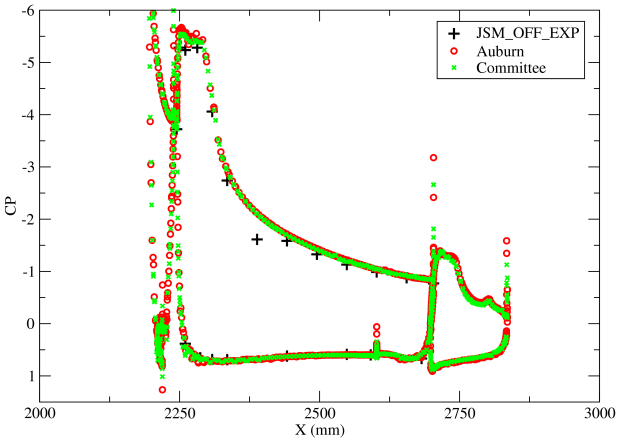

Flap C-C

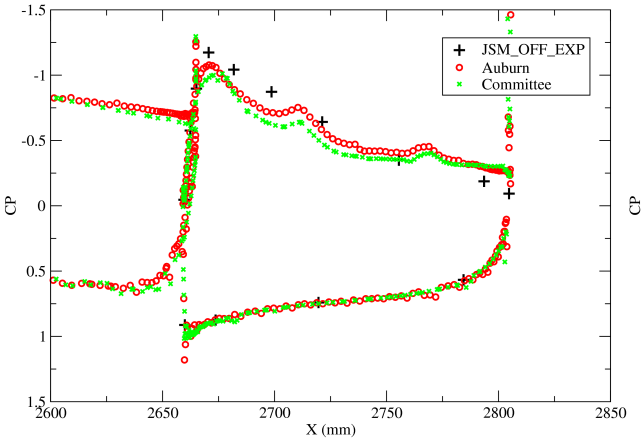

Flap D-D

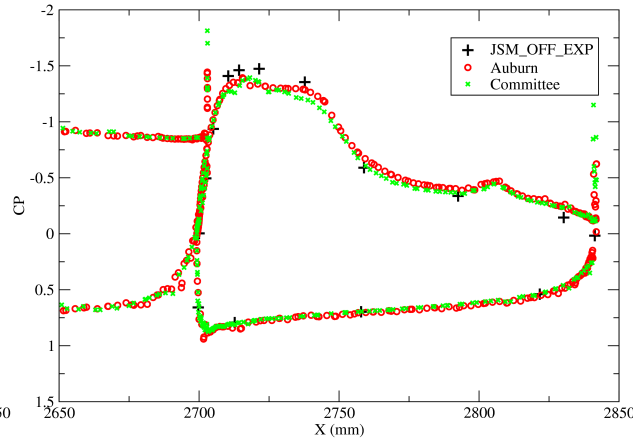

Slat E-E

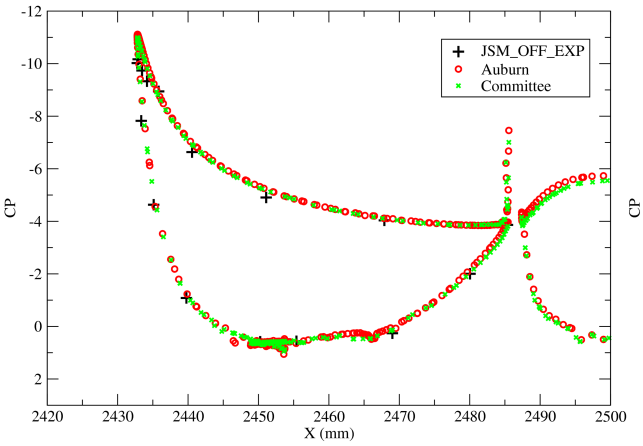

Slat G-G

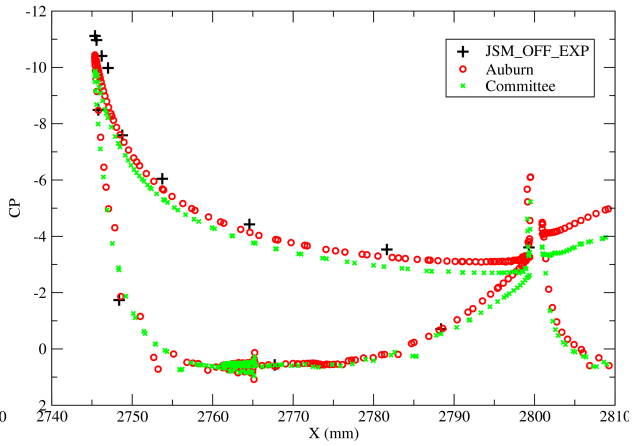

Wing E-E

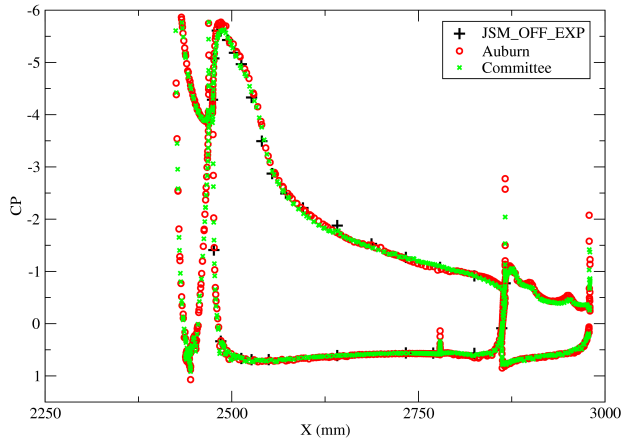

Wing G-G

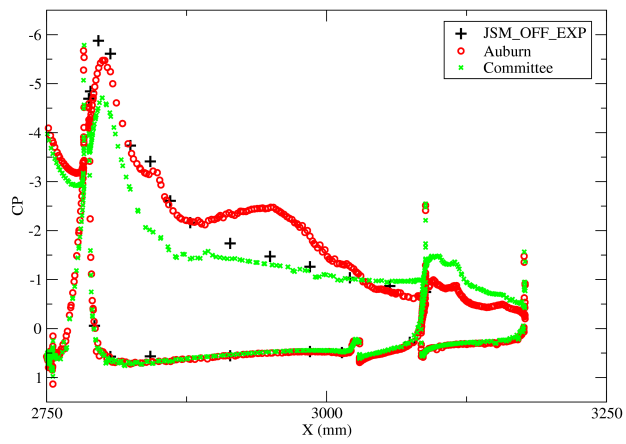

Flap E-E

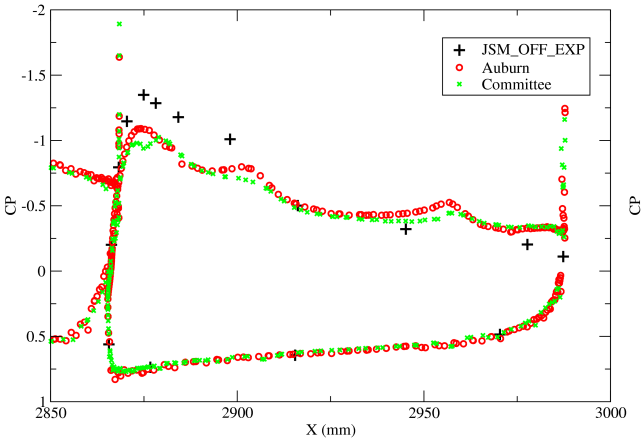

Flap G-G

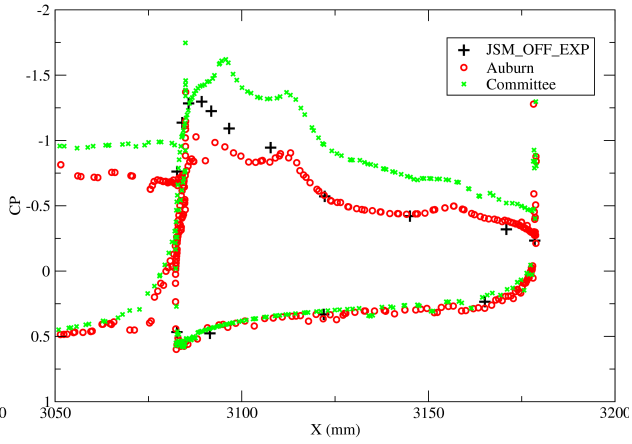

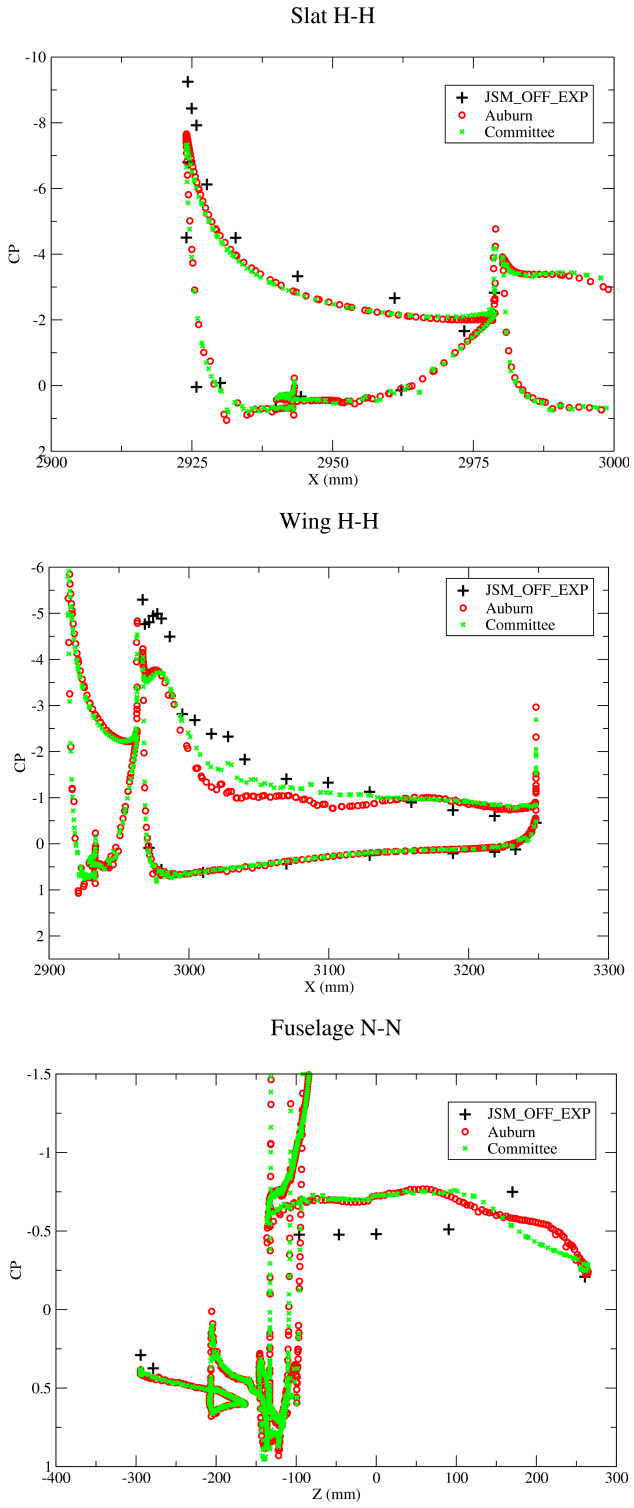

Figure 5.33: JSM: JSM Nacelle/Pylon OFF Configuration with Variable Mach Solver - C_P Comparison at AOA 21.57^0

The C_P calculated by CFD in this study using the variable Mach solver is closer to the experiments for most part of the wing. The results indicate that towards the root of the wing (section A-A and B-B), it takes longer distance for pressure recovery in CFD than in experiments. However, the pressure recovery distance in CFD matches with the experiments for other locations on the wing. The CFD accurately predicted the maximum C_P on the lower surface of the wing elements (high pressure side) with considerable accuracy. On the other hand, the C_P resolution on the low pressure side of the wing elements (upper surface) lacks the same amount of accuracy. The CFD seems to resolve the high pressure region more accurately than the low pressure region of the flow field. At a high angle of attack, CFD overpredicts the suction peaks towards the root of the wing and this could be a reason in CFD for not producing the stall characteristics, evident in Fig. 5.32 and 5.33 for section A-A and B-B in wing and slat locations.

Earlier workshops concluded the wingtip to be a difficult location for CFD to accurately predict the flow field and match the experiments. However in this study, the C_P towards the tip of the wing (section H-H) matches impressively with the experiments.

Incompressible Solution

Figure 5.34 - 5.39 show the comparison of C_P with experiments at different locations on the aircraft at an angle of attack of 4.36^0 to 21.57^0 for the JSM Nacelle/Pylon OFF configuration and Fig. 5.40 - 5.45 for JSM Nacelle/Pylon ON configuration with incompressible solver using the SAS turbulence model.

Slat A-A

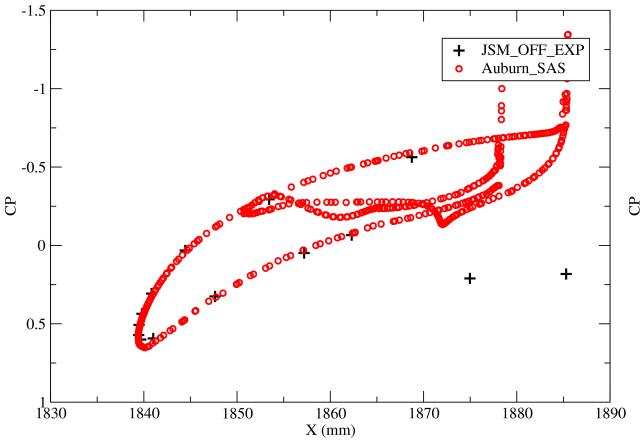

Slat B-B

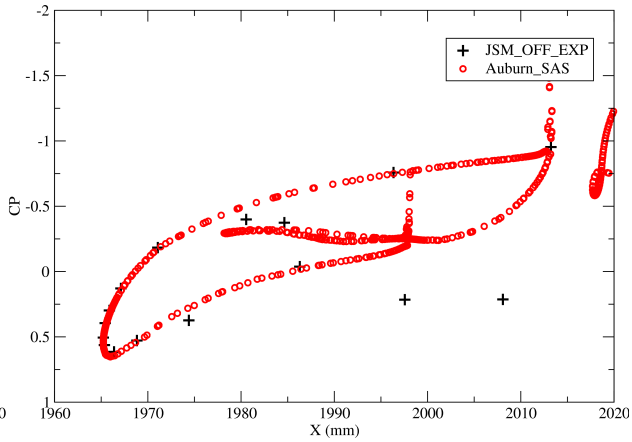

Wing A-A

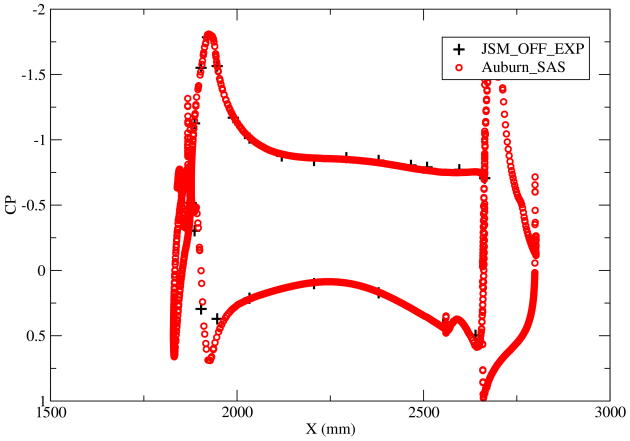

Wing B-B

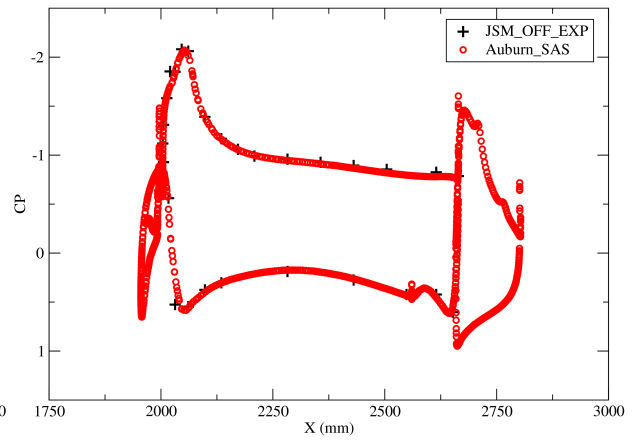

Flap A-A

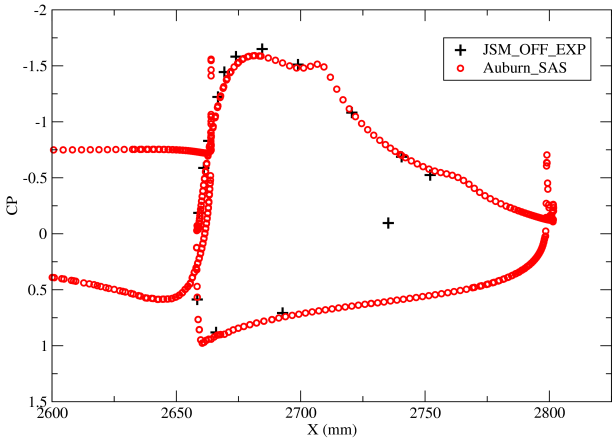

Flap B-B

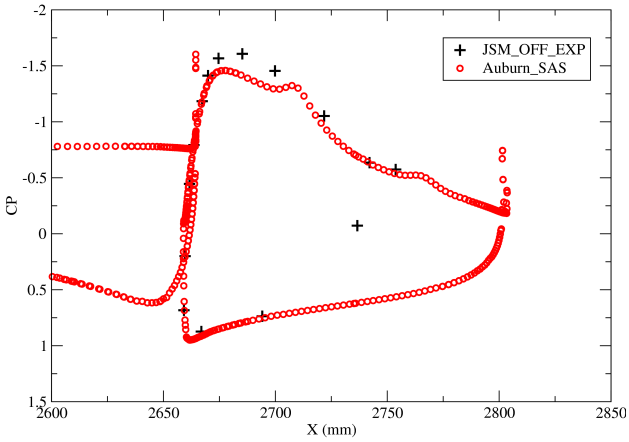

Slat D-D

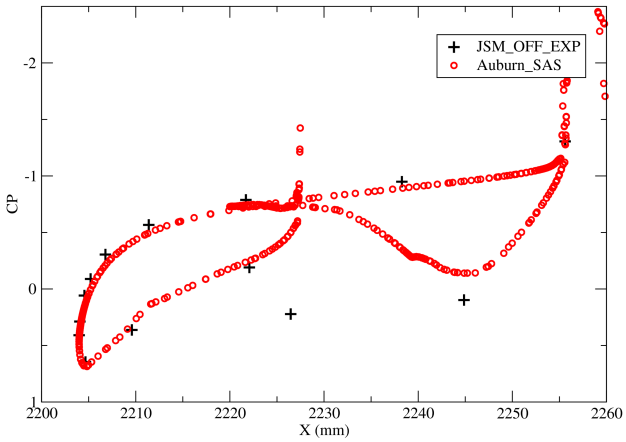

Wing C-C

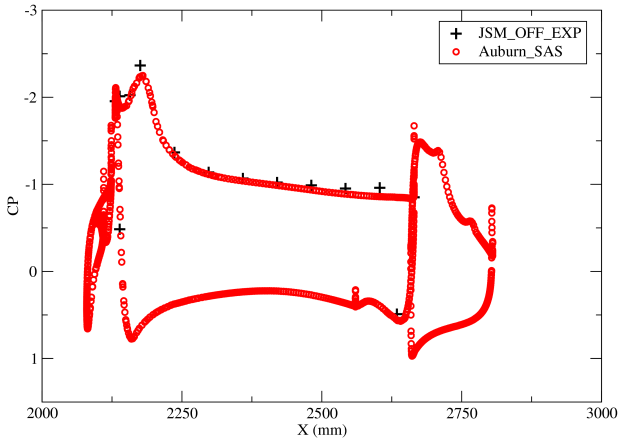

Wing D-D

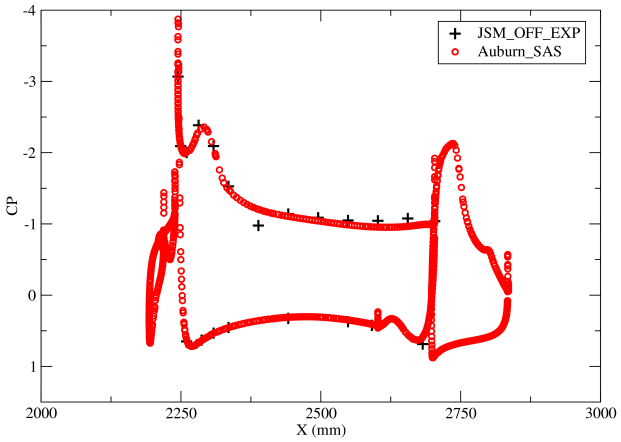

Flap C-C

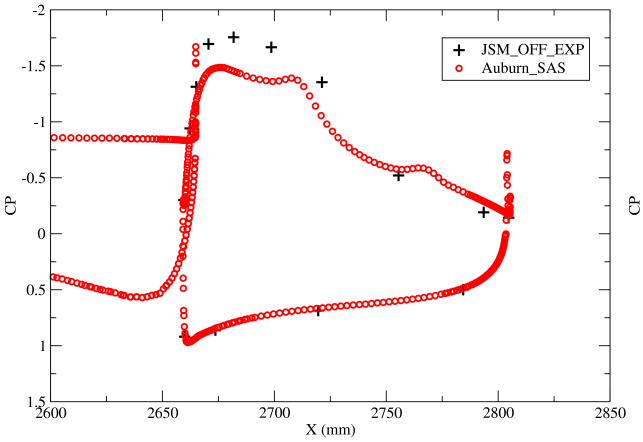

Flap D-D

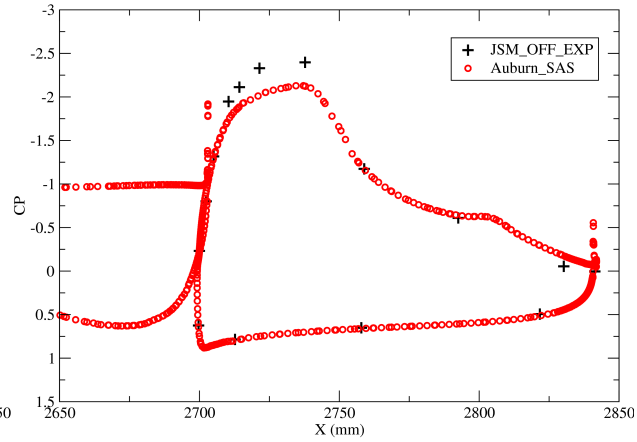

Slat E-E

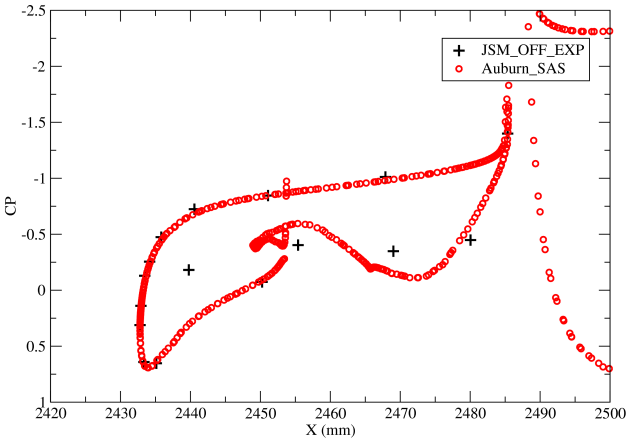

Slat G-G

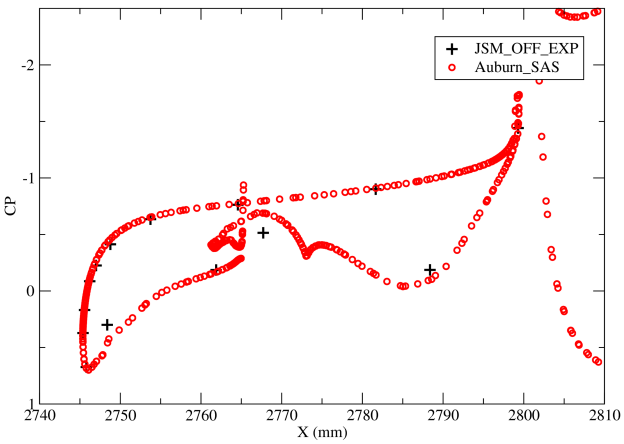

Wing E-E

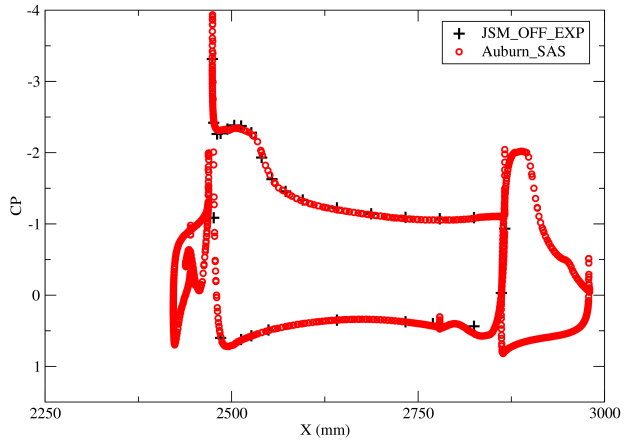

Wing G-G

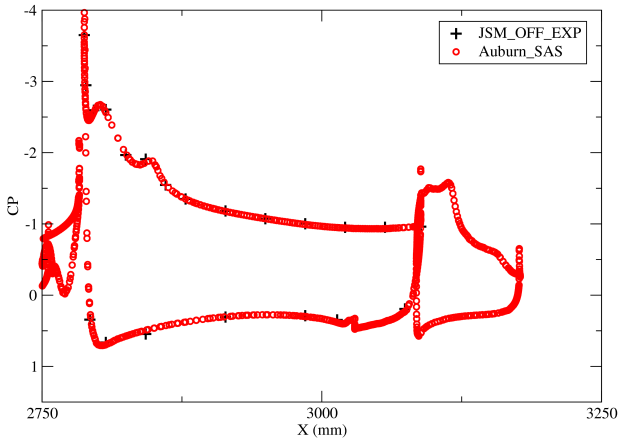

Flap E-E

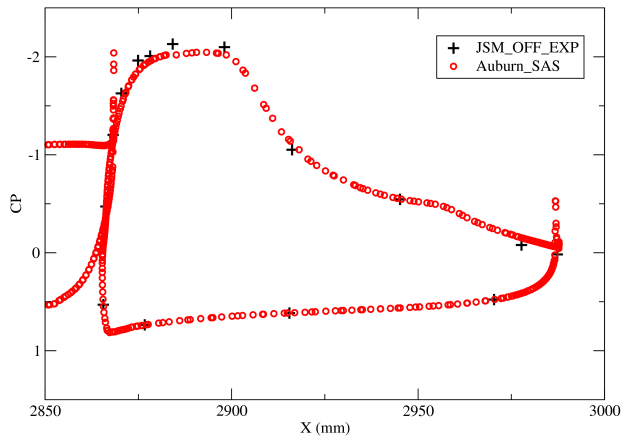

Flap G-G

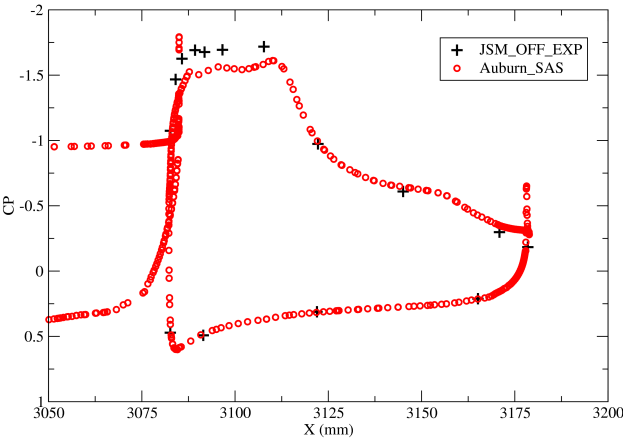

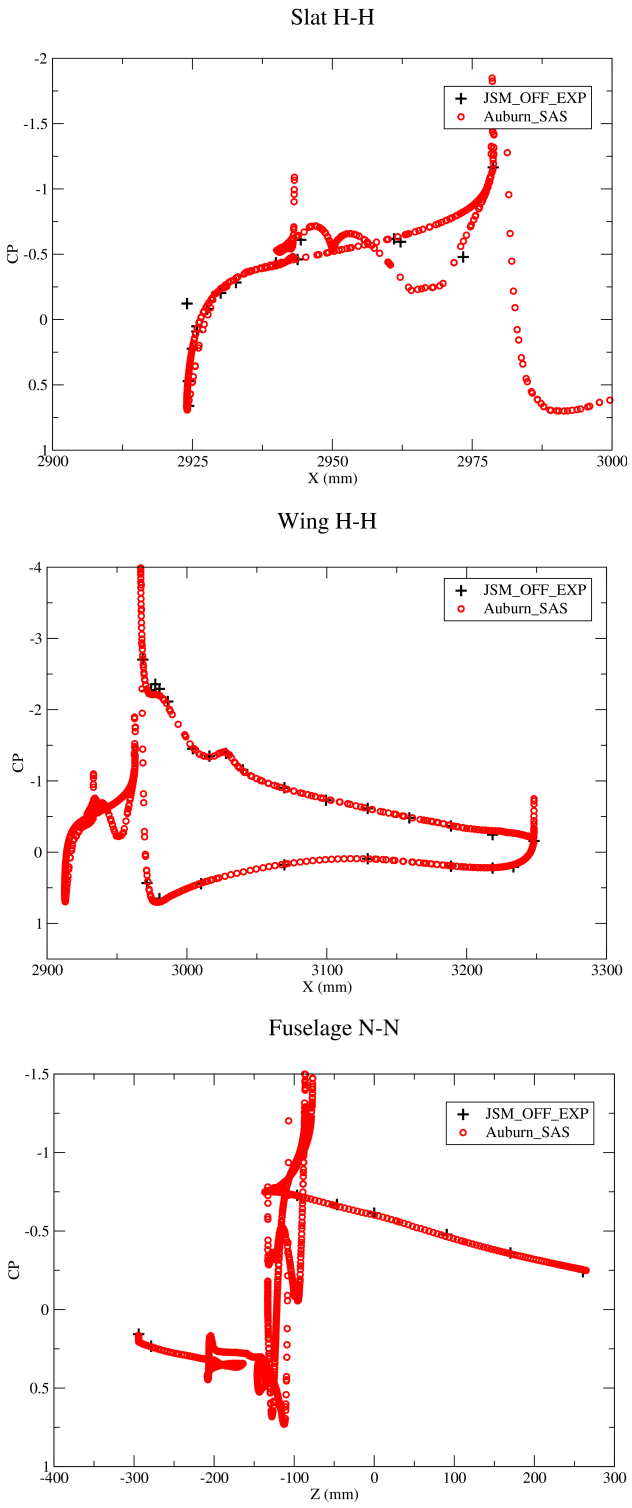

Figure 5.34: JSM: JSM Nacelle/Pylon OFF Configuration with Incompressible Solver - C_P Comparison at AOA 4.36^0

Slat A-A

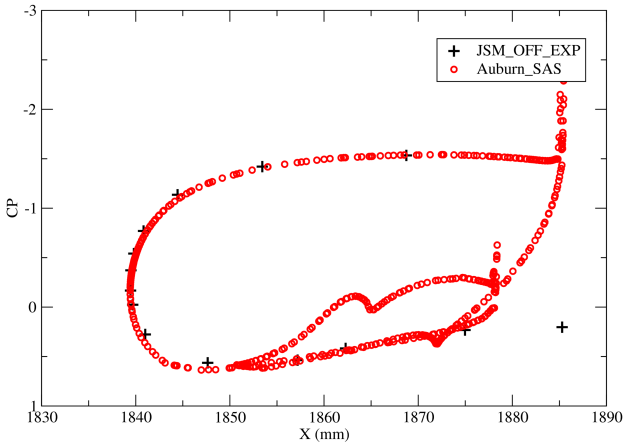

Slat B-B

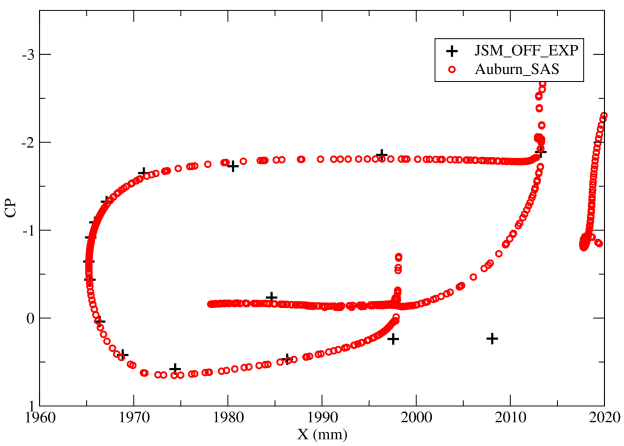

Wing A-A

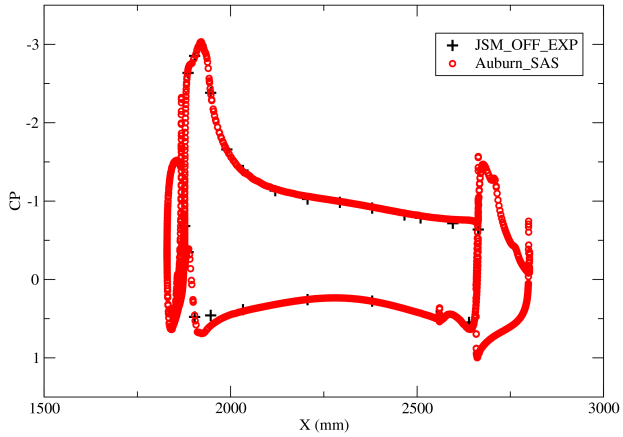

Wing B-B

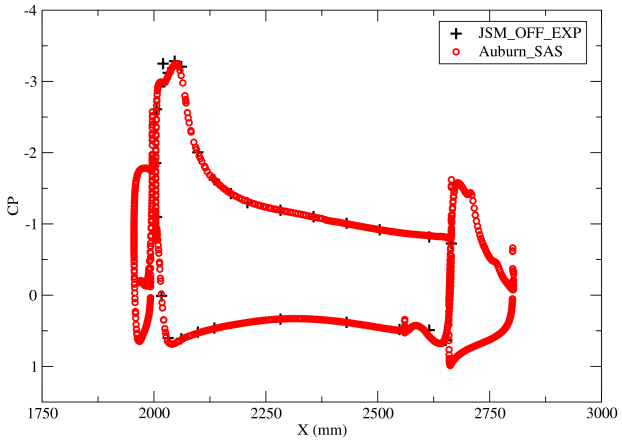

Flap A-A

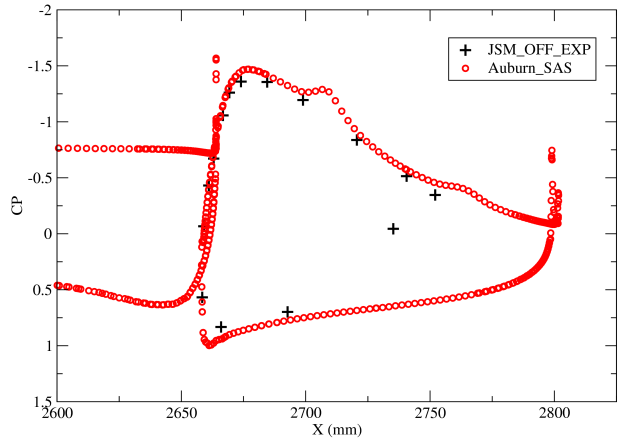

Flap B-B

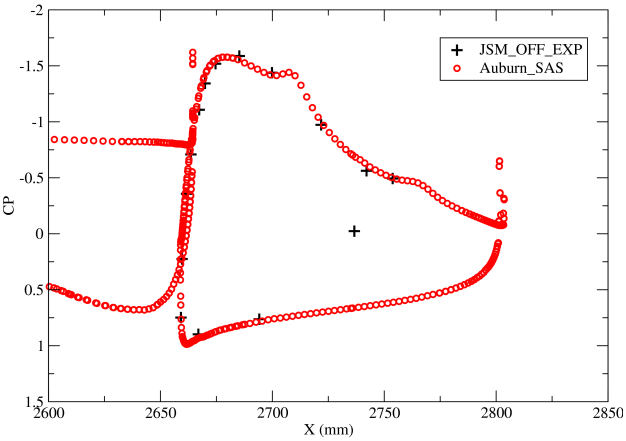

Slat D-D

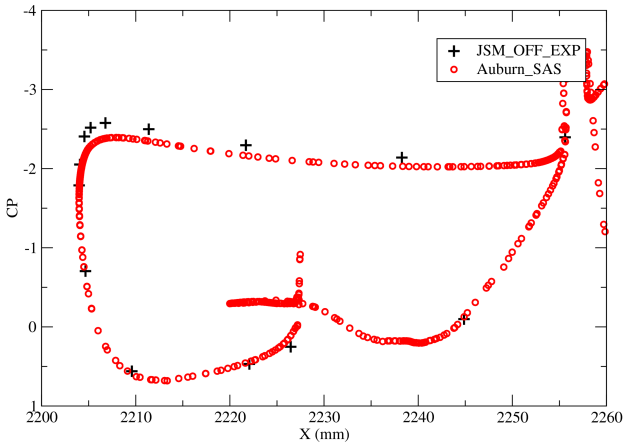

Wing C-C

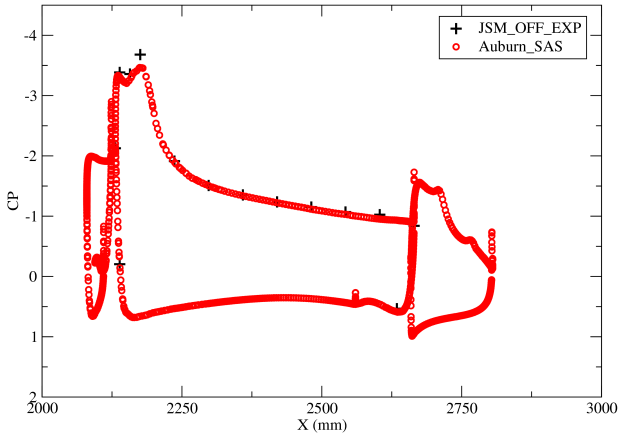

Wing D-D

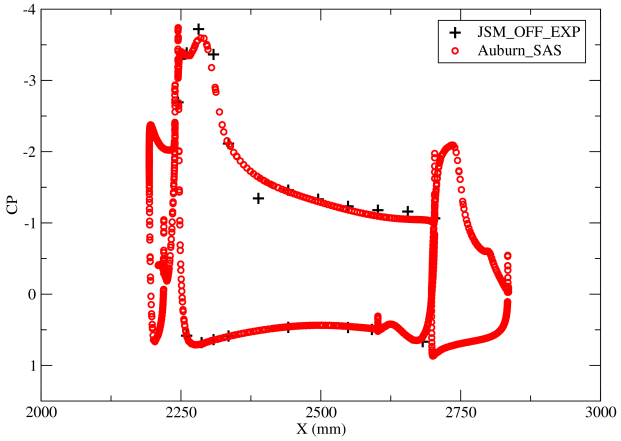

Flap C-C

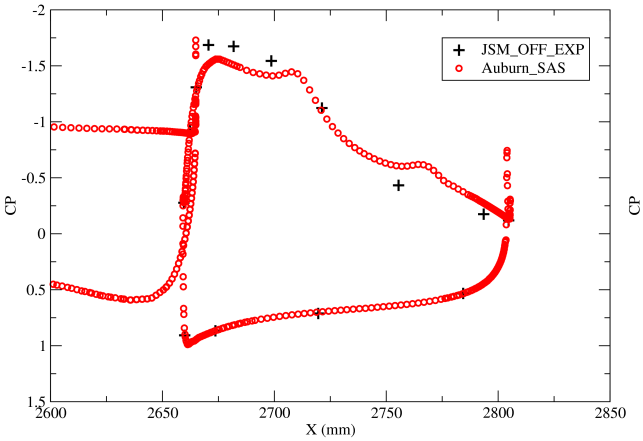

Flap D-D

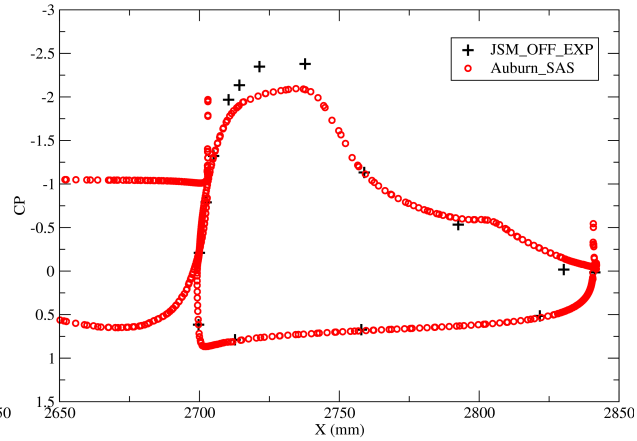

Slat E-E

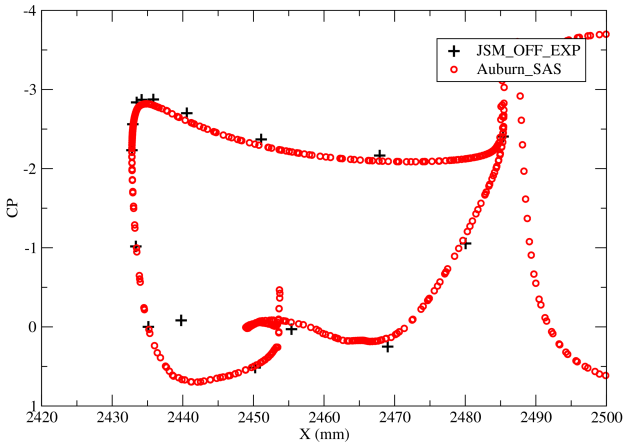

Slat G-G

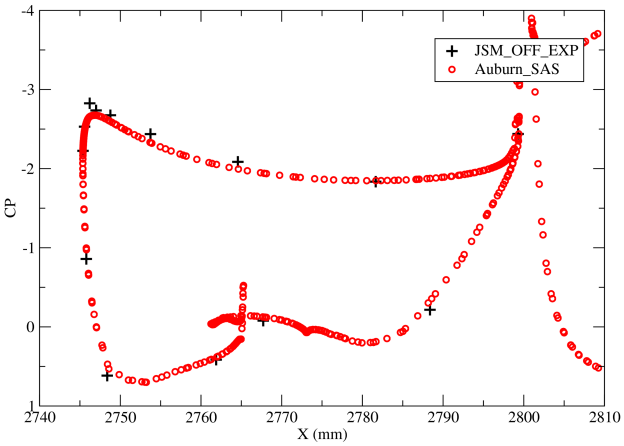

Wing E-E

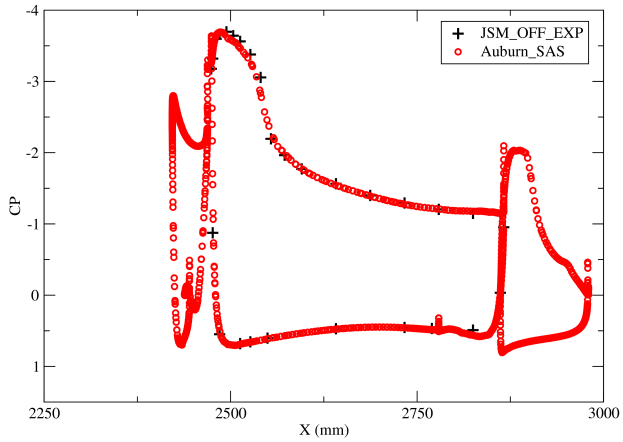

Wing G-G

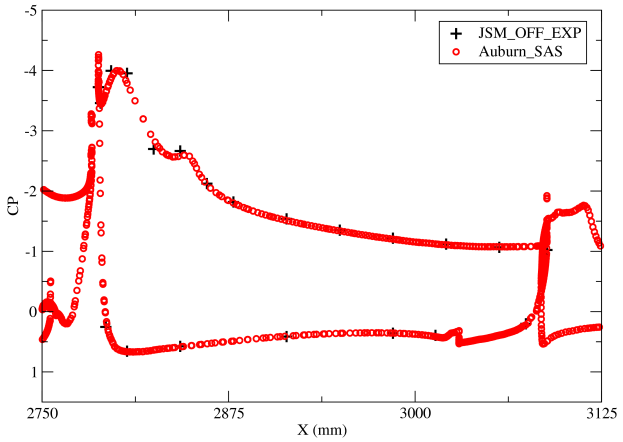

Flap E-E

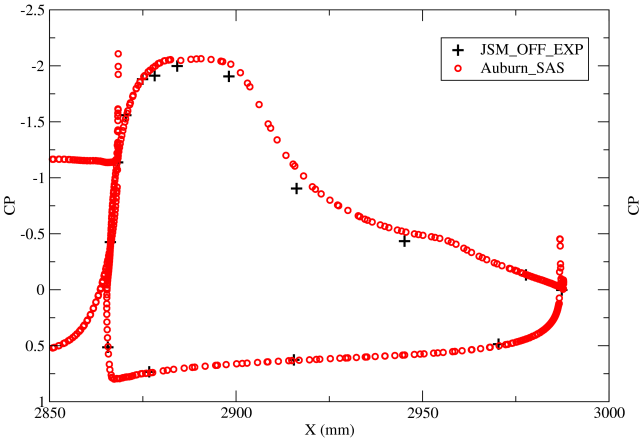

Flap G-G

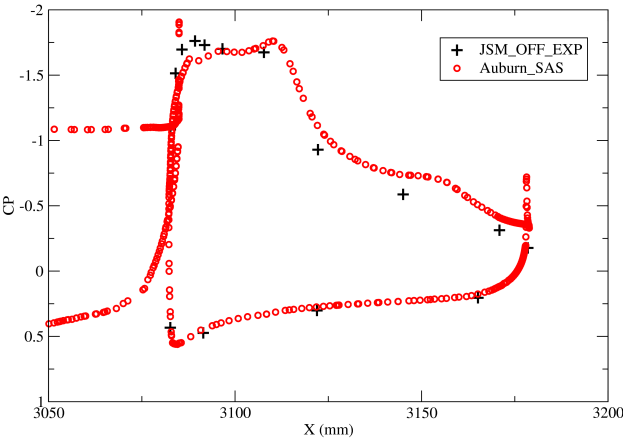

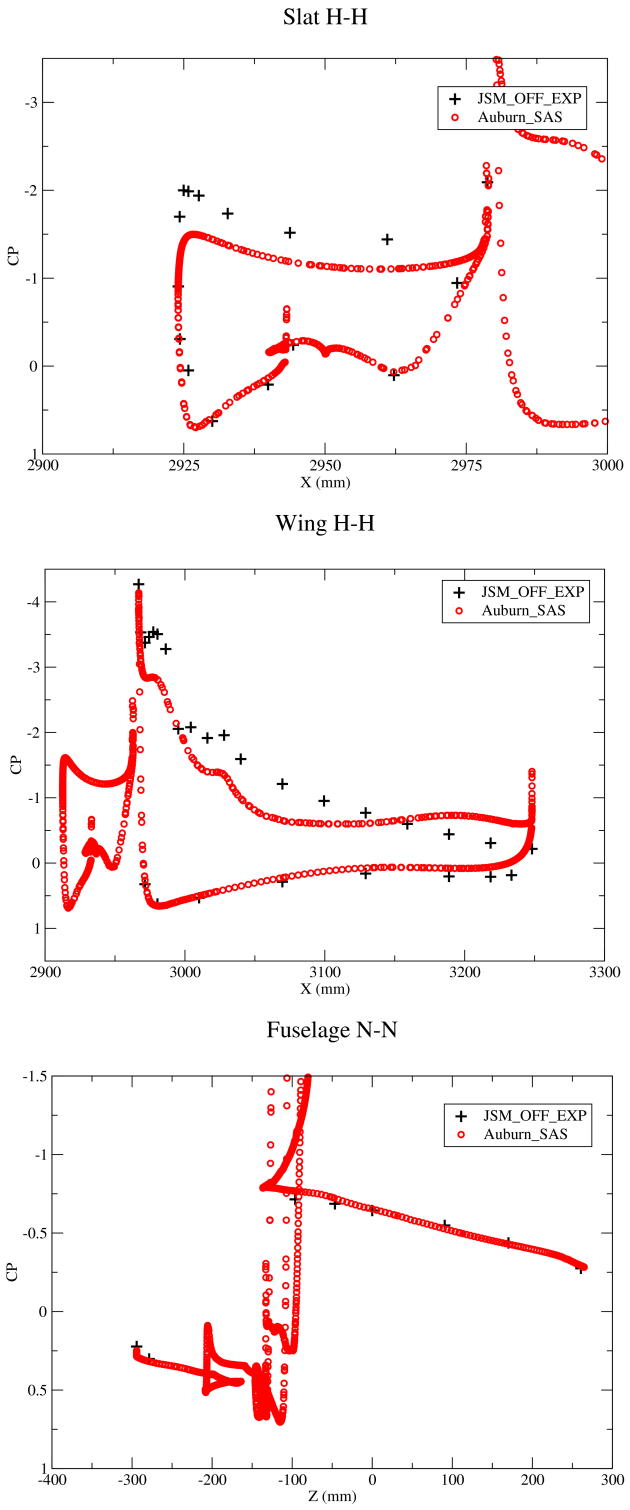

Figure 5.35: JSM: JSM Nacelle/Pylon OFF Configuration with Incompressible Solver - C_P Comparison at AOA 10.47^0

Slat A-A

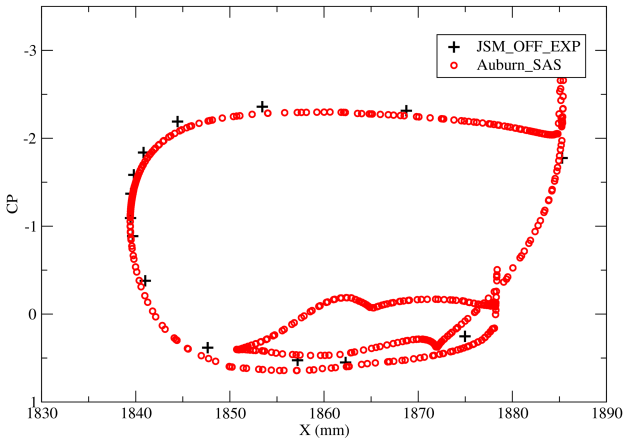

Slat B-B

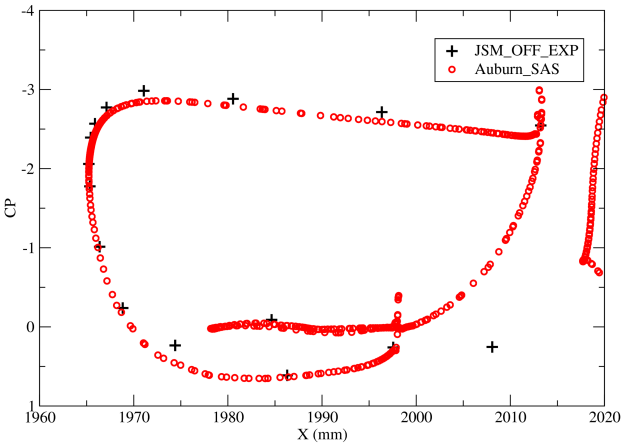

Wing A-A

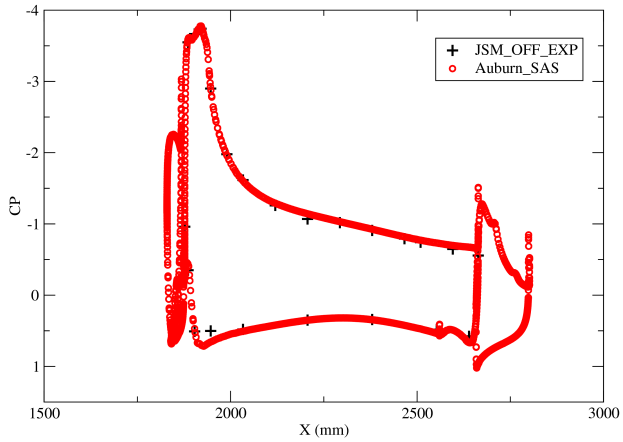

Wing B-B

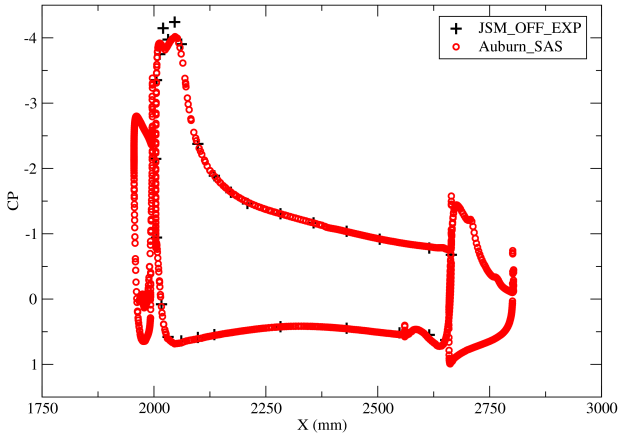

Flap A-A

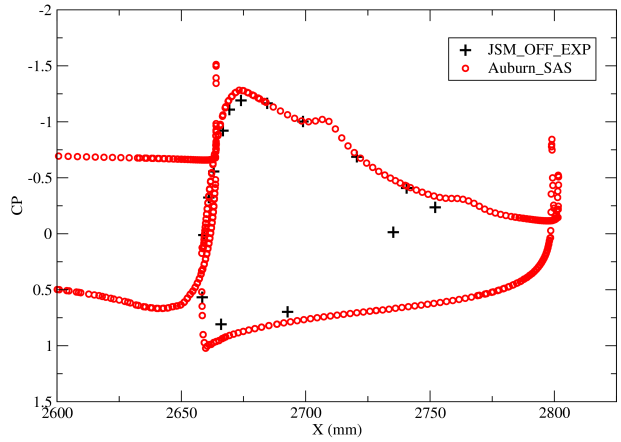

Flap B-B

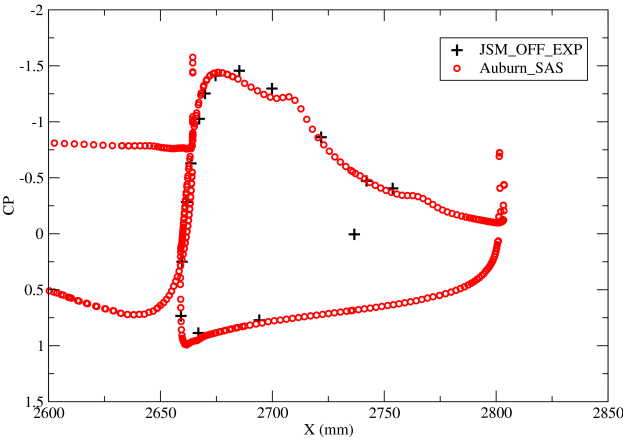

Slat D-D

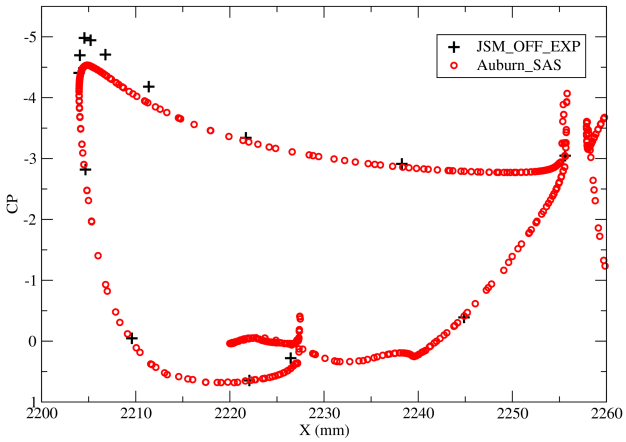

Wing C-C

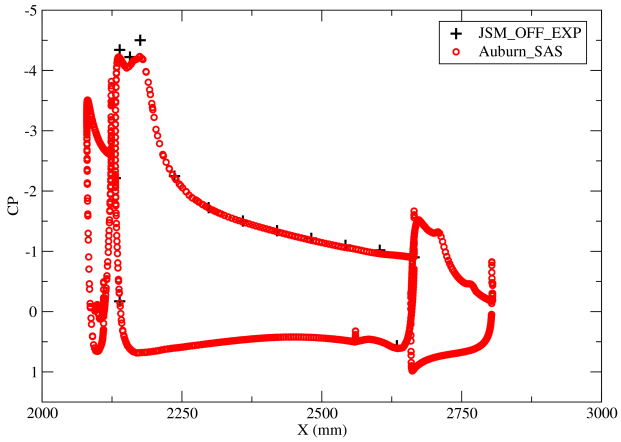

Wing D-D

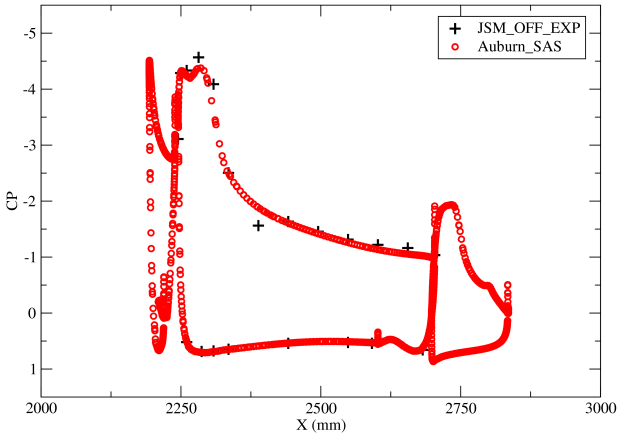

Flap C-C

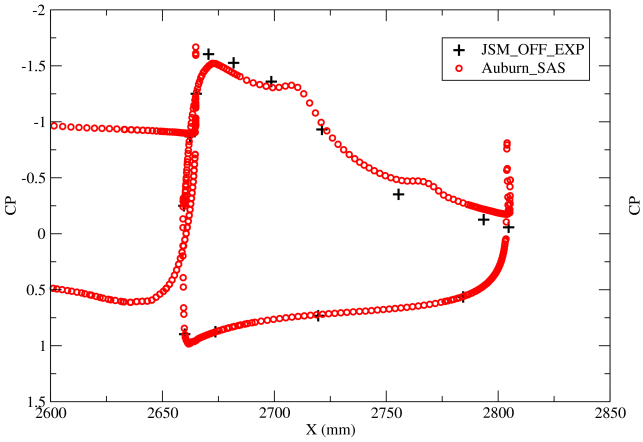

Flap D-D

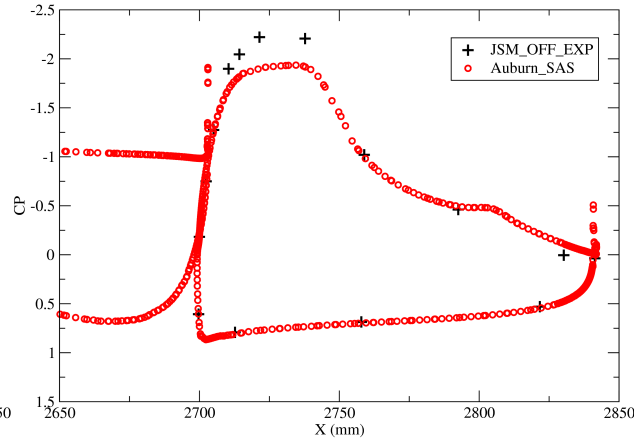

Slat E-E

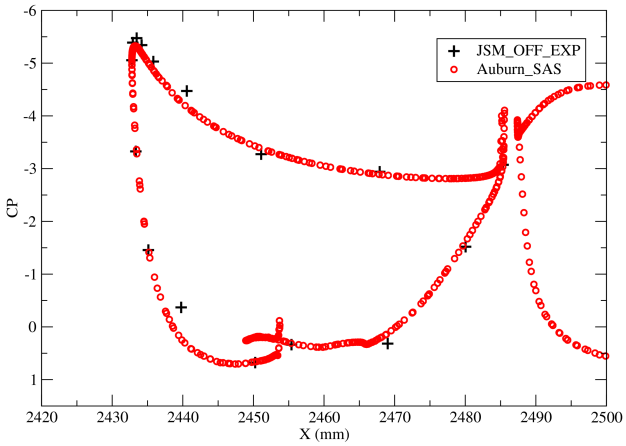

Slat G-G

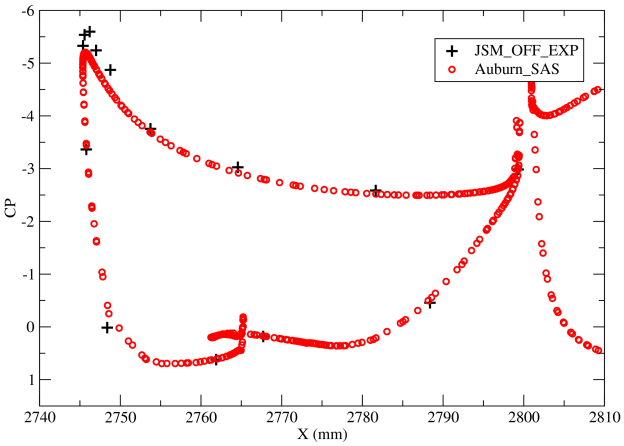

Wing E-E

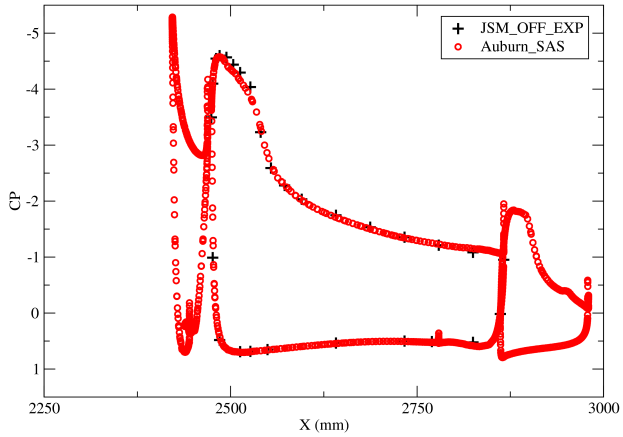

Wing G-G

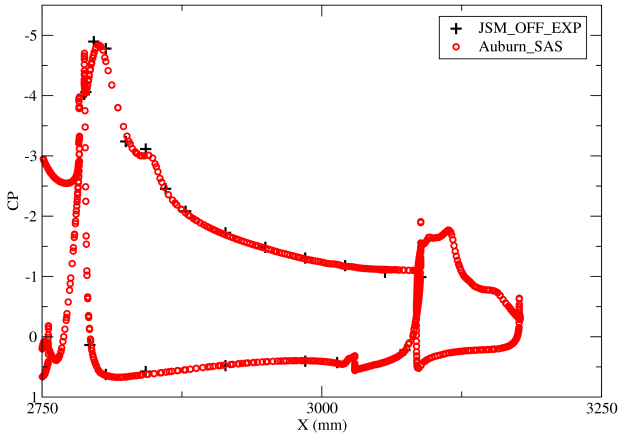

Flap E-E

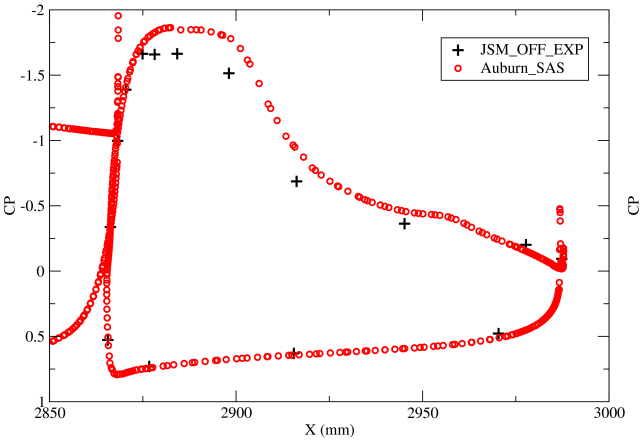

Flap G-G

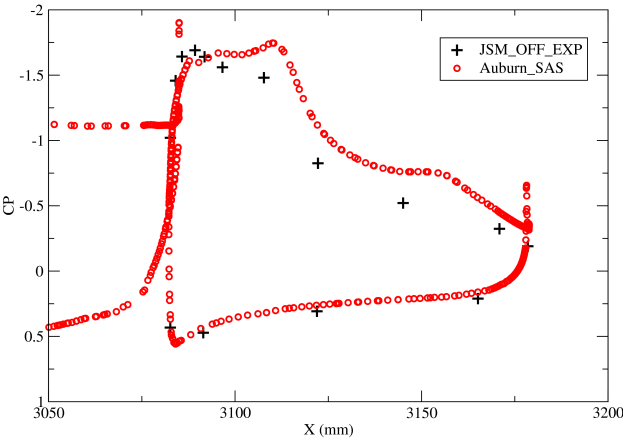

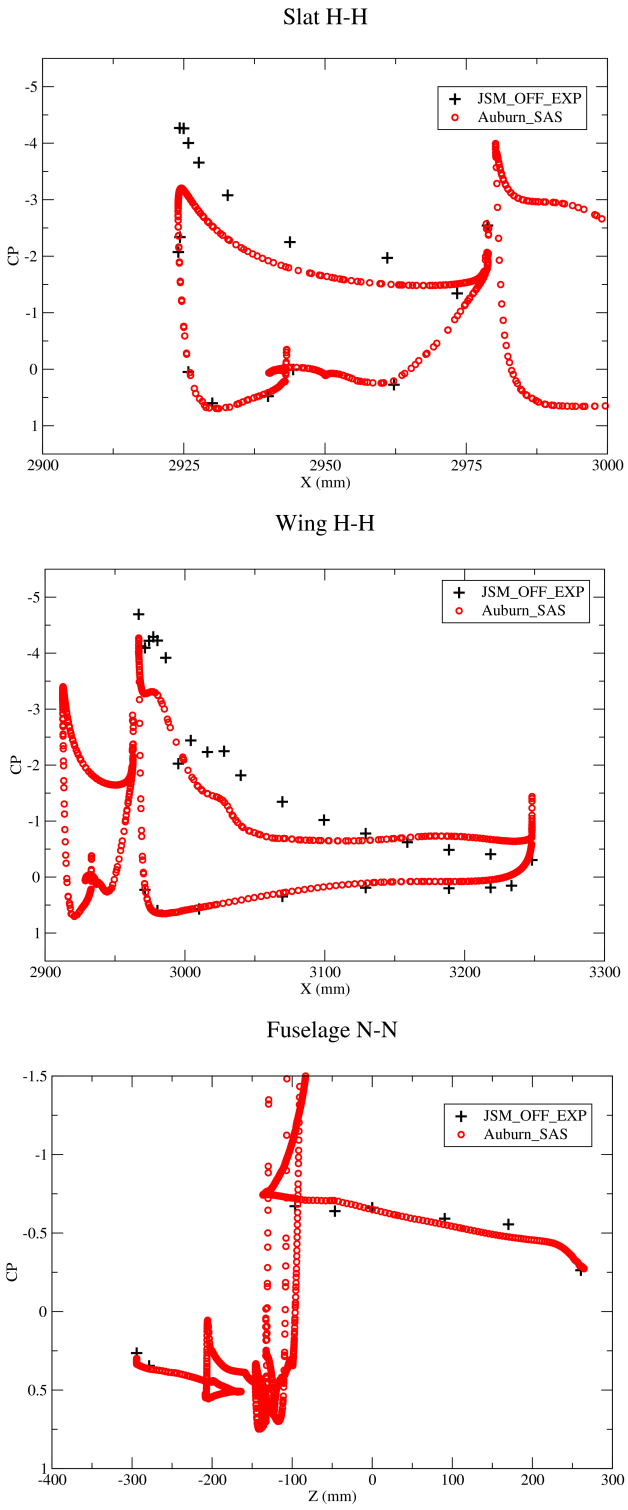

Figure 5.36: JSM: JSM Nacelle/Pylon OFF Configuration with Incompressible Solver - C_P Comparison at AOA 14.54^0

Slat A-A

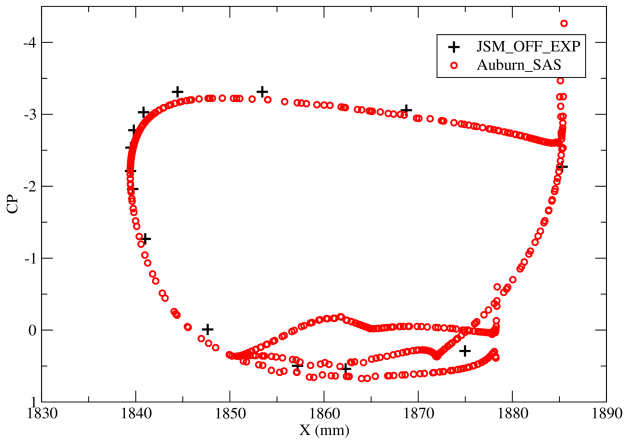

Slat B-B

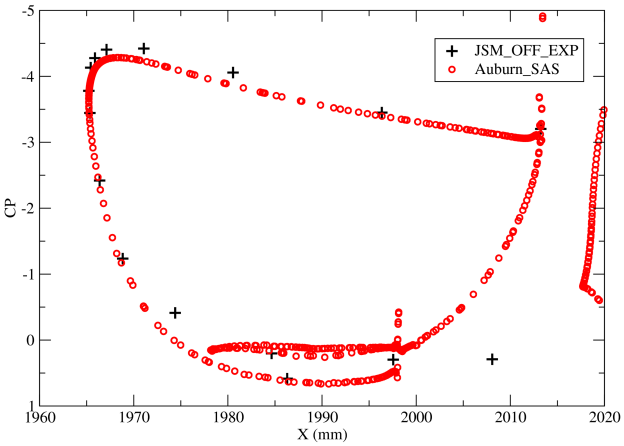

Wing A-A

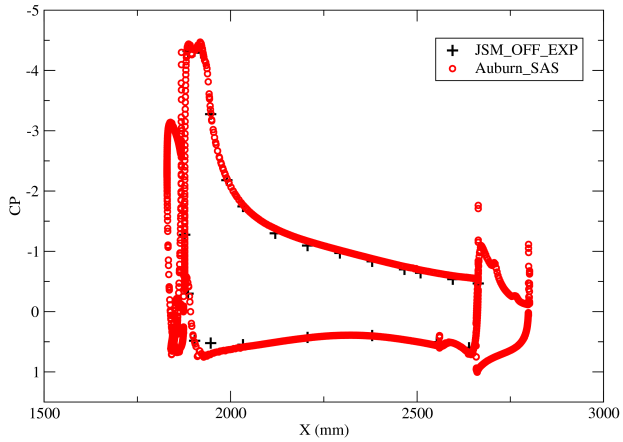

Wing B-B

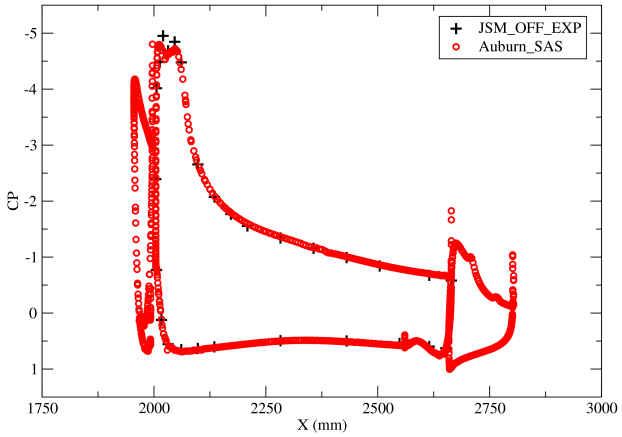

Flap A-A

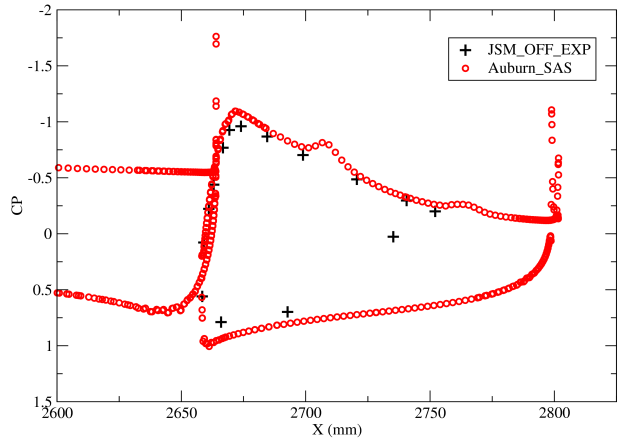

Flap B-B

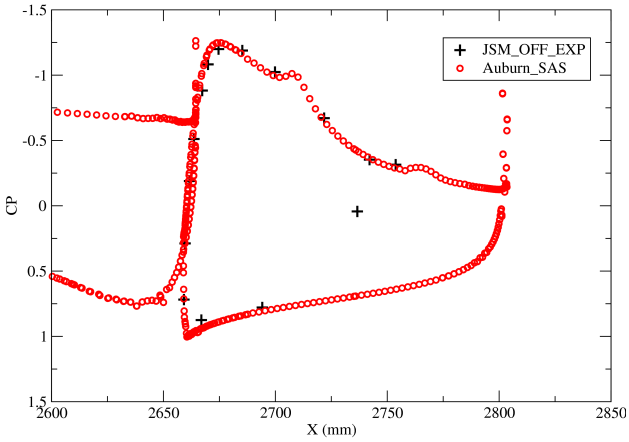

Slat D-D

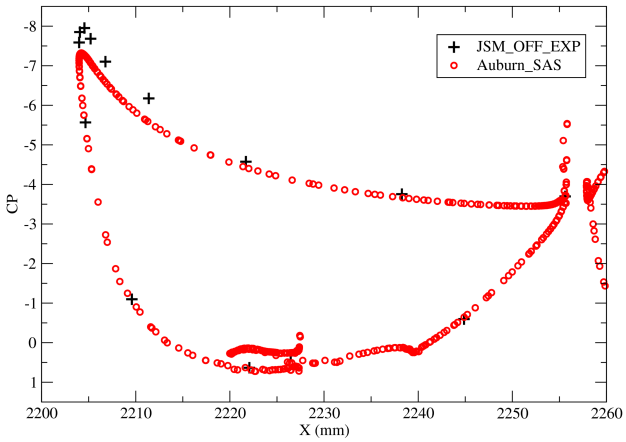

Wing C-C

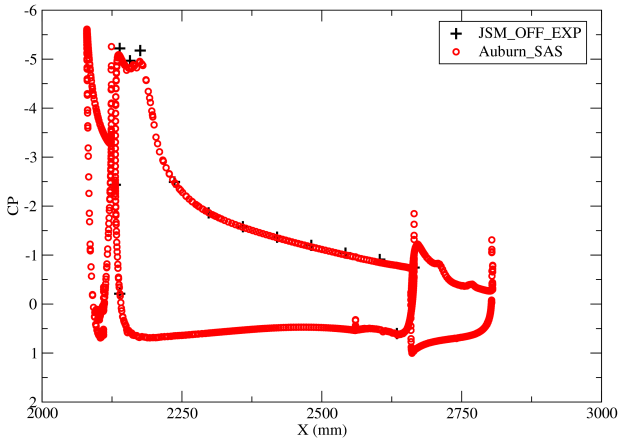

Wing D-D

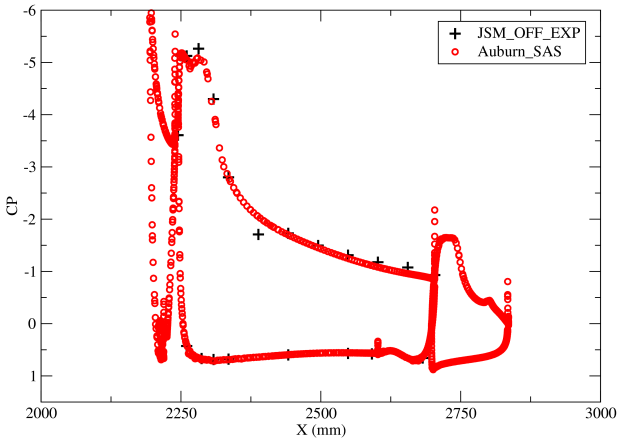

Flap C-C

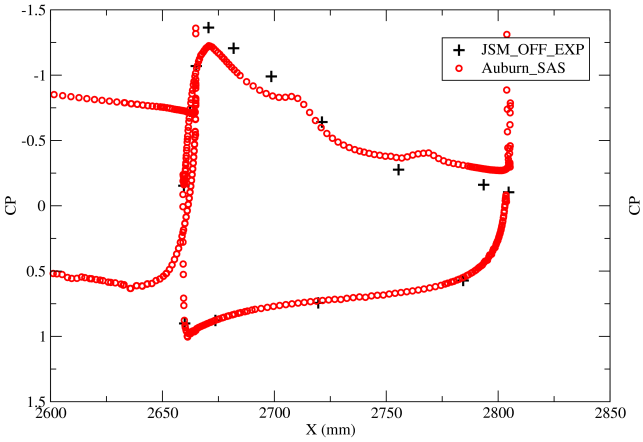

Flap D-D

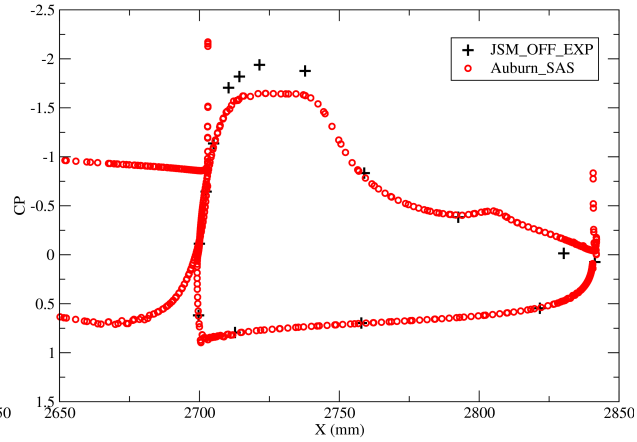

Slat E-E

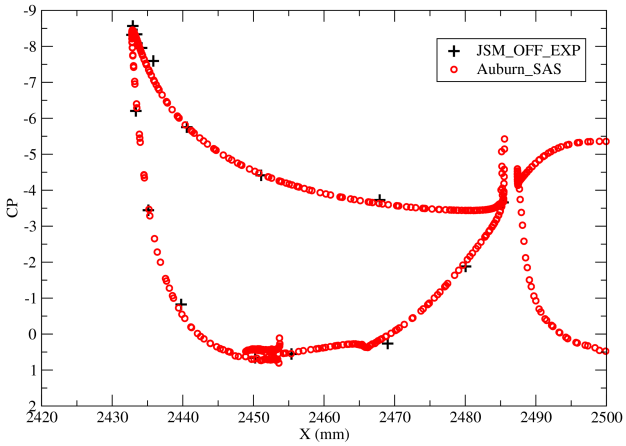

Slat G-G

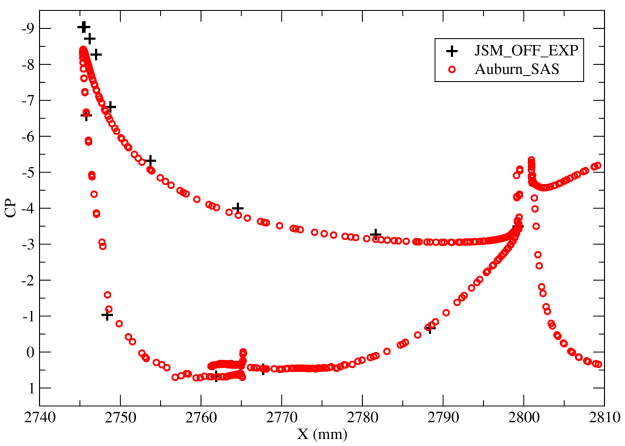

Wing E-E

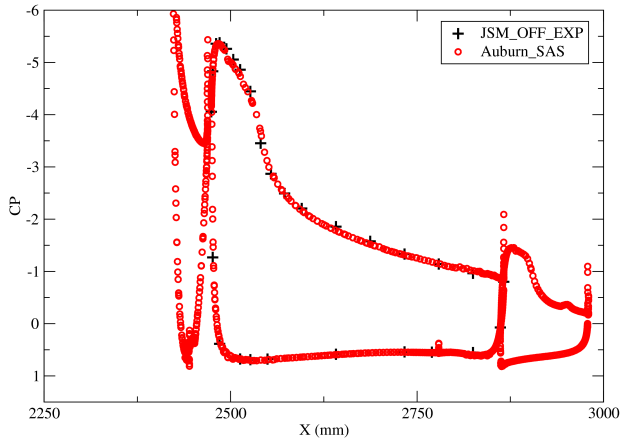

Wing G-G

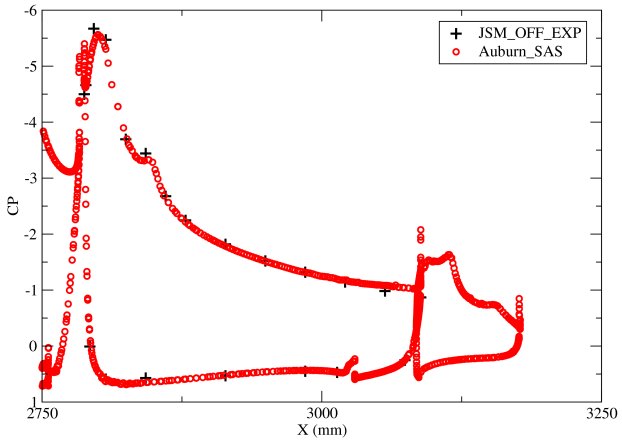

Flap E-E

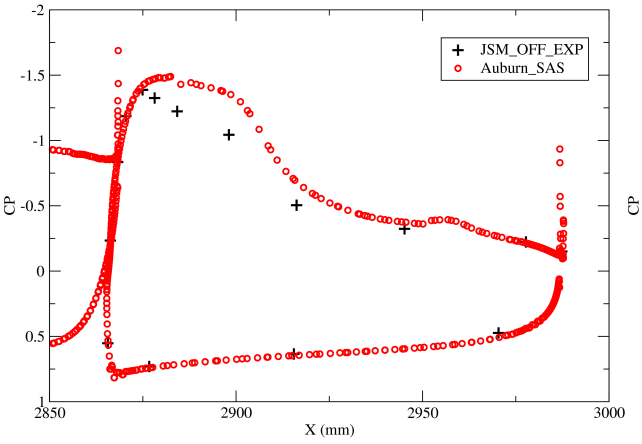

Flap G-G

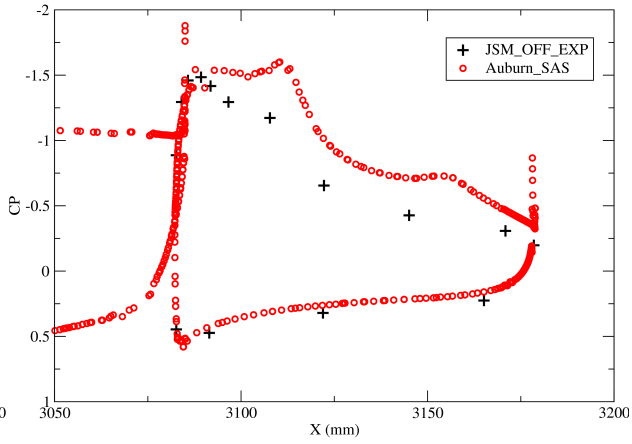

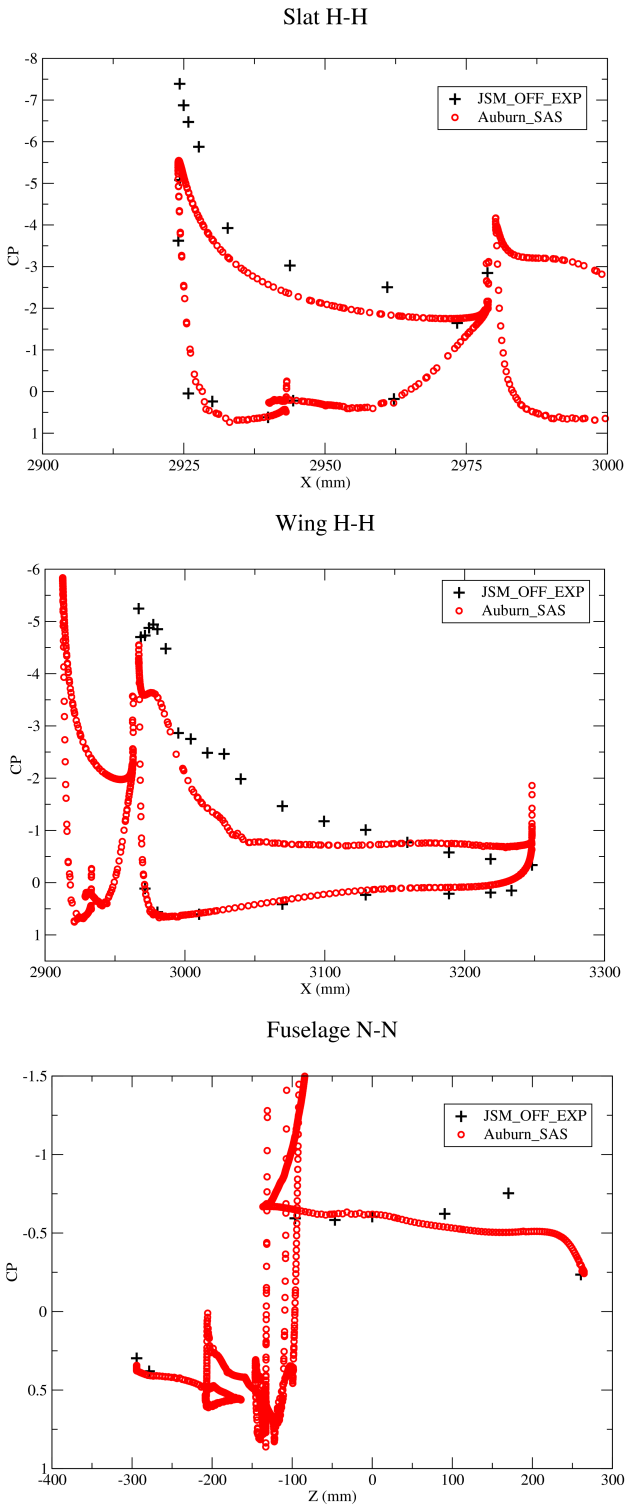

Figure 5.37: JSM: JSM Nacelle/Pylon OFF Configuration with Incompressible Solver - C_P Comparison at AOA 18.58^0

Slat A-A

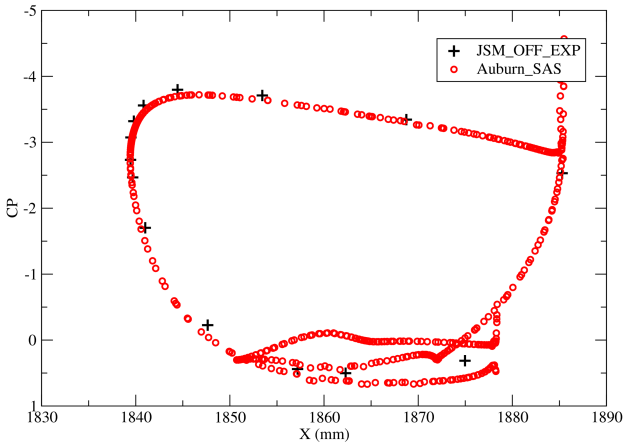

Slat B-B

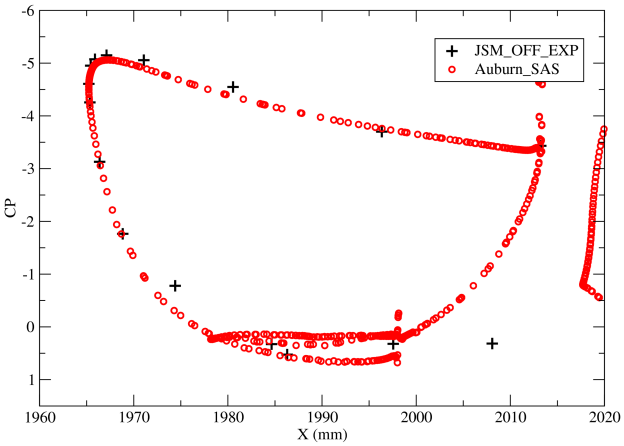

Wing A-A

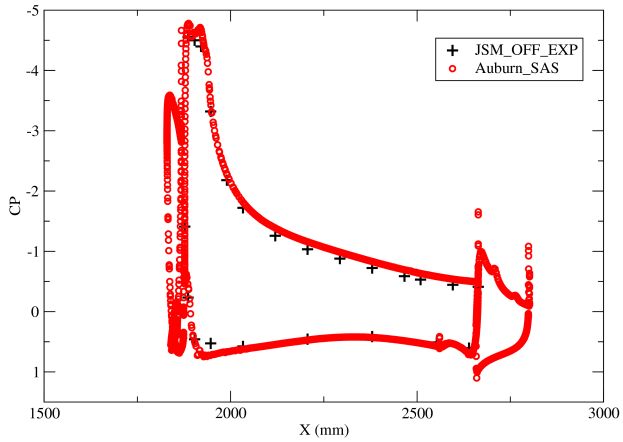

Wing B-B

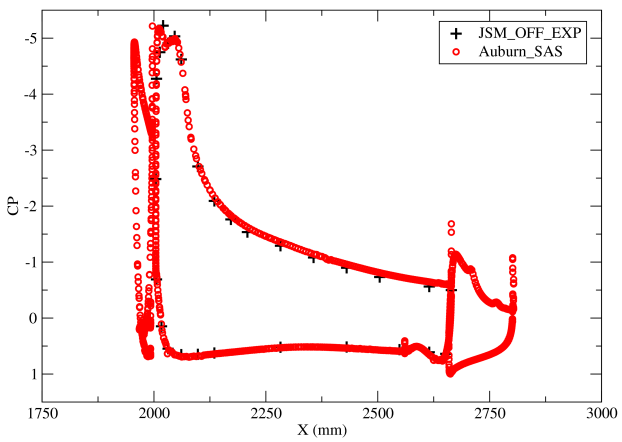

Flap A-A

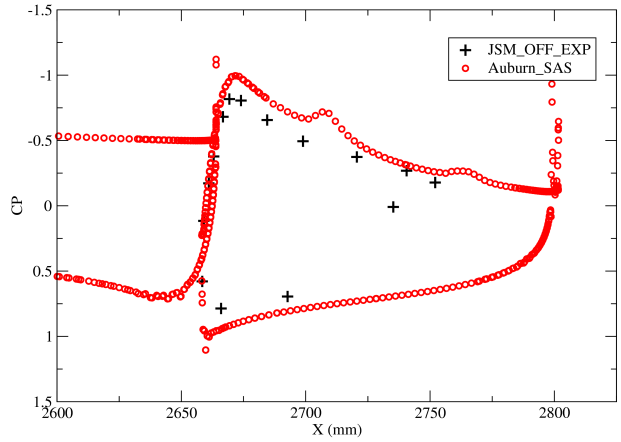

Flap B-B

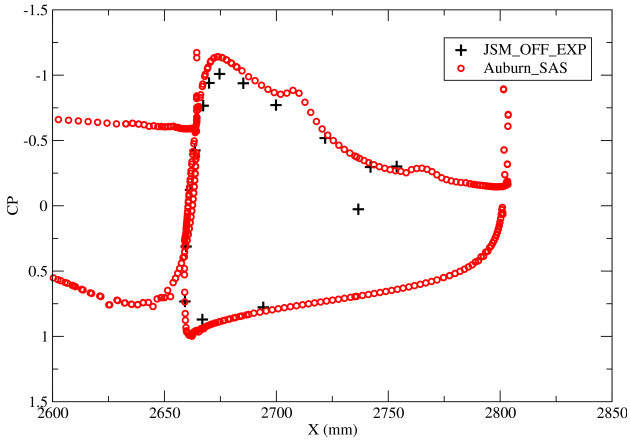

Slat D-D

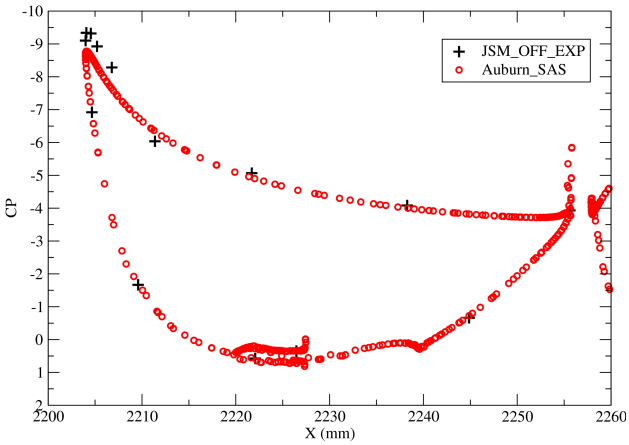

Wing C-C

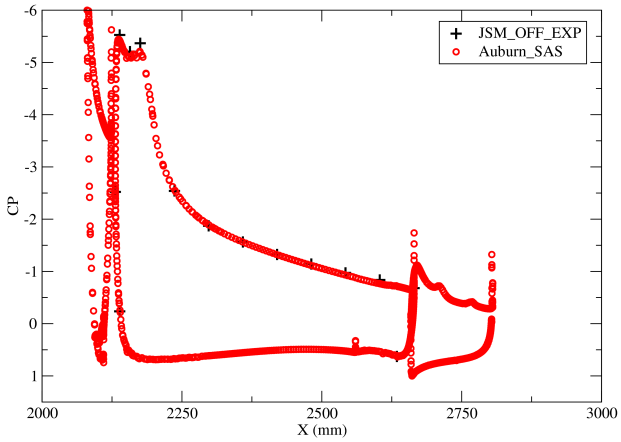

Wing D-D

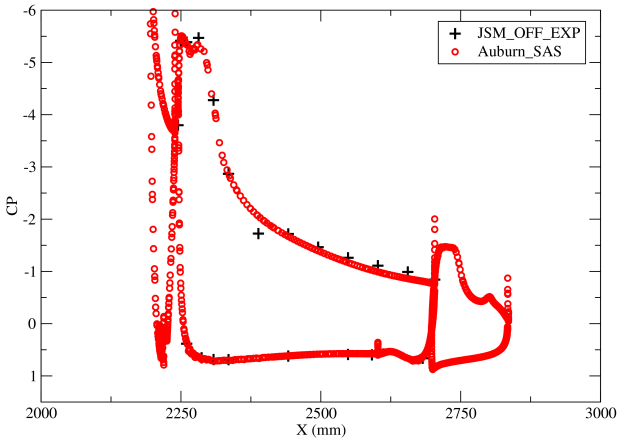

Flap C-C

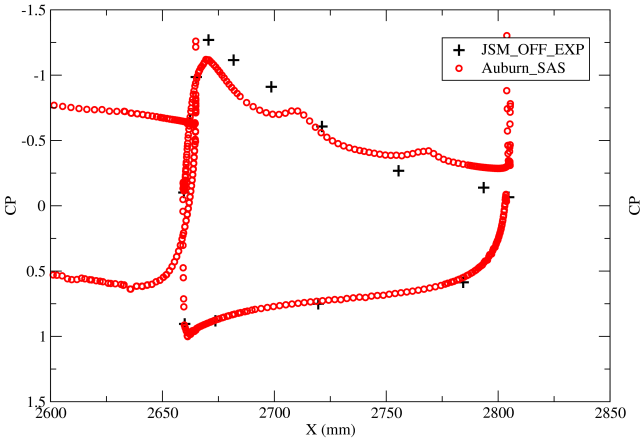

Flap D-D

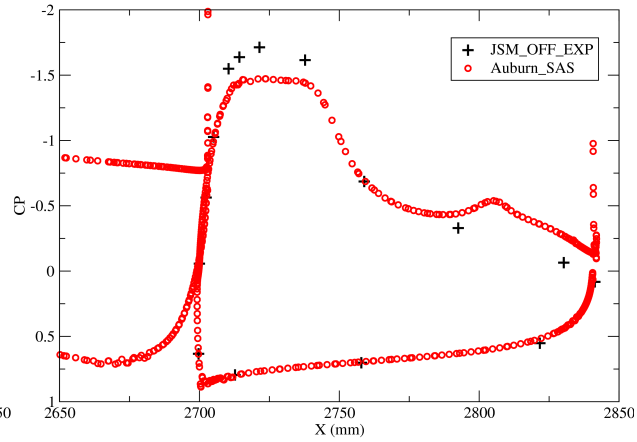

Slat E-E

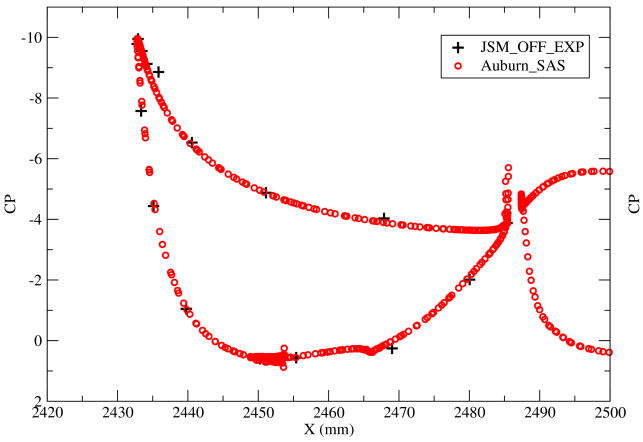

Slat G-G

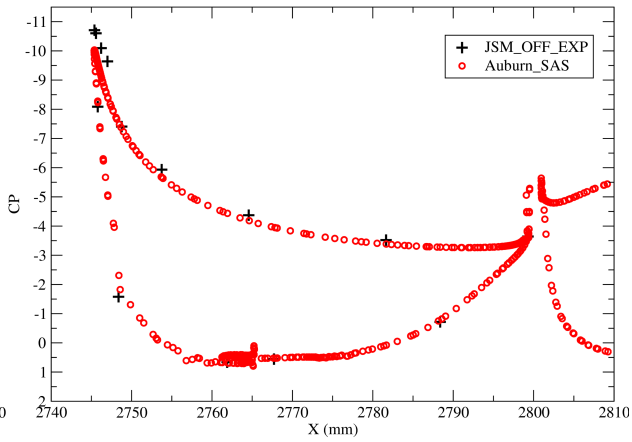

Wing E-E

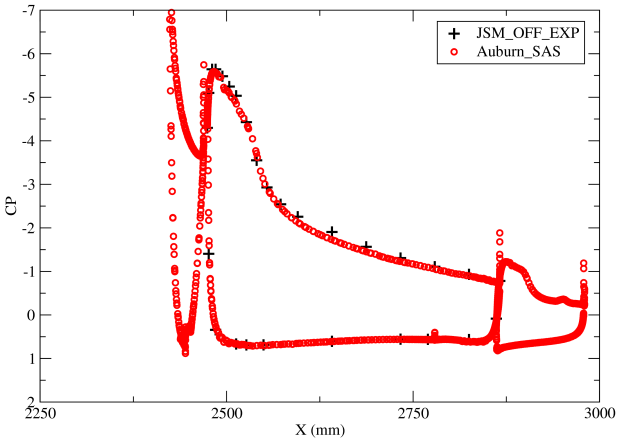

Wing G-G

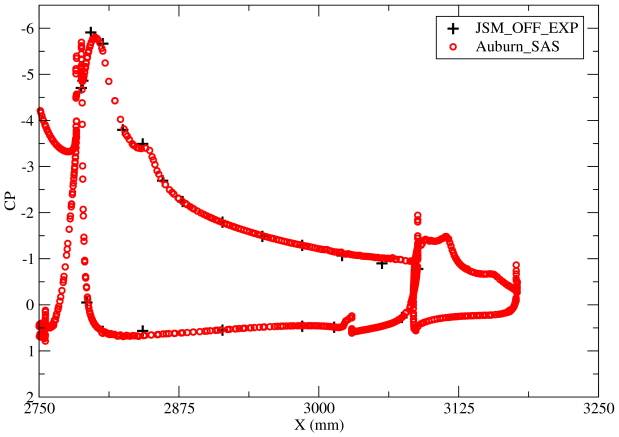

Flap E-E

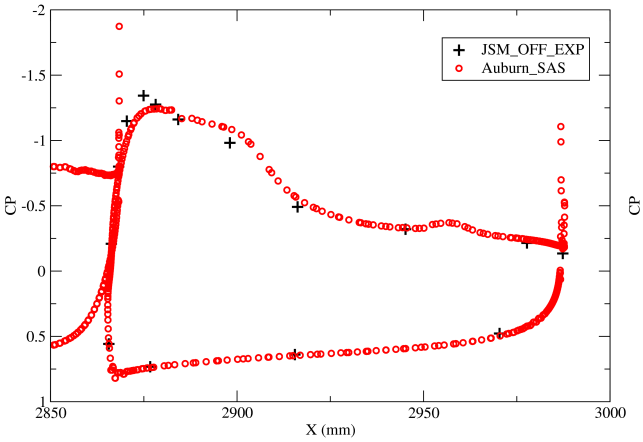

Flap G-G

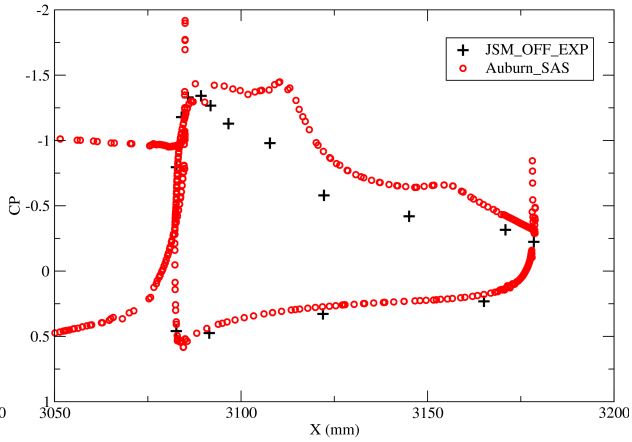

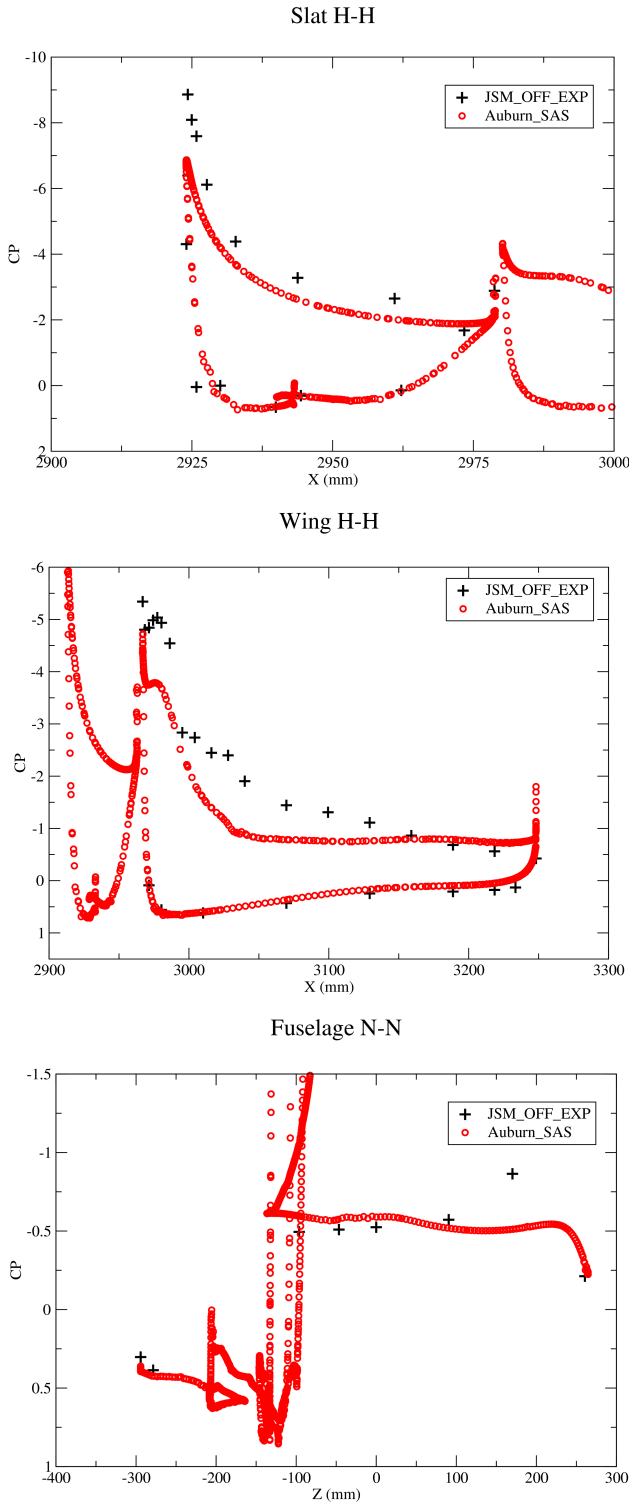

Figure 5.38: JSM: JSM Nacelle/Pylon OFF Configuration with Incompressible Solver - C_P Comparison at AOA 20.59^0

Slat A-A

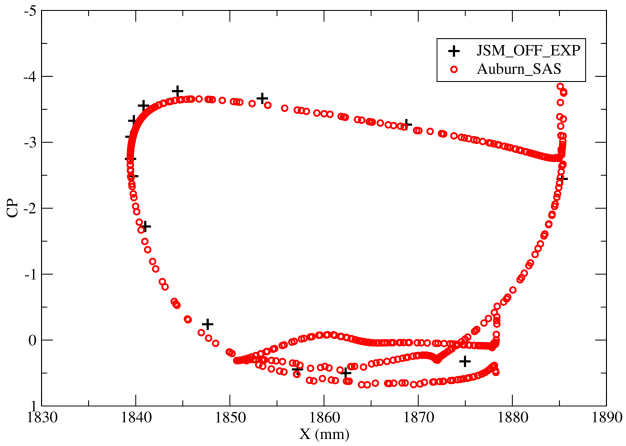

Slat B-B

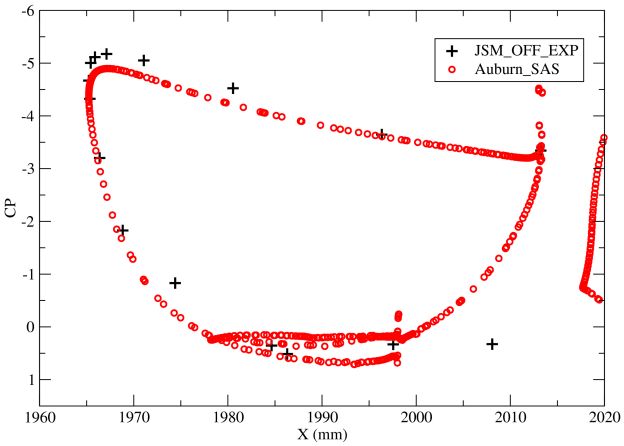

Wing A-A

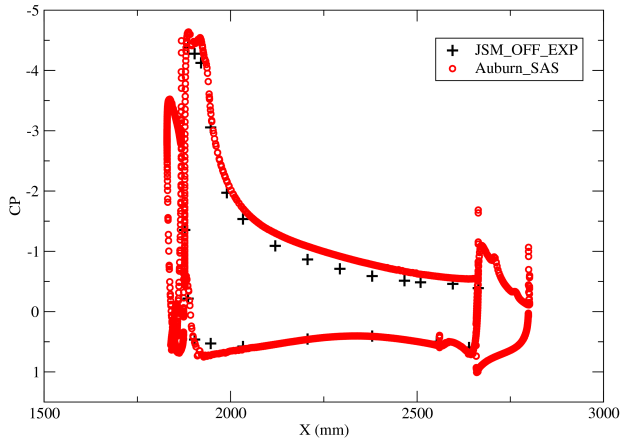

Wing B-B

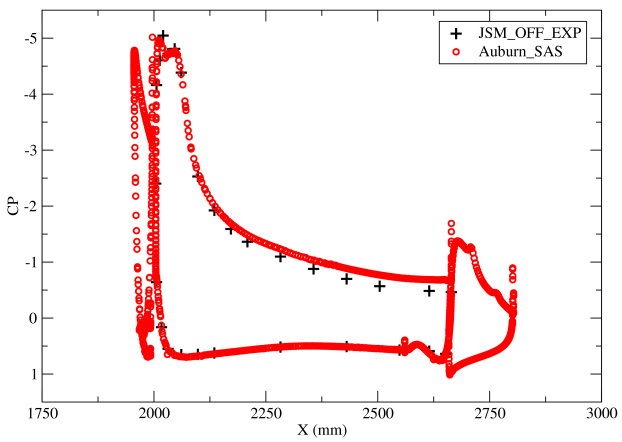

Flap A-A

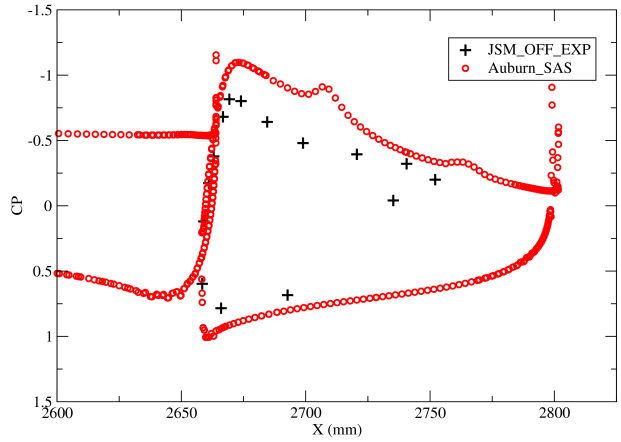

Flap B-B

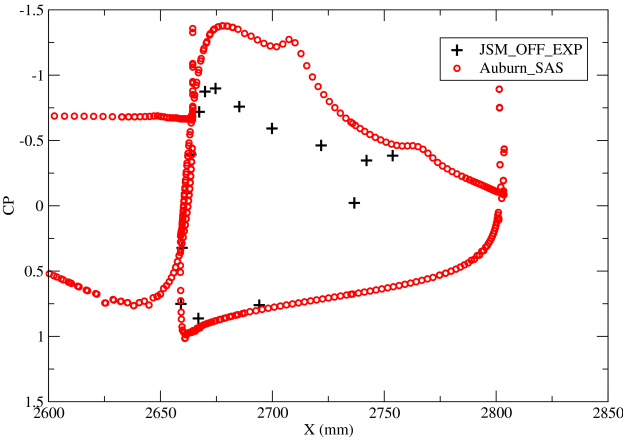

Slat D-D

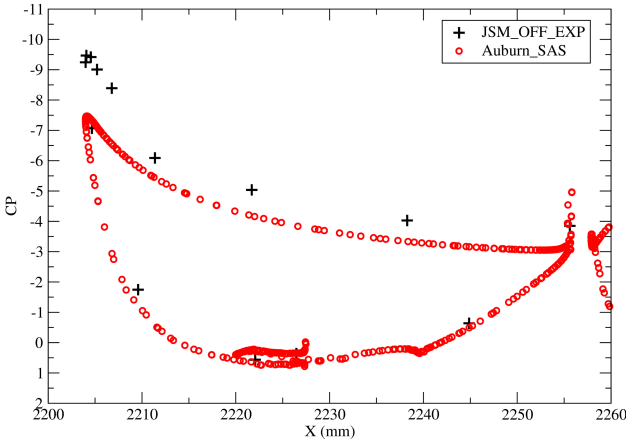

Wing C-C

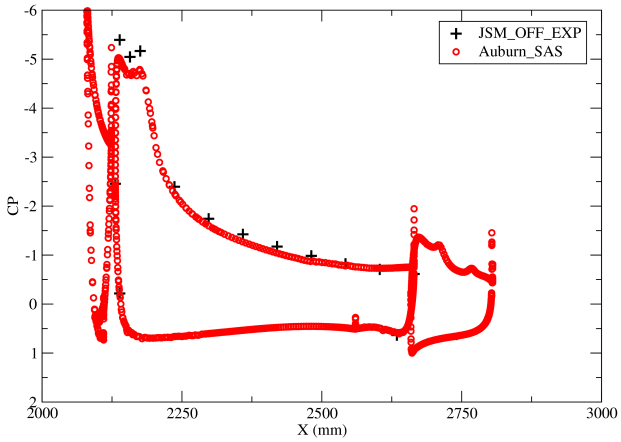

Wing D-D

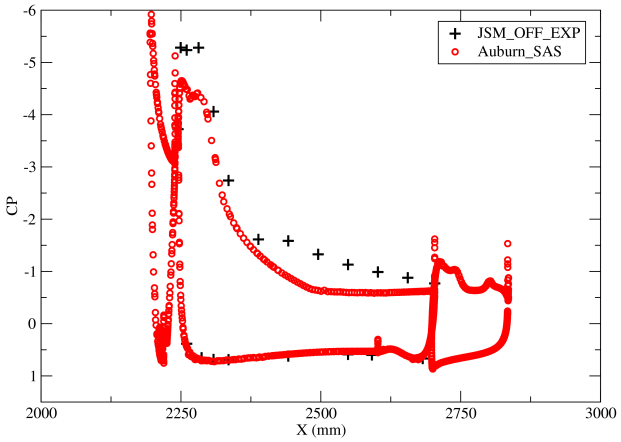

Flap C-C

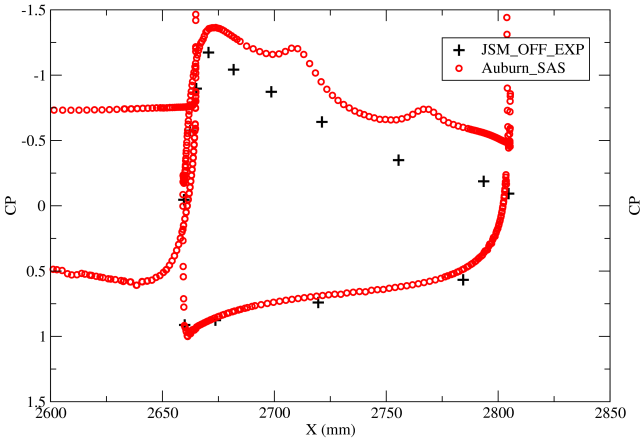

Flap D-D

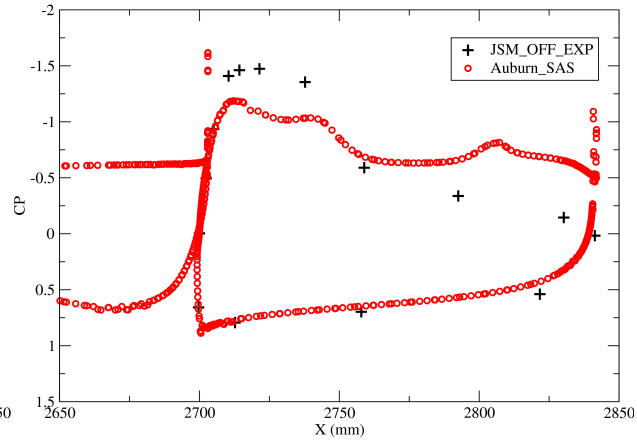

Slat E-E

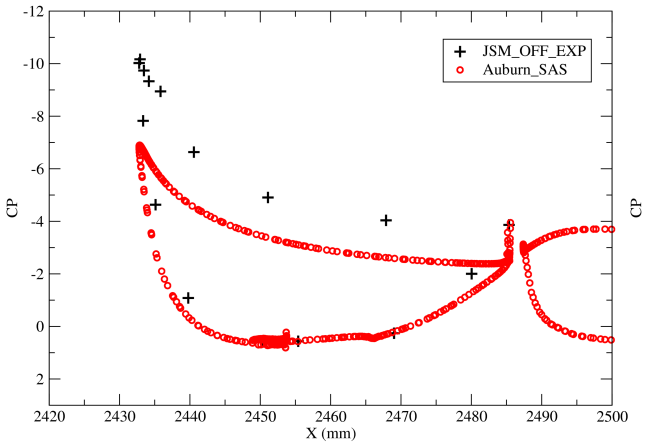

Slat G-G

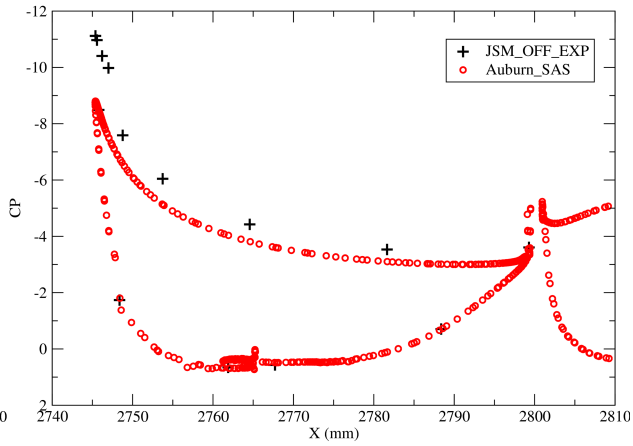

Wing E-E

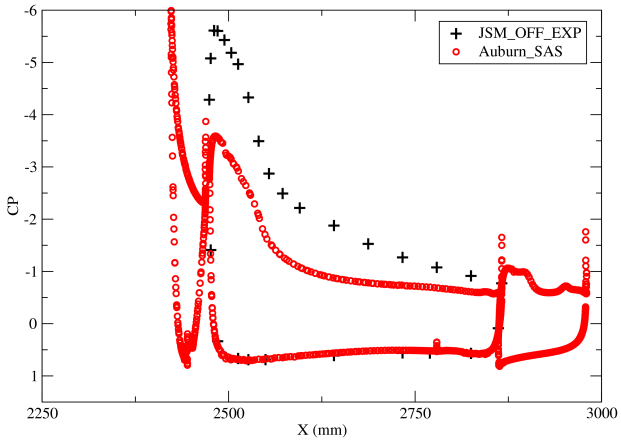

Wing G-G

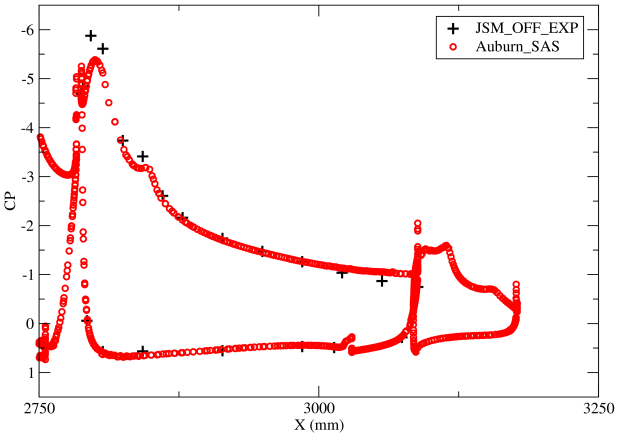

Flap E-E

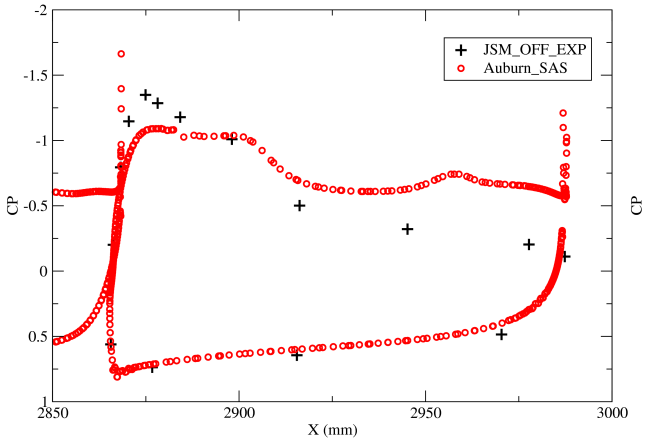

Flap G-G

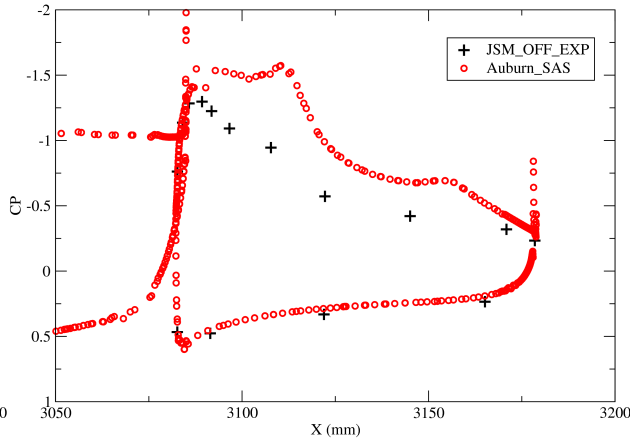

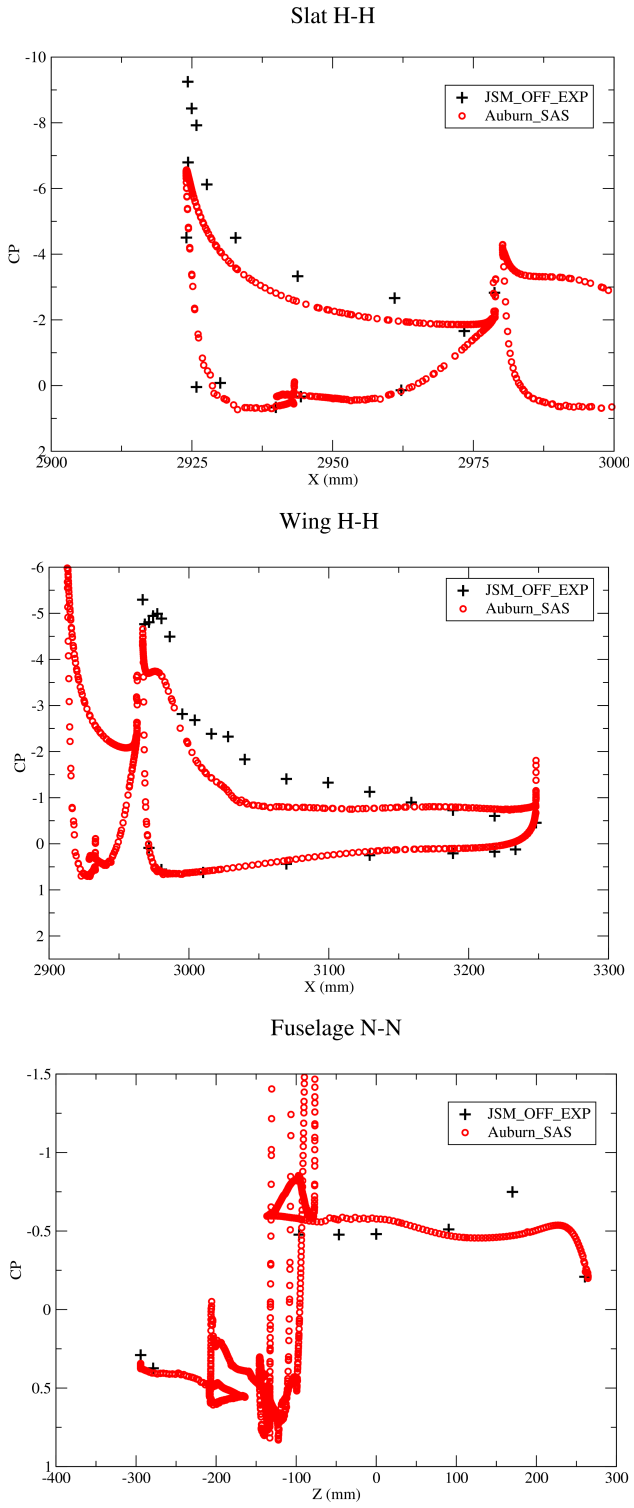

Figure 5.39: JSM: JSM Nacelle/Pylon OFF Configuration with Incompressible Solver - C_P Comparison at AOA 21.57^0

Slat A-A

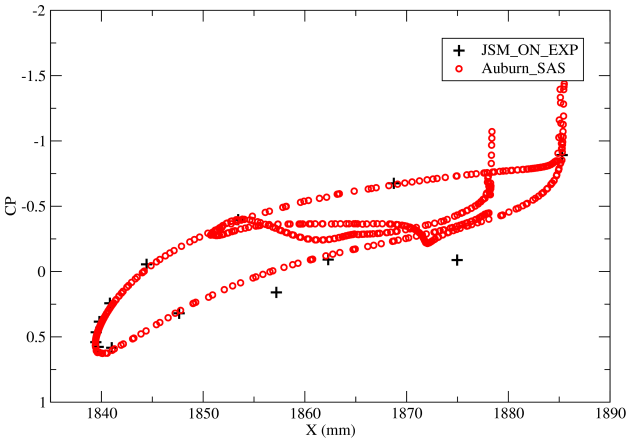

Slat B-B

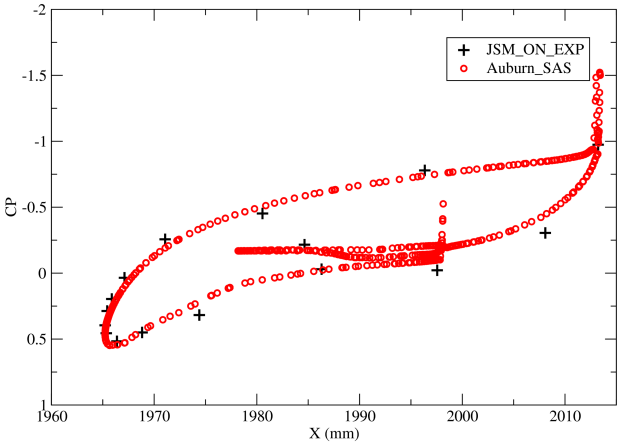

Wing A-A

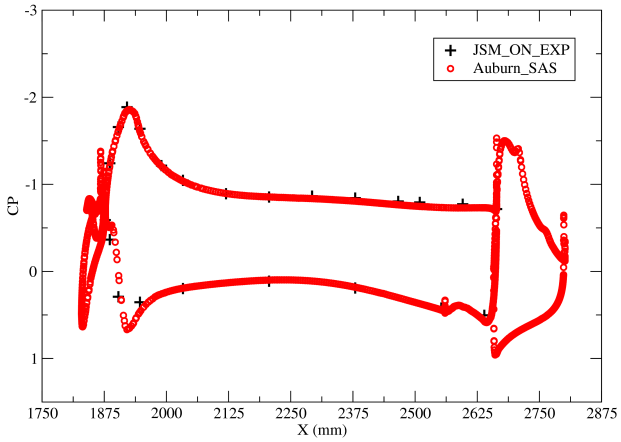

Wing B-B

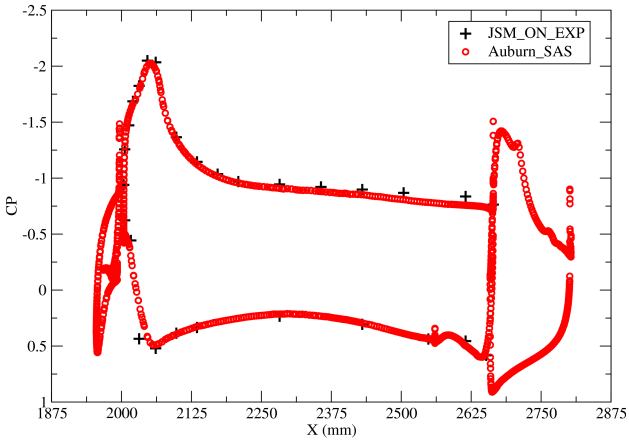

Flap A-A

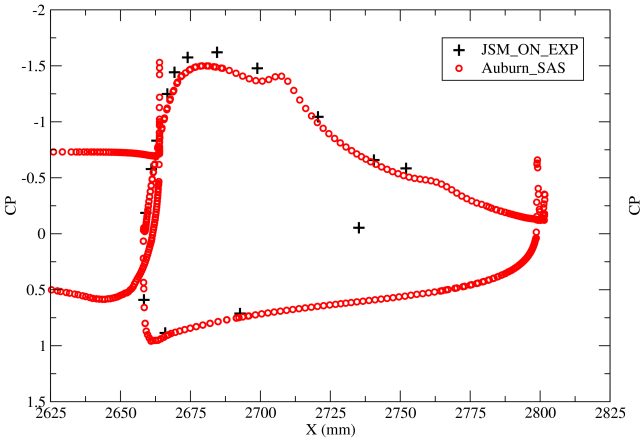

Flap B-B

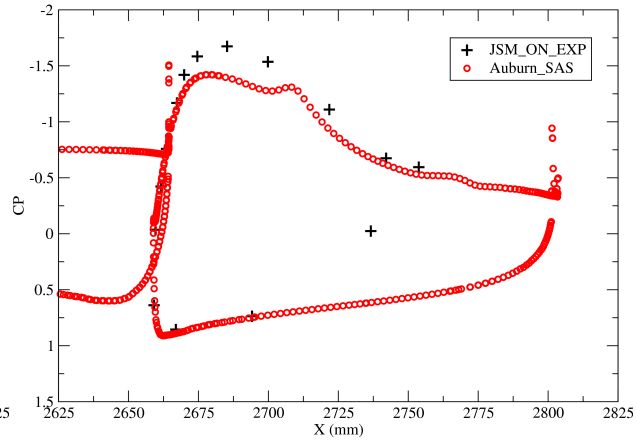

Slat D-D

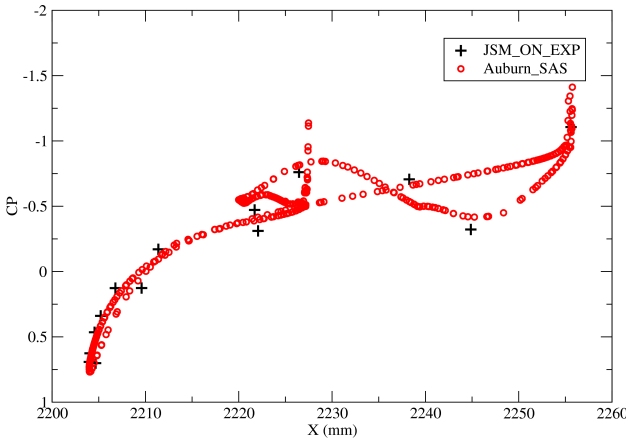

Wing C-C

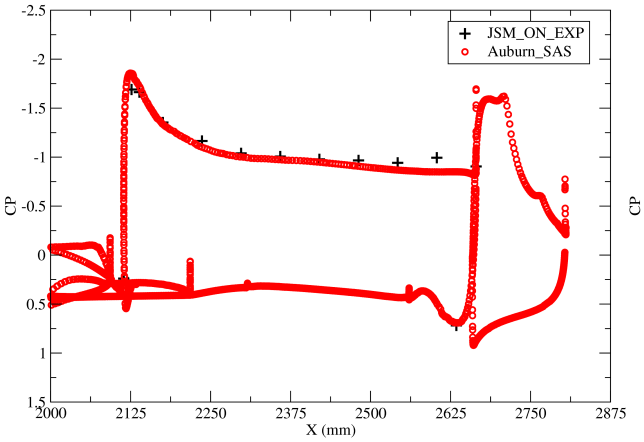

Wing D-D

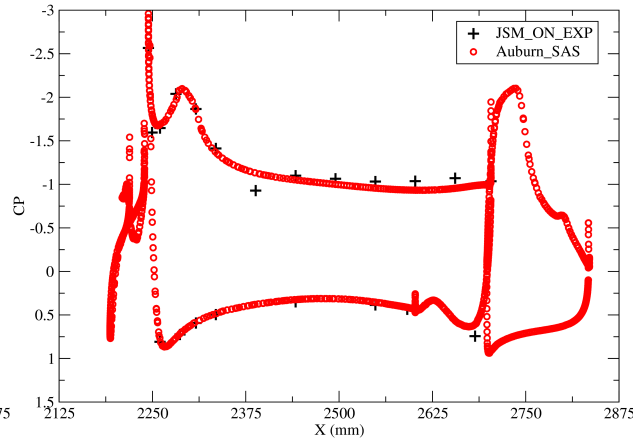

Flap C-C

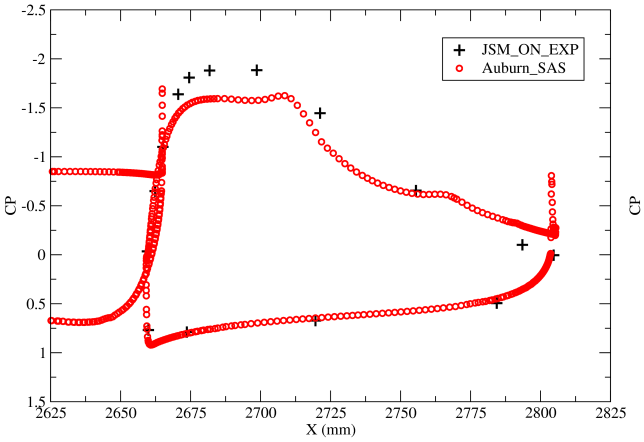

Flap D-D

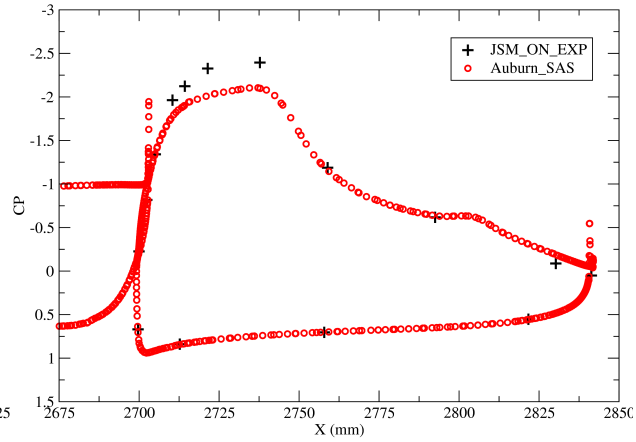

Slat E-E

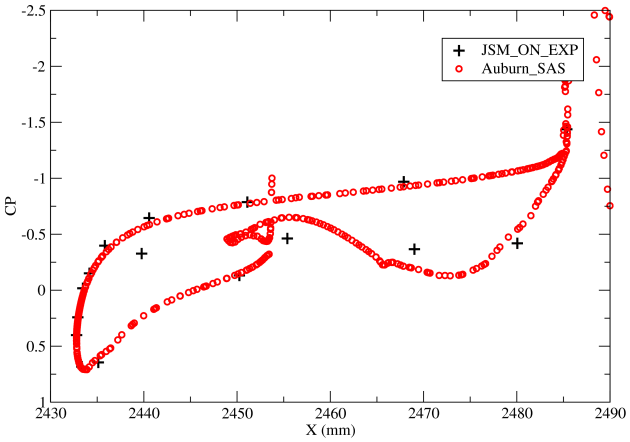

Slat G-G

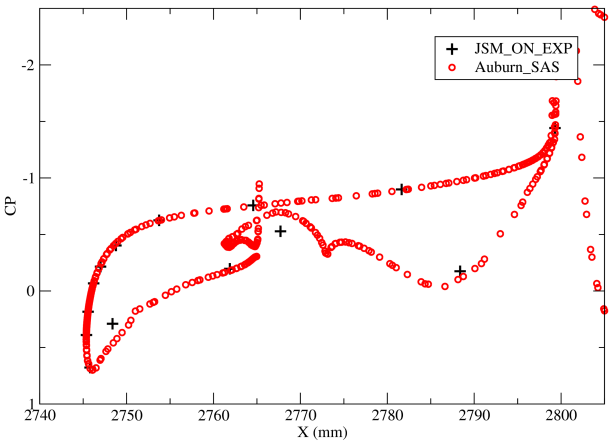

Wing E-E

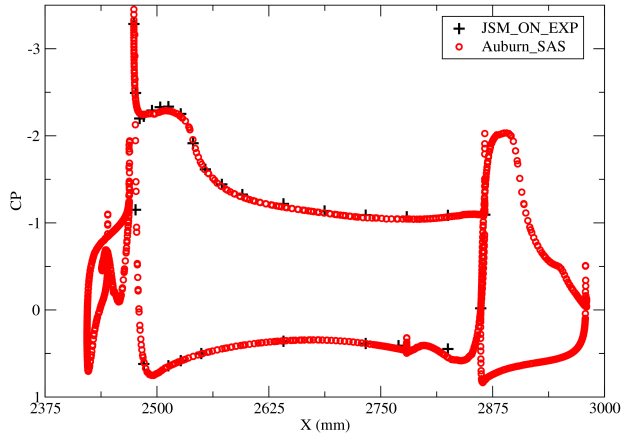

Wing G-G

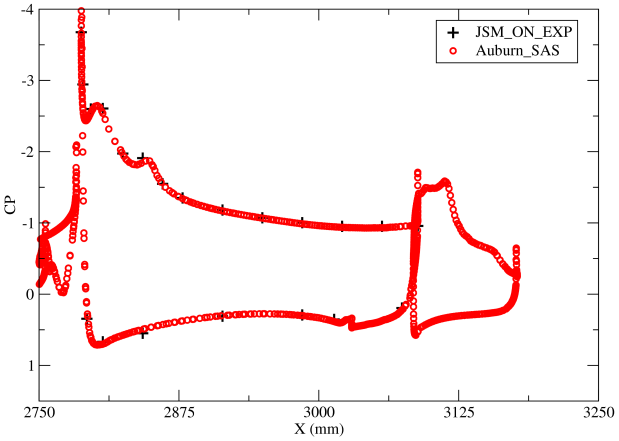

Flap E-E

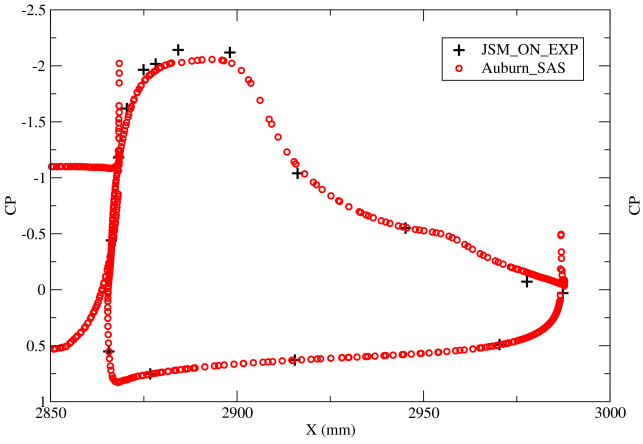

Flap G-G

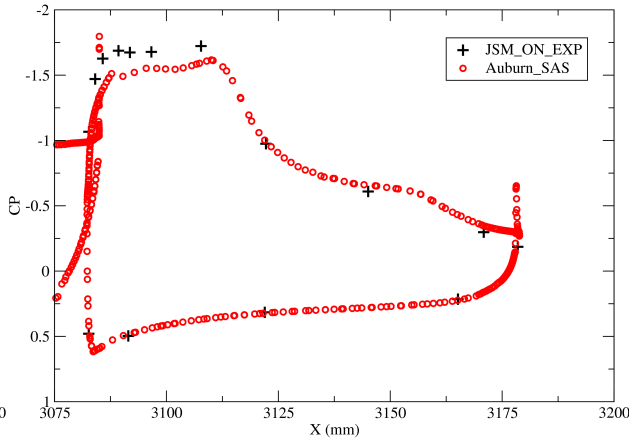

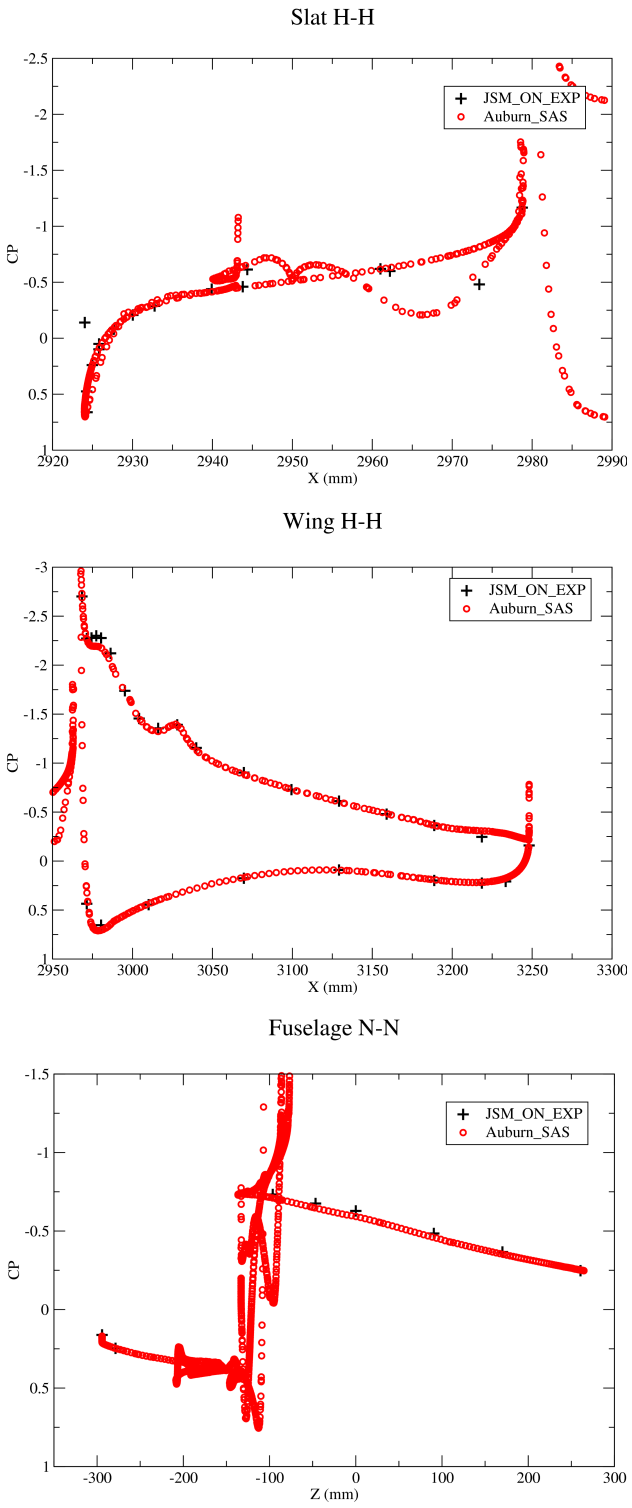

Figure 5.40: JSM: JSM Nacelle/Pylon ON Configuration with Incompressible Solver - C_P Comparison at AOA 4.36^0

Slat A-A

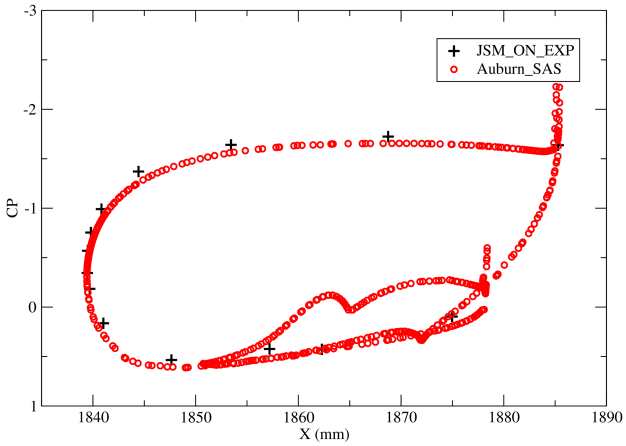

Slat B-B

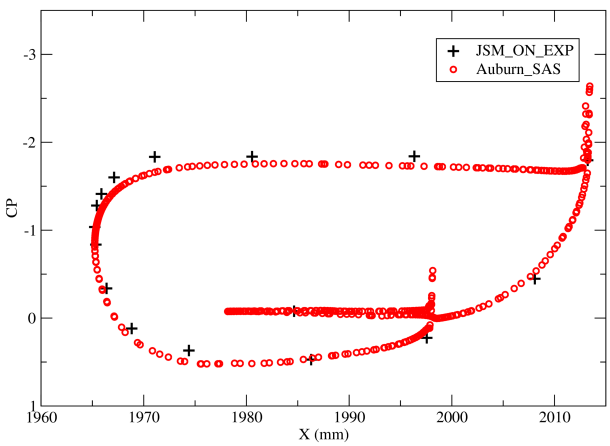

Wing A-A

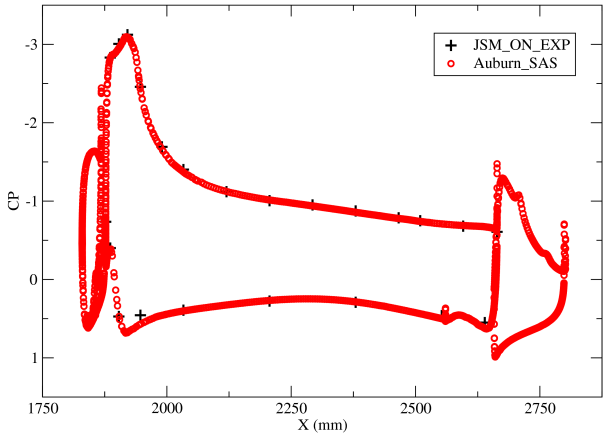

Wing B-B

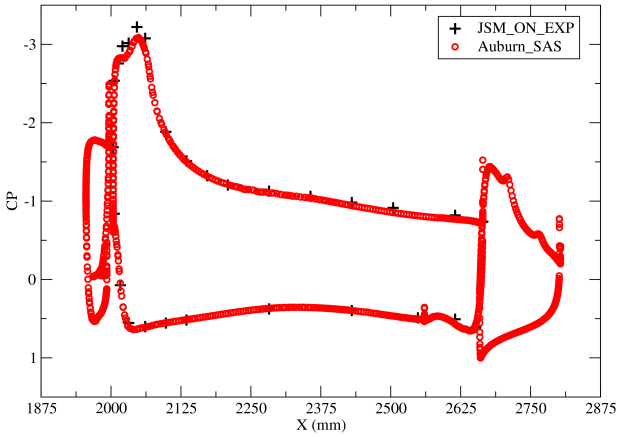

Flap A-A

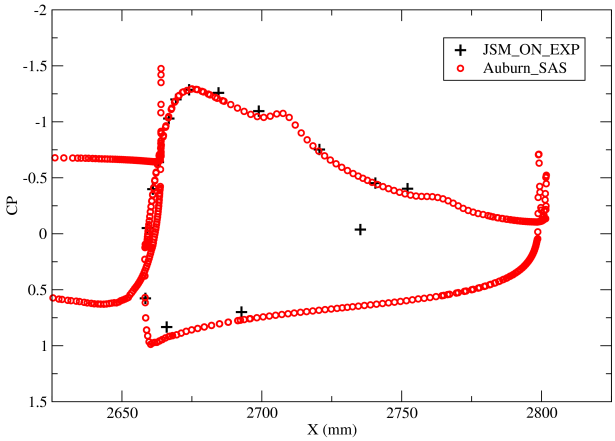

Flap B-B

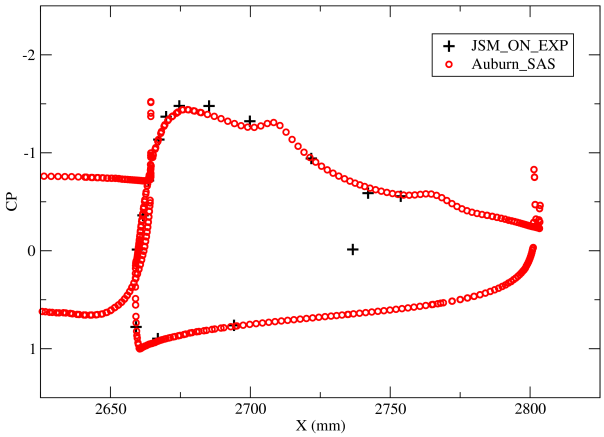

Slat D-D

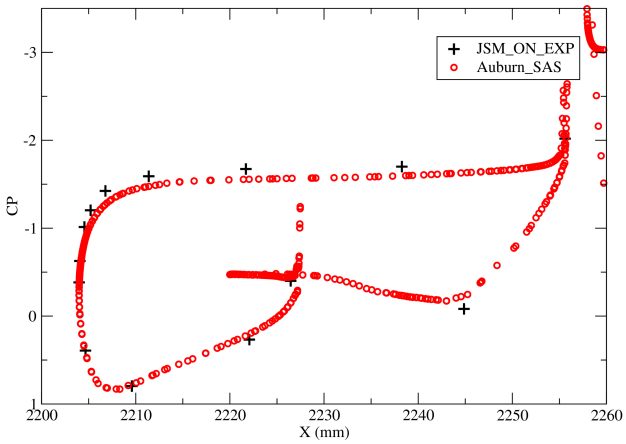

Wing C-C

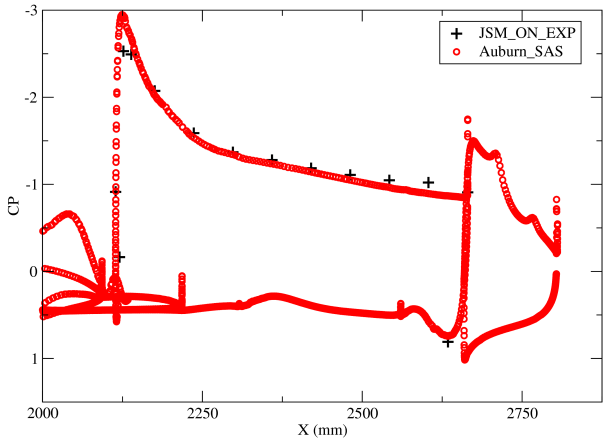

Wing D-D

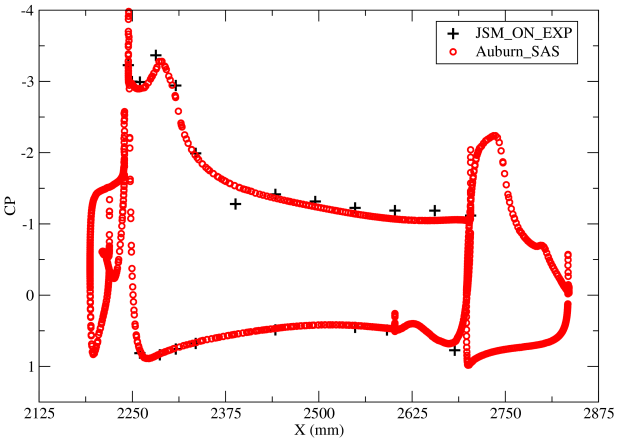

Flap C-C

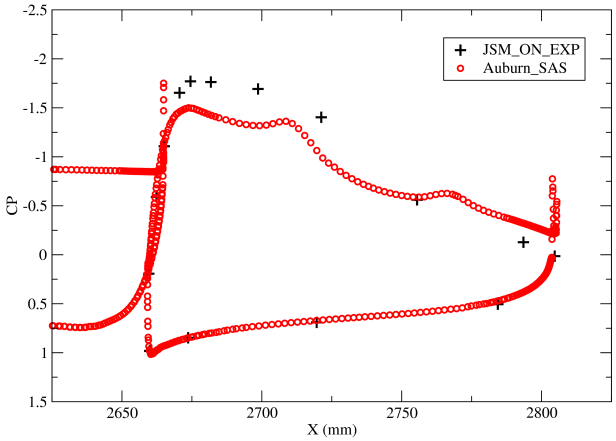

Flap D-D

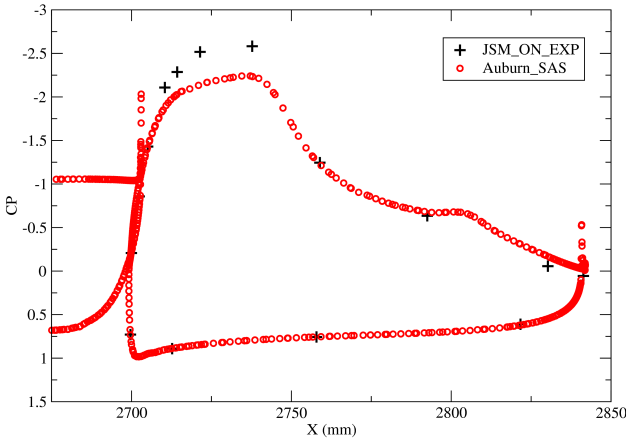

Slat E-E

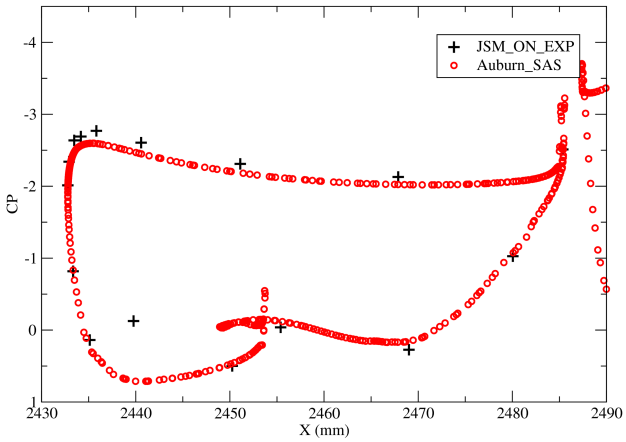

Slat G-G

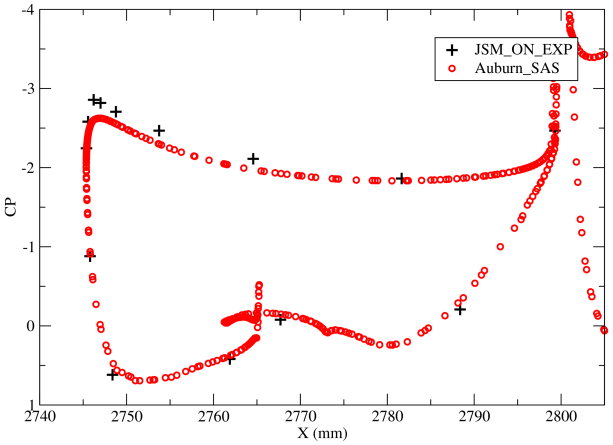

Wing E-E

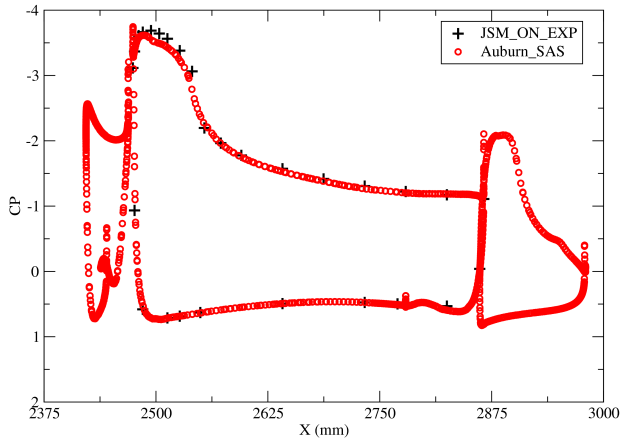

Wing G-G

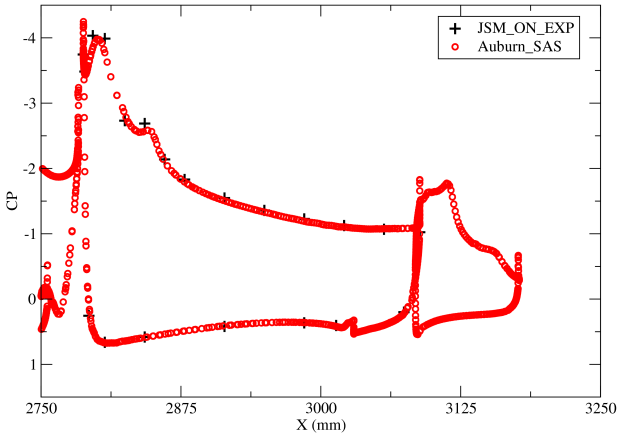

Flap E-E

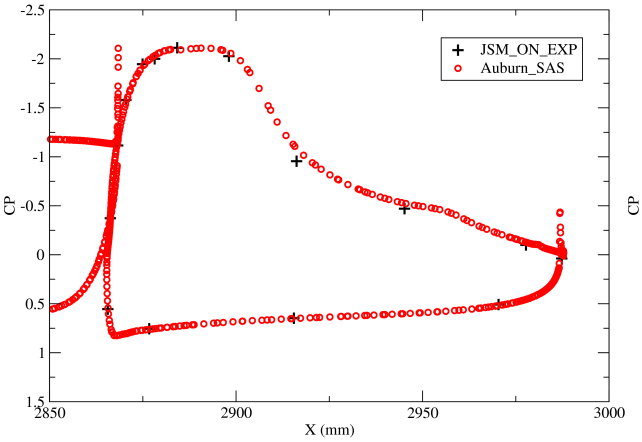

Flap G-G

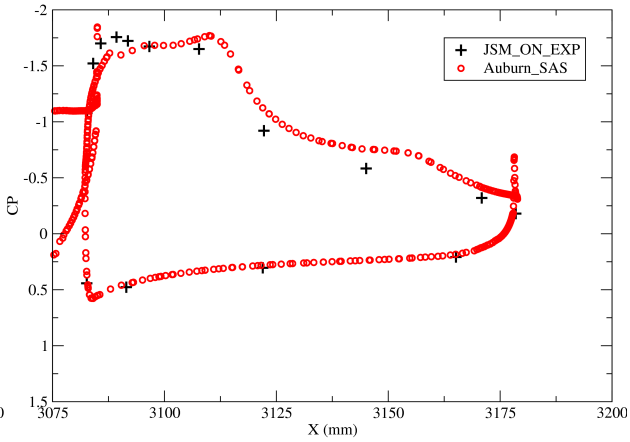

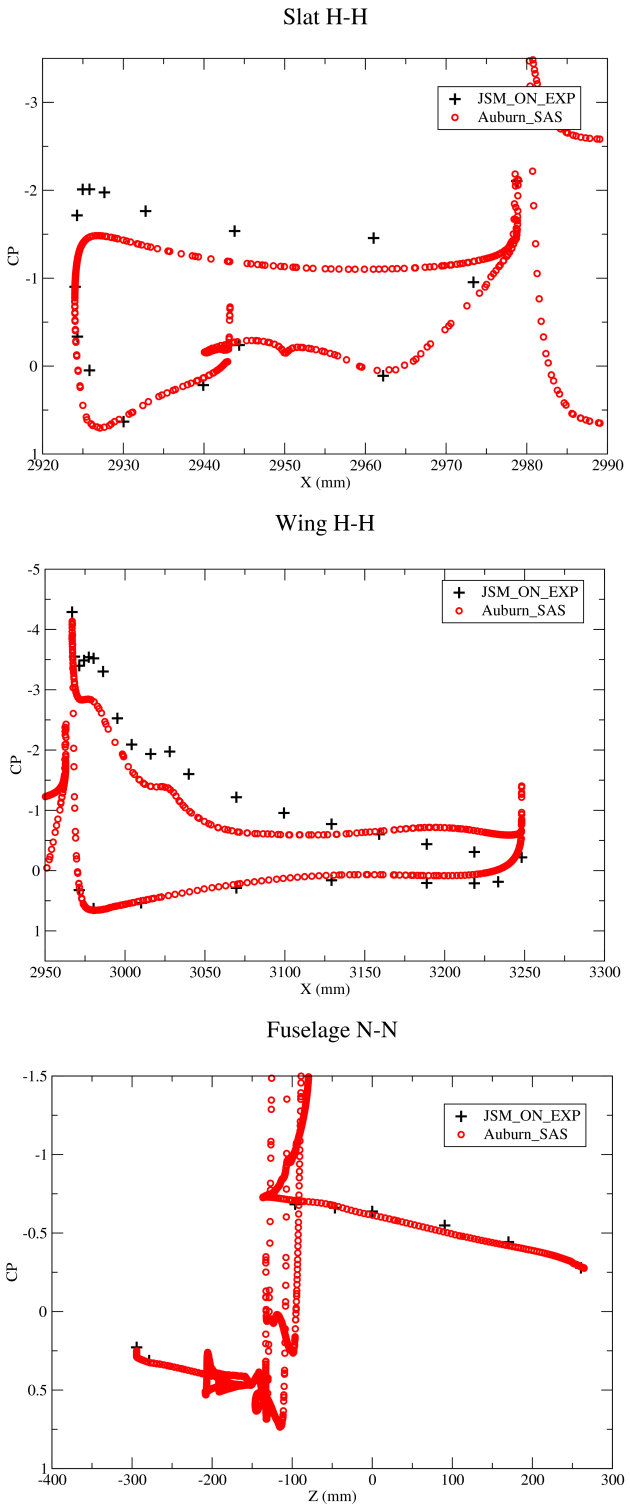

Figure 5.41: JSM: JSM Nacelle/Pylon ON Configuration with Incompressible Solver - C_P Comparison at AOA 10.47^0

Slat A-A

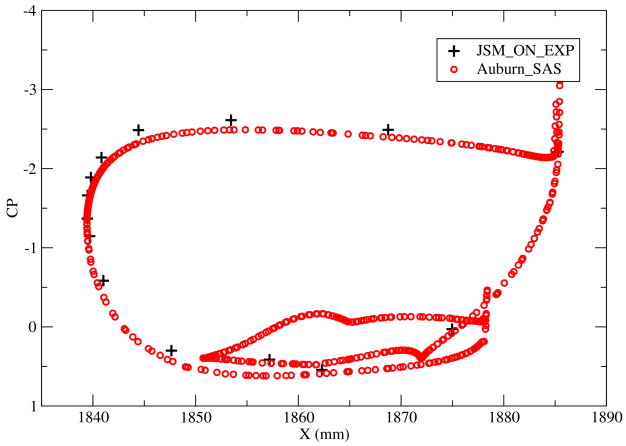

Slat B-B

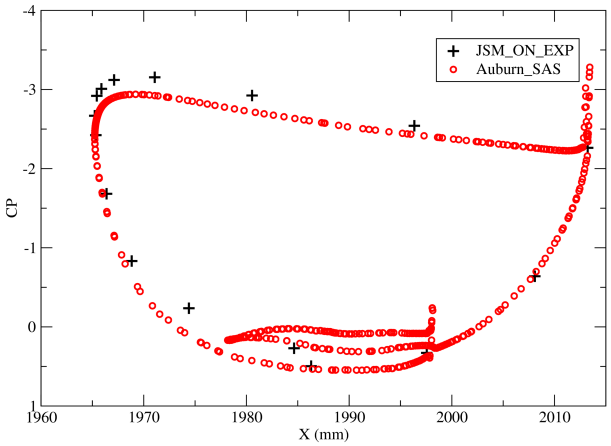

Wing A-A

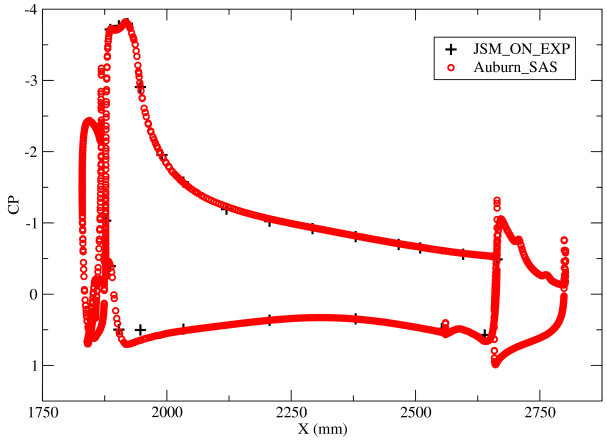

Wing B-B

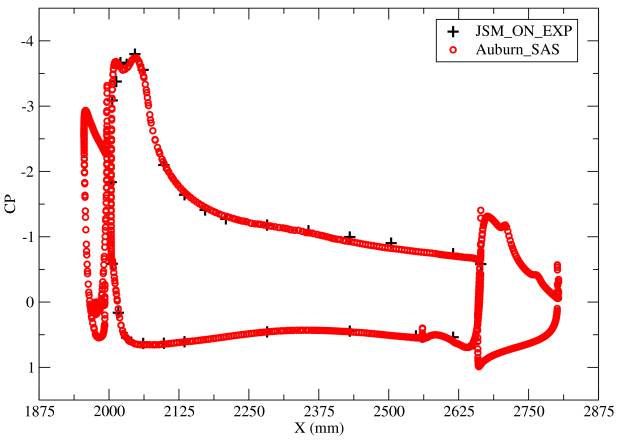

Flap A-A

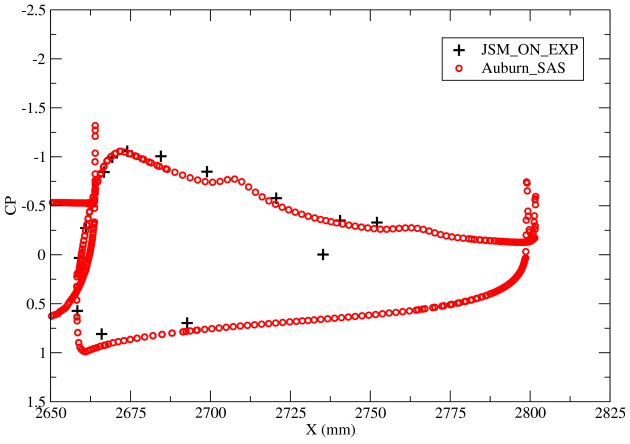

Flap B-B

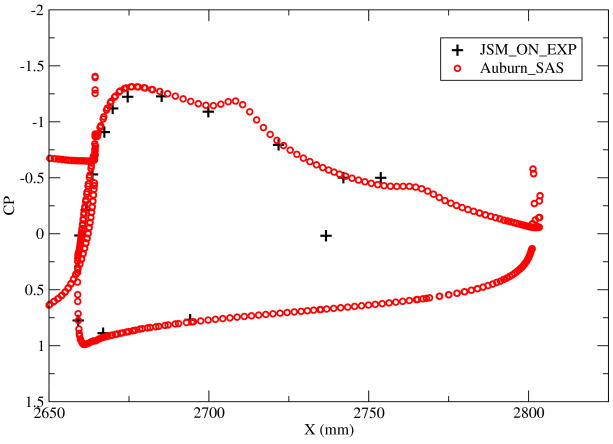

Slat D-D

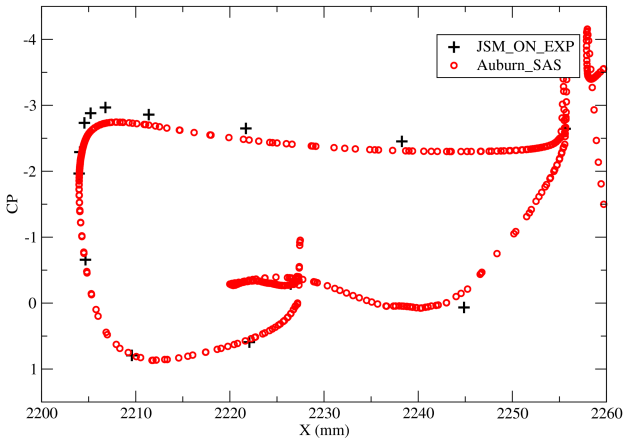

Wing C-C

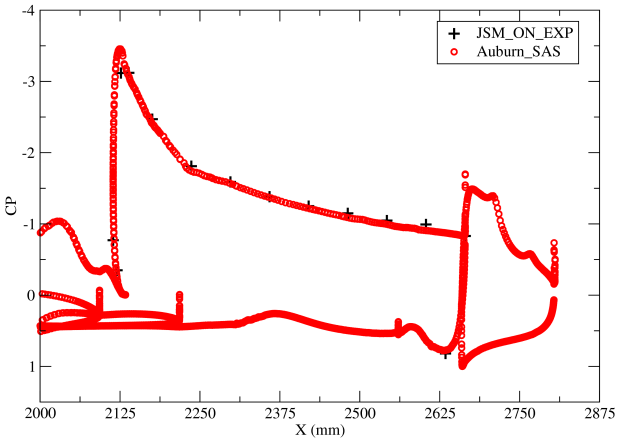

Wing D-D

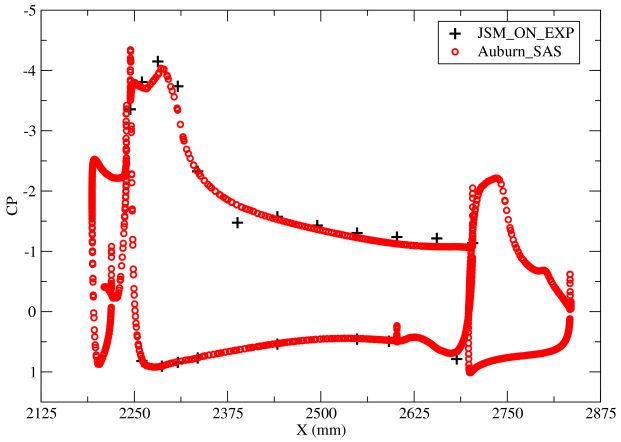

Flap C-C

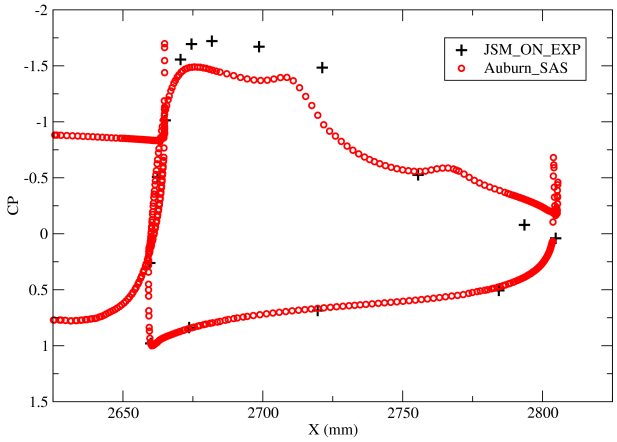

Flap D-D

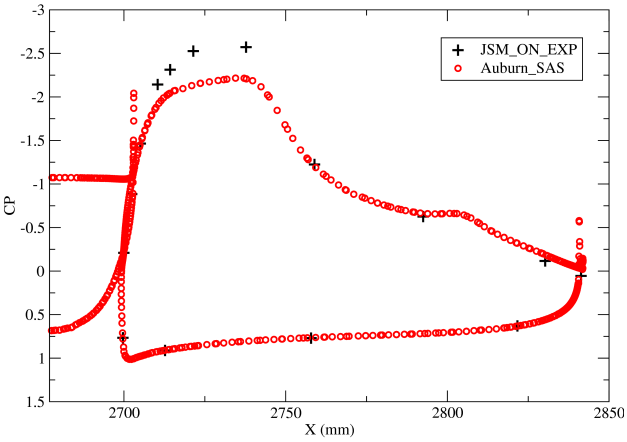

Slat E-E

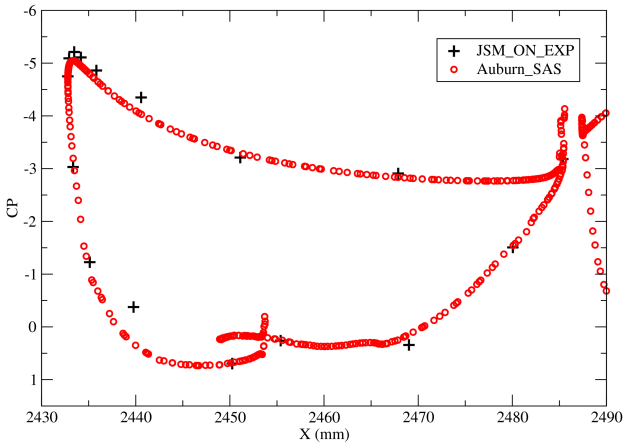

Slat G-G

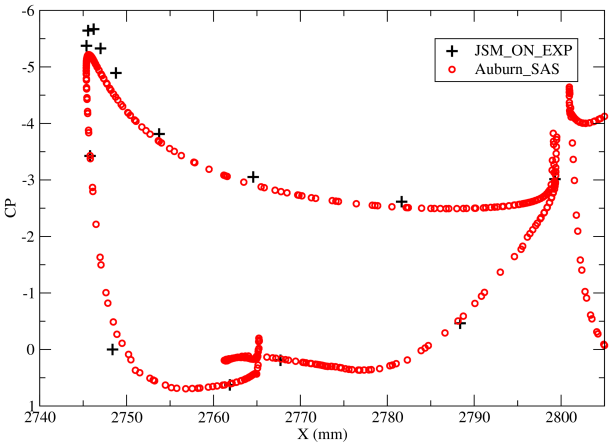

Wing E-E

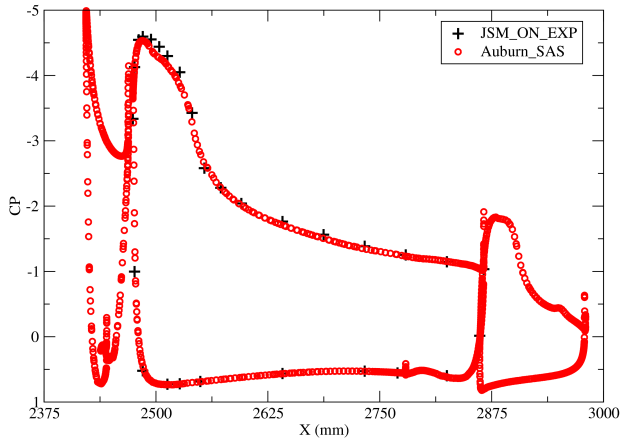

Wing G-G

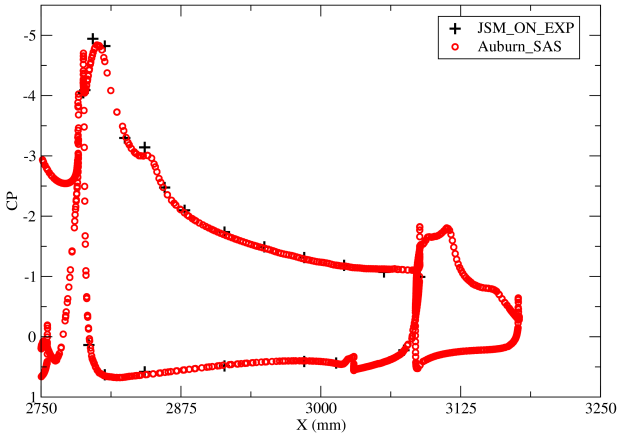

Flap E-E

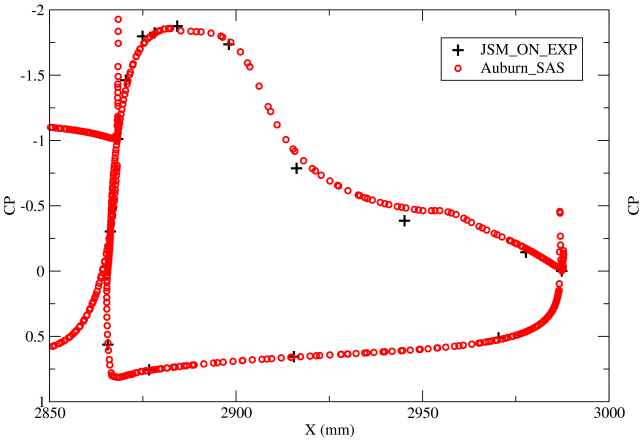

Flap G-G

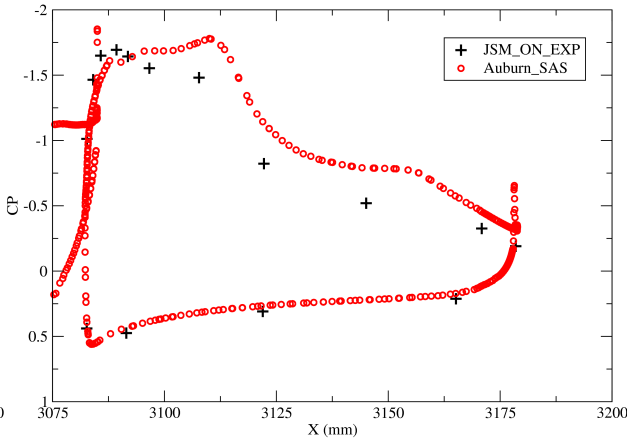

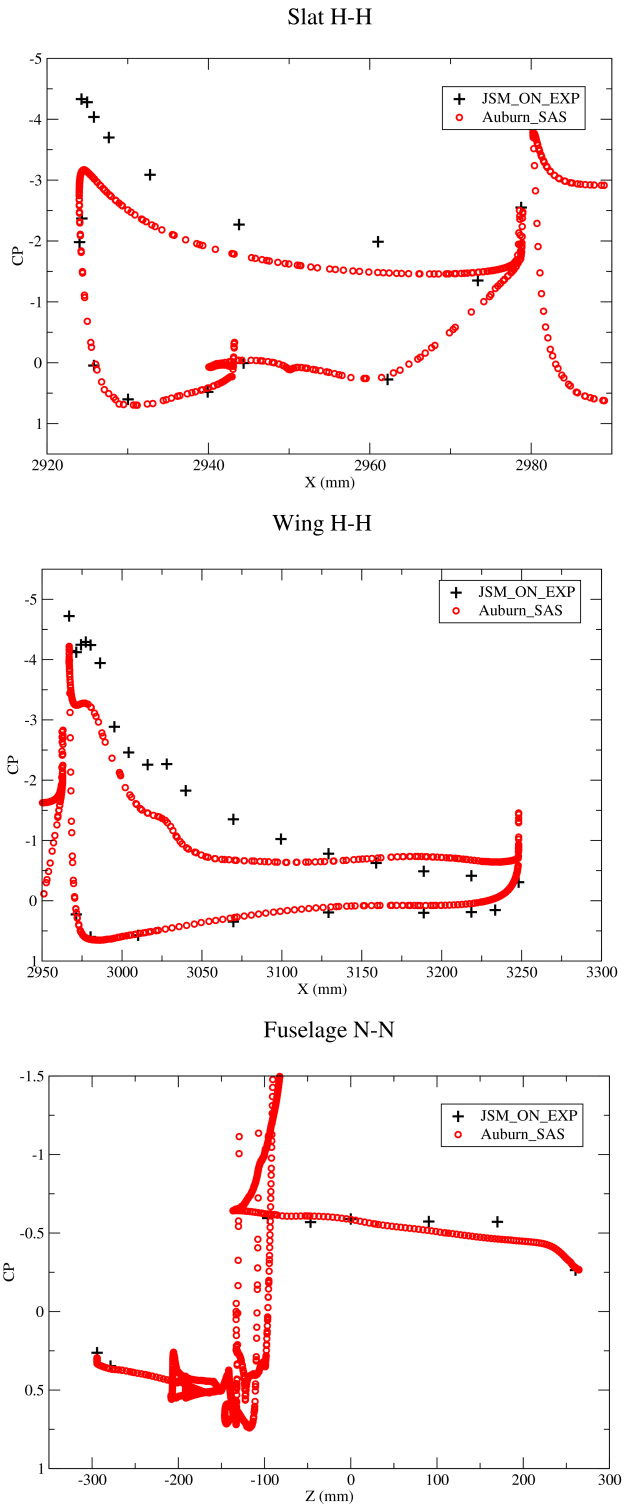

Figure 5.42: JSM: JSM Nacelle/Pylon ON Configuration with Incompressible Solver - C_P Comparison at AOA 14.54^0

Slat A-A

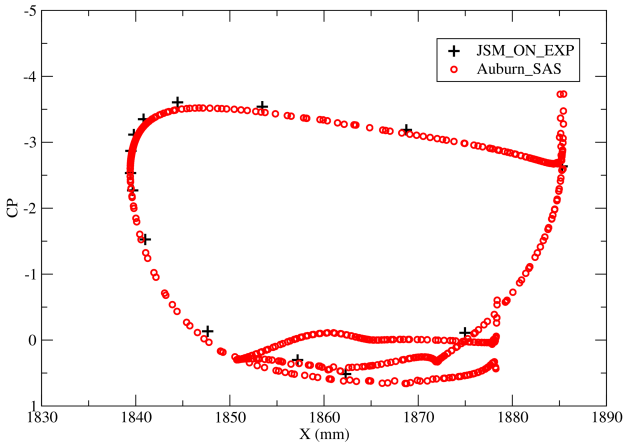

Slat B-B

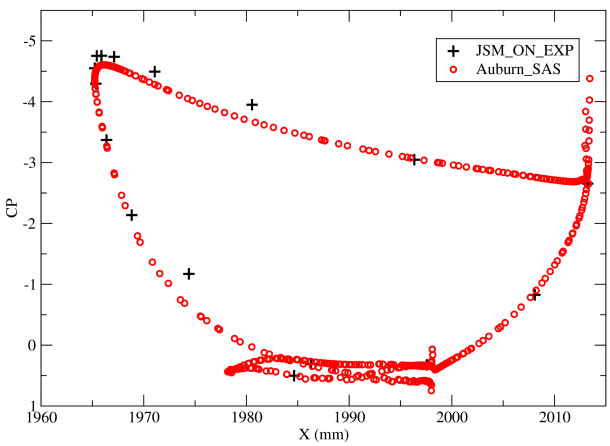

Wing A-A

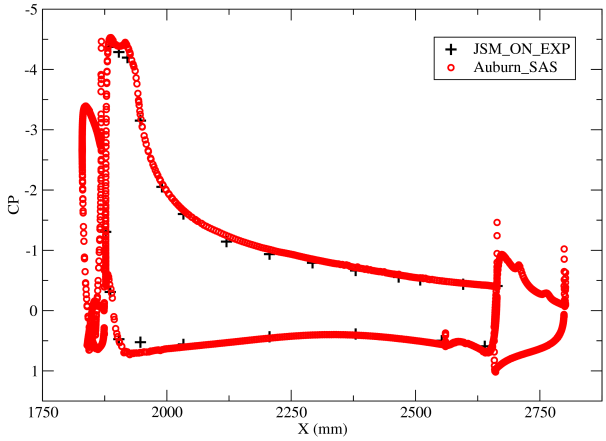

Wing B-B

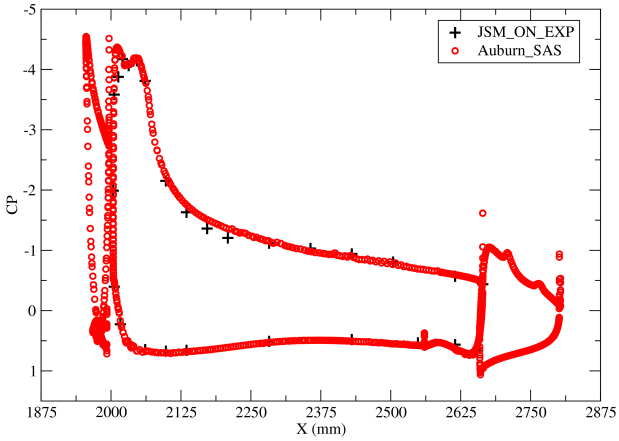

Flap A-A

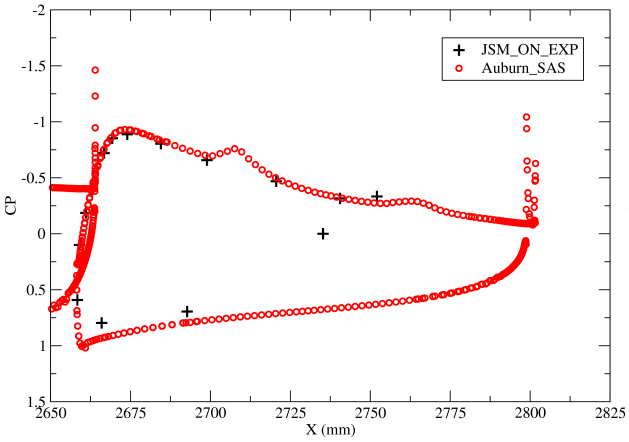

Flap B-B

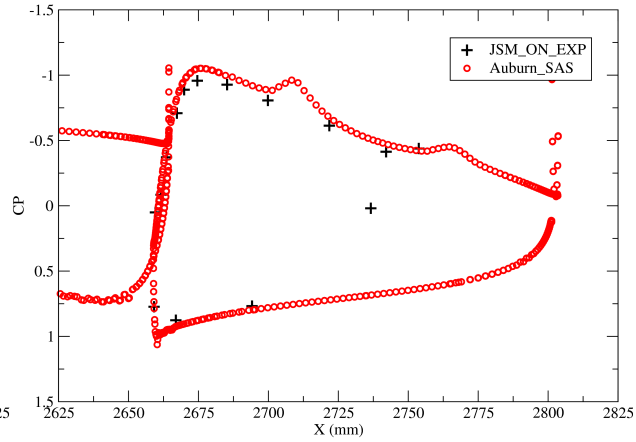

Slat D-D

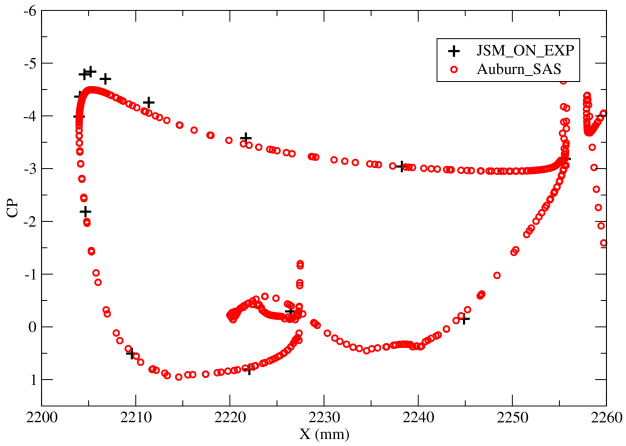

Wing C-C

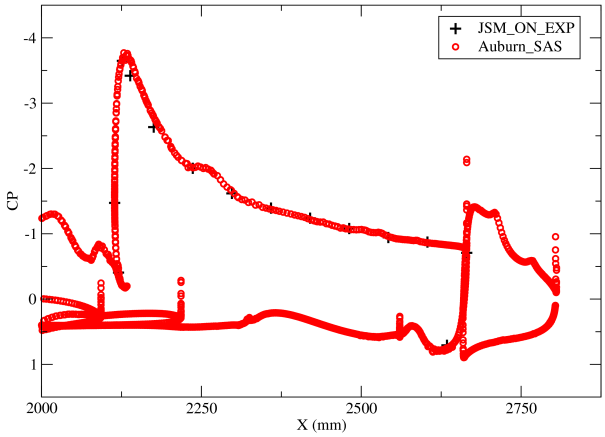

Wing D-D

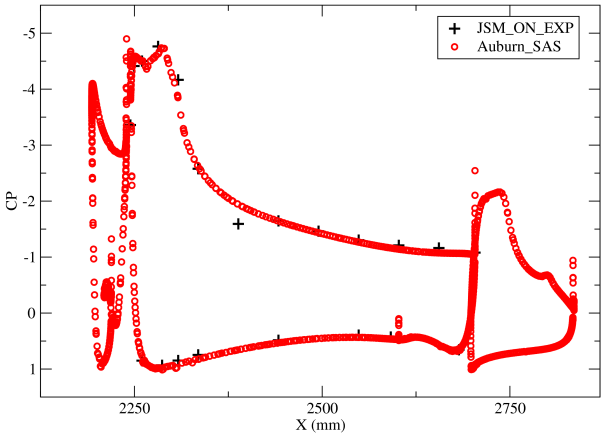

Flap C-C

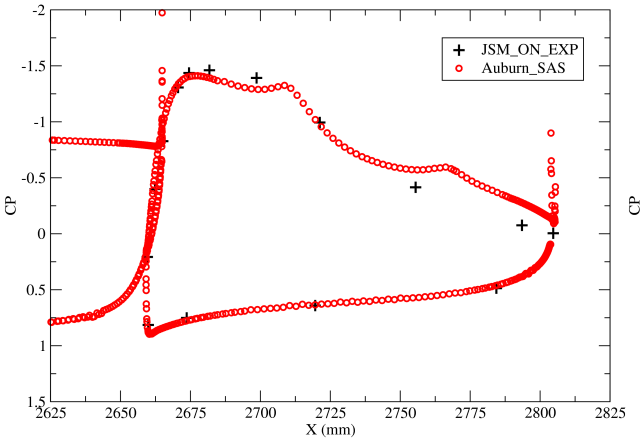

Flap D-D

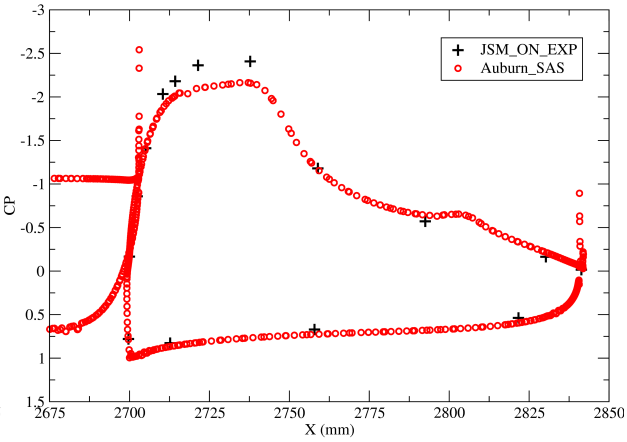

Slat E-E

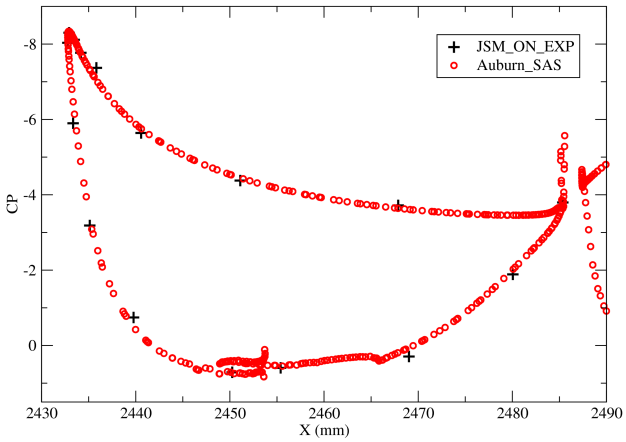

Slat G-G

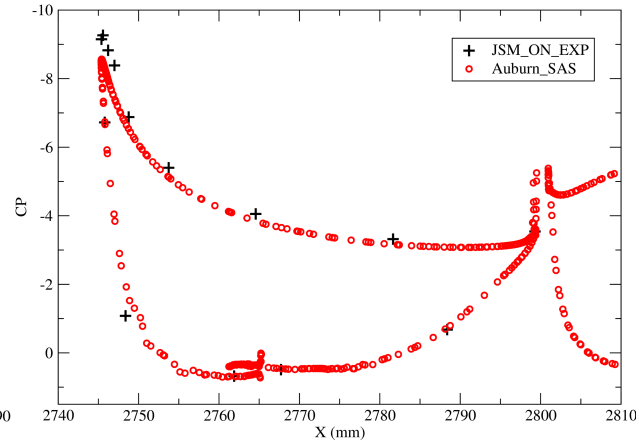

Wing E-E

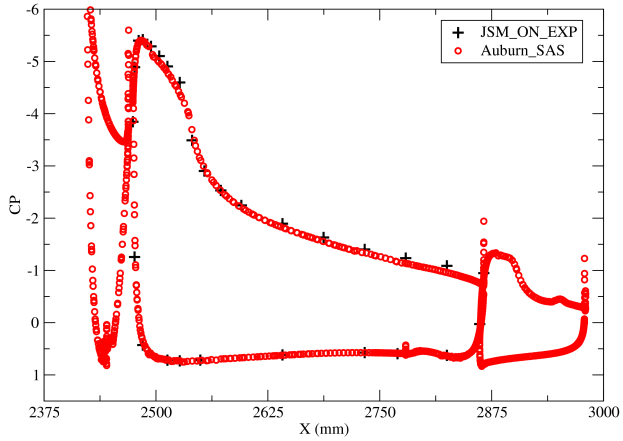

Wing G-G

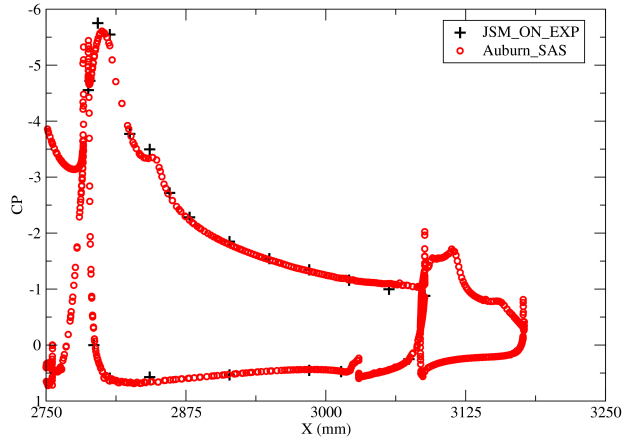

Flap E-E

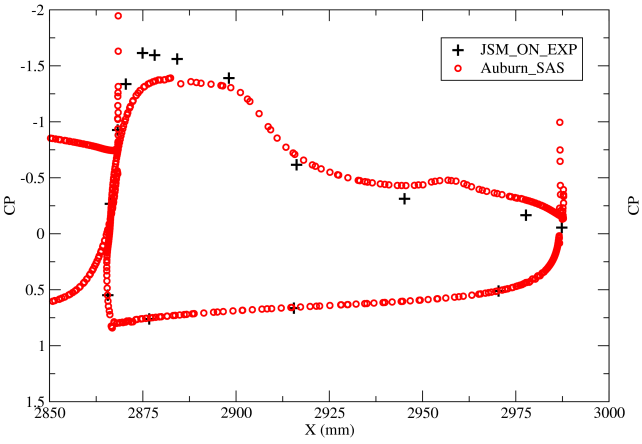

Flap G-G

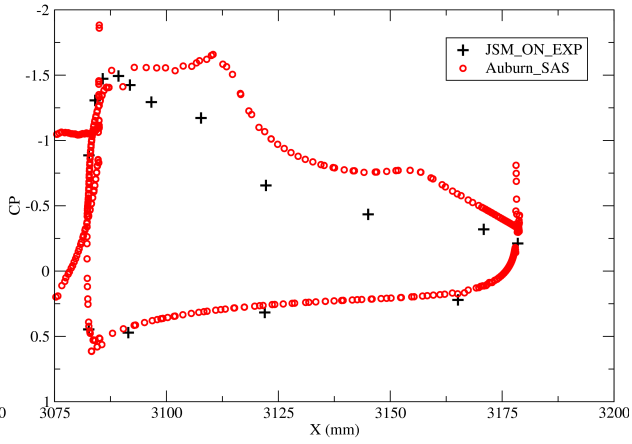

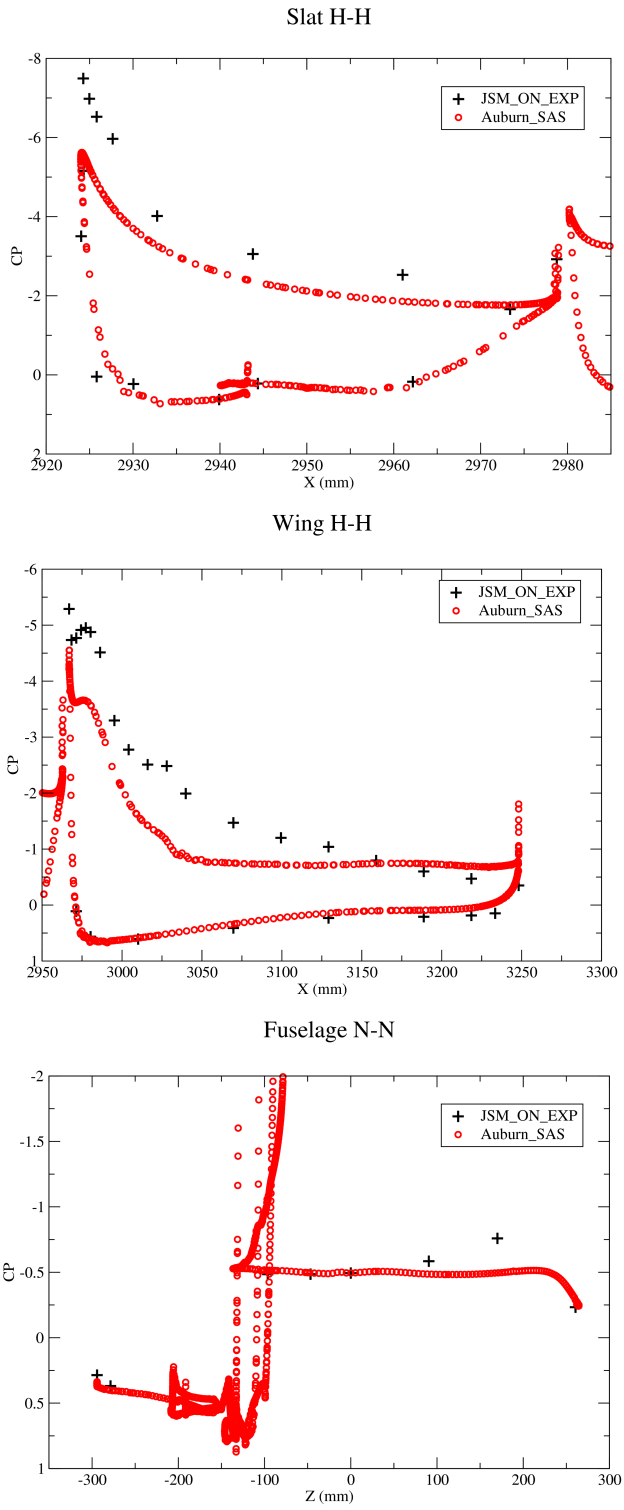

Figure 5.43: JSM: JSM Nacelle/Pylon ON Configuration with Incompressible Solver - C_P Comparison at AOA 18.58^0

Slat A-A

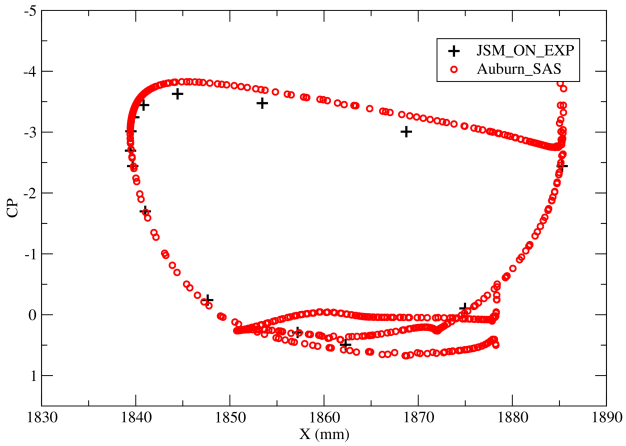

Slat B-B

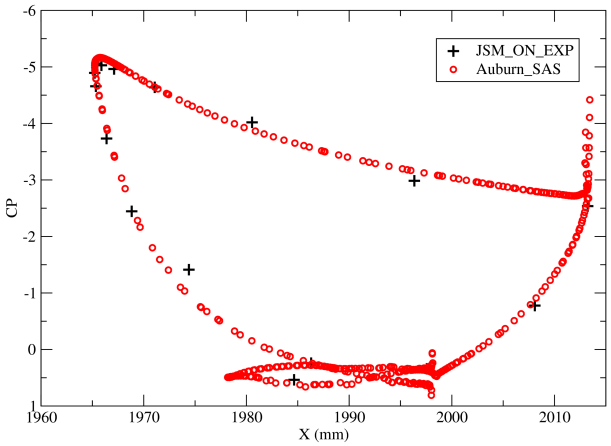

Wing A-A

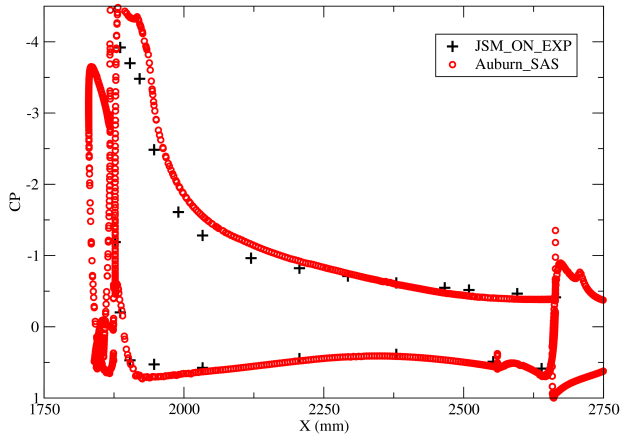

Wing B-B

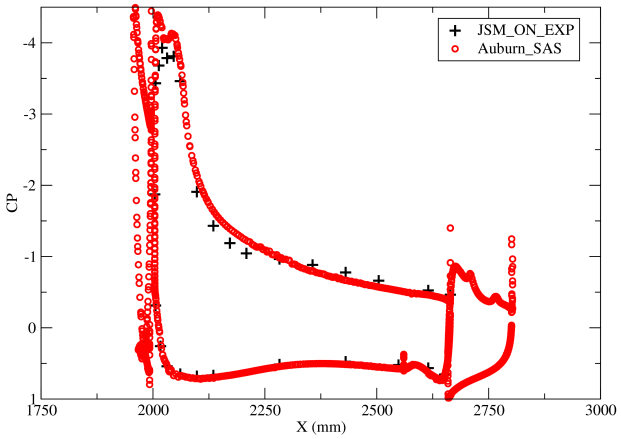

Flap A-A

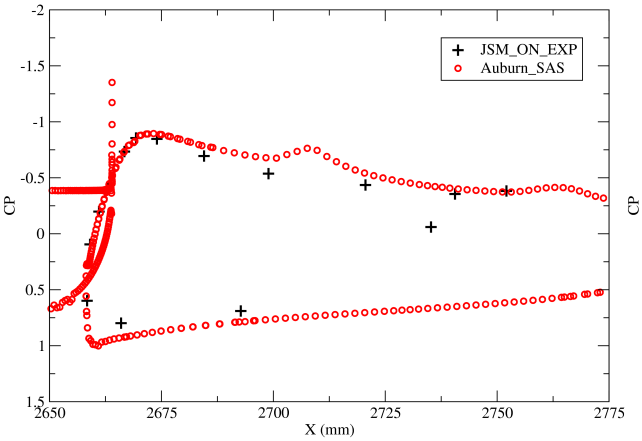

Flap B-B

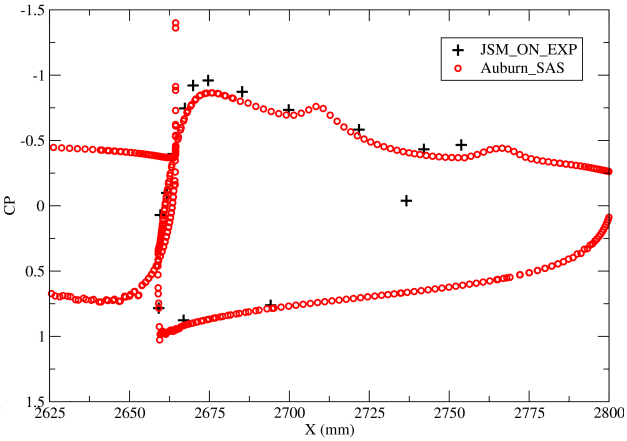

Slat D-D

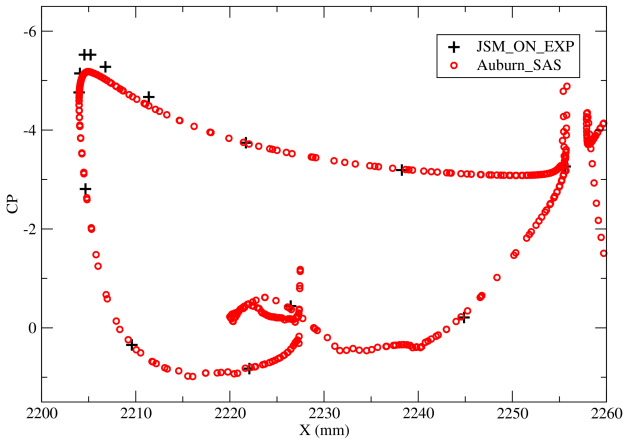

Wing C-C

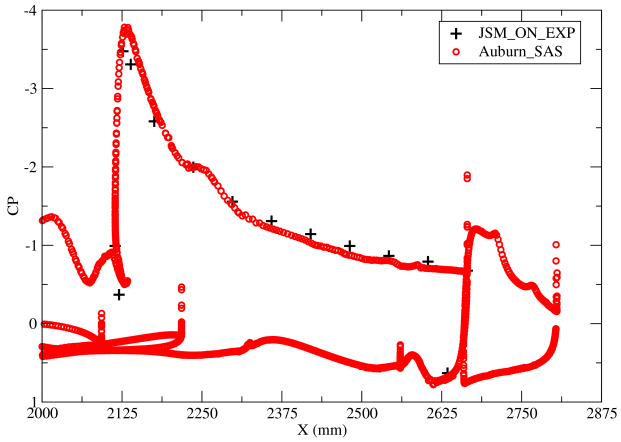

Wing D-D

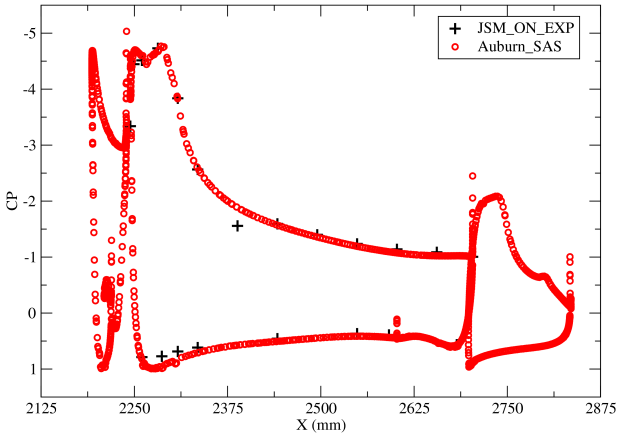

Flap C-C

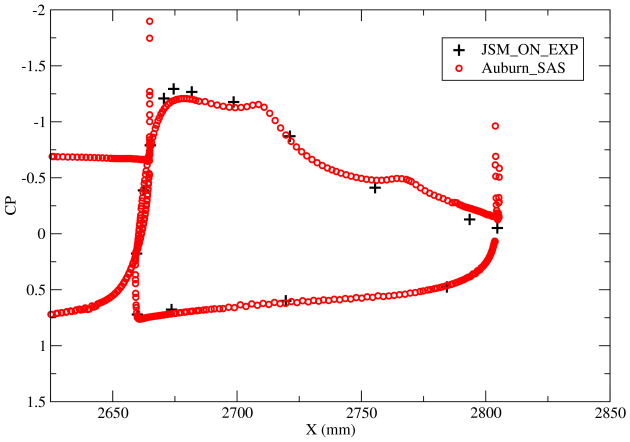

Flap D-D

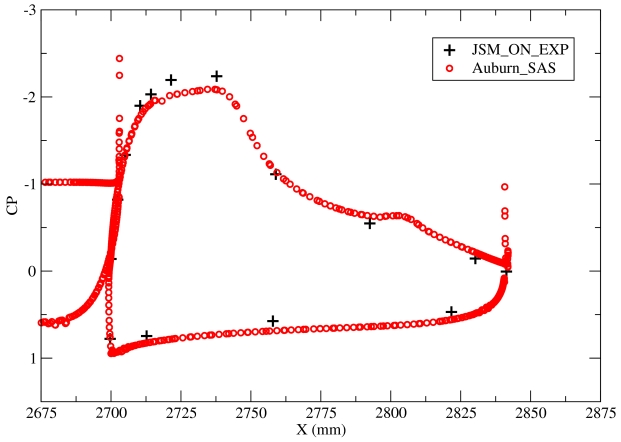

Slat E-E

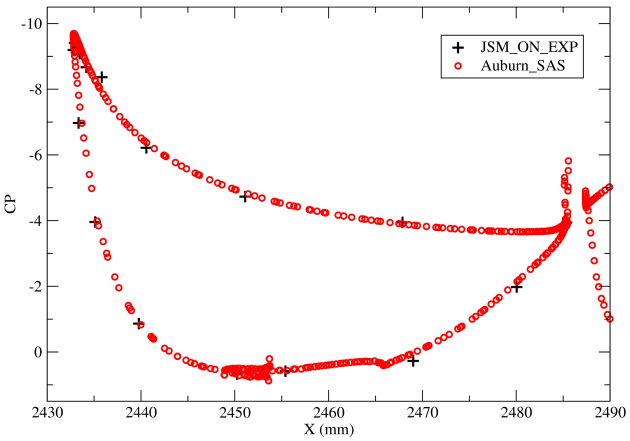

Slat G-G

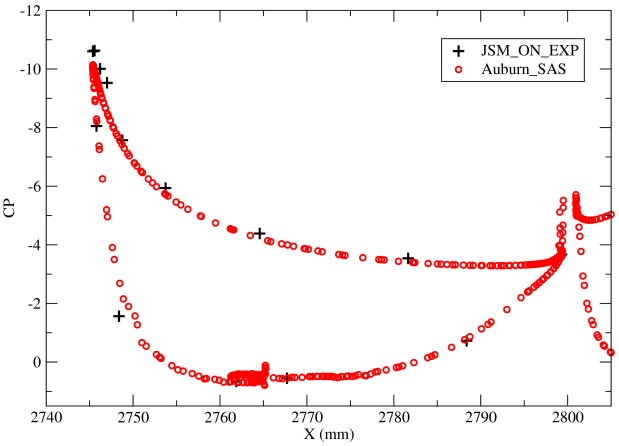

Wing E-E

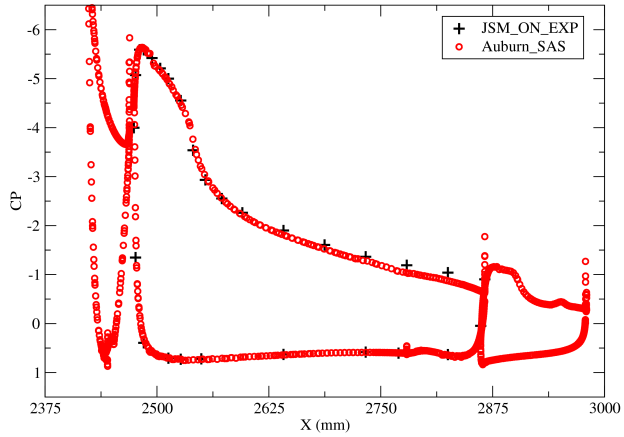

Wing G-G

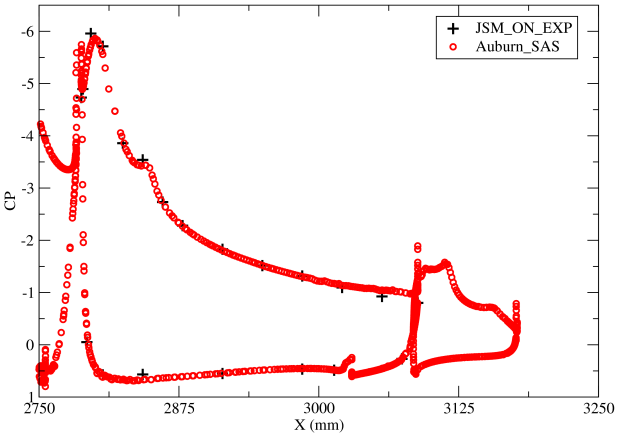

Flap E-E

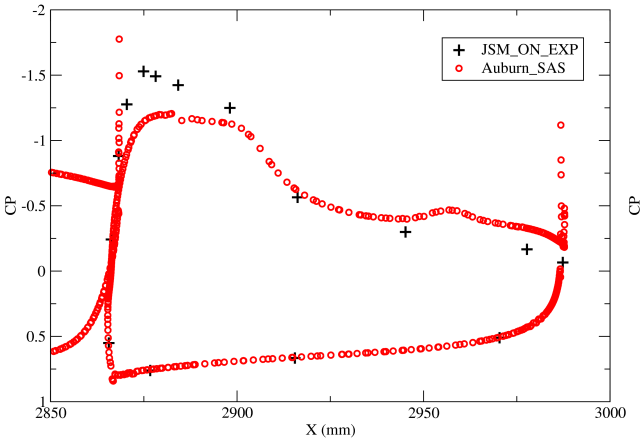

Flap G-G

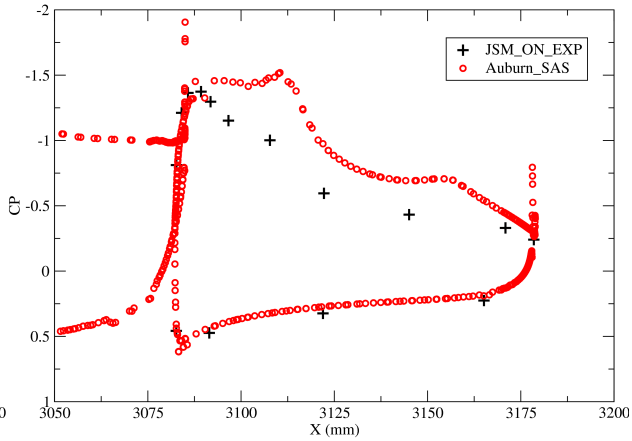

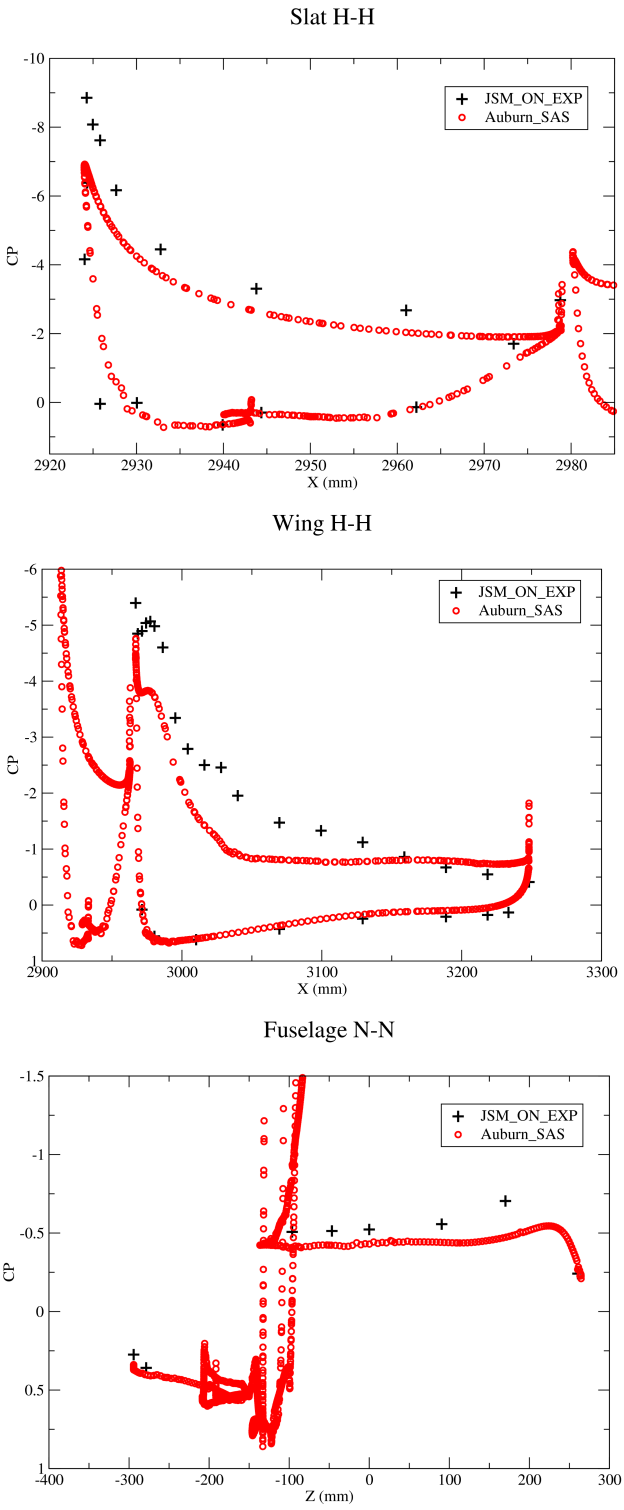

Figure 5.44: JSM: JSM Nacelle/Pylon ON Configuration with Incompressible Solver - C_P Comparison at AOA 20.59^0

Slat A-A

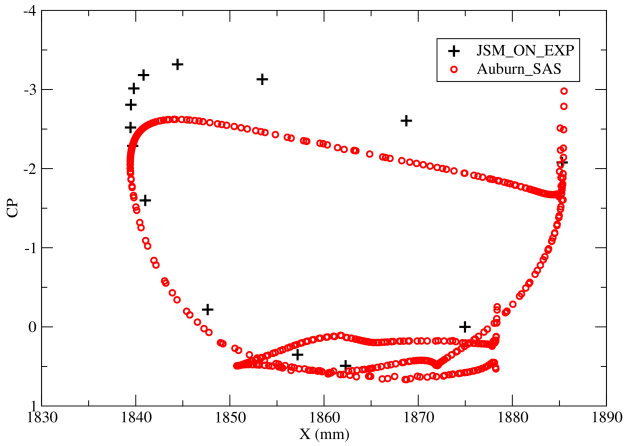

Slat B-B

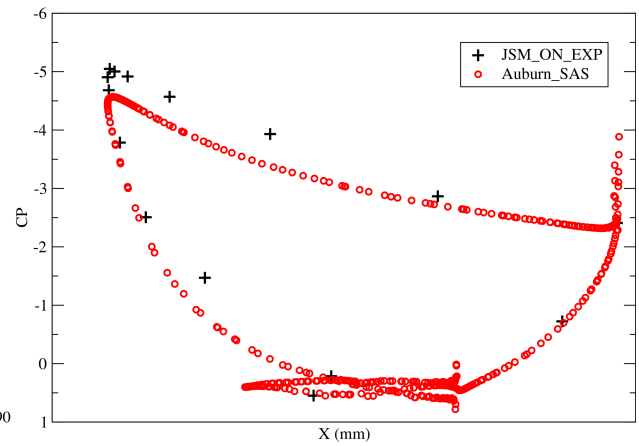

Wing A-A

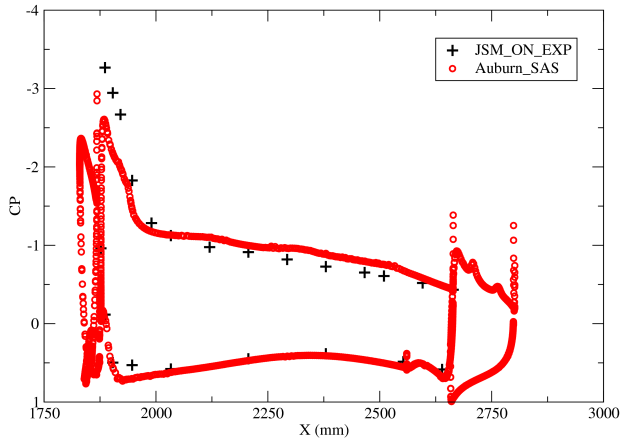

Wing B-B

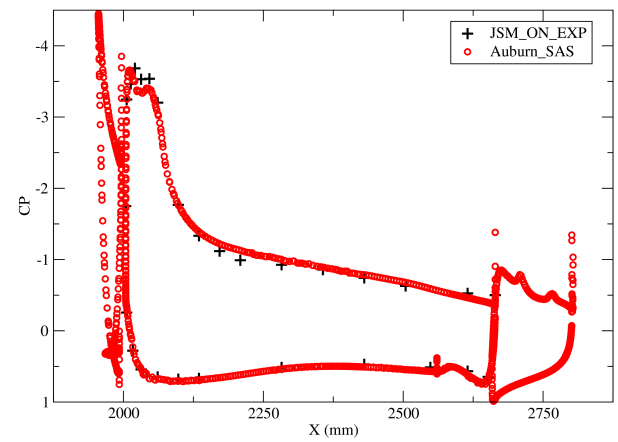

Flap A-A

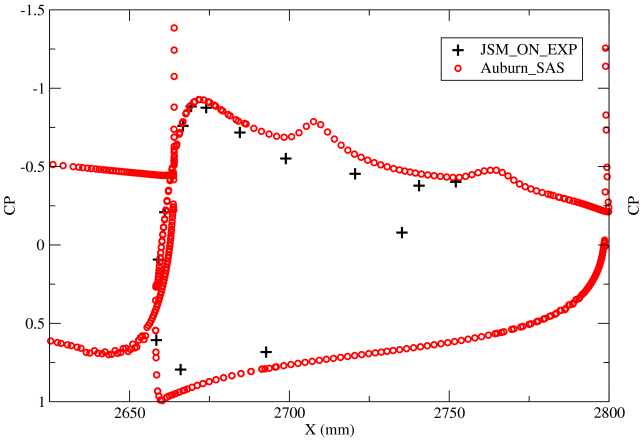

Flap B-B

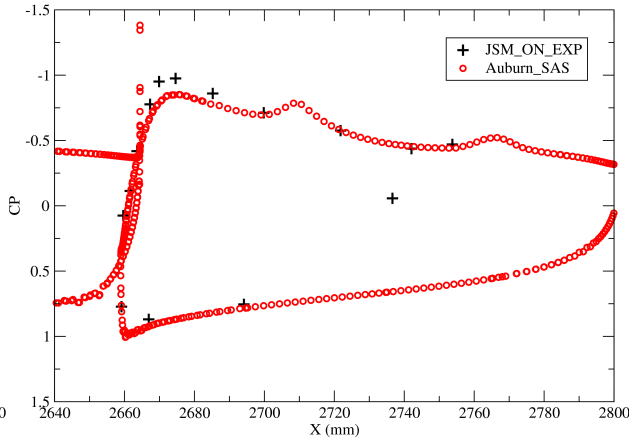

Slat D-D

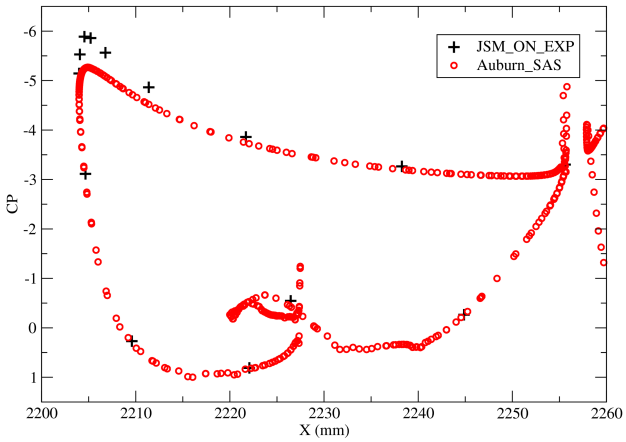

Wing C-C

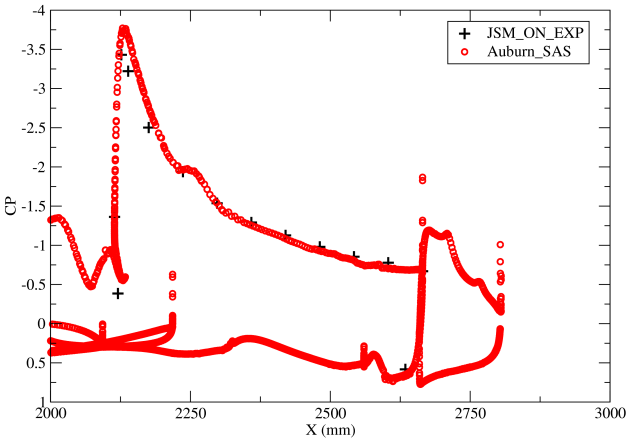

Wing D-D

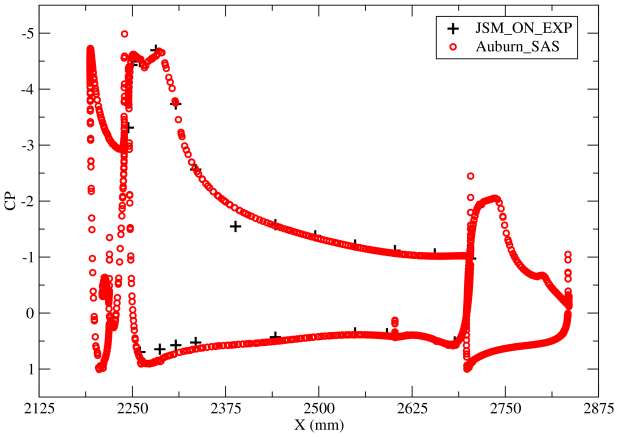

Flap C-C

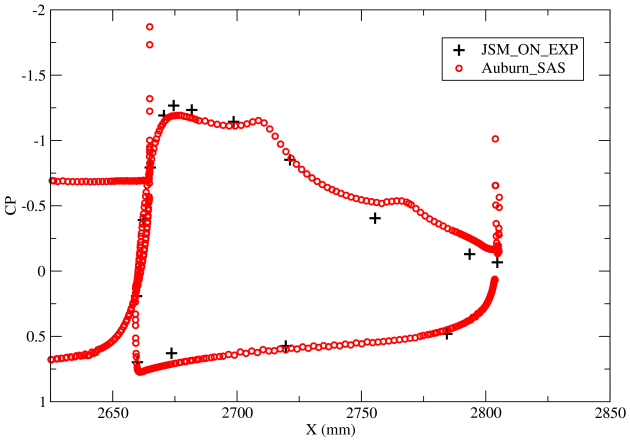

Flap D-D

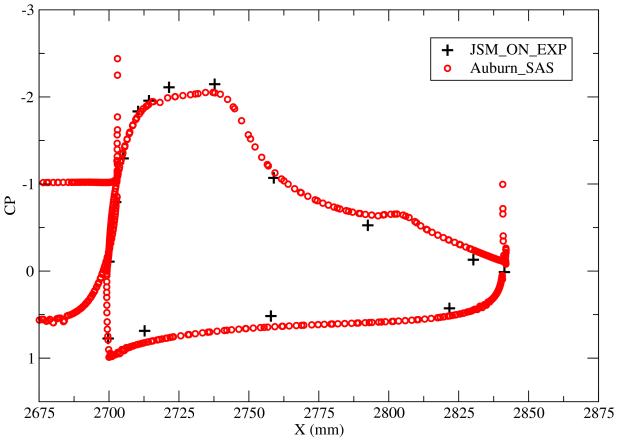

Slat E-E

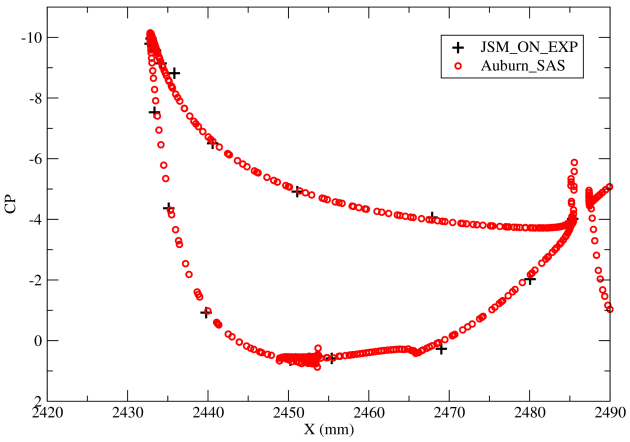

Slat G-G

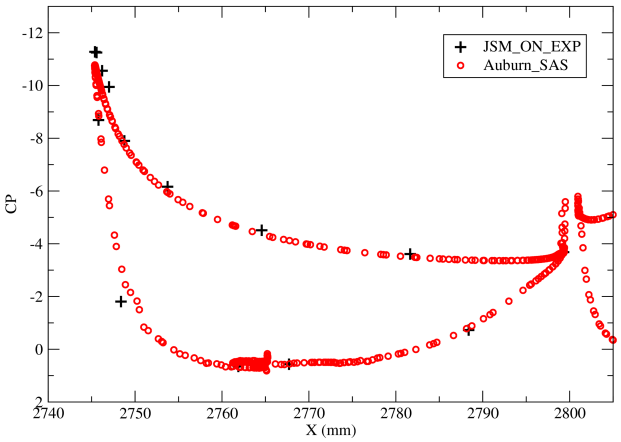

Wing E-E

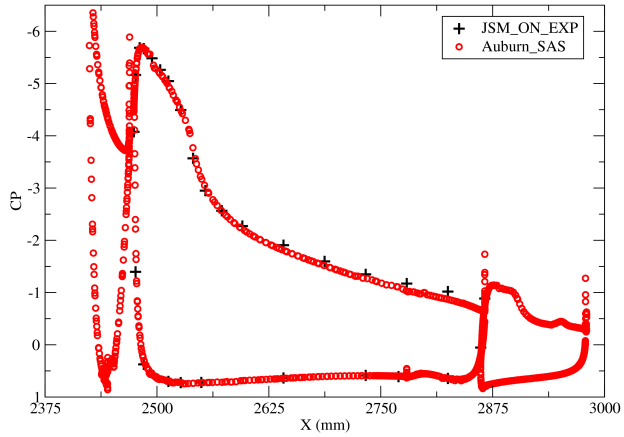

Wing G-G

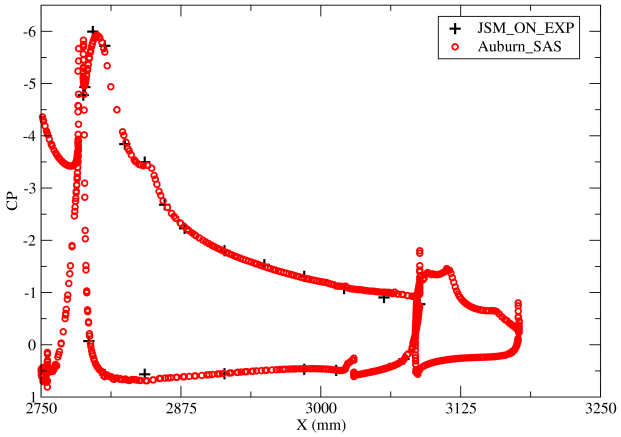

Flap E-E

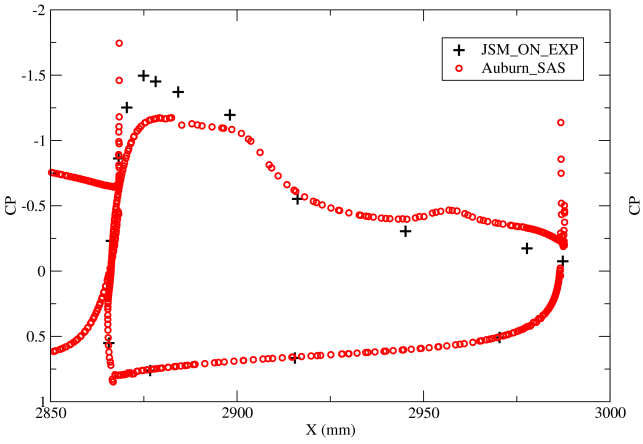

Flap G-G

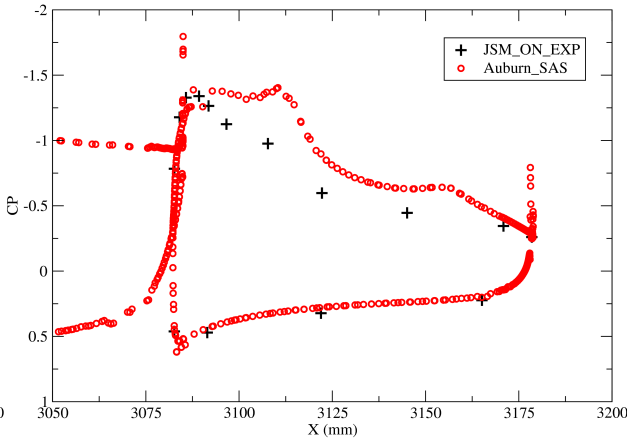

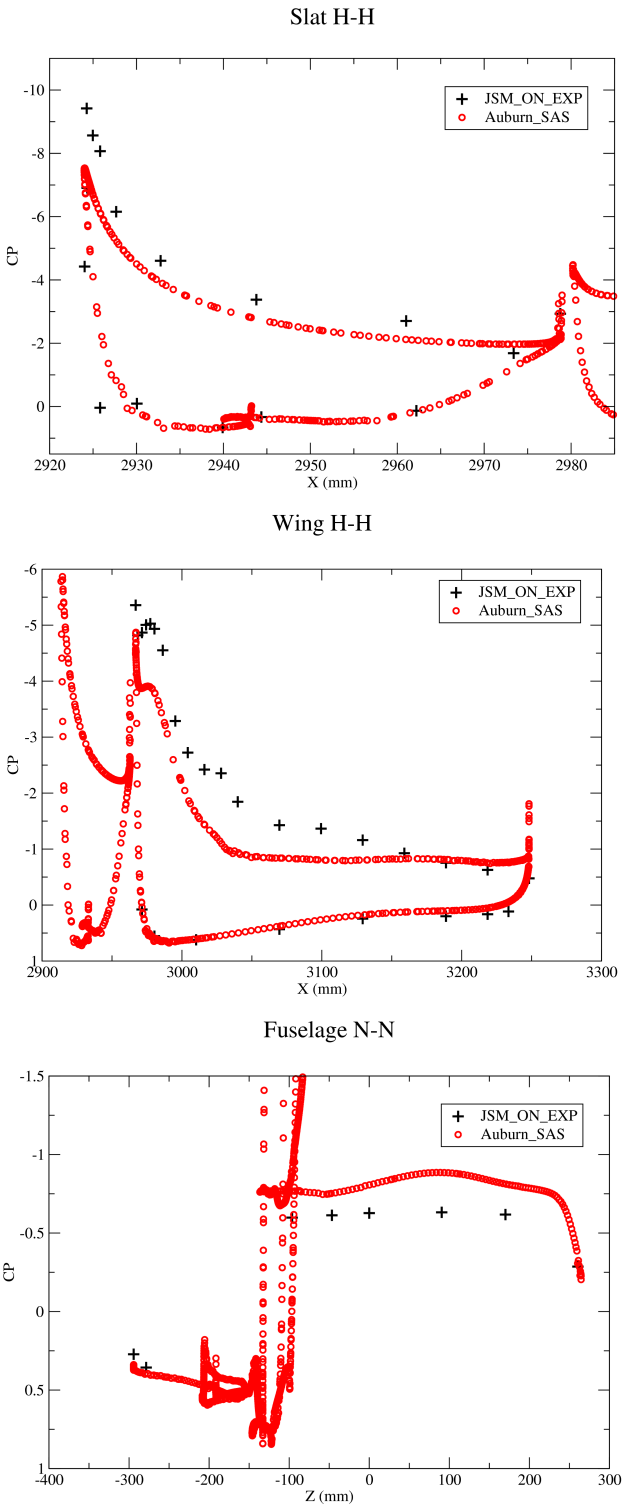

Figure 5.45: JSM: JSM Nacelle/Pylon ON Configuration with Incompressible Solver - C_P Comparison at AOA 21.57^0

The C_P plots in this study with the incompressible solver and the SAS turbulence model match accurately with experiments at lower angle of attack (linear region of the lift curve). The pressure peaks at suction and high pressure side also matches with experiments at lower angle of attack. But as the angle of attack increases, the differences between the suction peak of the numerical solution and the experiments increase drastically. This could be due to the separation on the upper surface of the wing at higher angle of attack. Although this solution with incompressible solver is obtained by pitching the aircraft gradually, the separation is still introduced to the solution. Also towards the tip of the wing (section H-H), the numerical solution deviates from the experiments with the increase in angle of attack. The trends in C_P prediction among JSM Nacelle/Pylon ON and OFF configurations are consistent to each other.

Chapter 6

Conclusions and Future Work

6.1 Conclusions

The main objective of this research was to assess the CFD predictability of high-lift flow fields. Based on this study using *TENASI* as a CFD solver, it can be concluded that CFD shows some promising results in the resolution of high-lift flow fields.

Grid Generation

The grid generation is one of the most challenging aspect of the CFD study of high-lift configurations. It is difficult to create a high quality grid for a high-lift configuration with support brackets which adds complexity to the model. Overly constrained grid with extremely small sized grid elements makes the numerical solution unstable by adding more dissipation and stiffness to the turbulence model especially in the boundary layer.

HL-CRM: Grid Convergence Study

Grid convergence plays a significant effect on the CFD solution of a high-lift configuration. Grid refinement affects the force and moments prediction as well as the C_P and wake velocity resolution of HL-CRM. The solutions obtained using the Auburn Grids and the (provided) Committee grids are comparable with each other with minor deviations which might be due to the differences in the size of the mesh elements used during the grid generation.

JSM: Nacelle Installation Study

Incompressible solver with the SAS turbulence model in *TENASI* shows better agreement with the experiments than a variable Mach version of the governing equations with the

Menter SST turbulence model. From the comparison with the experiment data, although incompressible solver shows better agreement, the incompressible solver with the SAS turbulence model underpredicts lift and overpredicts drag in overall. The solution matches experiments impressively in the linear region of the lift curve at low angle of attack. Unnecessary separation on the low pressure side of the wing at higher angle of attack is one of the reason for underprediction of lift and overprediction of drag. The numerical solution does not imitate the stall characteristics properly and the $C_{L,max}$ remains underpredicted. The angle of attack at which $C_{L,max}$ occurs however matches with the experiments accurately.

From this study it can be concluded that pitching the aircraft from a converged solution at a lower angle of attack improves the overall predictability of the stall characteristics and shows better agreement with the experiments. Although this process is computationally demanding, a better resolution of the flow features is evident using this technique.

The effects of nacelle and pylon installation on a high lift configuration shows improvement in the lift and pitching moment while increasing the overall drag on the JSM. The results obtained from this study is consistent with the experiments, however the change in drag and pitching moment with the nacelle and pylon installation shows better agreement with the experiments than the change in lift with the JSM.

Turbulence Modeling

Regarding the turbulence models, the Wilcox $k-\omega$ model is preferred over other turbulence model in resolving high lift flow fields accepting the model is stable with the given grid. The SAS turbulence model incorporated in *TENASI* was stable with all the configurations involved in this study. Although it slightly underpredicted lift and overpredicted drag, the SAS turbulence model showed impressive flow predictability of the high-lift flow fields. Thus, the SAS turbulence model can be taken as an ideal turbulence model for the resolution of high-lift aerodynamics.

6.2 Future Work

Even with the current advancement in the CFD techniques, the high-lift aerodynamics still seems to be a difficult scenario for CFD to model accurately. More research is needed in CFD to properly resolve the high-lift flow features.

Grid adaptation based on the flow features can be a better alternative to a fixed grid system. This will help to reduce the grid dependencies from a solution. Also, building the grid favorable to the solver in hand will be a better alternative to following the strict guidelines which might leads to some instability issues. More investigation is needed in the numerical aspects of the flow simulation to develop a better preconditioning scheme to the compressible solver which is stable for high-lift flow fields.

Turbulence model plays an important role on the overall CFD performance so there is always room for a better turbulence model. Also, a flow solution with a two equation turbulence model with transition modeling might improve the overall CFD predictability of high-lift flow fields.

Bibliography

[1] Christopher L. Rumsey, Jeffrey P. Slotnick, Michael Long, Robert A. Stuever, and Thomas R. Waymann, "Summary of the First AIAA CFD High-Lift Prediction Workshop," Journal of Aircraft, Vol. 48, No. 6, 2011.

[2] Jeffrey P. Slotnick, Judith A. Hannon, and Mark Chaffin, "Overview of the First AIAA CFD High Lift Prediction Workshop (Invited)," 49th AIAA Aerospace Sciences Meeting including the New Horizons Forum and Aerospace Exposition, AIAA 2011-862, Orlando, Florida, 2011.

[3] Christopher L. Rumsey, and Jeffrey P. Slotnick, "Overview and Summary of the Second AIAA High-Lift Prediction Workshop," Journal of Aircraft, Vol. 52, No. 4, 2015.

[4] Dimitri Mavriplis, Michael Long, and Troy Lake, "NSU3D Results for the Second AIAA High-Lift Prediction Workshop," Journal of Aircraft, Vol. 52, No. 4, 2015.

[5] Mitsuhiro Murayama, Kazuomi Yamamoto, and Yasushi Ito, "Japan Aerospace Exploration Agency Studies for the Second High-Lift Prediction Workshop," Journal of Aircraft, Vol. 52, No. 4, 2015.

[6] David C. Wilcox, "Reassessment of the Scale-Determining Equation for Advanced Turbulence Models," AIAA Journal, Vol. 26, No. 11, 1988.

[7] W. Roger Briley, Lafe Taylor, and Dave Whitfield, "High-Resolution Viscous Flow Simulations at Arbitrary Mach Number," Journal of Computational Physics, Vol. 184, 2003, pp. 79-105.

[8] L. K. Taylor, "Unsteady Three-Dimensional Incompressible Algorithm based on Artificial Compressibility," Ph.D thesis, Mississippi State University, 1991.

[9] D. Stephen Nichols, Kidambi Sreenivas, Steve L. Karman, and Brent Mitchell, "Turbulence Modeling for Highly Separated Flows," 45th AIAA Aerospace Sciences Meeting and Exhibit, AIAA-2007-1407, Reno, Nevada, 2007.

[10] D. Stephen Nichols, "Accounting for Shocks in the $k\epsilon k\omega$ Turbulence Model, "41st AIAA Fluid Dynamics Conference and Exhibit, AIAA-2011-3573, Honolulu, Hawaii, 2011.

[11] F. R. Menter, "Eddy Viscosity Transport Equations and Their Relation to the $k-\epsilon$ model," Journal of Fluids Engineering, Vol. 119, 1997, pp. 876-884.

[12] F. R. Menter, M. Kuntz, and R. Bender, "A Scale-Adaptive Simulation Model for Turbulent Flow Predictions," 41st AIAA Aerospace Sciences Meeting and Exhibit, AIAA-2003-0767, Reno, Nevada, 2003.

[13] Doug S. Lacy, and Anthony J. Sclafani, "Development of the High Lift Common Research Model (HL-CRM): A Representative High Lift Configuration for Transonic Transports," 54th AIAA Aerospace Sciences Meeting, AIAA 2016-0308, San Diego, California, 2016.

[14] Yuzuru Yokokawa, Mitsuhiro Murayama, Hiroshi Uchida, Kentaro Tanaka, Takeshi Ito, and Kazuomi Yamamoto, "Aerodynamic Influence of a Half-Span Model Installation for High-Lift Configuration Experiment," 48th AIAA Aerospace Science Meeting Including the New Horizons Forum and Aerospace Expositions, AIAA 2010-684, Orlando, Florida, 2010.

[15] The 3rd AIAA CFD High Lift Prediction Workshop (HiLiftPW-3), (2017), https://hiliftpw.larc.nasa.gov/index.html.

[16] Saikat Dey, Romain Aubry, B. Kaan Karamete, Eric L. Mestreau, and James L. Dean, "Mesh Generation for High-Lift Aircraft Geometry Configurations," 55th AIAA Aerospace Sciences Meeting, AIAA 2017-0364, Grapevine, Texas, 2017.

[17] William M. Chan, "Best Practices on Overset Structured Mesh Generation for the High-Lift CRM Geometry," 55th AIAA Aerospace Sciences Meeting, AIAA 2017-0362, Grapevine, Texas, 2017.

[18] Carolyn D. Woeber, Erick J. S. Gantt, and Nicholas J. Wyman, "Mesh Generation for the NASA High Lift Common Research Model (HL-CRM)," 55th AIAA Aerospace Sciences Meeting, AIAA 2017-0363, Grapevine, Texas, 2017.

[19] P. A. Davidson, "Turbulence: An Introduction for Scientists and Engineers," 2nd Edition, Oxford University Press, Oxford, UK, 2015.

Appendices

Appendix A

Some Important Equations

1. Coefficient of Lift (C_L)

$$C_L = \frac{Lift}{\frac{1}{2}\rho_\infty V_\infty^2 S_{ref}} \tag{A.1}$$

2. Coefficient of Drag (C_D)

$$C_D = \frac{Drag}{\frac{1}{2}\rho_\infty V_\infty^2 S_{ref}} \tag{A.2}$$

3. Coefficient of Moment (C_M)

$$C_M = \frac{PitchingMoment}{\frac{1}{2}\rho_\infty V_\infty^2 S_{ref} MAC} \tag{A.3}$$

4. Coefficient of Pressure for an Incompressible Flow (C_P)

$$C_P = \frac{P - P_\infty}{\frac{1}{2}\rho_\infty V_\infty^2} \tag{A.4}$$

5. Coefficient of Pressure for a Compressible Flow (C_P)

$$C_P = \frac{P - P_\infty}{\frac{1}{2}\gamma P_\infty M_\infty^2} \tag{A.5}$$